11-6-2015

# Plasma Process Control for Improved PEO Coatings on Magnesium Alloys

Riyad Omran Hussein
*University of Windsor*

# Plasma Process Control for Improved PEO Coatings on Magnesium Alloys

by

**Riyad Omran Hussein**

A Dissertation
Submitted to the Faculty of Graduate Studies
through Engineering Materials
in Partial Fulfillment of the Requirements for
the Degree of Doctor of Philosophy
at the University of Windsor

Windsor, Ontario, Canada

2015

# Plasma Process Control for Improved PEO Coatings on Magnesium Alloys

by

Riyad Omran Hussein

Approved by:


----------------------------------------------

F. Cheng, External Examiner
University of Calgary


----------------------------------------------

S. Das
Civil &Environmental Engineering


----------------------------------------------

H. Hu
Department of Mechanical, Automotive, & Materials Engineering


----------------------------------------------

V. Stoilov
Department of Mechanical, Automotive, & Materials Engineering


----------------------------------------------

X. Nie, Co-advisor
Department of Mechanical, Automotive, & Materials Engineering


----------------------------------------------

D. O. Northwood, Co-advisor
Department of Mechanical, Automotive, & Materials Engineering

June 2$^{nd}$ 2015

# DECLARATION OF CO-AUTHORSHIP / PREVIOUS PUBLICATION

This thesis includes 10 original papers that have been previously published in peer reviewed journals and conference proceedings, as follows:

| Chapter | Publication title/full citation | status |
|---|---|---|
| Chapter 2 | **A-** Hussein R. O., Nie X. and Northwood D. O. (2013), The Application of Plasma Electrolytic Oxidation (PEO) to the Production of Corrosion Resistant Coatings on Magnesium Alloys: a Review, Corrosion and Materials 38 (1), pp. 53-63. | Published |
| | **B-** Production of anti-corrosion coatings on light alloys (Al, Mg, Ti) by Plasma Electrolytic Oxidation (PEO), Riyad O. Hussein, Derek O Northwood, 'In: Developments in Corrosion Protection, (M. Aliofkhazraei, Ed.) InTech Open Publishers, ISBN 980-953-307-1100-2. 2013 | Published |
| Chapter 4 | A- Hussein R.O., Zhang P., Xia Y., Nie X. and Northwood D.O (2011) The effect of current mode and discharge type on the corrosion resistance of plasma electrolytic oxidation (PEO) coated magnesium alloy AJ62, Surface & Coatings Technology, 206 (7) , pp. 1990-1997. | Published |
| | B- Hussein R.O., Zhang P., Northwood D.O. and Nie X. (2011) Improving the corrosion resistance of magnesium alloy AJ62 by a plasma electrolytic oxidation (PEO) coating process, Corrosion and Materials 36 (3), pp. 38-49. | Published |
| Chapter 5 | Hussein R. O., Northwood D. O. and Nie X. (2014) Processing-Microstructure Relationships in the Plasma Electrolytic Oxidation (PEO) Coating of a Magnesium Alloy, Materials Sciences and Applications (MSA), 5 (3), pp. 124-139 | Published |
| Chapter 6 | Hussein R. O., Northwood D. O., Su, J.F. and Nie X. (2013) A study of the interactive effects of hybrid current modes on the tribological properties of a PEO (plasma electrolytic oxidation) | Published |

| | | |
|---|---|---|
| | coated AM60B Mg-alloy, Surface & Coatings Technology, 215, pp. 421–430. | |
| Chapter 7 | Hussein R. O., Nie X. and Northwood D. O. (2013) An investigation of ceramic coating growth mechanisms in Plasma Electrolytic Oxidation (PEO) processing, Electrochimica Acta 112, pp. 111-119. | Published |
| Chapter 8 | Hussein R. O., Northwood D. O. and Nie X. (2013) The effect of processing parameters and substrate composition on the corrosion resistance of plasma electrolytic oxidation (PEO) coated magnesium alloys, Surface & Coating Technology, 237, pp. 357-368. | Published |
| Chapter 9 | Hussein R. O., Nie X. and Northwood D. O. (2013) Effect of cathodic current density on the corrosion protection of the oxide coatings formed on AZ91D magnesium alloy by plasma electrolytic oxidation. Corrosion and Prevention 2013", Australia 2013, paper no. 112. | Published |
| Chapter 10 | Hussein R. O., Nie X. and Northwood D. O. (2014) The roles of the electrolyte composition and concentration on the corrosion resistance of the oxide coatings formed on AZ91D magnesium alloy by plasma electrolytic oxidation, Corrosion and Prevention 2014; Australia 2014; Code 109535 | Published |

I certify that I have obtained a written permission from the copyright owner(s) to include the above published material(s) in my thesis. I certify that the above material describes work completed during my registration as graduate student at the University of Windsor. I am aware of the University of Windsor Senate Policy on Authorship and I certify that I have properly acknowledged the contribution of other researchers to my thesis, and have obtained written permission from each of the co-authors to include the above materials in my dissertation.

In all ten original published papers I was the sole student investigator on the projects reported and had a major role in conducting the wear test, surface analyses and the preparation of the manuscripts. I acknowledge the co-authors as they contributed to the data and results interpretation (wear tests and surface analyses) along with the valuable discussion to reach the main conclusions and also contributed to the final editing of the papers.

I declare that, to the best of my knowledge, my thesis does not infringe upon anyone's copyright nor violate any proprietary rights and that any ideas, techniques, quotations, or any other material from the work of other people included in my thesis, published or otherwise, are fully acknowledged in accordance with the standard referencing practices. Furthermore, to the extent that I have included copyrighted material that surpasses the bounds of fair dealing within the meaning of the Canada Copyright Act, I certify that I have obtained a written permission from the copyright owner(s) to include such material(s) in my thesis.

I declare that this is a true copy of my thesis, including any final revisions, as approved by my thesis committee and the Graduate Studies office, and that this thesis has not been submitted for a higher degree to any other University or Institution.

# ABSTRACT

Plasma Electrolytic Oxidation (PEO) is a high voltage plasma-assisted oxidation process uses an environmentally-friendly aqueous electrolyte to oxidize the metal surfaces to form ceramic oxide coatings which impart a high corrosion and wear resistance. One of the main advantages of PEO process is that it can be applied to treat samples with complex shapes, and surfaces with different composition and microstructure. The PEO process of Mg alloys is strongly influenced by such parameters as electrolyte composition and concentration, current or voltage applied and substrate alloy. Generally, these parameters have a direct influence on the discharging behavior. The discharges play an essential role in the formation and resulting composition of the 3-layer oxide structure. A detailed knowledge of the coating mechanisms is extremely important in order to produce a desired coating quality to reach the best performance of the PEO coatings in terms of corrosion resistance and tribological properties (wear rate, COF). During PEO processing of magnesium, some of the metal cations are transferred outwards from the substrate and react with anions to form ceramic coatings. Also, due to the high electric field in the discharge channels, oxygen anions transfer towards the magnesium substrate and react with $Mg^{2+}$ cations to form a ceramic coating. Although, in general, PEO coating of Mg alloys produces the three-layered structure, the relative proportions of the three-layers are strongly influenced by the PEO processing parameters. In PEO process, the ceramic coating grows inwards to the alloy substrate and outwards to the coating surface simultaneously. For the coating growth, there are three simultaneous processes taking place, namely the electrochemical, the plasma chemical reactions and thermal diffusion. Optical emission spectroscopy (OES) was employed for the discharge characterization by following the substrate and electrolyte element present in the plasma discharge during the coating growth, and to determine plasma electron temperatures. The coating requirements for good tribological properties are somewhat different than for good corrosion performance. However, good tribological performance combined with good corrosion performance can be obtained through control of the PEO processing parameters.

# DEDICATION

To My Lovely Family

# ACKNOWLEDGEMENTS

I would like to express my whole-hearted gratitude to Dr. Derek. O. Northwood and Dr. Xueyuan Nie for both, their instructive and excellent supervision during my studies and research work, as well as their kindness and patience.

Last but not least, my deepest love and gratitude to my beloved family whose spiritual presence was a constant inspiration for continuation.

# TABLE OF CONTENTS

# LIST OF TABLES

**Chapter 10**

# LIST OF FIGURES

**Chapter 5**

**Chapter 6**

**Chapter 7**

## Chapter 8

## Chapter 9

**Chapter 10**

**Chapter 11**

# CHAPTER 1

# INTRODUCTION

## 1.1 Background to this Dissertation

There are many who believe that magnesium is the most exciting engineering material due to its intrinsic characteristics, particularly its light weight, that make it an attractive material wherever weight saving is at a premium, including the automotive and aerospace sectors. The United States federal government has mandated that all automobile manufacturers increase their vehicle fleet miles per gallon average to 35.5 by 2016 [1]. This will challenge automakers to focus on a new, highly fuel-efficient design and strongly suggests extensive use of magnesium alloys in construction [2]. In 2011, the United States Council for Automotive Research (USCAR) proposed a reduction of the mass of the baseline vehicle by 50% by light weighting, or replacing steel with lighter materials Al or Mg [3]. USCAR proposed a list of candidates for substitution materials including: carbon fiber composites, magnesium, aluminum, titanium, metal matrix composites and advanced high-strength steels. By comparing the cost, the recyclability and weight reduction of the proposed new materials, magnesium is the most promising material that fulfills all of the above requirements. This has led to extensive evaluation of the potential use of magnesium in transportation systems, but up to now substantial applications have been limited, e.g. in aircraft components [4]. Currently, magnesium alloys are widely used for automobile components, and are mostly produced by a high pressure die-casting process. Components made from high pressure die-cast, (HPDC) magnesium alloy, such as front and support assemblies, steering wheel armatures, instrument panels and steering column support brackets are playing a vital role in the automotive industry [5]. Indeed, more and more parts, such as the crank cases, doors, camshaft sprocket, gearbox housing, several covers, and the arm of an electric generator, in automobiles have been replaced by magnesium and its alloys [6,7]. But, in fact, many other applications, including aerospace, electronics, textile machinery, printing machines [4,8] and bicycle components, can benefit from a switch to lighter materials given the appropriate surface characteristics. With increasing capacity and falling prices, more and

more design engineers are turning to magnesium as an alternative to plastics, composites, zinc, aluminum, or even steel.

However the limitations of magnesium alloys are primarily their inherently poor corrosion and low wear resistance. Song and Atrens [9] have concluded that internal galvanic attack and the instability of the magnesium hydroxide film formed on the surface of Mg alloys are the two main causes for corrosion of magnesium alloys. There are generally two possible ways to improve the corrosion behaviour of Mg and Mg alloys; modify the composition and microstructure, not only through alloying [10] but also through the development of optimized manufacturing methods and the availability of suitable raw materials and secondly by surface treatments or form coatings [11], which produce protective ceramic, polymer or composite layers. In order for a coating to provide adequate corrosion protection for Mg and Mg alloys, the coating must be uniform, pore-free, well adhered, and self-healing in case physical damage to the coating may occur. However Mg alloys low wear resistance, and galling phenomena which occurs with the counter material, was attributed to their low hardness and to the atomic structure of their crystals respectively [12]. Generally wear can be reduced by using a lubricant with appropriate anti-wear additives or surface treating of the alloys to create hard coating. Recent developments in the plasma electrolytic oxidation (PEO) process allows for the production of oxide layers on magnesium alloys with excellent tribological properties, and the potential to be used in many applications [13].

1.2 **Objective of this Research**

Although a wider picture of the PEO coating growth mechanisms, discharge behaviour and the fundamental characteristics of PEO processing parameters has become more clear, a number of challenges still remain concerning the correlation between processing-structure-properties and performance. This is essential in order to specify the essential elements that can lead to more reproducible and consistent coatings. A detailed study of the relationship between PEO processing parameters and the resulting microstructure properties and, hence, coating performance is required. The present study examines possible approaches for improving the corrosion and wear resistance of Mg alloys by changing the current mode, current density and electrolyte chemistry.

The objectives of this study were to:

- Study plasma/substrate interaction and plasma chemistry using an optical emission spectroscopy (OES) method and to characterize plasmas in terms of their electron density and discharge temperature, and their relationships with the layer formation mechanisms.
- Better understand the parameters that influence the discharge phenomena and their effect on the mechanisms of coating formation.
- Study the ceramic coating growth mechanisms in PEO processing
- Study the relationships between the alloy composition and microstructure and the coating microstructure.
- Study the interactive effects of PEO process parameters on corrosion and tribological properties as a general guide to the coatings qualities.

## 1.3 Organization of the Dissertation

This dissertation is divided into eleven main chapters. Following an introduction in Chapter 1, a literature review of the PEO coating process, and specific aspects of plasma electrolytic oxidation of magnesium alloys, is given in Chapter 2. Chapter 3 describes the materials and experimental details. The influence of current mode on the PEO process performance and improving the corrosion properties of the coatings on the Mg AJ62 alloy are described in Chapter 4. Chapter 5 describes a study of processing-microstructure relationships in the PEO coating of AM60B magnesium alloy. A study of the interactive effects of hybrid current modes on the tribological properties of a PEO coated AM60B Mg-alloy are presented in Chapter 6. Chapter 7 presents an investigation of ceramic coating growth mechanisms in PEO processing. In Chapter 8, the effect of processing parameters and substrate composition on the corrosion resistance of PEO coated magnesium alloys are presented. Chapter 9 describes the effect of cathodic current density on the corrosion protection of the oxide coatings formed on AZ91D magnesium alloy by plasma electrolytic oxidation. The roles of the electrolyte composition and concentration on the corrosion resistance of the oxide coatings formed on AZ91D

magnesium alloy by PEO process are given in Chapter 10. Chapter 11 summarizes the results from the present study and offers some suggestions for future work.

## References

[1]     Aleen M and Javers E, Obama announces new fuel standards. www.politico.com. May 19, 2009

[2]     Brettmann M, Reinhold B, and Schnattinger H, "The use of magnesium in cars – Aspects of corrosion," Magnesium Alloys and Their Applications, 2006, ed. K. U. Kainer, (Wiley-VCH, Verlag)

[3]     Automotive Materials Partnership LLC (USAMP), Department of Energy (DOE), Final Report, Projects from January 1, 2002 through January 31, 2011, USAMP REPORT # DOE/OR22910, 2011

[4]     Ehrenberger S., Friedrich H. EAssessment of Greenhouse Gas Emissions of Magnesium Use in Transport. Light Metal Age ( February 2014) 50-53.

[5]     Cho K, Sano T, Doherty K, Yen C, Gazonas G, Montgomery J, Moy P, Davis B and DeLorme R, Magnesium technology and manufacturing for ultra lightweight armored ground vehicles, ARL-RP-236. Aberdeen Proving Ground, MD: Army Research Laboratory; 2009.

[6]     Hakamada M, Furuta T, Chino Y, Chen YQ, Kusuda H, Mabuchi M. Life cycle inventory study on magnesium alloy substitution in vehicles. Energy 32 (2007) 1352-60.

[7]     Kulekci M K, Magnesium and its alloys: applications in automotive industry, The International Journal of Advanced Manufacturing Technology, 39 (2008) 851– 865

[8]     Evans G B, "Applications of magnesium in aerospace," Magnesium Technology, Proc. London Conf., November 1986, (Institute of Metals, London, (1987), 103-109.

[9]     Song G L, Atrens A, Corrosion mechanisms of magnesium alloys, Advanced Engineering Materials, 1 (1999) 11-33.

[10]    Kaesel VT, Tai PT, Bach FW, Haferkamp H, Witte F, Windhagen H. Approach to control the corrosion of magnesium by alloying. In: Proceedings of the Sixth International Conference on Magnesium Alloys and their Applications. New York: Wiley VCH, 2004. p. 534–539.

[11]    Gray JE, Luan B. Protective coatings on magnesium and its alloys – a critical review. J Alloys and Compounds 336 (2002) 88–113.

[12]    Dobrzanski, L.A., Tanski, T., Cizek, L. and Domagala, J., Mechanical properties and wear resistance of magnesium casting alloys, Journal of Achievements in Materials and Manufacturing Engineering, 31 (2008), 83-90.

[13]    Walsh FC, Low CTJ, Wood RJK, Stevens KT, Archer J, Poeton AR, et al. Review. Plasma electrolytic oxidation (PEO) for production of anodised coatings on lightweight metal (Al, Mg, Ti) alloys. Transactions of the Institute of Metal Finishing, 87(3) (2009) 122–35.

# CHAPTER 2

# LITERATURE REVIEW

**Published in:**

## 2.1. Introduction

There seems to be general agreement that magnesium is a most exciting engineering material due to its intrinsic characteristics particularly its light weight, that make it an attractive material wherever weight saving is at a premium, including the automotive and aerospace sectors. With increasing capacity and falling prices, more and more design engineers are turning to magnesium as an alternative to plastics, composites, zinc, aluminum, or even steel. However, the application of magnesium alloys has been limited by their susceptibility to corrosion and inferior wear performance. Magnesium alloys exhibit very poor corrosion resistance caused by their chemically active nature, especially galvanic corrosion, which can further cause severe pitting corrosion on the metal surface resulting in decreased mechanical stability and an unattractive appearance [1,2]. One of the major steps in improving the corrosion resistance of magnesium alloys is considered to be the introduction of high purity alloys [3]. These impurities and intermetallic compounds "serve as intense local cathodes, driving anodic dissolution" of the magnesium and hence, reducing the corrosion resistance [4]. The relatively poor wear performance of magnesium and its alloys is related to a low hardness, magnesium's high reactivity and relatively low melting point. The study by Chen and Alpas [5] for AZ91D alloy has shown two wear regimes, mild wear and severe wear, which are identified to be

due to oxidational wear for the mild wear regime and melt wear and severe plastic deformation wear, for the severe wear regime.

## 2.2. Coatings for Magnesium Alloys.

So far, a number of theoretical and experimental studies had been performed addressing different aspects of the corrosion of magnesium alloys. An overview of the different techniques used for the coatings of Mg and Mg alloys is shown in Fig. 2.1 [6].
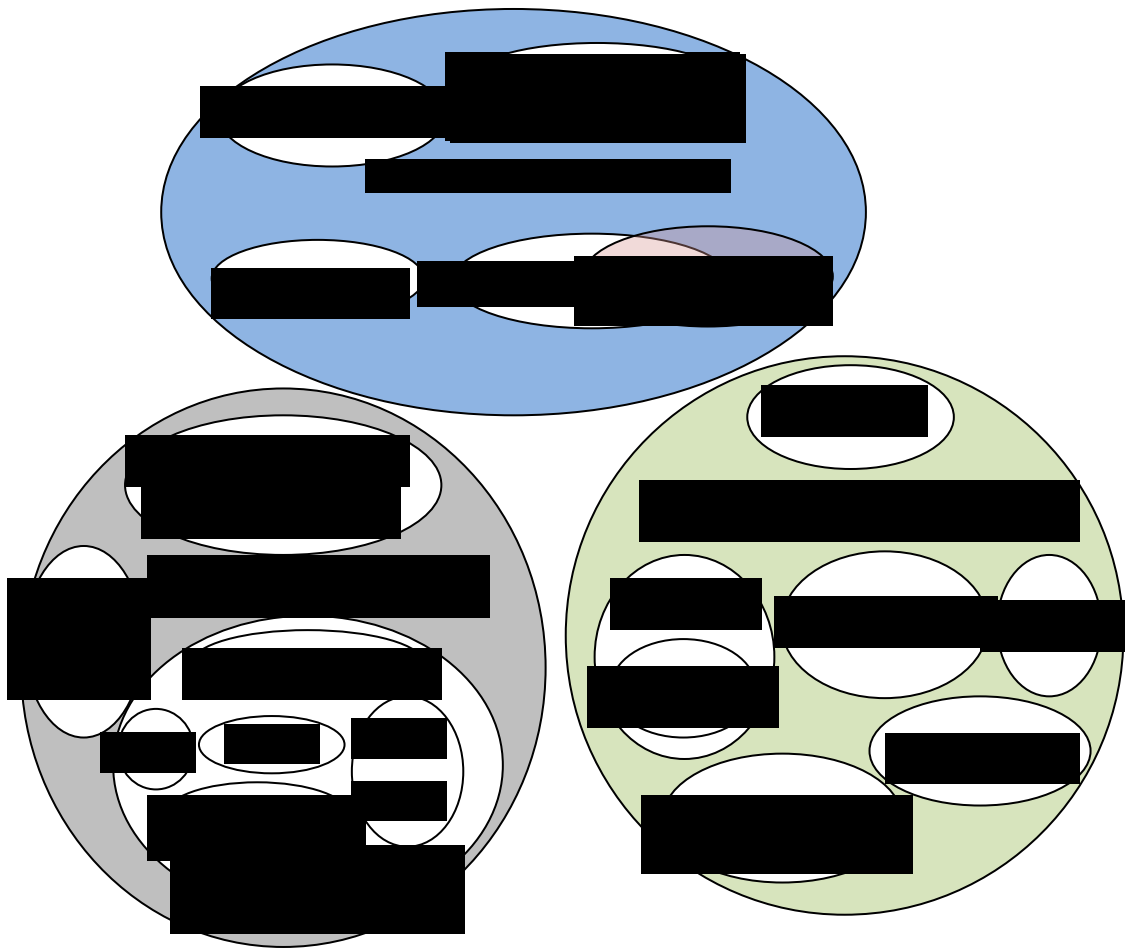


Fig. 2.1 Schematic Diagram showing coatings technologies for magnesium alloys [adapted from [6]].

Generally, coatings can be divided into three classes: conversion coatings, organic and inorganic deposited coatings. Conversion coatings are produced by chemical or electrochemical reactions between the substrate and the aqueous solutions to form an

oxide layer that simultaneously grows inwards and outwards. Such conversion coatings represent an effective way to increase the corrosion and wear resistance of magnesium alloys or, as a pre-treatment, to enhance the adhesion of a final deposited coating [7]. Organic finishing including Sol-gel, painting and powder coating is typically used in the final stages of coating process. The method most applied to obtain organic coatings is simple dipping in an organic based solution. Protective coatings can also be produced from inorganic deposition coatings such as from the gas phase or other physical methods including plasma spraying, chemical vapor deposition (CVD), Diamond like coating (DLC) and lasers. Gas phase coatings are inappropriate for applications involving geometrically complex components. Moreover, physical deposition methods involve high energy consumption, high costs and complex facilities.

The most common conversion layers are from electrochemical anodization. Recently, much research has been focused on the selection of electrolytes, including alkaline solutions with additives of phosphate, silicate, and borate substances [8,9]. However, the anodizing process sometimes suffers from relatively poor performance for example; the European Space Agency was having problems with the black anodizing process [10]. A comparison of the common surface treatments and coatings is given in Table 2.1 [11]. It is also common to combine two or more techniques for surface coating and/or modification, in order to obtain properties that are unattainable using an individual technique.

The PEO process can be considered as a combination of anodizing (electrolytic oxidation) and plasma discharging processes. The main similarities between the PEO and anodizing processes are that both of them involve oxidation of the substrate using an electrolytic bath, and that the first stage of the PEO process is an anodization process.

The PEO process can be distinguished from low voltage anodizing in aqueous solutions by its operation at electrode potentials greater than the typical breakdown voltages of the original oxide films (350-600 V) in AC, DC or pulsed AC/DC modes with asymmetric anodic and cathodic potential peak waveforms, depending on the alloy and electrolyte composition [12,13]. PEO also operates differently from high energy plasma coating under dry conditions in a controlled gas pressure chamber.

Table 2.1 A comparison of the common surface treatments and coatings for Mg- alloys [adapted from [11]].

| Treatment/coating | Drawback (general) | Drawback (environment) |
|---|---|---|
| Conversion (chromate, phosphate) | Easily damaged | Toxic, particularly Cr(VI) |
| Anodizing | Sensitive to impurities in the base metal to be coated | Sulphuric acid baths |
| Organic/polymer | Weak mechanical and corrosion resistant properties | Poor recyclability |
| Gas phase deposition (PVD, CVD) | Thin, porous | Chlorine emission |
| Thermal spray, cold spray | Not suitable for components with complex geometry. Use of more noble materials that can cause corrosion at interface | None |
| Plasma electrolytic oxidation | Lack of data on coating performance in practice | None |

It has been shown that PEO room temperature technology has a number of unique advantages: including technological simplicity and the possibility to coat any size and/or complex structure including welded and riveted joints, and heterogeneous alloys [8]. Pretreatments and post treatments are not strictly necessary for the PEO, except for water rinses; this reduces environmental concerns with respect to pretreatment and post treatment solutions. The PEO process is capable of producing uniform and very thick coatings on the inner and outer surfaces of the substrate materials [14]. One of the main advantages of the PEO coating is that the oxide coating is integral with the metal substrate because the coating is a result of substrate oxidation. A comparison between PEO and the hard anodization processes is given in Table 2.2.

Table 2.2 Comparison of PEO with HA processes.

| Process | PEO | HA |
|---|---|---|
| Voltage and current density | High | Low |
| Deposition rate | Fast (1~2μm/min) | Slow (~0.3μm/min) |
| Oxidation mechanism | Chemical/ electrochemical and plasma chemical reactions | Chemical/electrochemical reactions |
| Coating on selected alloys | Practical for various kinds of Al, Mg and Ti alloys | Limited (not used for 2000-series alloys, high zinc or silicon Al alloys and Al casting alloys) |
| Microstructure | Amorphous and crystalline phase / Inner dense layer and outer porous layer | Amorphous / Columnar porous layer and very thin barrier |
| Corrosion resistance (Relative) | Excellent (5) | Good (1) |
| Hardness | High (~Hv1600) | Low (Hv600 max) |
| Wear resistance (relative) | Excellent (30) | Fair (2) |
| Thermal protection | Excellent | Good |
| Electrolyte | Alkaline solution | Acid solution |
| Dielectric strength | Excellent | Fair |

## 2.3 PEO Processing

The formation of oxide films on metals using a PEO-like process was first investigated at the beginning of the twentieth century by Günterschulze and then Günterschulze and Betz [15]. They published their first studies on the electrolytic spark discharge produced on an aluminum foil in the early 1930s. In the 1960s and 70s scientists in the former Soviet Union investigated the anodizing process at potentials of over 200 volts for developing parts for the submarine sector and for military purposes. This led to plasma electrolytic oxidation (PEO) technology. The process for depositing an oxide coating on aluminum using the PEO process was first reported by Markov and co-workers in the 1970s [16,17], and Yerokhin et al [18] identify Markov as the 'father' of the PEO process. Many other researchers worked with the plasma electrolytic oxidation process throughout the 1980s [19,20]. It wasn't until the 1990s that the PEO process gained worldwide recognition as an eco-friendly technology for depositing the tribologically superior ceramic coatings on aluminum and magnesium alloys [18]. Plasma electrolytic oxidation (PEO) technique has been developed quickly in recent years and is attracting

increased attention from both academic institutions and many industries [7,21]. To date, there are thousands of a scientific publications dealing with a plasma electrolytic oxidation technology that are distributed in a wide variety of journals and conference proceedings.

Plasma Electrolyte Oxidation (PEO) is a novel surface engineering technology, considered as one of the most cost-effective and environmentally friendly ways to improve the corrosion and wear resistance of magnesium and magnesium alloys [22-23]. A driving force for these developments is the avoidance of expensive equipment required for competing vacuum-based plasma technologies. The PEO method can be used to form a thick, hard and adherent ceramic-like coating on the surface of Mg alloys as well as of lightweight metals (Al and Ti) and their alloys [18]. The substrate is immersed in an alkaline electrolyte (containing neither the concentrated sulphuric acid nor the chromate ions used for hard anodizing) and a high potential is applied to it. Different current modes have been utilized in the PEO treatment including, DC, AC, unipolar and bipolar current modes [18,24]. The formation mechanisms of the coating layer by PEO are complex due to the involvement of electro-, thermal-, and plasma- chemical reactions in the electrolyte [8]. PEO is certainly one of the most promising surface treatments for magnesium and magnesium alloys since it can provide both corrosion protection, and wear resistance. The high dielectric strength of the ceramic layers also reduces contact corrosion by preventing or eliminating the flowing of the current between dissimilar metals.

The effects of the process parameters on the characteristics of the PEO coatings have been investigated in a number of different studies. Some publications deal with the influence of the electrolytes which are based on an alkaline solution with additions of silicates, phosphates and or aluminate [8] where the effect of using a combination of electrolytes is the production of different cations and anions in the solution which accordingly influences the resultant coating: see for example the work of Ghasemi et al [9, 22]. Other studies have examined the effect of current mode [13], current density [25], process time [26] and the chemical composition of the substrate materials [27].

PEO technology can be applied to coat a variety of materials, such as aluminum, magnesium, titanium, and zirconium. It can also be applied to alloys that are difficult to anodize with conventional anodizing processes, such as high copper content and high

silicon content aluminum alloys (2000 series and A380), and magnesium alloys, with the deposition of layers such as phosphates, silicates and aluminates oxides [18]. This enables the surfaces of metals such as steel, stainless steel and titanium to be converted into very hard materials like $TiN_2$, $TiB_2$ or iron carbides.

A schematic diagram of the commercial setup for PEO coating shown in Figure 2.2, where the PEO coating system used to produce the oxide coatings is similar to that used for electroplating or anodizing. It consists basically of a water-cooled container, with the alkaline electrolyte, a high anodic potential is applied to it (typically several hundreds of volts) that trigger numerous micro-discharge events at the metal-electrolyte interface, generating high instantaneous temperatures and pressures (T > 4000 K [12] and p ~ 100 GPa, [18]). A stainless steel plate in the bath acts as a counter-electrode (cathode) with the coupons as the anode. Different current modes have been utilized in the PEO treatments [7,13,28] which play important roles in the consequent voltage breakdown, local melting and oxidation of the substrate, quenching and re-crystallization processes. The growth rate, porosity level and microstructure of PEO coatings are significantly influenced by the current mode. Technically, PEO can be made either by current or voltage controlled. For the current control, during the coating process, the voltage is increasing gradually with process time, as the coating thickness increased, so as to maintain the fixed current density. However, for the voltage control, the current decreases with process time as the oxide film thickness increased. The optimization of the timing (frequency), amplitude, and pulse shape of both anodic and cathodic electrical pulses are essential to achieve controllable, hard, smooth, high growth rates with minimum defect coatings structure [29].
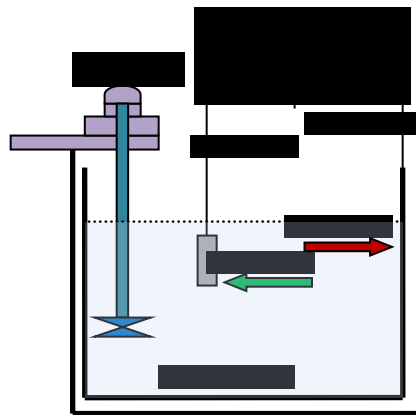


Fig. 2.2 Schematic diagram of the PEO apparatus.

During the PEO process different type of discharges will take place [12,29]. An important consequence of the occurrence of those discharges is the development of metallurgical processes in the growing oxide layer, which are induced by the heat liberated in discharge channels from electron avalanches. Because of the local high temperature and the strong electric field, molten oxide is ejected from the coating/substrate interface into the coating surface where it is rapidly solidified and re-crystallized by the electrolyte. Hence, the formation mechanisms for the coatings are complex due to the involvement of electro-, thermal-, and plasma- chemical reactions in the electrolyte [12].

The PEO process can be distinguished from low voltage anodizing in aqueous solutions by its operation at electrode potentials greater than the typical breakdown voltages of the original oxide films (400-600 V) in AC, DC or pulsed AC/DC modes with asymmetric anodic and cathodic potential peak waveforms, depending on the alloy and electrolyte composition [18]. PEO also operates differently from high energy plasma coating under dry conditions in a controlled gas pressure chamber. It is commonly accepted that the discharge in PEO occurs when the applied voltage reaches a certain critical value corresponding to the breakdown of the oxide layer (or at least of the barrier part of it) formed on the sample surface: this leads to the development of intense light emission generated at the numerous micro-discharge sites [18].

## 2.4 PEO coatings for magnesium alloys.

The PEO process involves the creation of plasma discharges around a metal component immersed in an environmentally friendly electrolyte. The discharge events have a profound effect on coating microstructure, and hence on the physical and mechanical properties of the coating [12]. During PEO coating, there are three simultaneous processes taking place, namely the electrochemical reactions, the plasma chemical reactions and thermal oxygen diffusion.

In general PEO coatings on Mg alloys have been found to have a three-layered structure as shown in Figure 2.3 for an AM60B alloy. Figure 2.3(a) is a SEM micrograph of the surface of the coating. Figure 2.3(b) is a SEM micrograph of a cross-section of the coated alloy. Figure 2.3(c) is a schematic showing a porous outer layer, an intermediate layer

that is relatively dense and a thin inner dense (barrier) layer that is well adhered to the substrate. Although it is the intermediate dense layer that can provide good mechanical properties (eg wear) and corrosion protection, it is the inner dense layer that ultimately provides the best corrosion performance [30].

Examination of the surface morphology of the coatings, Figure 2.3(a), shows pores of different size: the size reflecting the strength of the discharges that produced the pores. There are both open and closed pores. The relatively large open pores are concentrated on the surface of the PEO coatings whereas the closed pores are present in the middle region of the coating. The surface of the coatings shows a 'pancake' structure where the center of each pancake is a discharge channel through which the molten magnesium surged out of the channel and was quickly solidified by the relatively cool electrolyte, leaving distinct boundaries that define each pancake. The uneven melting and sintering effect causes the formation of a rough surface which could adversely affect the wear performance through an increase in the coefficient of friction (COF). The channels at the center of the pancake can penetrate as far as the substrate surface which will degrade the overall corrosion resistance. Thus, in producing PEO coatings, the elimination, or at least minimization, of the discharge channels is of primary concern.
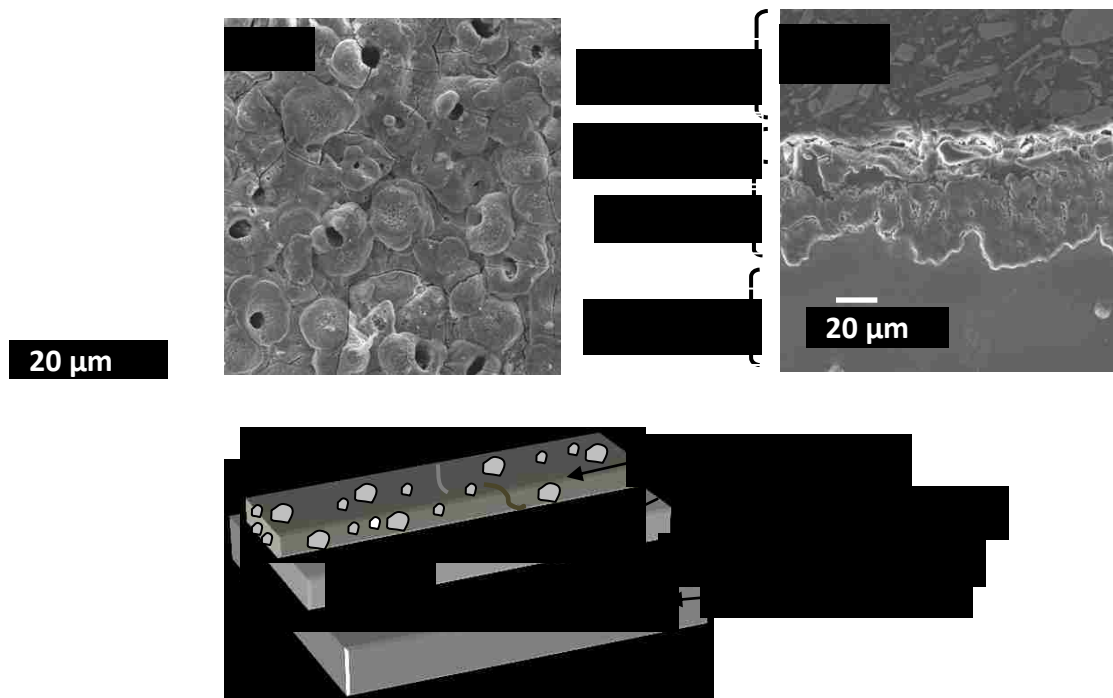


Fig. 2.3 SEM micrographs of PEO coating on AM60B alloy showing (a) the surface morphology and (b) cross-section. (c) general schematic.

## 2.5 Specific Aspects of Plasma Electrolytic Oxidation Of Magnesium Alloys.

Coating surface morphology, porosity, structure and corrosion behavior of ceramic coatings on Mg-alloys, are affected by many parameters including, electrolyte composition and concentration, the substrate composition, and the process parameters (including current density, current mode, applied voltage, temperature, and treatment time.

### 2.5.1 Electrolyte Effects.

The electrolyte chemistry (concentration and composition) is an important parameter affecting the PEO discharge characteristics and breakdown voltage, and thereby microstructure, porosity, and thickness of the PEO coatings. Electrolytes typically used in PEO are environmentally friendly, free of chrome ions, non-corrosive, inexpensive, and easy to make up and maintain. The PEO coatings on Mg alloys and other lightweight alloys are normally produced in KOH/NaOH (base electrolyte) with the addition of the silicate, phosphate, aluminate [28,31-32] which can cause an increase of electrolyte conductivity and decreases the voltage breakdown. XRD patterns for PEO coatings on Mg alloys show that the coatings are comprised of amorphous and crystalline phases such as MgO, $Mg_2SiO_4$, $Mg_3(PO_4)_2$ or $MgAl_2O_4$, depending on the electrolyte [22,31]. While the temperature of the electrolytes should be kept below 40 $^o$C, normally using a water cooling system, the local plasma temperature in the discharge channels is higher than 4,OOO K, and it is this very high temperature leads to the formation of oxide coatings. Tungstate, zirconate and permanganate have also been explored as additives in the electrolytes used to prepare PEO coatings on Mg alloys [33]. An enrichment of the $MgAl_2O_4$ phase in the coating, together with a minimum amount of cubic MgO, has been shown to improve the corrosion resistance of the coated alloy [34]. $MgAl_2O_4$, which is a spinel phase is also much harder (7.5-8.0 Mohs scale) than MgO (6.0-6.5) or Mg (2.5) and can provide better wear resistance.

The coatings formed using only KOH at different concentrations, consist of the unstable and easily corroded MgO phase [25,31]. The phosphate electrolytes and silicate electrolytes enhance both the corrosion resistance and the hardness of the PEO coatings [31,32], where the insoluble phases in water $Mg_2SiO_3$, $Mg_2SiO_4$, $MgAlPO_5$ and $Mg_2Si_3O_8$

are formed in the coatings [34,35]. The use of sodium aluminate (NaAlO$_2$) on AJ62 Mg-alloys was investigated by Zheng et al [34] using unipolar current mode and the effects of additives (KF, NaOH, and KOH) in a (NaAlO$_2$) based electrolyte, on the corrosion characteristics of PEO coatings on AZ91D Mg alloy were examined by Ryu et al [36]. Fluoride is incorporated into the oxides during PEO, where there is the addition of potassium fluoride KF in the electrolyte. This resulted in coatings with minimum defects and pores and a high growth rate of the coatings, together with the formation of the insoluble MgF$_2$ phase, which enhances the corrosion resistance [33], and may be attributed to the large number of small discharges [37]. The PEO coating obtained in a KF-NaAlO$_2$ electrolyte exhibited the highest corrosion resistance, which has been attributed to the presence of a thick, fluoride (F)-containing inner dense barrier layer with crystalline MgAl$_2$O$_4$ [38]. However, due to environmental protection or health concerns, other additives such as CrO$_3$, H$_3$BO$_3$ [39], KF [31] are not extensively used [40].

## 2.5.2. Electrical Parameters.

Although, in general, PEO coating of Mg alloys produces the three-layered structure shown in Figure 2.3, the relative proportions of the three-layers, their thicknesses, microstructure, porosity, phase content and composition are strongly influenced by the substrate composition, electrolyte composition and concentration and the PEO process parameters, including current density, current mode, applied voltage, frequency and duty cycle ($t_{on}/(t_{on}+t_{off})$), and treatment time. Increasing the current density and/or voltage leads to an increase in layer thickness, an enlargement of the surface craters and increased porosity and other coating defects. The growth rate, porosity level and microstructure of PEO coatings formed on Mg alloys are significantly influenced by the current mode. By adjusting the cathodic to anodic current ratio and their timing ($t_{on}$ and $t_{off}$) the strongest plasma discharges can be eliminated, or at least reduced.

With the aim of improving the characteristics of the ceramic coatings, many attempts have been made to improve the supplied current regimes, incorporating different forms and duration of the current pulses. For all PEO power sources, the electrical parameters (current density, duty ratio and pulse timing) play very important roles in the growth of the coating. Different current modes have been utilized in the PEO processing including

15

DC, AC, unipolar and bipolar current modes [13,39,41]. For a DC source, due to the difficulties in controlling the surface discharge characteristics, it is only used for simple-shape components and thin coatings. A pulsed DC source can generate different current waveforms, providing the potential to adjust the plasma discharge duration. Thus the coating composition and structure can be controlled. Usually for the DC and pulsed DC PEO of magnesium alloys, the coating includes significant amounts of magnesium oxide and hydroxide, leading to poor corrosion protective properties and weak coating adhesion to the substrate [7,9,42]. An AC source can also control the process by means of arc interruption [41,43]. By changing the capacitance of the source in both half-cycles, the ratio of amplitudes of positive and negative current can be independently adjusted. However, the limitations in power (usually $\leq$ 10kW) constrain the range of its application. Also, the commonly used current frequency (50 Hz) can provide only a limited ability to control the discharge duration [43]. Recent studies on the effect of power supply modes on PEO coating properties have paid more attention to the bipolar current mode. Researchers [13,44] have tried to modify the morphology and structures of oxide coatings by altering the sparks during the PEO process. The properties of the plasma discharges themselves in the bipolar current mode differ from those of discharges obtained using a unipolar current mode. From the plasma discharge point of view, a significant reduction in the strong discharges [12] can reduce the detrimental effects associated with such discharge events. Coatings produced using a bipolar pulsed DC have a dense and fine-grained morphology. No trace of brittle fracture was observed. Comparatively, the coatings treated using AC exhibited brittle fractures indicating formation of some brittle fused phases on the surface. At present, the pulsed bipolar PEO power source is being widely used due to its ability to achieve high quality coatings that have a higher normalized thickness of functional layer (dense layer), high corrosion resistance, and good adhesion to substrates [13] than those coated by the AC method. Recent work by Gnedenkov et al. [13] utilized a pulsed bipolar current mode to make a dense and uniform oxide coating on a MA8 magnesium alloy with a fine-grained microstructure.

**2.5.3 Electrochemistry of Plasma Electrolytic Oxidation (PEO)**

The growth of the oxide coating mainly occurs due to three different, yet simultaneous, processes, namely: the electrochemical reactions [18], the plasma chemical reactions [8,45-47] and thermal diffusion [24]. The electrochemical formation of surface oxide layers can occur through different mechanisms depending on the electrolyte, eg. silicates, aluminates, phosphates. The PEO coatings are usually produced by AC or bipolar current mode, containing both anodic and cathodic components. An early investigation of the basic electrochemical processes of AC PEO coatings on Ti, has been carried out by Yerokhin et al [47] using AC current mode and a complex aluminate-base electrolyte. According to their study an oxide layer formation is induced both by the ionic component of the current which is transmitted via surface discharges and by the anodizing current passing across the surface which is free of discharges (Figure 2.4). The other components of the current cause secondary electrochemical processes which lead to liberation of electrode gases ($H_2$ and $O_2$) and anodic dissolution of the titanium metal as shown in Figure 2.4.
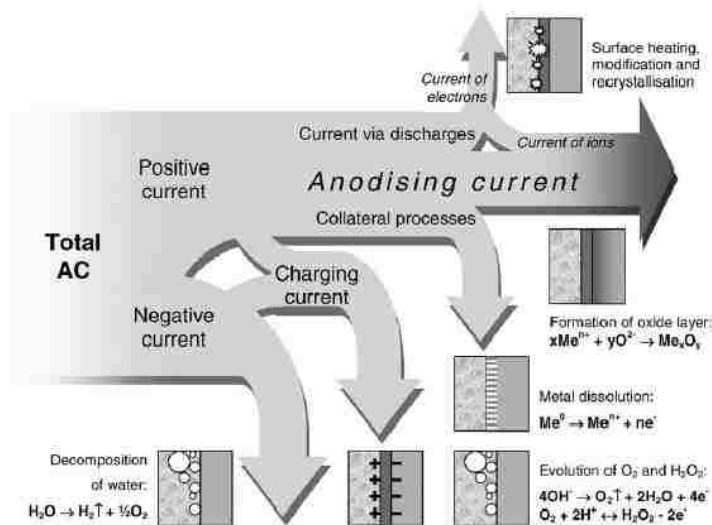


Fig. 2.4 Schematic diagram of current distribution during the PEO treatment of metals in AC mode [47].

For the PEO process on Mg alloys, the main electrochemical reactions occurring at the coating/electrolyte interface using silicate-, aluminate- or phosphate- containing electrolytes are as follows [48]:

During the PEO process the Mg ions are produced by the following reaction:

$$Mg \rightarrow Mg^{2+} + 2e^- \qquad\qquad \textbf{2.1}$$

These ions can be combined with $AlO_2^-$ anions in the alkaline solution to form $MgAl_2O_4$ as in reaction (2.2)

$$Mg^{2+} + 2AlO_2^- \rightarrow MgAl_2O_4\downarrow \qquad\qquad \textbf{2.2}$$

For $SiO_3^{2-}$ anions

$$2Mg^{2+} + SiO_3^{2-} + 2OH^- \rightarrow Mg_2SiO_4\downarrow + 2H_2O \qquad\qquad \textbf{2.3}$$

For $PO_4^{3-}$ anions

$$3Mg^{2+} + 2PO_4^{3-} \rightarrow Mg_3(PO_4)_2\downarrow \qquad\qquad \textbf{2.4}$$
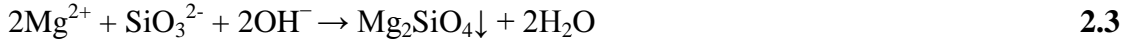
Also, magnesium hydroxide $Mg(OH)_2$ is formed on the magnesium surface by:

$$Mg^{2+} + 2OH^- \rightarrow Mg(OH)_2 \qquad\qquad \textbf{2.5}$$

The cation released from the metal (reaction (2.1)) combines with the anion in the electrolyte to form compounds, $Mg_2AlO_4$, $Mg_2SiO_4$, $Mg_3(PO_4)_2$ or $Mg(OH)_2$ by reactions (2.2), (2.3), (2.4) and (2.5) depending on the electrolyte. Due to the thermal energy from the discharges in all PEO stages, the hydroxide is dehydrated to produce magnesium oxide MgO [48]. This reaction requires a high temperature, which is achieved during the discharge process and depends on the applied current density

$$Mg(OH)_2 \rightarrow MgO\downarrow + H_2O \qquad\qquad \textbf{2.6}$$

Hsiao and Tsai [49] showed that the presence of $Al(NO_3)_3$ in the base electrolyte resulted in the formation of $Al_2O_3$ and $Al(OH)_3$ phases in the coating. The presence of $Al_2O_3$ in the coating improves the corrosion resistance in 3.5% NaCl.

## 2.6. Corrosion protection afforded by PEO coatings for Mg-Alloys.

Magnesium alloys exhibit very poor corrosion resistance due to their chemically active nature, especially internal galvanic corrosion [50], which can further cause severe pitting corrosion on the metal surface resulting in decreased mechanical stability and an unattractive appearance. For coated metals, including Mg-alloys, the corrosion performance of coatings is determined by the time taken to initiate corrosion in the metal substrate since this is much shorter than the time taken for the coating to degrade [51]. Generally the corrosion resistance of PEO-coated magnesium alloys depends on many factors that are summarized schematically in Fig 2.5.

The overall protective abilities of the PEO coatings are governed by:

- Coating structures, mainly coating compactness in terms of porosity and other defect levels

- Relative thicknesses of the three layers, particularly the coating/substrate interface layer,

- Chemical composition of the coating.

Therefore, the more compact and thicker the coating layers, the more difficult it is for the corrosive anions or oxidants ($Cl^{-1}$ ions) to penetrate to the base magnesium substrate. The coating/substrate barrier layer plays a key role in decreasing the substrate area exposed to the aggressive solution. The phases present in the oxide coatings are also important in the overall corrosion resistance. The spinel phases ($MgAl_2O_4$, $Mg_2SiO_4$) are more resistant to dissolution than MgO which can quite readily be converted to $Mg(OH)_2$ [52].
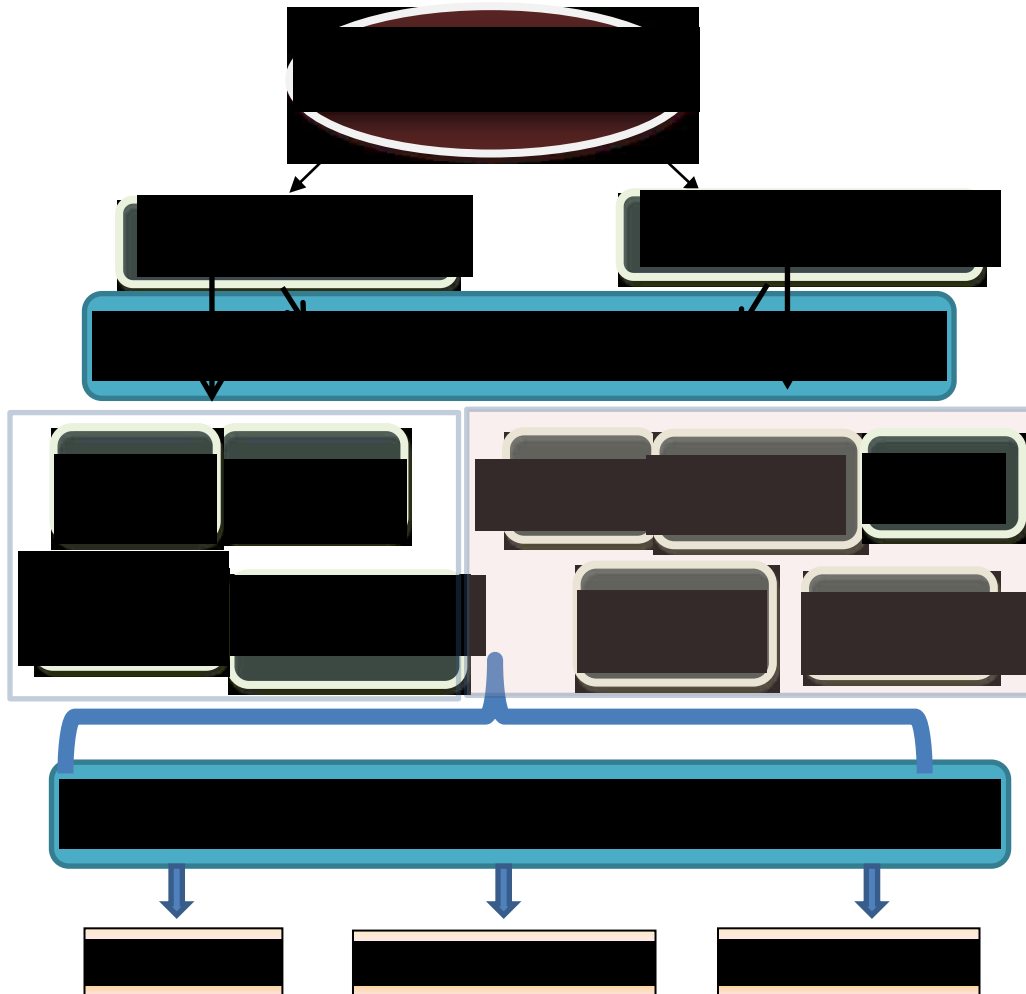


Figure 2.5 PEO processing parameters and performance

Since PEO coatings contain unavoidable pores, although most of them are discontinuous and the number of through thickness pores is very small, the overall corrosion resistance of PEO coated magnesium alloy depends on the retarding effect of the oxide layer porosity level and on the substrate/coating interface corrosion resistance. However, the more compact and thicker the coating and presence of phases more, the slower and more difficult access of the corrosive species can be. The presence of a PEO coated layer on the magnesium alloys causes a decrease of the corrosion current density by up to four orders of magnitude [7].

Song and Atrens have concluded that internal galvanic attack, due to potential difference between matrix and precipitates, and the instability of the magnesium hydroxide film formed on the surface of Mg alloys are the two main causes for corrosion of magnesium alloys [2]. When magnesium is exposed to an aqueous solution, both $Mg(OH)_2$ and $MgO$ can be formed: $Mg(OH)_2$ is in contact with the metal, and on top of the hydroxide layer is a $MgO$ layer that has direct contact with the aqueous solution. For pure Mg, this layer is not protective at pH values below 10.5, unless additional alloying elements are added to pure Mg. The corrosion mechanism for the Mg alloys is more complex than that for pure magnesium, due to a multi-phase microstructure. Shi et al [53] pointed out that corrosion rate of Mg alloys is strongly dependent on the composition of the α-Mg matrix and the distribution of the other phases. Such phases have the tendency to accelerate the corrosion of the α-phase. In order for a coating to provide adequate corrosion protection for Mg and Mg alloys, the coating must be uniform with minimum defects and pores and well adhered.

Test methods most commonly used to determine a corrosion rate of the PEO coatings are potentiodynamic polarization studies and impedance spectroscopy (EIS) [54]. The electrochemical technique of Tafel extrapolation of polarization curves is also widely used for the evaluation of the corrosion of Mg alloys, in particular coated Mg alloys, because it is simple and fast. Electrochemical impedance spectroscopy (EIS) can provide valuable information about surface treatment layers on PEO-coated magnesium, and the interfaces between electrolyte/coating/substrate [55]. It also allows the kinetics of heterogeneous electron-transfer reactions, coupled chemical reactions, or adsorption

processes to be studied, and can provide information about pitting and crevice corrosion [1].

Comparison of the corrosion protection results offered by PEO is very difficult, due to the variation of the experimental test parameters including solution composition, concentration, test time and other parameters. Ma et al. [25] reported that oxide films grown on a AM50 magnesium alloy from a phosphate solution have better corrosion resistance compared with coatings prepared in silicate solutions. However, Liang et al. [56] when comparing the PEO coatings on AM60B magnesium alloy formed in silicate and phosphate electrolytes concluded that PEO coatings produced in a silicate electrolyte are compact and uniform hence exhibit better corrosion resistance than coatings formed in a phosphate electrolyte, which were relatively porous. Liang et al [57] investigated the electrochemical degradation of a silicate- and phosphate-based PEO coatings on a AM50 magnesium alloy using a pulsed DC power supply in NaCl solutions of different chloride ion concentrations (0.01, 0.1, 0.5 and 1 mol/L). They conclude that the corrosion resistance of the Si-PEO coating was superior and the corrosion deterioration was slower than that of the P-PEO coating in mild corrosive electrolytes (0.01M and 0.1M NaCl). However, in the more concentrated electrolytes (0.5M and 1M NaCl), the Si-PEO and P-PEO coatings cannot provide a long-term protection to the magnesium alloy substrate due to the initiation of localized corrosion, and undergo further deterioration. Ding et al [58] investigated the influences of the addition of $Na_2WO_4$ to the silicate based electrolyte and breakdown voltage on the PEO coatings microstructure, hardness and wear resistance. In the presence of $Na_2WO_4$, the coatings have excellent compatibility and wear resistance. However, with increasing sodium tungstate concentration, the size of micropores in the PEO coatings prepared in a NaOH electrolyte increased and the corrosion resistance of the PEO coatings decreased [59]. Using potentiodynamic polarization curves and electrochemical impedance spectroscopy, Barik et al [60] studied the corrosion performance of PEO coatings, and demonstrated that unsealed PEO coating allows permeation of the solution through the pores in the coating [60]. The corrosion rate of the various magnesium alloys coated using either the PEO method and composite polymer-containing coatings has recently been investigated by Gnedenkov et al [61] using a scanning vibrating probe method (SVP). They established the origin of the superior

corrosion stability of the MA8 (Mg\Mn\Ce) alloy as compared to that the VMD10 (Mg\Zn\Zr\Y) magnesium alloy, and relate that to that the secondary phases in the VMD10 composition have more positive potential values compared with the α-phase of magnesium that results in the acceleration of the dissolution of the α-phase [61].

Arrabal et al [41] conclude that the AC PEO coating on Mg alloys reduces the corrosion rate by 2-4 orders of magnitude compared with uncoated alloys. Ma et. al. [25] showed that an enrichment of the $MgAl_2O_4$ spinel phase in the coating, together with the minimum amount of cubic MgO, improves the corrosion resistance of the coating. The study of Barchiche et al [62] shows that increasing the treatment time rather than current density will improve corrosion resistance of the PEO oxide layer on AZ91D as well as a more passive behaviour of anodized layer was obtained with the higher concentrated electrolyte (3M KOH) due to the formation of more compact layer with minimum defects. The corrosion protection effect of PEO coatings of Mg alloys shows that a considerable variation in the corrosion current density $i_{corr}$ were obtained, which is not directly related to the coating thickness [60-62].


**2.7 Tribological and Mechanical Properties of PEO Coatings.**

PEO coatings on Mg alloys have been studied under various testing methods to evaluate their physical and mechanical properties [32,63-64]. Different adhesion and tribological friction and wear tests have been performed on range of PEO coating thicknesses, including scratch adhesion, sliding wear, ball-on-plate and impact tests.

As a result of the PEO coating process, the magnesium alloy surface is converted into ceramic-like coating layers that are hard, well adhered to the substrate and wear resistant [65]. PEO coatings mechanical and tribological properties depend on the characteristics shown schematically in Fig. 2.5:

- Hardness is strongly dependent on the coating thickness, the nature of the dominant phases present, their ratio and distribution, and the density of porosity and micro-cracks in the coatings [12,66,67].

- The sintering process during the formation of the PEO coatings occurs at extremely high temperatures and pressures, which results in the formation of magnesia phases. Bonding between coating and substrate created during thermal and plasma-chemical

process. The adhesion is influenced by the coating thickness. As the coating process progresses, significant changes take place in the inner layer structure as result of diffusion processes [68] and adhesion is improved.

- The load that can be supported is affected by the coating thickness. Thicker coatings will give lower stresses at the coating-substrate interface and hence give better load support [12].

- The wear resistance of coatings mainly depends on hardness, coefficient of friction and roughness. Hence, porosity levels, chemical composition, thickness, and structure of the coatings are key parameters for wear performance of Mg alloys [66]. As coating growth continues, the coating surface roughness and outer layer porosity level will increase with increasing processing time.

Since the coating hardness depends directly on the coating compactness, coatings produced with more porosity have lower hardness. Hence, a change of the process parameters, such as a current density and modes [66] and electrolyte composition and concentration [69], are important in controlling porosity levels to improve coating hardness. Coatings produced in silicate solutions generally have a higher hardness than coatings produced in a phosphate solution under the same process conditions [67] since the oxide layers made in a silicate solutions contain $Mg_2SiO_4$, which has a higher micro-hardness than MgO, $MgAlPO_5$ and $Mg_3(PO_4)_2$ that are produced in phosphate solutions [21]. PEO coatings can increase the hardness of the magnesium alloys 5-9 times compared with the hardness of the base substrate [66]. However, the values of micro-hardness close to the substrate/coating interface generally have the highest value compared to other locations, which may be attributed to its higher compactness compared with the outer porous layer [70]. The wear resistance of the coated samples is a complex process that involves surface roughness and hardness which are controlled by phase contents and porosity levels.

The tribological performance of PEO coatings is not only affected by the PEO coatings and processing parameters, but are also influenced by other factors including: sliding loads (low, medium and heavy loads), sliding speed, counterpart materials, lubricated conditions, temperature and humidity [21]. The effect of two different coating thickness (10 and 20 μm) and normal load on the wear behaviour of PEO coated AZ91 Mg alloy in

silicate based solution using dry sliding wear tests were studied by Srinivasan et al. [71]. For PEO coatings of 10 μm thickness, the increasing normal load damaged the coating, and causes a cracking and flaking off of the coating. When the coating thickness increased, the wear resistance increased due to the enhancement of the load bearing capacity of the coating [71]. Li et al. [72] studied PEO coatings on AM60B with a thickness of 22–32 μm produced in aluminate solutions and showed an improvement of a pin on disc wear resistance of the coatings produced in higher aluminate concentrations. Miao et al. [73] found that CrN–TiN multilayer coatings on AZ91D magnesium alloy could effectively improve the performance of wear resistance and corrosion resistance.

The tribological properties of PEO coatings on Mg alloys have been evaluated under the dry sliding condition [67,71,72,74-75]. The PEO coatings showed a higher coefficient of friction but a lower wear rate than the untreated Mg alloys [76]. The tribological properties of PEO coatings on Mg alloys under lubrication conditions have been studied by Guo et al [64] and Zhang et al [75]. Guo et al [64] found for an Mg AM60B alloy that the micro-porosities on the coating surfaces acted as oil reservoirs and were beneficial to the oil-lubricated wear performance. Zhang et al [75] show that the lubricate sliding wear test results of AZ91D Mg alloy in the Hank's solution is improved after PEO coatings and that the mass loss of untreated AZ91D Mg is 1.5 times higher compared with the PEO samples. The tribological properties of the PEO coatings on the Mg AJ62 alloy were evaluated by the reciprocating sliding wear tests under the boundary lubrication condition at the room temperature [34,77]. The coatings were composed of $MgAl_2O_4$ and MgO phases and a nano-structured interface about 400 nm thick and composed of nano-grains with the grain size of 10-20 nm in size. The interlayer was beneficial to the load-bearing capability of the thick coatings [34].

There are situations where the structures for good corrosion and wear performance are not the same. An example would be for oil-lubricated wear where the presence of a porous outer layer in the PEO coating could act as an oil reservoir, improving wear performance [64].

**References**

[1]     Shrestha S, Magnesium and Surface Engineering-Technology Vision', Editorial in Surface Engineering, 26 (2010), 313-316.

[2]    Song G L, Atrens A, Corrosion mechanisms of magnesium alloys, Advanced Engineering Materials, 1 (1999) 11-33.

[3]    Key to Metals, Automotive uses of magnesium alloys: part two, pp. 1-3, August 2010.
http://www.Keytometals.com/page.aspx?ID=CheckArticle&amp;site=ktn&amp;NM=248

[4]    Guo KW, A review of magnesium/magnesium alloys corrosion and its protection, Recent Patents on Corrosion Science, 2 (2010) 13-21.

[5]    Chen H, Alpas AT, Sliding Wear Map of Magnesium Alloy Mg-9Al-0.9Zn (AZ91),  Wear, 246 (2000) 106–116.

[6]    Hornberger H, Virtanen S, Boccaccini AR, Biomedical coatings on magnesium alloys – A review. Acta Biomaterialia, 8 (2012) 2442–2455.

[7]    Walsh FC, Low CTJ, Wood RJK, Stevens KT, Archer J, Poeton AR, et al. Review. Plasma electrolytic oxidation (PEO) for production of anodised coatings on lightweight metal (Al, Mg, Ti) alloys. Transactions of the Institute of Metal Finishing 87[3] (2009) 122–35.

[8]    Duan H, Yan C, Wang F, Effect of electrolyte additives on performance of plasma electrolytic oxidation films formed on magnesium alloy AZ91D, Electrochimica Acta, 52 (2007) 3785-3793.

[9]    Ghasemi A, Raja VS, Blawert C, Dietzel W, Kainer KU, The role of anions in the formation and corrosion resistance of the plasma electrolytic oxidation coatings. Surface & Coatings Technology, 204 (2010) 1469-1478.

[10]   Goueffon Y, Arurault L, Mabruc C, Tonond C, Guiguea P, Black anodic coatings for space applications, Study of the process parameters, characteristics and mechanical properties. Journal of Materials Processing Technology 209 (2009) 5145–5151.

[11]   Xue W, Wang C, Tian H and Lai Y, Corrosion behaviors and galvanic studies of microarc oxidation films on Al-Zn-Mg-Cu alloy. Surface and Coatings Technology, 201(21) (2007) 8695-8701.

[12]   Hussein RO, Nie X, Northwood DO, Yerokhin A, Matthews A, Spectroscopic study of electrolytic plasma and discharging behaviour during the plasma electrolytic oxidation (PEO) process. Journal of Physics D: Applied Physics, 43 (2010) 105203.

[13]  Gnedenkov SV, Khrisanfova OA, Zavidnaya AG, Sinebryukhov SL, Egorkin VS, Nistratova MV, Yerokhin A and Matthews A, PEO coatings obtained on an Mg–Mn type alloy under unipolar and bipolar modes in silicate-containing electrolytes. Surface & Coatings Technology, 204 (2010) 2316-2322.

[14]   Suminov IV, Apelfeld AV, Ludin VB, Krit BL and Borisov AM, (2005) Microarc oxidation theory, technology and equipment, Moscow Ecomet, ISBN 5-89594-110-9.

[15]  Gunterschulze A, Betz H, *ElektrolytKondensatoren* (Herbert Cram, Berlin, 1937; Oborongiz, Moscow, 1938) [in German and in Russian].

[16]   Markov G A, Markova G V: USSR patent 526961, 1976.

[17]  Markov G A, Tatarchuk V V,  Mirnova M K: Izvest. SO AN SSSR, Ser. Khim. Nauk, 3 (1977) 32 (in Russian).

[18]  Yerokhin AL. Nie X, Leyland A, Matthews A and Dowey S J, Plasma electrolysis for surface engineering. Surf. Coat. Technol., 122(2-3) (1999) 73-93.

[19]  Snezhko L A and Tchernenko V I: USSR patent 973583, 1982.

[20]  Kurze P, Schreckenbach J, Schwarz Th, Krysmann W Beschichten durch anodische oxidation unter Funkenentladung (ANOF).// Metalloberflaeche, B.40 (1986 S.539-540

[21]  Li Q, Liang J, Wang Q, Plasma Electrolytic Oxidation Coatings on Lightweight Metals, 'In: Modern Surface Engineering Treatments, (Aliofkhazraei M., Ed), InTech Open Publisher. 2013 ISBN 978-953-51-1149-8,

[22]  Ghasemi A, Raja VS, Blawert C, Dietzel W and Kainer KU, Study of the structure and corrosion behavior of PEO coatings on AM50 magnesium alloy by electrochemical impedance spectroscopy. Surface & Coatings Technology, 202 (2008) 3513-3518.

[23]  Nie X, Wang L, Konca E and Alpas AT, Tribological behaviour of oxide/graphite composite coatings deposited using electrolytic plasma process, Surface & Coatings Technology. 188–189 (2004) 207-213.

[24]  Curran J A and Clyne W T, Thermo-physical properties of plasma electrolytic oxide coatings on aluminum. Surface & Coatings Technology, 199 (2005) 177–183

[25]  Ma Y, Nie X, Northwood DO and Hu H, Systematic study of the electrolytic plasma oxidation process on a Mg alloy for corrosion protection. Thin Solid Films 494 (2006) 296-301.

[26]  Chang SY, Kim YL, Song BH, Lee JH, Effect of current ratio on plasma electrolytic oxide coatings on Mg-Al alloy. Solid State Phenomena 124–126 (2007) 767-770.

[27]  Cakmat E, Tekin KC, Malsyooglu U and Shrestha S, The effect of substrate composition on the electrochemical and mechanical properties of PEO coatings on Mg alloys. Surface & Coatings Technology, 204 (2010) 1305-1313.

[28]  Cheng Y, Wu F, Matykina E, Skeldon P, Thompson GE, The influences of microdischarge types and silicate on the morphologies and phase compositions of plasma electrolytic oxidation coatings on Zircaloy-2. corrosion science 59 (2012) 307-315

[29]  Dunleavy CS, Golosnoy IO, Curran JA, Clyne TW, Characterisation of discharge events during plasma electrolytic oxidation. Surface & Coatings Technology, 203 (2009) 3410-3419.

[30]  Sankara Narayanan TSN, Song Park Il, Ho Lee M, Strategies to improve the corrosion resistance of microarc oxidation (MAO) coated magnesium alloys for degradable implants: Prospects and challenges. Progress in Materials Science 60 (2014) 1–71

[31]  Cai Q, Wang L, Wei B, Lin Q, Electrochemical performance of microarc oxidation films formed on AZ91D magnesium alloy in silicate and phosphate electrolytes. Surface & Coatings Technology 200 (2006) 3727-3733.

[32]  Weiyi M, Yong H, Study on Micro-Arc Oxidized Coatings on Magnesium in Three Different Electrolytes. Rare Material and Engineering, 39 (2010) 1129-1134

[33]  Lv G, Chen H, Wang XQ, Pang H, Zhang GL, Zou B, Lee HJ, Yang SZ, Effect of additives on structure and corrosion resistance of plasma electrolytic oxidation

coatings on AZ91D magnesium alloy in phosphate based electrolyte. Surface & Coating Technology, 205 (2010) S36-S40.

[34]  Zhang P, Nie X, Hu H, Liu Y, TEM analysis and tribological properties of Plasma Electrolytic Oxidation (PEO) coatings on a magnesium engine AJ62 alloy. Surface & Coatings Technology 205 (2010) 1508–1514

[35]  Lin C S, Fu Y C J, Characterization of anodic films of AZ31 magnesium alloys in alkaline solutions containing fluoride and phosphate anions. Journal of The Electrochemical Society, 153 (2006) B417-B424.

[36]  Ryu H S and Hong SH, Effects of KF, NaOH, and KOH electrolytes on properties of microarc-oxidized coatings on AZ91D magnesium alloy. Journal of The Electrochemical Society 156 (2009) C298-C303.

[37]   Liang J, Guo B, Tian J, Lin H, Zhou J, Xu T, Effect of potassium fluoride in electrolytic solution on the structure and properties of microarc oxidation coatings on magnesium alloy. Applied Surface Science 252 (2005) 345-351

[38]  Arrabal R, Matykina E, Viejo F, Skeldon P, Thompson G E, Merino M C, AC plasma electrolytic oxidation of magnesium with zirconia nanoparticles. Applied Surface Science, 254(21) (2008) 6937-6942.

[39]  Blawert C, Heitmann V, Dietzel W, Nykyforchyn H M, Klapkiv M D, Influence of electrolyte on corrosion properties of plasma electrolytic conversion coated magnesium alloys. Surface and Coatings Technology, 201(21) (2007) 8709-8714.

[40]  Northwood D. O., Hussein R. O. and Nie X. (2011) Environmentally Friendly Surface Treatment of Light Alloy Materials for Automotive Applications. The 18th International Corrosion Congress in Perth, Australia 2011 2, pp. 825-836.

[41]   Arrabal R, Matykina E, Hashimoto T, Skeldon P, Thompson GE, Characterization of AC PEO coatings on magnesium alloys. Surface & Coatings Technology, 203 (2009) 2207-2220.

[42]  Liang J, Bala Srinivasan J P, Blawert C, Störmer M, Dietzel W, Electrochemical corrosion behaviour of plasma electrolytic oxidation coatings on AM50 magnesium alloy formed in silicate and phosphate based electrolytes. Electrochimica Acta 54 (2009) 3842–3850.

[43]  Lee K, Lee B, Yoon S, Lee E, Yoo B, Shin D, Evaluation of plasma temperature during plasma oxidation processing of AZ91 Mg alloy through analysis of the melting behavior of incorporated particles. Electrochimica Acta 67 (2012) 6– 11

[44]   Jin F, Chu PK, Xu G, Zhao J, Tang D and Tong H, Structure and mechanical properties of magnesium alloy treated by micro-arc discharge oxidation using direct current and high-frequency bipolar pulsing modes. Materials Science and Engineering: A, 435-436 (2006) 123-126.

[45]  Snizhko LO, Yerokhin AL, Pilkington A, Gurevina NL, Misnyankin DO, Leyland A, Matthews A., Anodic processes in plasma electrolytic oxidation of aluminium in alkaline solutions. Electrochimica Acta., 49[13] (2004) 2085-2095.

[46]  Chang L, Growth regularity of ceramic coating on magnesium alloy by plasma electrolytic oxidation. Journal of Alloys and Compounds, 468 (2009) 462–465.

[47]  Yerokhin AL, Leyland A, Matthews A, Kinetic aspects of aluminium titanate layer formation on titanium alloys by plasma electrolytic oxidation. Applied. Surface. Science, 200 (2002) 172-184.

[48]    Zhang P, Nie X, Northwood D O, Influence of coating thickness on the galvanic corrosion properties of Mg oxide in an engine coolant. Surface and Coatings Technology, 203 (2009) 3271-3277.

[49]    Hsiao H, Tsai W, Characterization of anodic films formed on AZ91D magnesium alloy, Surface & Coatings Technology 190 (2005) 299– 308

[50]     Roberge, P.R., Corrosion Engineering Principles and Practice, McGraw Hill, New York, 2008.

[51]    George, G. A., Colwell, J. M., Trueman, T. and Will, G. Sensitive methods for studying the environmental performance of protective coatings. Corrosion & Materials, 39(2) (2014) 46-53,.

[52]    Liu L, Yang P, Guo H, An M, Microstructure and corrosion behavior of micro-arc oxidation film on magnesium alloy. International Journal of Electrochemical Science 8 (2013) 6077-6084,.

[53]    Shi Z, Liu M, Atrens A, Measurement of the corrosion rate of magnesium alloys using Tafel extrapolation. Corrosion Science 52 (2010) 579–588.

[54]    Gu XN, Li N, Zhou WR, Zheng YF, Zhao X, Cai QZ,  Corrosion resistance and surface biocompatibility of a microarc oxidation coating on a Mg–Ca alloy. Acta Biomaterialia 7 (2011) 1880–1889.

[55]    Huang VM, Wua S-L, Orazema ME, Pébèreb N, Tribollet B, Vivier V, Local electrochemical impedance spectroscopy: A review and some recent developments. Electrochimica Acta 56 (2011) 8048– 8057

[56]    Liang J, Hu L, Hao J, Characterization of microarc oxidation coatings formed on AM60B magnesium alloy in silicate and phosphate electrolytes. Applied Surface Science, 253 (2007) 4490-4496.

[57]    Liang J, Srinivasan PB, Blawert C, Dietzel W. Influence of chloride ion concentration on the electrochemical corrosion behavior of plasma electrolytic oxidation coated AM50 magnesium alloy. Electrochimica Acta, 55 (2010) 6802−6811.

[58]    Ding J, Liang J, Li TH, Hao J, Xue Q, Effects of sodium tungstate on characteristics of microarc oxidation coatings formed on magnesium alloy in silicate–KOH electrolyte. Transactions of Metals Society of China, 17 (2007) 244–249.

[59]    Zhao F, Liao AD, Zhang RF, Zhang SF, Wang HX, Shi XM, Li MJ, He XM, Effects of sodium tungstate on properties of micro-arc coatings on magnesium alloys. Transaction of Nonferrous Metals Society of China, 20 (2010) s683- s687.

[60]    Barik RC, Wharton JA, Wood RJK, Stokes KR, Jones RL, Corrosion, erosion and erosion–corrosion performance of plasma electrolytic oxidation (PEO) deposited $Al_2O_3$ coatings. Surface & Coatings Technology, 199 (2005), 158-167.

[61]    Gnedenkov AS, Sinebryukhov SL, Mashtalyar DV, Gnedenkov SV, Features of the corrosion processes development at the magnesium alloys surface. Surface & Coatings Technology, 225 (2013)  112–118.

[62]    Barchiche C E, Rocca E, Juers C, Hazan J, Steinmetz J, Corrosion resistance of plasma anodized AZ91D magnesium alloy by electrochemical methods. Electrochimica Acta 53 (2007) 417–425.

[63]    Tekin KC, Malayoglu U, Shrestha S, Tribological properties of plasma electrolytic oxide coatings on magnesium alloys. Tribology, 6 (2012), 67-74.

[64]   Guo J, Wang L, Liang J, Xue Q, Yan F, Tribological behavior of plasma electrolytic oxidation coating on magnesium alloy with oil lubrication at elevated temperatures. Journal of Alloys and Compounds, 481 (2009), 903–909.

[65]   Khan R, Yerokhin A L, Pilkington T, Leyland A, and Matthews A, Residual stresses in plasma electrolytic oxidation coatings on Al alloy produced by pulsed unipolar current. Surface & Coatings Technology,, 200 (2005) 1580-1586.

[66]   Durdu S, Bayramoglu S, Demirtas A, Usta M, Ücısık AH, Characterization of AZ31 Mg alloy coated by plasma electrolytic oxidation. Vacuum, 88 (2013) 130–133,.

[67]   Liang J, Hu L, Hao J, Characterization of microarc oxidation coatings formed on AM60B magnesium alloy in silicate and phosphate electrolytes. Applied Surface Science. 253(10) (2007) 4490–4496.

[68]   Mécuson F, Czerwiec T, Belmonte T, Dujardin L, Viola A, Henrion G. Diagnostics of an electrolytic microarc process for aluminum alloy oxidation. Surface & Coatings Technology, 200 (2005) 804-808.

[69]   Forno AD, Bestetti M. Effect of the electrolytic solution composition on the performance of micro-arc anodic oxidation films formed on AM60B magnesium alloy. Surface & Coatings Technology,  205 (2010) 1783–1788.

[70]   Li Z, Yuan Y, Jing X, Effect of current density on the structure, composition and corrosion resistance of plasma electrolytic oxidation coatings on Mg–Li alloy. Journal of Alloys and Compounds, 541 (2012), 380–391.

[71]   Srinivasan P B, Blawert C, Dietzel W, Dry sliding wear behaviour of plasma electrolytic oxidation coated AZ91 cast magnesium alloy. Wear, 266 (2009) 1241–1247.

[72]   Li X, Liu X, Luan BL, Corrosion and wear properties of PEO coatings formed on AM60B alloy in NaAlO2 electrolytes, Appl. Surf. Sci. 257 (2011) 9135–9141.

[73]   Miao Q, Cui C E, Pan J D, CrN-TiN multilayer coating on magnesium alloy AZ91 by arc-glow plasma depositing process. Surface & Coatings Technology, 201 (2007) 5077-5080.

[74]   Bala Srinivasan P, Liang J, Blawert C, Dietzel W, Dry sliding wear behaviour of magnesium oxide and zirconium oxide plasma electrolytic oxidation coated magnesium alloy. Applied Surface Science, 256(10) (2010) 3265-3273.

[75]   Zhang X, Zhao Z, Wu F, Wang Y, Wu J, Corrosion and wear resistance of AZ91D magnesium alloy with and without microarc oxidation coating in Hank's solution. Journal of Materials Science, 42(20) (2007) 8523-8528.

[76]   Liang J, Wang P, Hu L, Hao J, Tribological properties of duplex MAO/DLC coatings on magnesium alloy using combined microarc oxidation and filtered cathodic arc deposition. Materials Science and Engineering. 454–455A (2007) 164–169.

[77]   Zhang P, Nie X, and Hu H, (2009) Wear and Galvanic Corrosion Protection of Mg alloy via Plasma Electrolytic Oxidation Process for Mg Engine Application, SAE Technical Paper 2009-01-0790, doi:10.4271/2009-01-0790.

# Chapter 3

## Experimental Procedures

The collective behavior of the plasma discharge over the entire surface, rather than the individual discharges, is addressed in this work. The PEO process of Mg-alloys is strongly influenced by experimental parameters. These parameters have a direct influence on the discharging behavior which, in turn, plays an essential role in the formation and resulting composition of oxide structure as shown in Fig. 1.1. This, then, affects the physical, mechanical and chemical properties of the coating. Various current regimes including unipolar, bipolar, and hybrid (combination of unipolar and bipolar) modes, were used in this wok.
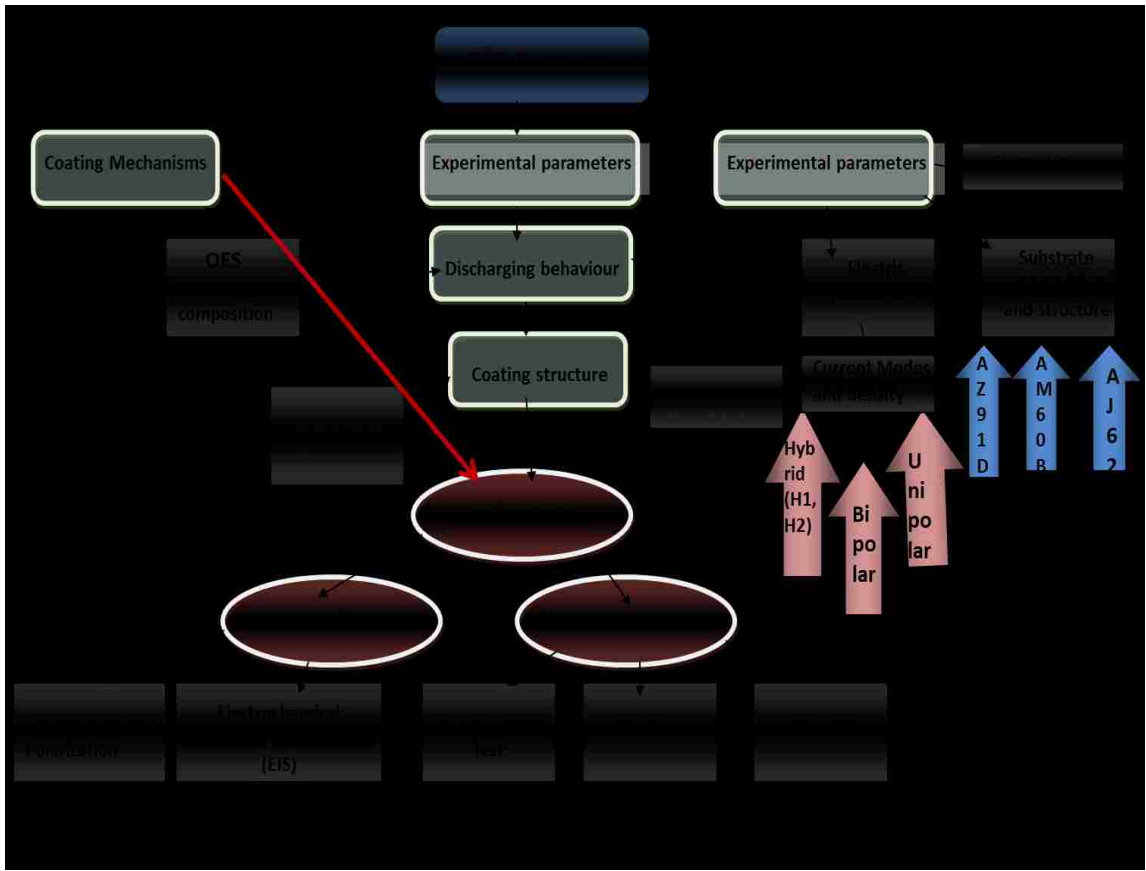


Fig. 3.1 Effects of PEO process parameters on corrosion and tribological properties

This Chapter details the materials and techniques used for PEO processing of Mg alloys, characterizing the coatings produced and investigating the effects of these PEO coatings on corrosion and mechanical and tribological response.

## 3.1 Experimental

### 3.1.1 Material

In this work three different types of Mg alloys (Table 3.1); AM60B, AJ62, and AZ91D were examined. Disc-shaped coupons (25×7mm) cut from Mg bars were used as the test samples in this study. The coupons were manually ground and polished on 240, 400, 600, and 1200 grit silicon carbide (SiC) waterproof abrasive papers to obtain a uniform surface roughness of $0.1 \pm 0.02$ μm. After cleaning with water, the samples were cleaned with acetone before the PEO treatment to ensure a similar initial surface condition for each sample.

**Table 3.1 Alloys Investigated**

| Mg Alloys | Composition (wt.%) | | | | | | General properties |
|---|---|---|---|---|---|---|---|
| | Al | Mn | Zn | Si | Sr | Mg | |
| AM60B | 5.5 to 6.5% | 0.25% | 0.22% | 0.10% | N/A | balance | Excellent combination of mechanical properties, castability, and reasonable corrosion resistance |
| AJ62 | 6.1% | 0.34% | N/A | N/A | 2.1% | balance | Superior thermal stability at 150 °C, good die-castability |
| AZ91D | 8.3-9.7% | 0.15% | 0.35-1.0% | 0.10% | N/A | balance | Excellent ductility and toughness, with reasonable yield and tensile properties and castability |

Two samples were tested mechanically (compression or sliding). There were two samples for corrosion testing: 1 sample for cross-sectional analysis to study the coating thickness distribution and morphology and 1 sample for microstructure (phases present and elemental distribution).

### 3.1.2 PEO coating Process

PEO processing involves the submersion of the metallic substrate in an aqueous electrolyte. The coatings were obtained mainly in an alkaline electrolyte containing sodium aluminate ($Na_2Al_2O_4$) and potassium hydroxide (~1 g/l KOH) added to balance the pH at 12. Figure 3.2 is the schematic of a typical treatment unit. The unit consists of a container with the electrolyte and a powerful electrical source. The container is usually a water-cooling bath placed on a dielectric base and fixed in a grounded steel frame, which has an insulated current supply and a window to observe the process in operation. A stainless steel tank acts as the counter-electrode. The temperature of the electrolytes was kept below 25 $^o$C by a water cooling system. In order to obtain a good connection between the power supplies to the samples, a threaded hole was drilled on one side of each sample. Then the sample was screwed onto an Al rod (and insulated by Teflon tape from the electrolyte) which carried the current from the power supply. The Mg samples (as the anode) and a stainless steel tank (as the cathode) were connected to two pulsed DC power supplies operating under a constant current control function to generate a different current modes: unipolar, bipolar and hybrid (combination of unipolar and bipolar) current mode.

Two different current generators (MPE Magna-power supply and MDX Magnetron Drive) were used, which deliver current to the substrate with an amplitude in the range of 0-5 A and 0-15 A respectively. These power supplies were specially designed to allow independent control over the main pulse parameters, such as pulse duration, amplitude and duty cycle, during both positive and negative biasing using a Spik 2000A controller.

The pulse unit SPIK2000A can be operated in many modes (Bipolar, Unipolar, DC- and DC+ modes) with pulse duration (the ON and OFF times) being freely adjustable from the 5μs per pulse unit range to the 32ms per pulse duration range (30Hz to 50 KHz). The DC sources can be used in the voltage, the current or in the power controlled mode. Experiments were conducted using pulsed DC power supply (AE Magnetron MAX, the output voltage ranging from 0 to 1000V) with current control. A constant current density was set for each set of experiments. Since the conductance of the oxide film decreases with the increase in coating thickness, the input voltage between anode and cathode has

to be increased gradually to maintain the current density. Voltage increment verses treatment time was recorded for each sample.
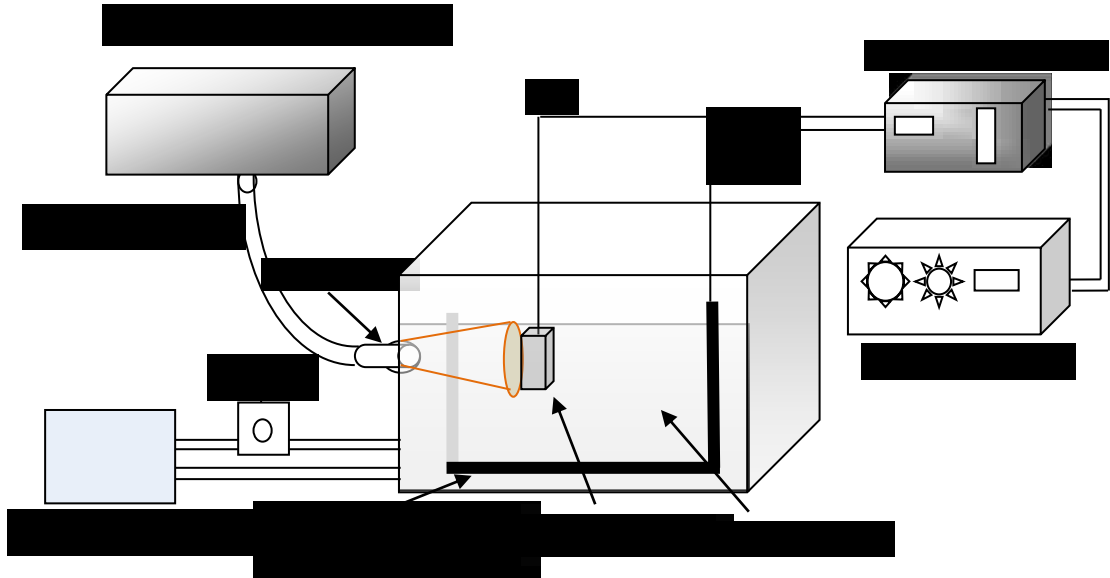


**Fig. 3.2**. Schematic diagram of the experimental apparatus.

## 3.2 Coating Characterization Methods

In order to correlate between processing parameters-resulting oxide structure-desired properties and performance it was important to study the distribution and nature of the coating, microstructures, and mechanical properties of these coatings. These studies were undertaken in this work utilizing different experimental techniques, which are explained in the following sub-sections.

### 3.2.1 Surface morphology and coating thickness

Scanning electron microscopy (FEI Quanta 200 FEG with solid state backscattered detector operated at 15 KV) in both the back scattered secondary electron (BSE) mode and in the secondary electron (SE) mode was used to observe both the coating surface morphology and, through observation of sample cross sections, coating thickness and integrity. EDX is a technique that interprets the interactions between a source of high energy electrons and an atomic structure of a given sample. In this work, elemental composition and spatial distributions, both over surface and through the thickness, of different coatings, produced under different processing parameters, were studied by

energy-dispersive X-ray spectroscopy (EDX, Kevex 5100C), with an electron beam spot size of 3 nm operated at 12 kV, which was fitted in FEI Quanta SEM microscope. Major elements such as magnesium, aluminum and oxygen are expected to be present at different amounts in each coating and can form most of the coating volume. The surface and cross-sections for each coating were sputter-coated with carbon before examination to avoid surface charging. Cross-sections of samples were mounted with resin and polished first with a SiC abrasive paper of gradually decreasing grit size, then with an alumina suspension for the final polishing.

The coating thicknesses for different treatment times were also determined using a PosiTector 6000 coating thickness meter with N type probes: this instrument uses the eddy current principle to measure the thickness of non-conductive coating (ceramic) on non-ferrous metal (magnesium). The dimensions of the magnesium alloy sample before and after oxidation were measured using a Mitutoyo Absolute ID-S112 spiral "Absolute Position" digital micrometer, from which the inner and outer thickness values at different treatment time were calculated. The meter was set to zero-position for the uncoated substrate then the total outer thickness measured after the coating, which represents twice the thickness of the sample dimension changes.

### 3.2.2. X-ray Diffraction (XRD)

It is expected that processing parameters can have major influence on microstructures of PEO coatings. As the coating starts to build up during processing, transformation processes take place, and more amorphous phases will transform into crystalline To identify the phases generated during the PEO coating, analytical X-ray diffraction (XRD) was performed on coated samples. Copper Kα radiation ($\lambda$= 0.15406 nm) was employed at a tube current of 45 mA and a voltage of 45 kV. For phase identification, the scan range varied from 10 to 80° (in 2θ) with a step size of $0.05^o$ and 1.5s in each step.

### 3.2.3 Surface roughness

The surface roughness (Ra) was measured using a stylus type surface profilometer (Mitutoya Surftest SJ-201P). Each roughness value given was an average of five test values. The accuracy of roughness tests is ± 0.01 μm.

### 3.3 Optical Spectrometry

Since the discharges are occurring randomly (source is not emitting equally over the whole sample area), we therefore used an integrated signal that covers whole sample surface area, by focusing all signal emitted from the sample on the fiber optics that connect it to the spectrometer. In this study one spectrometer formed the main visible spectroscopy diagnostic arsenal. The Ocean Optics OES Sensor is PC2000-UV-VIS Fiber Optic Spectrometer with effective range of 200 nm~1100 nm. Its detector consists of a 2048-element linear CCD-array (a charge- coupled device array detector) with a grating of (600 lines/mm). The optical bench is compactly mounted on a PC plug-in 1 MHz ISA-bus A/D card, which fits into a slot in the PC. The entrance slit is fixed at 10 mm in width, 1000 mm in height. With no moving part, the optical bench is compactly mounted on a PC plug-in 1 MHz ISA-bus A/D card, which fits into a slot in the PC. The spectrometer collects light transmitted from Ocean Optic P400-2-UV/VIS fiber, which is a 2-meter-long, 400-mm-patch fiber (Fig. 3.2). The light emitted by the plasma was transmitted and focused through a quartz window and 20mm UV-grade fused-silica lenses mounted on the tank on to the 74-UV collimating lens, 5 mm in diameter, 10 mm in length, and screws on the end of the 400μm diameter optical fiber leading to the entrance slit of the spectrometer.

### 3.4 Electrochemical testing

### 3.4.1. Test procedures

Cyclic potentiodynamic polarization tests were performed to study the general corrosion properties of the substrates and the as- fabricated coating at a temperature of about 25°C. A Solartron 1285 Potentiostat (with Corrware Software) and a conventional three-electrode cell were employed for the corrosion tests.  A specimen with an exposed area of 1.0 cm$^2$ was the working electrode; a saturated calomel electrode (SCE) served as the reference electrode; a platinum rod was used as the counter electrode. The ratio of the volume of test solution to the sample contact area was 200 ml/cm$^2$. All potentials are given with respect to the SCE.

Before conducting the potentiodynamic polarization tests, the electrodes were placed in the test solutions under open circuit potential (OCP) for at least 20 mins. After the

electrochemical testing system was stable (the OCP reached a stationary value). The measurements were carried out in the test solution at a scan rate of 1 mV/s for 1 cycle. The cycle polarization curves were recorded from a potential -1.0 V to +1.0 V, and back to -1.0 V (Vs. OCP).

Following the potentiodynamic polarization testing, the corrosion current densities were determined by linear extrapolation of the polarization curves, and the polarization resistance of the specimens was calculated for comparison.

### 3.4.2 Electrochemical impedance spectroscopy (EIS)

Electrochemical impedance spectroscopy (EIS) was also used, through a frequency response analyzer which enabled the scan to be generated automatically under computer control. A three electrode cell with both the uncoated and PEO coated samples as the working electrode, exposing 1.0 cm$^2$ of area to the solution during electrochemical measurements, an Ag/AgCl/sat KCl reference electrode, and platinum as a counter electrode, was used in the experiments. The EIS technique was employed using a 3.5 wt % sodium chloride solution and the impedance spectra were acquired over the frequency range between 100 mHz and 200 kHz with an AC signal amplitude of ±10 mV with respect to the open circuit potential (OCP). All EIS data were analyzed by curve fitting and equivalent circuit modeling using EC-Lab® electrochemical analysis software version 10.02. Measurements were performed three times to ensure reproducibility of the results. Electrochemical impedance spectroscopy (EIS) measurements were performed at the open circuit corrosion potential on the PEO coatings after different initial delay times to stabilize the open-circuit potential (OCP).

### 3.5. Tribological testing

### 3.5.1. Pin-on-disk

The wear resistance of coated and uncoated samples was evaluated using a pin-on-disk tester (FALEX ISC tribometer) under dry conditions with a 10 mm AISI 52100 steel ball as the wear medium (pin) and the samples as the disk. The tests were conducted at room temperature (20 °C), ~ 50% humidity, using a 2 N applied load and a rotation speed of 75.0 mm/s with the sample running on a 4 mm radius track. The tests were stopped after

reaching a total wear distance of 100 m. After wear testing, the samples were cleaned in acetone, and dried in air. The wear tracks of the samples were characterized using a WYKO NT1100 optical profiler. The volume loss due to wear of the samples was calculated based on geometries (width and depth) of the wear tracks.

### 3.5.2. Inclined impact–sliding wear instrument

In this method, a hard ball (10 mm AISI 52100 steel ball) is mounted on the shaft of a double-way air cylinder with the piston driven by compressed air producing vertical oscillatory motions (see Fig 3.3). A steel ball is used in this test rather than a ceramic ball, since a ceramic ball could potentially fracture on the initial impact loading. The sample is set on an inclined sample holder which is returned to its position by a spring.

An OMEGA LCKD-500 load cell is placed on the sample holder to record the normal force on the sample surface during the impact–sliding movement. The desired normal impact and compression forces were obtained by adjusting the pre-strain of the spring and the pressure in the air cylinder. The load cell was removed and the coated samples were placed on the sample holder for impact tests. After the counterpart ball completed the first full contact with the coating surface and formed a deep impact crater, a series of rebounds and impacts occurred. After the vibration stage, the load continues to change gradually until the pre-setup compression load (Fc) is reached, and then the ball starts to move up. This is named as the compression force stage, in which a tail with sliding failures was formed.
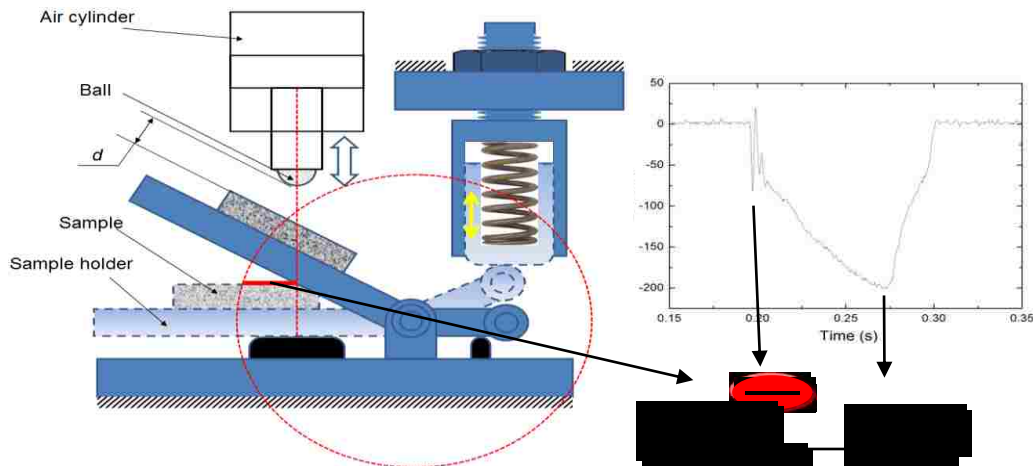


Fig. 3.3 Inclined Impact-sliding Fatigue Test

**CHAPTER 4**

**INFLUENCE OF THE CURRENT MODE ON THE PLASMA ELECTROLYTIC OXIDATION (PEO) PROCESS PERFORMANCE AND IMPROVING THE CORROSION PROPERTIES OF THE COATINGS ON THE MG AJ62 ALLOY**

**Published in:**

- Hussein R.O., Zhang P., Xia Y., Nie X. and Northwood D.O (2011) The effect of current mode and discharge type on the corrosion resistance of plasma electrolytic oxidation (PEO) coated magnesium alloy AJ62, Surface & Coatings Technology, 206 (7) , pp. 1990-1997.

- Hussein R.O., Zhang P., Northwood D.O. and Nie X. (2011) Improving the corrosion resistance of magnesium alloy AJ62 by a plasma electrolytic oxidation (PEO) coating process, Corrosion and Materials 36 (3), pp. 38-49.

**4.1 Introduction**

With the aim of improving the characteristics of the PEO coatings, many attempts have been made to improve the supplied current regimes, suggesting different forms and duration of the current pulses [1,2]. The properties of the plasma discharges themselves in the bipolar current mode differ from those of the discharges obtained with a unipolar current mode. From the plasma discharge point of view, a significant reduction in the strong discharges [3] can reduce the detrimental effects associated with such discharge events. Recent studies on the effect of power supply modes on PEO coating properties have paid more attention to the bipolar current mode. Various researchers [4-6] have tried to modify the morphology and structure of the oxide coatings by altering the nature and intensity of the sparks produced during the PEO process. Gnedenkov et al [4] utilized a pulsed bipolar current mode to fabricate a dense and uniform oxide layer with a fine-grained microstructure on a MA8 magnesium alloy. A high corrosion resistance (Rp $=3.3\times10^5$ $\Omega$ cm$^2$) was reported for the coated alloy made with a silicate-fluoride electrolyte.

A study by Zhang et al [7] on the AJ62 Mg alloy coated using the PEO process and a DC unipolar current mode showed that as the coating thickness increased, the galvanic corrosion resistance was improved. Also they showed that 5 micrometers of coating thickness effectively prevent the galvanic corrosion of magnesium, and did not significantly affect the heat transfer properties. The present study investigated the effect of current modes on the plasma discharge behavior and plasma temperature which were believed to have a significant effect on morphology and microstructures of the resultant oxide coatings for the Mg alloy. Thus, in this work, the PEO process operated at two different current modes (i.e., unipolar and bipolar pulsed DC current modes) with different electrical charge ratio CR to produce oxide coatings on an AJ62 magnesium alloy substrate. The application of both current modes, and the effect on coating morphology, structure and corrosion protection properties are discussed with respect to the plasma discharge behaviour and plasma temperature profiles.

## 4.2. Experimental Procedures

### 4.2.1 Materials and PEO Processing Method

Since the current mode plays a significant effect in providing the appropriate conditions for the formation of a corrosion resistant layer on magnesium alloy produced by the PEO process, the PEO coating process was carried out using two different current modes:

- A unipolar pulsed-DC mode (UPDC), i.e. under only positive polarization of the metal electrode operating at 2 KHz and duration time of 80% duty cycle (Fig. 4.1(a)). The specific frequency was chosen based on the dependence of coating growth rate and coating characteristics to current frequency [8].

- A Bipolar current mode (BPDC), comprising two components i.e., a positive component and a negative component (Fig. 4.1(b)). In each pulse, the pulsed current reached its maximum, after which it remains constant for $T_{0n}$ time. In this work, it is represented by $T_{on}^+$, whereas, $T_{off}$ corresponded to $T_{off}^+ + T_{on}^- + T_{off}^-$.

- Two different current generators (MPE Magna-power supply and MDX Magnetron Drive) were used, which deliver current to the substrate with an amplitude in the range of 0-5 A and 0-15 A respectively. These power supplies were specially designed to allow independent control over the main pulse parameters, such as pulse

duration, amplitude and duty cycle, during both positive and negative biasing obtained using a Spik 2000A controller.
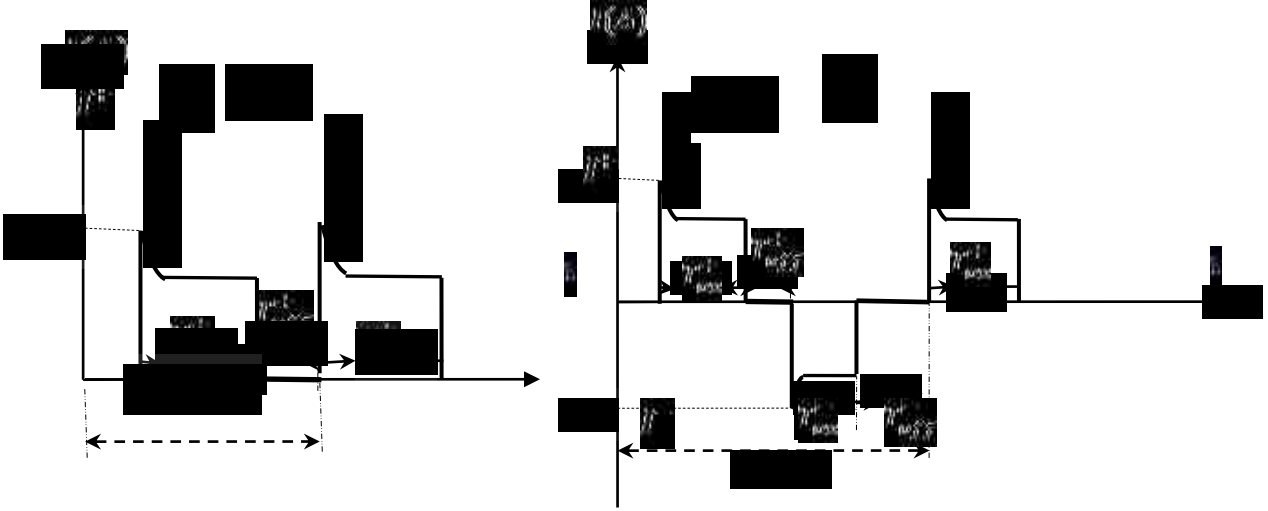


Figure 4.1. Schematic form of the (a) unipolar and (b) bipolar current waveforms, showing the main controllable parameters of the pulses.

The charge ratio parameter, $C_R$, is introduced to represent the ratio of positive to the negative charge quantity:

$$C_R = \frac{q_+}{q_-} = \frac{\int_0^{T_{on}} (I^+)\, dt}{\int_{T_{on}}^{T_{on}+T_{off}} (I^-)\, dt} \qquad \textbf{4.1}$$

where $I^+$ and $I^-$ represent the values of the positive and negative currents respectively. Both pulse duration and current density were controlled in order to provide appropriate conditions to attain desirable coating morphology and microstructure. Process parameters, such as the frequency ($f=1/T$, where $T$ is the pulse period), the duration of each pulse ($T_{on}^+$ and $T_{on}^-$, the period of positive and negative pulse respectively) and the resting gap (break) between the positive and negative pulses ($T_{off}^+$ and $T_{off}^-$ respectively) are listed in Table 4.1.

**Table 4.1. PEO Process parameters for coating depositions on Mg**

| Sample | Current mode | Time (min) | $I^+$ (A) | $I^-$ (A) | $T_{on}^+$ ($\mu s$) | $T_{off}^+$ ($\mu s$) | $T_{on}^-$ ($\mu s$) | $T_{off}^-$ ($\mu s$) | $C_R$ |
|--------|--------------|------------|-----------|-----------|----------------------|------------------------|----------------------|------------------------|-------|
| S1 | Unipolar | 45 | 1.0 | N/A | 400 | 100 | N/A | N/A | N/A |
| S2 | bipolar | 45 | 1.0 | 0.9 | 400 | 100 | 400 | 100 | 0.74 |
| S3 | bipolar | 45 | 1.0 | 0.7 | 400 | 200 | 600 | 100 | 0.63 |
| S4 | bipolar | 45 | 1.0 | 0.5 | 400 | 100 | 600 | 100 | 1.0 |

AJ62 Magnesium alloy disc coupons ($\Phi25\times7mm$) were used after grounding and polishing as the test samples in this study. The coating was obtained in an alkaline electrolyte containing sodium aluminate (10g/l $Na_2Al_2O_4$) and potassium hydroxide (~1 g/l KOH) added to balance the pH at 12. The temperature of the electrolytes was kept below 25 $^o$C by a water cooling system. Scanning electron microscopy (JEOL 2100 operating at 15 KV and FEI Quanta 200 FEG with solid state backscattered detector operated at 10 KV) in both the secondary electron and back-scattered electron (BSE) modes was used to observe both the coating surface morphology and coating thickness and integrity through observation of sample cross sections. The samples were first sputtered with a gold film to make conductive before SEM analysis. The phases in the coatings on the Mg were studied by X-ray Diffraction (XRD) analysis using a Siemens D5000 X-ray powder diffractometer with Cu Kα radiation.

### 4.2.2 Electron temperature measurement using OES.

The main characterization of the micro-discharges was performed by means of optical emission spectroscopy (OES). Light emission of the discharges was collected using one spectrometer; this spectrometer has 4 channel slots, each of which covers a certain wavelength region. Six different spectral lines were recorded simultaneously, which eliminates discrepancies that may otherwise happen if the spectra are recorded at different times or with different samples. Spectroscopy with the OES spectrometer was utilized to examine the spectral lines (Table 4.2) [8] at 285.2 nm (Mg I), 383.8 nm (Mg

I), 518.3 nm (Mg I), 486.1 nm (H$_\beta$), 589.5 nm (Na I), and 777 nm (OI). Atomic and ionic spectral lines were identified using the NIST online spectral database [9].

The plasma studied here falls into the category of optically thin plasma [10]. The relative intensities of spectral lines of the same atomic species can be used to calculate the plasma electron temperature. Once relative intensities are known, the temperature corresponding to a given line ratio is [10]:

$$\frac{I(1)}{I(2)} = \frac{A_{mn}(1)g_m(1)\lambda_0(2)}{A_{mn}(2)g_m(2)\lambda_0(1)} \exp - \left\{ \frac{E_{m(2)} - E_{m(1)}}{KT} \right\}$$  **4.2**

where kT is the thermal energy, $I(1)$ and $I(2)$ relative line intensities of lines of the same species in question, $A_{mn}(i)$ the transition probabilities, $m$ the upper and $n$ the lower level of the respective lines, $g_m(i)$ the statistical weight of the upper levels, $E_m(i)$ energies of the upper levels of lines and $\lambda_0$ (i) the wavelengths of the line centers in vacuum. Equation (4.2) is valid if the level populations of the lines in question are populated according to the Boltzmann law: in other words, at least partial thermodynamic equilibrium (LTE) must exist for these levels.

Table 4.2. Spectral lines observed in this experiment with the wavelength ($\lambda$), transition, statistical weight of the upper and lower state $g_k$ and $g_i$ (respectively), energy difference and the transition probabilities ($A_{ki}$) [9].

| Line | $\lambda$ nm | Transition | $g_k$ | $g_i$ | Energy eV | $A_{ki}$ $10^8$ S$^{-1}$ |
|---|---|---|---|---|---|---|
| Mg I | 285.2 | 3s3p $^1$P → 3s$^2$ $^1$S | 3 | 1 | 4.34 | 5.00 |
| Mg I | 383.8 | 3s3d $^3$D → 3s3p $^3$P | 7 | 5 | 3.22 | 1.68 |
| Mg I | 518.3 | 3s4s $^3$S → 3s3p $^3$P | 3 | 5 | 2.38 | 0.57 |
| H$_\beta$ | 486.1 | 4d $^2$D → 2p $^2$P | 4 | 2 | 2.55 | 0.172 |
| Na I | 589.5 | 3p $^2$P → 3s $^2$S | 3 | 3 | 1.36 | 0.614 |
| O I | 777.2 | 2s$^2$2p$^3$ 3p $^5$P → 2s$^2$2p$^3$ 3s $^5$S | 3 | 5 | 1.59 | 0.369 |

The emission intensities of the selected Mg spectral lines were simultaneously recorded, and the intensity ratio of 518.3 nm (Mg I) to 383.8 nm (Mg I) (from the same ionization stage) was used to calculate the plasma electron temperature ($T_e$) based on the partial thermodynamic equilibrium model (LTE). Since it has negligible effects, the line broadening effect was ignored in this experiment.

**4.2.3 Corrosion Testing**

To determine the corrosion resistance of the PEO coating, potentiodynamic polarization in a 3.5% NaCl solution tests were carried out at $25\pm2$ $^{o}$C using a Solartron 1285 Potentiostat with Corrware software. A three electrode cell with the samples as the working electrode, an Ag/AgCl/sat KCl reference electrode, and platinum as a counter electrode, was used in the experiments. When the corrosion potential remained stable, the potential was scanned from -0.15 V versus open circuit potential, up to -1.25 V versus the open circuit potential (OPC) at a rate of 1.0 mV/s.

Electrochemical impedance spectroscopy (EIS) was also used, through a frequency response analyzer which enabled the scan to be generated automatically under computer control. A three electrode cell with both the uncoated and PEO coated samples as the working electrode, exposing 1.0 cm$^2$ of area to the solution during electrochemical measurements, an Ag/AgCl/sat KCl reference electrode, and platinum as a counter electrode, was used in the experiments. The EIS technique was employed using a 3.5 wt % sodium chloride solution and the impedance spectra were acquired over the frequency range between 100 mHz and 200 kHz with an AC signal amplitude of $\pm10$ mV with respect to the open circuit potential (OCP). All EIS data were analyzed by curve fitting and equivalent circuit modeling using EC-Lab® electrochemical analysis software version 10.02. Measurements were performed three times to ensure reproducibility of the results. Electrochemical impedance spectroscopy (EIS) measurements were performed at the open circuit corrosion potential on the PEO coatings after different initial delay times to stabilize the open-circuit potential (OCP).

**4.3. Results and Discussion**

**4.3.1 Optical Emission Characterization and Plasma Electron Temperatures**

In this experiment the OES spectrometer was utilized to examine the atomic spectral lines from the neutral atoms at 383.8 nm (Mg I). As the plasma coating process proceeds, the discharge appearance changes and the plasma emission intensities varied as shown in Fig. 4.2.
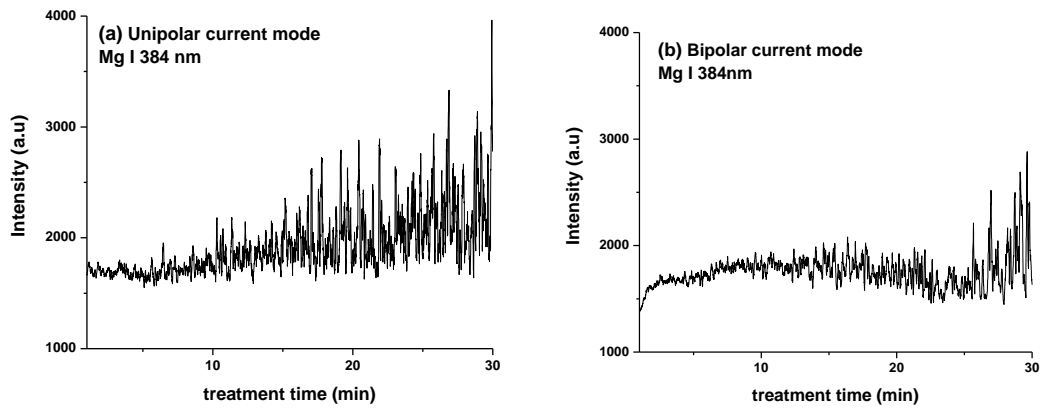
Figure 4.2. Typical time variation of the emission line intensity during the PEO process (a) unipolar current mode and (b) bipolar current mode.

Based on our discharge model [3], the Mg emission intensity signals were due to three different types of discharge which are classified according to the origins of such signals. The B-type discharge is due to dielectric breakdown in a strong electric field occurring through the oxide layer. The radiation intensities of the species are related to the excitation caused by electron impact under the high electric field imposed in the discharge channel. The A and C types of discharge are due to gas discharges occurring in micropores of the oxide film: type A are from the surface holes while type C are discharges in the relatively deep holes. While the high intensity spikes mainly correspond to B-type discharges, the remainder of the intensity profile was related to A and C discharges. Since the B-type discharge was the strongest, it would have the greatest effect on the plasma temperature, and hence on the surface morphology and coating microstructure.

Fig. 4.2(a) shows the emission intensity profile for the Mg emission line using a unipolar current mode for a total treatment time of 30 min. As the PEO process proceeded, strong variations in the microdischarges were observed. When looking at the variation of the Mg emission line (Mg I 384 nm) as shown in Fig. 4.2(a), one distinguishes the strong discharges effects, where the curve shows many intense spikes which correspond to strong discharges initiated from the magnesium surface-coating interface. The spike height increases as the process proceeds, especially for process times longer than 25 minutes. One of our main goals of this work is to eliminate such strong discharges (B-

type discharge), therefore, a bipolar current mode was used for that purpose. Fig. 4.2(b) shows the emission intensity profile of Mg I 384 nm for the bipolar current mode. The spikes on this curve were reduced dramatically which may be due to the presence of the negative part of the current pulse and the off time of both the positive and negative parts of the pulses. Such an effect would allow enough time for the sample to cool down until the next discharge starts to appear.

The intensity ratio of the recorded 383.8 nm (Mg I) to 518.3 nm (Mg I) spectra ($I_{Mg\,(3d\,\rightarrow\,3p)}$ / $I_{Mg\,(4s\,\rightarrow\,3p)}$) was used to determine plasma electron temperature ($T_e$). The temperature results of experiments carried out under different conditions (Table 4.1) are presented in Fig 4.3.
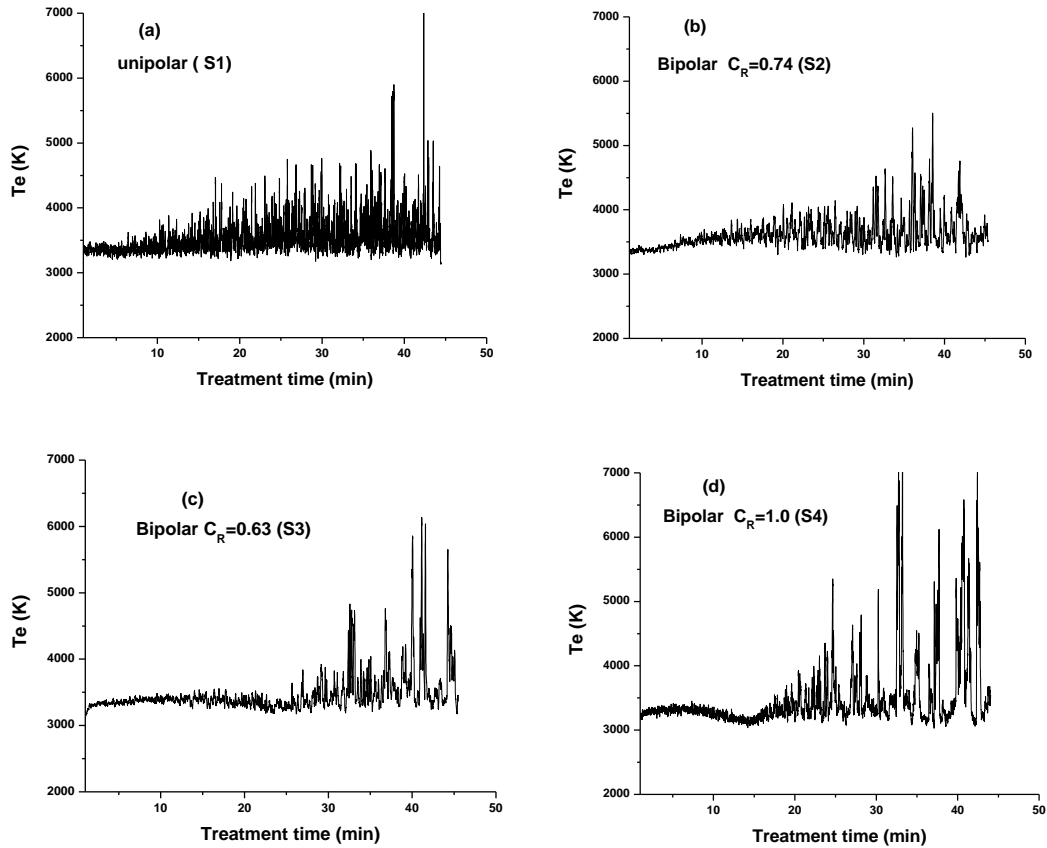


**Fig. 4.3.** Plasma temperature as a function of treatment time (min) determined from the intensity ratio of $I_{Mg\,(3d\,\rightarrow\,3p)}$ / $I_{Mg\,(4s\,\rightarrow\,3p)}$, for the samples S1 (at unipolar current mode), and S2-S4 for the bipolar current mode.

It can be seen that the temperatures measured are in the range of 3300 - 7000 K for the unipolar case and for the bipolar case the range depends on the $I^+/I^-$ current ratio and the phase current and the pulse duration time. For the S2 case the range is 3300 - 4500 K whereas for the S4 case the range is 3300-6800 K. The low temperature range (~3300 K) corresponds to the early stage discharges.

Fig. 4.3(a) shows plasma temperature profile for the unipolar current mode (S1), where the temperature fluctuated around 3300 K within the first 10 min, then the curve started to show a high number of closely-spaced temperature spikes ranging from 3300-4500 K with some of them reaching more than 6000K. These spikes corresponded to relatively strong discharges initiated from the sample surface-coating interface, the so-called B-type discharge [3], whereas the base line average is at ~3500 K. For the bipolar case S2 where $C_R$-0.74 the curve shown in Fig. 4.3(b) shows that the small spikes start to appear after 20 min, however, these spikes are less frequent and cooler than that of the other samples. The temperature was less than 4500 K which may be attributed to the negative current phase as well as the timing of the pulses. Hence, it is believed that the strong B-type discharges were reduced or eliminated Fig. 4.3(b). For the case of S3, within the 30 min after the start of the process the temperature is in the range 3300 - 3500 K. The average base temperature then started to increase to around 3500 K as can be seen from Fig. 4.3(c), and the maximum temperature was less than 6000 K. For the bipolar case S4 where $C_R$ -1.0 the curve shown in Fig. 4.3(d) shows that after 18 min from the start of the process, the spikes begin to appear with less density but the temperature reaches nearly 7000 K in some cases. The competition between the current phases from one side and the pulse durations from the other side can have a significant influence on the discharge mechanisms of the PEO process. Therefore, the $T_e$ profile depends strongly on the type of discharge and the current mode, and by using a bipolar current mode, the strong temperature spikes (due to B-type discharges) could be suppressed, or only appear at later times.

### 4.3.2 Surface morphology and coating cross section.

The surface morphologies of three sets of PEO coatings, prepared under the process parameters listed in Table 4.1 are shown in the SEM micrographs in Fig. 4.4. However,

sample S1, which was fabricated with the unipolar current mode, contained relatively large holes, Fig. 4.4(a). Some microcracks appeared on the coating surface, which could be attributed to the thermal stresses during the progress of coating as a result of melting and solidification of the ceramic compounds such as magnesium oxide [11]. Samples S2 and S3, which were fabricated using the bipolar current mode, Fig. 4.4 (b-c), showed a reduction in pore density and size. Such morphology was expected since both the number and strength of the strong B-type discharges were reduced by using the bipolar current mode, mainly due to the negative part of the pulses, as well as the off time of the pulses. Compared to sample S3, sample S2 showed an increase of small curly projections which added more irregularity to the surface morphology. The effect of the negative part of the pulse is critical, since it acts to dramatically reduce the effect of the strong B-type discharges, i.e. there will be a balance of the discharge effect. By allowing enough time for the oxide to cool down before other pulses were initiated, provides for longer sintering times and, therefore, a thick and hard coating with minimum porosity was produced.
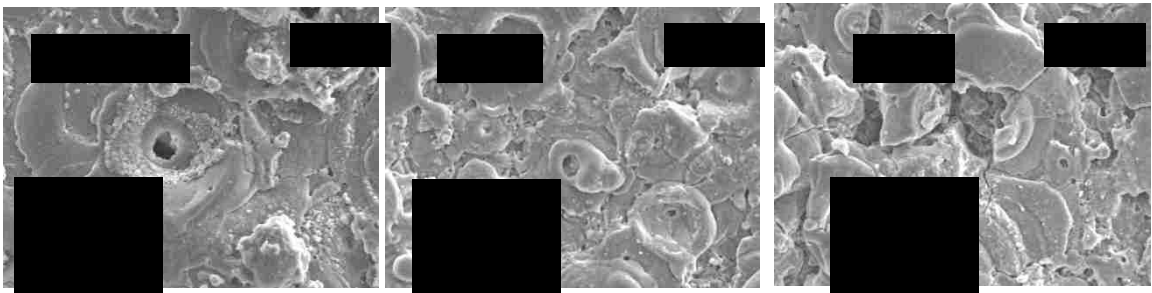


**Fig. 4.4.** SEM micrographs showing surface morphology of oxide coating on an Mg AJ62 alloy for: (a) unipolar and (b-c) bipolar current modes.

Fig. 4.5 shows the SEM micrographs of cross-sections of the PEO coated Mg samples at two different current modes for treatment times of 45 min obtained using (a) back-scattered electron mode (BSE) and (b) secondary electron mode. Back-scattered electrons emerge from an appreciable depth (a few micrometers), and BSE images are better able to reveal features such as microporosity and microcracks which appear as a fine network of channels. All coating-substrate interfaces had a wavy-jagged appearance, which may be the result of dissolution of the substrate in the early stages of the treatment. The

coating-substrate interface appears to follow the α-Mg grain boundaries which are often decorated with the (Al, Mg)$_4$Sr and Al$_3$Mg$_{13}$Sr intermetallics [28]. The BSE images for S2 given in Fig. 4.5 shows some evidence of intermetallics being retained at, or near, the coating/substrate interface. A similar interface appearance has been seen in a PEO-coated AM50 magnesium alloy [22]. This irregularity in the coating/substrate interface has a beneficial effect in improving the adhesion between the coating and substrate. The transverse section clearly shows that the coating is composed of two distinct layers, a porous outer layer on top of a denser inner layer. Also, there is evidence of a network of through-coating defects (micro cracks). Coating S1 at the unipolar current mode presented relatively porous microstructures, Fig. 4.5 (S1).

The coating appeared to have significant connected porosity, holes and other structure defects existed within the coating and near the coating/substrate interface, which would have a detrimental effect on the corrosion resistance, since localized electrochemical impedance spectroscopy on a PEO-coated MA8 magnesium alloy has shown that the corrosion process develops predominantly at the Mg/coating interface [13].

The coating thickness after the 45 min treatment time was about 40-60 μm at different locations of the cross section, and the loose layer accounts for about 30% or so of the total thickness. Such defects and porosity were likely caused by the strong B- type discharges. The high temperature generated by strong discharges melted the oxide and then some gases were likely trapped in the interface layer between the substrate and the coating.

By using the bipolar current mode, there will be a balance of the discharge effects. The T$_{off}$ duration should be long enough for the local molten oxide to be cool down before another pulse were initiated, while the T$_{on}$ provided a long enough time for sintering and therefore a thick and hard coating with minimum porosity was produced. An inner layer was found underneath the relatively thin porous top layer in coatings S2 and S3, Fig. 4.5(S2-S3), obtained with the pulsed bipolar current mode, with a smooth surface and less porosity and defects close to surface/coating interface compared to S1. Fig. 4.5(S2) shows the oxide coating on samples S2 having thickness about 35-45 μm with very thin loose layer, while, the lower inner (dense) layer appeared to be smooth with minimum porosity.
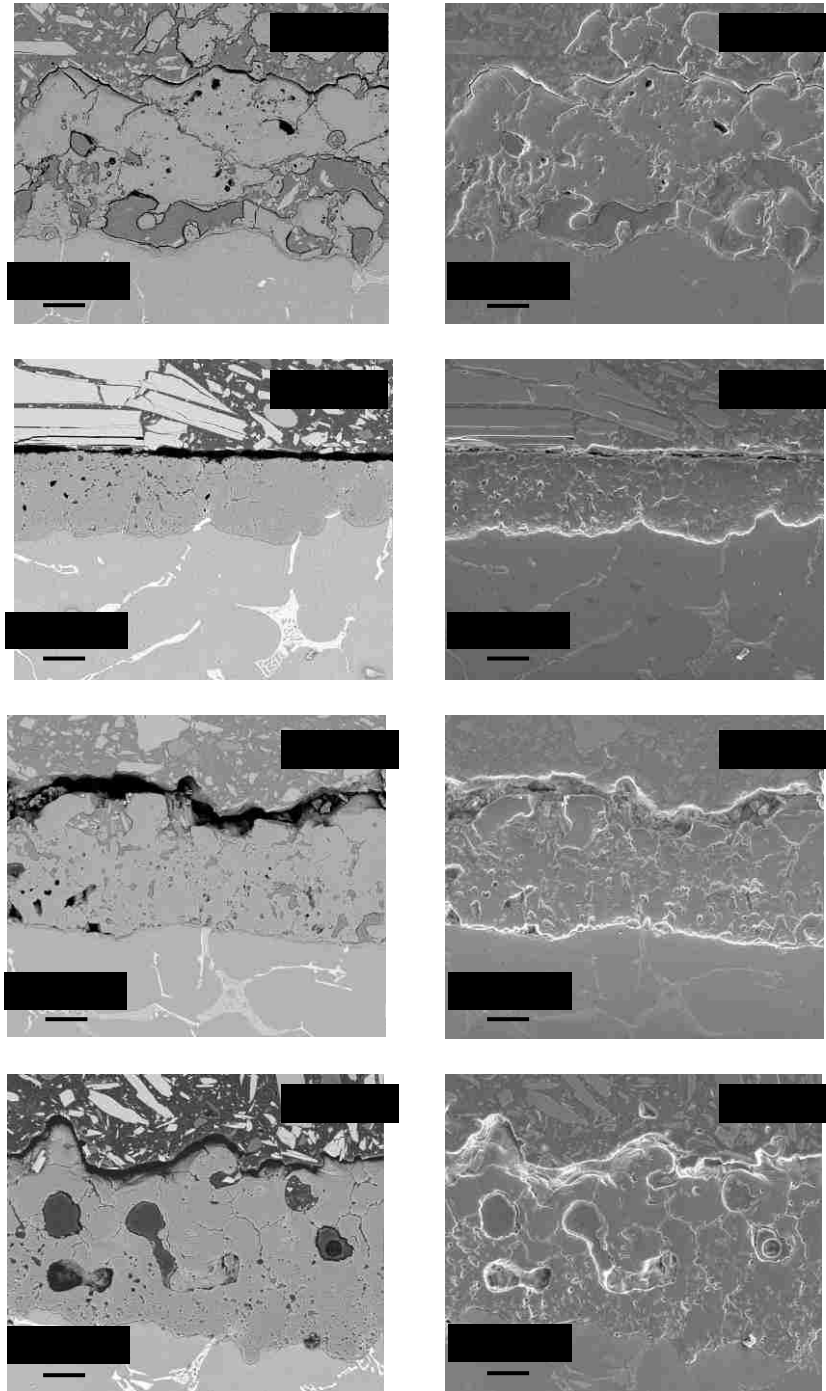
**Fig. 4.5.** SEM micrographs using (a) back-scattered electron mode and (b) secondary electron mode of a polished section of coatings on an Mg AJ62 alloy by means of unipolar (S1) and bipolar (S2-S4) current modes**.**

It is clear that beside the improvement of the surface morphology, Fig. 4.4(b), which results in formation of dense surface layer with less porosity and defects, the cathodic component of the bipolar current might suppress the strong discharges through draining out the electrical charges accumulated in the positive phase. The S2 sample was applied with the largest negative current, thus the strong discharges and plasma temperature spikes were reduced significantly, Fig. 4.3. As a result, the coating on S2 had a dense microstructure. However, the coating growth rate was slowed down. Compared to the sample S2, the sample S3 showed a thicker coating with relatively more porosity in the inner layer, Fig. 4.5 (S3). The thickness of the oxide layer was in the range of 40-55 μm, and the ratio of outer loose layer thickness over the total coating thickness was less than 24%. Compared to samples S2 and S3, sample S4 showed a thicker coating, about 55-80 μm, with relatively more porosity in the dense layer with some microcracks, Fig. 4.5(S4). The phase composition and thickness of the coatings affect the corrosion resistance of the coatings. XRD analysis of the PEO coatings indicated that all the PEO coatings were mainly composed of $MgAl_2O_4$ and MgO. The melting point of the magnesia-alumina-spinel, $MgAl_2O_4$, is 2135°C, and the presence of $MgAl_2O_4$ in the oxide layer is known to improve the corrosion resistance of Mg alloys. Ma et. al. [1] showed that an enrichment of the $MgAl_2O_4$ spinel phase in the coating, together with the minimum amount of cubic MgO, improves the corrosion resistance of the coating. The XRD patterns for PEO oxide coatings on a AJ62 alloy have previously been reported [7]. The coatings were composed of $MgAl_2O_4$ and the MgO phases. The (220), (311), (440) and (531) peaks of the $MgAl_2O_4$ phase were identified. The (200) and (220) peaks of MgO phase were found on all coatings. The (311) and (531) peaks of the $MgAl_2O_4$ phase overlapped with those of the Mg substrate. These phase compositions have recently been confirmed using a transmission electron microscopy (TEM) analysis using a unipolar mode [14].

### 4.3.3 Corrosion Properties of the Coatings
### 4.3.3.1 Potentiodynamic Polarization (E-I) Characteristics
The overall corrosion reaction of magnesium in aqueous environments which is generally an electrochemical reaction with water generating magnesium hydroxide and hydrogen gas [29, 30]:

$$Mg + 2H_2O \rightarrow Mg(OH)_2 + H_2 \qquad\qquad\qquad\qquad\qquad\qquad \textbf{4.3}$$

This overall reaction may be divided into the following anodic and cathodic partial reactions:

$$Mg \rightarrow Mg^{2+} + 2e^- \text{ (anodic/oxidation reaction)} \qquad\qquad\qquad \textbf{4.4}$$

$$2H_2O + O_2 + 4e^- \rightarrow 4OH^- \text{ (cathodic/reduction reaction)} \qquad\qquad \textbf{4.5}$$

$$Mg^{2+} + 2OH^- \rightarrow Mg(OH)_2 \text{ (product formation)} \qquad\qquad\qquad \textbf{4.6}$$
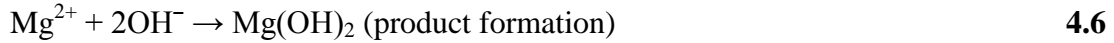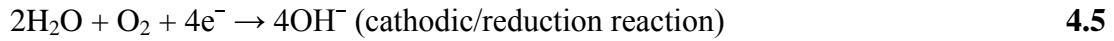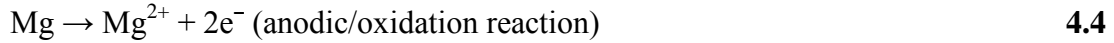
While the corrosion reaction of magnesium alloys has not yet received efficient study, Song et al [31] show that the above overall reaction of pure Mg are also applicable for the corrosion processes of AZ91D Mg alloy. However the existence of the alloying elements (Al, Zn) will have some effects on the reactions.

Fig. 4.6 shows the potentiodynamic polarization curves of the uncoated AJ62 Mg alloy (S0) and the PEO coated specimens using either unipolar or bipolar current modes (curves S1 and S2-S4 respectively). The corrosion potentials, corrosion current density, and anodic/cathodic Tafel slopes $b_a$ and $b_c$ were derived from the test data. Based on the approximately linear polarization at the corrosion potential ($E_{corr}$), the polarization resistance ($R_p$) was determined from the following equation [15]:

$$R_p = \frac{b_a b_c}{2.3 i_{corr}(b_a + b_c)} \qquad\qquad\qquad\qquad\qquad\qquad \textbf{4.7}$$

where $i_{corr}$ is the corrosion current density. A summary of the results of the potentiodynamic corrosion tests in a 3.5% NaCl solution is given in Table 4.3. The data clearly show the enhanced corrosion resistance afforded by the coatings.

 Coating S1 exhibits the lowest corrosion potential and polarization resistance but highest corrosion current density. The porous structure leads to the poorer corrosion resistance of the coating. Comparatively, coatings S2-S4, having a thick and relatively dense oxide layers, present higher corrosion potentials and polarization resistances but lower corrosion current densities than the coating S1.
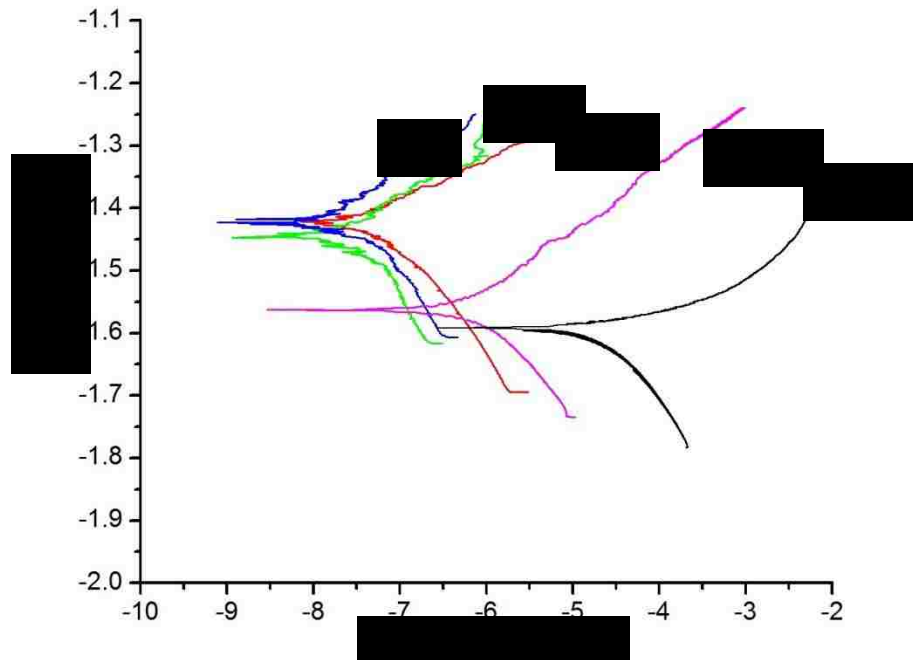
**Fig. 4.6.** Potentiodynamic polarization curves of the uncoated (S0) and coated samples using unipolar (S1) and bipolar (S2-S4) current modes.

**Table 4.3. Potentiodynamic polarization corrosion test results in 3.5%wt NaCl solution**

|  | S0 | S1 | S2 | S3 | S4 |
|---|---|---|---|---|---|
| $E_{corr}$ (V) | -1.58 | -1.54 | -1.416 | -1.448 | -1.422 |
| $I_{corr}$ (μA/cm$^2$) | $2.24 \times 10^{+1}$ | $5.39 \times 10^{-1}$ | $1.20 \times 10^{-2}$ | $1.50 \times 10^{-2}$ | $4.30 \times 10^{-2}$ |
| $\beta_a$ (V) | 0.19 | 0.14 | 0.07 | 0.06 | 0.09 |
| $\beta_c$ (V) | 0.05 | 0.08 | 0.06 | 0.13 | 0.10 |
| $R_p$ (Ω • cm$^2$) | $7.11 \times 10^{+2}$ | $4.10 \times 10^{+4}$ | $1.24 \times 10^{+6}$ | $1.19 \times 10^{+6}$ | $4.72 \times 10^{+5}$ |
| $P_i$ (mm/year) | $5.12 \times 10^{-1}$ | $1.23 \times 10^{-2}$ | $2.74 \times 10^{-5}$ | $3.43 \times 10^{-5}$ | $9.83 \times 10^{-5}$ |

Since the bipolar current mode produces a thicker and denser coating, samples S2-S4 show a higher polarization resistance up to $1.24 \times 10^6$ Ω for S2 case (see Table 4.3) and lower corrosion current density than sample S1 coated by unipolar current mode, with a

polarization resistance of $4.10 \times 10^4$ Ω and higher corrosion current density. Although the sample S4 has a thicker coating than S2 and S3, its corrosion resistance is lower than those of S2 and S3. This is likely attributed to the micro cracks and relatively porous inner layer. It is expected that a thicker coating gives rise to better corrosion resistance. However as the porosity level in the unipolar sample coating (S1) was quite high, it exhibited a lower corrosion potential compared to samples S2-S4 prepared using a bipolar current mode. Therefore, for better localized corrosion resistance the coating needs to be not only thicker, but also should be free from defects such as porosity [11,16]. The properties of the plasma discharges themselves in the bipolar current mode differ from those of the unipolar one. An increase of the A and C discharge types, and decrease of strong B discharges, moving over the surface being oxidized, have a significant effect on the coating properties, where a dense coating morphology could be achieved by adjusting the positive to negative current ratio and their timing to eliminate or reduce the strongest plasma discharges and thus the high temperature spikes [3].

In the potentiodynamic polarization method for measuring the corrosion rate of Mg alloys, the corrosion current density, $i_{corr}$ ($\mu A/cm^2$) can be related to the average corrosion rate, $P_i$ (mm/year) by the Stern–Geary equation [17]:

$$p_i = \frac{3.28 \times 10^{-3} M}{2\rho} i_{corr}$$

**4.8**

where M is the atomic mass in g, $\rho$ is the density in $g/cm^3$ of Mg and $i_{corr}$ is the corrosion current in $\mu m/cm^2$. The corrosion current density, $i_{corr}$ ($\mu A/cm^2$) can be related to the average corrosion rate, Pi (mm/year) by equation (4.9).

$P_i = 0.02285 \times i_{corr}$ **4.9**

The calculated values for $P_i$ are also given in Table 4.3. Whilst it is recognized that corrosion rates obtained from Tafel extrapolations differ from those obtained from weight loss or hydrogen evolution measurement [17], they do illustrate the protective nature of the PEO coatings.

It is illustrative to compare our measured corrosion rate ($P_i$ values) with other data in the literature for uncoated Mg and Mg alloys in 3.5 wt % NaCl solutions at ambient or near-ambient temperature: see Table 4.4. The corrosion rate measured for AJ62 alloy is, in general, consistent with other data in the literature. The corrosion rates are influenced by

53

many factors including alloy composition, microstructure and phase distribution, temperature and environment [18]. All data in Table 4.4 are for 3.5 wt % NaCl solutions. The effect of temperature is nicely illustrated by the data for AZ91D where there was a significant increase in corrosion rate on increasing the temperature from 20 $^{o}$C to 35 $^{o}$C. Another important factor is time of immersion in 3.5 wt % NaCl before performing the potentiodynamic polarization testing. Shi et al [17], for instance, have shown $P_i$ can vary from 0.9 to 1.8 mm/year for pure Mg and from 0.2 to 7.3 mm/year for AM60 alloy when the immersion time is varied from zero minutes to 7 days. Our data for the AJ62 alloy were obtained for an immersion time of 30 minutes.

**Table 4.4. Corrosion rate data for uncoated (bare) magnesium and magnesium alloys from potentiodynamic polarization studies in 3.5 wt % NaCl solutions.**

| Mg alloy | Temperature ($^{o}$C) | $i_{corr}$ ($\mu$A/cm$^2$) | $P_i$ (mm/year) | Reference |
|----------|------------------------|-----------------------------|------------------|-----------|
| AJ62 | 25±2 | 22.4 | 0.51 | Current study |
| Mg pure | 25 | 12.5 | 0.29 | 19 |
| AZ91D | 35±2 | 112 | 2.55 | 20 |
| AZ91D | 20±2 | 6.2 | 0.14 | 21 |
| AM50B | 20±2 | 12 | 0.28 | 21 |
| AM60B | 20±2 | 8.2 | 0.19 | 21 |
| AZ31B | 20±2 | 8.9 | 0.20 | 21 |

**4.3.3.2 Electrochemical Impedance Spectroscopy (EIS) Measurements**

The Nyquist diagrams are given in Fig. 4.7. The electrochemical properties of the coatings were examined using electrical equivalent circuits representing the various elements of the coatings. Taking both the physical structure of the PEO coatings and their impedance responses into account, and based on previous studies [22] an equivalent circuit model for the PEO-coated specimens was developed. Different combinations of elements (such as resistor, capacitor, and Warburg diffusion) in different sequences (i.e. parallel, series) were tried. The impedance data were analyzed using EC-Lab$^{®}$ software and best-fitted to the appropriate equivalent circuit model. In the fitting method, a combination of randomize followed by the most widely used optimization algorithm, Levenberg-Marquardt fitting, was used [23]. A randomization has been added before the

fitting in order to help the algorithm to find the best couple of parameter values as close as possible to the real one (with minimum $X^2$ value). The goodness of the fit for this method is around $X^2 \leq 1$. $X^2$ used in this method is defined as follows [24]:

$$X^2 = \sum \frac{/Z_{meas}(i) - Z_{model}(f_i, param)/^2}{\sigma_i^2}$$  **4.10**

where $Z_{meas}(i)$ is the measured impedance at the $f_i$ frequency, $Z_{model}(f_i, param)$ is function of chosen model, $f$ is the frequency, *param* is the model parameters (ex: Rs, CPE1,…) and $\sigma_i$ is the standard deviation. Taking both the physical structure of the PEO coatings and their impedance responses into account, and based on previous studies, the model chosen for the fitting was a commonly used model for PEO [12,22,25] and other ceramic coatings [26]. The choice of the circuit was a balance between a reasonable fitting of the experimental values and a good description of the electrochemical system by keeping the number of circuit elements at a minimum. It is recognized that any electrode process is complex and usually consist of a many different sub-processes. The sub-processes include both mass transfer and charge transfer and can be in series or parallel with each other [27].More complex equivalent circuits have been proposed by Ghasemi et al [12] for PEO-coatings produced with KOH/Na$_3$PO$_4$ and KOH/NaAlO$_2$ electrolytes. In this model, a more general Constant Phase Element (CPE) was used instead of a capacitive element, which reflects the distributed surface reactivity, surface roughness, electrode porosity, and current and potential distributions associated with electrode geometry [27]. The proposed equivalent circuit (Fig. 4.8) consists of two time constants. $R_S$ is the solution (electrolyte) resistance. $R_1$ is the coating resistance (virtual pore resistance [28]) which is parallel with a constant phase element *CPE1* (*CPE1* in model of Ryu et al [28]). *CPE2* is the constant phase element for the double layer capacitance of the interface electrical double layer at or near the coating/substrate interface. $R_2$ represent the polarization resistance which is the Faradic charge transfer resistance related to electrochemical reactions in the same coating/substrate interface region [15]. The use of a frequency-dependent CPE ($Fs^{n-1}cm^{-2}$) instead of pure capacitance will give better fitting between the theoretical and experimental data [22,23] due to a distribution of the relaxation times as a result of inhomogeneities in the morphologies, such as surface

roughness/porosity, or diffusion. The impedance of CPE is expressed by the following equation:

$$Z_{CPE} = 1/[Q(j\omega)^n] \hspace{4cm} \textbf{4.11}$$

where $Z_{CPE}$ ($\Omega cm^2$) is the impedance of the constant-phase-element. The $Q$ is CPE constant ($\Omega^{-1}s^n cm^{-2}$) is a combination of properties related to both the surface and the electroactive species, and is independent of frequency, $j$ is the imaginary unit ($\sqrt{-1}$), $\omega$ is the angular frequency (1 rad/s) of the sine wave being considered as $\omega = 2\pi f$, $f$ is the frequency in Hz; the value of n ranges between 0 and 1.
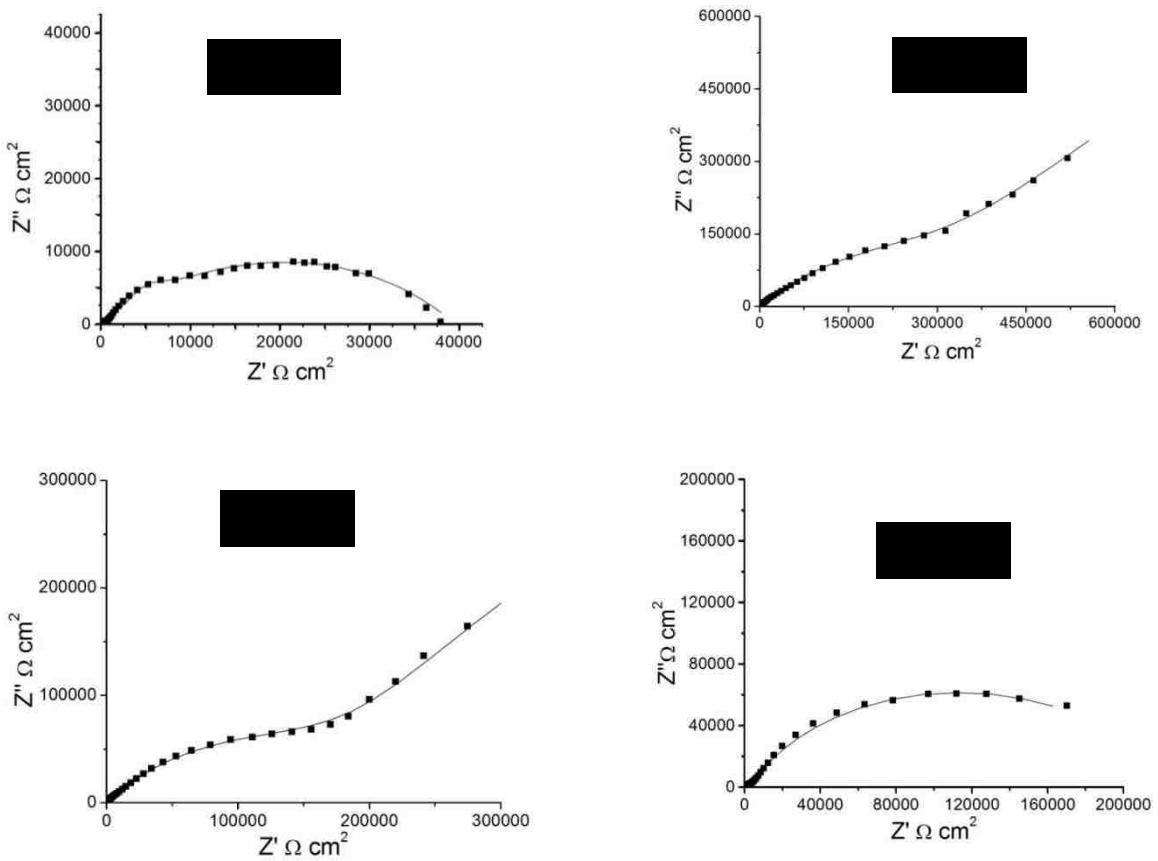


**Fig. 4.7.** Nyquist diagrams of the EIS tests (a) S1, (b) S2, (c) S3 and (d) S4; the dots represent the experimental data; the solid lines correspond to the simulated values based on the equivalent circuit model.

Depending on the value of exponent n, the physical meaning of the CPE of the circuit can be related to pure resistance (n=0), pure capacitance (n=1), pure inductance (n=−1), or mass transport related impedance, i.e. Warburg impedance (n=0.25–0.5).

A good fit was observed between the experimental data and the simulated values (Fig. 4.7 (a) and (b)). The circuit elements calculated from the fitting are summarized in Table 4.5.
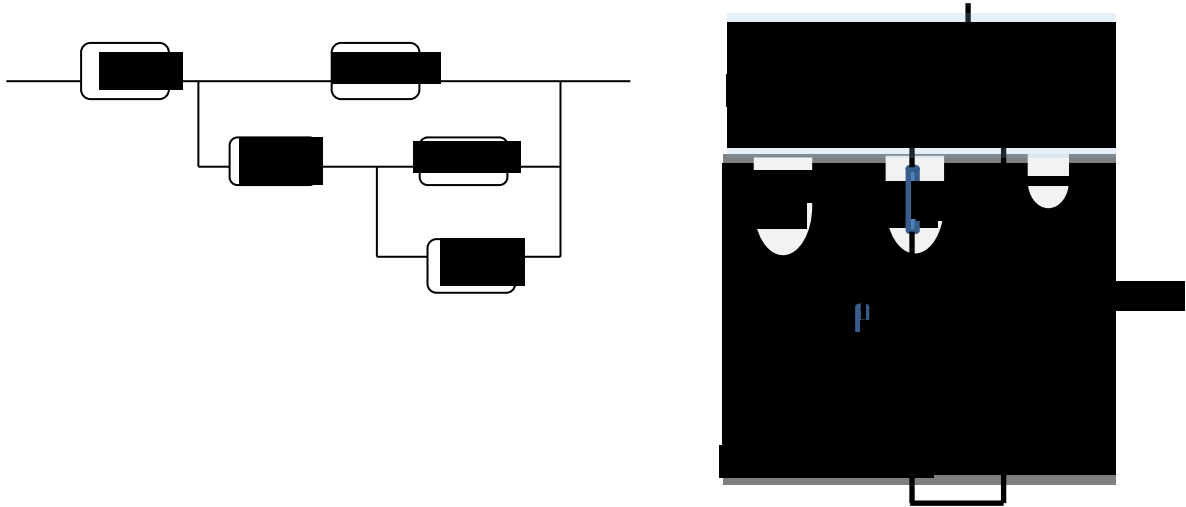


Fig. 4.8 The equivalent circuit model for coated samples.

Table 4.5. Equivalent circuit data

|  | S1 | S2 | S3 | S4 |
|---|---|---|---|---|
| $R_s$ ($\Omega \cdot cm^2$) | 20 | 25 | 27 | 28 |
| CPE1-Q ($\mu F/cm^2 \, s^{1-n}$) | 5.11 | 0.59 | 0.69 | 0.22 |
| CPE1-n | 0.5378 | 0.5296 | 0.5631 | 0.5256 |
| $R_1$ ($\Omega \cdot cm^2$) | 3.91E+04 | 4.7 E+05 | 2.4 E+05 | 6.3 E+03 |
| CPE2-Q ($\mu F/cm^2 \, s^{1-n}$) | 0.076 | 2.97 | 4.64 | 1.01 |
| CPE2-n | 0.9195 | 0.5664 | 0.7026 | 0.7752 |
| $R_2$ ($\Omega \cdot cm^2$) | 3.19E+02 | 2.33E+06 | 1.56E+06 | 2.29E+05 |
| $R_{total}$ ($\Omega \cdot cm^2$) | 3.94E+04 | 2.80E+06 | 1.80E+06 | 2.35E+05 |

The n values that are close to 0.5 for CPE1 indicates a diffusion (mass transfer) process of oxidized and reduced species. Diffusion components can be readily seen by the diffusion tails in the Nyquist diagrams for S2 and S3 coatings: see Fig. 4.7 (b) and (c). The relatively high coating resistance ($R_1$) and lower coating capacitances (*CPE1*) of

bipolar samples S2 and S3 compared to the unipolar sample S1, reflect the smaller amount of ionic conducting pathways which could be pores or microcracks in the bipolar coatings. The very high $R_2$ resistance values for samples S2 and S3 compared to S1 and S4 indicates that the microstructure at the coating/substrate interface in these two samples (S2 and S3) acts as a much better barrier to penetration of the aggressive electrolyte to the metal substrate. It is interesting to note that the values obtained by EIS for the total resistances of the coating $R_1 + R_2$ (see Table 4.5) follow the same order, S2>S3>S4>S1, as for Rp in the potentiodynamic polarization tests.

## 4.4. Discussion

The influence of current mode and pulse duration on the coating morphology, thickness and corrosion resistance was significant. The use of the unipolar current mode results in the production of significant porosity and other structural defects, eg microcracks, which degrade the coatings, corrosion resistance. The application of a bipolar mode with a cathodic component, changes the sample surface morphology, resulting in the formation of a thicker and denser inner layer with fewer defects, and a thin, porous outer layer. The properties of the plasma discharges themselves in the bipolar current mode differ from those of the unipolar one. An increase of the A and C discharge types, and decrease of strong B discharges [3], moving over the surface being oxidized, have a significant effect on the coating properties. The cathodic component not only helps to eliminate, or at least reduce, the strong B-type discharges during the subsequent anodic period, but also directly affects the coating growth process. By reducing or eliminating the strong B-type discharges, and hence reducing the high temperature spikes, the average plasma temperature was to some extent also decreased. However, these reduced temperatures are still sufficient to allow reaction between the magnesium and aluminum oxides leading to the formation of a surface layer with the magnesium aluminate spinel structure with good anticorrosion properties. This confirms the importance of current regimes together with the pulse timing in providing appropriate thermodynamic conditions for the formation of corrosion resistant PEO layers on magnesium alloys.

**4.5. Conclusions**

- Two different current modes during the PEO processes in sodium aluminates electrolytes were used to produce oxide coatings on an AJ62 alloy. Both modes successfully improve the corrosion resistance compared to the uncoated alloy. However, the coating made using the bipolar current mode is more beneficial in improving the corrosion resistance of the PEO coating than the unipolar current mode.

- The plasma temperatures were characterized by means of OES, and it was found that the plasma temperature vs. process time relationship were different under different current operating modes. The plasma temperature spikes were believed to be caused by the strongest plasma discharges initiated at the interface between the oxide coating and substrate. Controlling or reducing the strong discharges had significant effects on the plasma temperature profiles and the quality and characteristics of the coating layers. Compared to the unipolar current process, the application of pulsed bipolar current resulted in reducing the high spikes on temperature profiles and the average plasma temperature. This work showed that by appropriately controlling the ratio of the positive to negative pulse currents as well as their timing, the very strong plasma discharges and the resulted high temperature spikes could be eliminated and hence the quality of the coatings was considerably improved.

- The results showed that the anions in the electrolyte solution directly contributed to the coating formation process. Apart from MgO which is a common phase in the coatings, a specific phase, $MgAl_2O_4$, resulted from the aluminate electrolyte.

-This work shows that using a bipolar current mode helps to reduce the strong discharges (B-type discharge) that usually cause detrimental defects in the oxide layer for long treatment times (typically greater than 30-40 min for magnesium alloys). This result was confirmed by spectroscopic measurements of the discharges during the PEO process. As a consequence, thick homogeneous layers may be grown with minimum porosity and defects.

-The electrochemical corrosion experiments show that the corrosion resistance of the AJ62 alloy was considerably increased by PEO oxide coating 50 times for unipolar current mode and 2000 times for bipolar current mode. The corrosion resistance of the PEO specimens was mainly determined by the structure of the oxide at, or near, the

coating/substrate interface. Samples coated using the bipolar current mode exhibit higher

*R2* –values indicating the presence of a good barrier to the penetration of the aggressive

electrolyte to the metal surface.

## REFERENCES

[1]     Ma Y, Nie X, Northwood DO and Hu H, Systematic study of the electrolytic plasma oxidation process on a Mg alloy for corrosion protection. Thin Solid Films 494 (2006) 296-301.

[2]     Ma Y, Nie X, Northwood DO and Hu H, Corrosion and erosion properties of silicate and phosphate coatings on magnesium. Thin Solid Films, 469–470 (2004) 472-477.

[3]     Hussein RO, Nie X, Northwood DO, Yerokhin A and Matthews A, Spectroscopic study of electrolytic plasma and discharging behaviour during the plasma electrolytic oxidation (PEO) process. Journal of Physics D: Applied Physics, 43 (2010), 105203.

[4]     Gnedenkov SV, Khrisanfova OA, Zavidnaya AG, Sinebryukhov SL, Egorkin VS, Nistratova MV, Yerokhin A and Matthews A, PEO coatings obtained on an Mg–Mn type alloy under unipolar and bipolar modes in silicate-containing electrolytes. Surface & Coatings Technology, 204 (2010) 2316-2322.

[5]     Yerokhin AL, Shatrov A, Samsonov V, Shashkov P, Leyland A and Matthews A, Fatigue properties of Keronite coatings on a magnesium alloy. Surface & Coatings Technology, 182 (2004) 78-84.

[6]     Arrabal R, Matykina E, Hashimoto T, Skeldon P and Thompson GE, Characterization of AC PEO coatings on magnesium alloys. Surface & Coatings Technology, 203 (2009) 2207-2220.

[7]     Zhang P, Nie X and Northwood DO, Influence of coating thickness on the galvanic corrosion properties of Mg oxide in an engine coolant. Surface & Coatings Technology, 203 (2009) 3271-3277.

[8]     Hussein RO, Nie X and Northwood DO, Coating growth behavior during the plasma electrolytic oxidation process. The Journal of Vacuum Science and Technology A, 28 (2010) 766-773.

[9]     Sansonetti JE and Martin WC, Handbook of Basic Atomic Spectroscopic Data. Journal of Physical and Chemical Reference Data, 34 [4] (2005) 1559-2260.

[10]    Griem H R, Plasma Spectroscopy (Cambridge: McGraw-Hill) (1964).

[11]    Srinivasan PB, Liang J, Blawert C, Stormer M and Dietzel W, Effect of current density on the microstructure and corrosion behavior of plasma electrolytic oxidation treated AM50 magnesium alloy. Applied Surface Science, 255 (2009) 4212-4218.

[12]    Ghasemi A, Raja VS, Blawert C, Dietzel W and Kainer KU. Surface & Coatings Technology, 204 (2010) 1469-1478.

[13]    Sinebryukhov SL, Gnedenkov AS, Mashtalyar DV and Gendenkov SV. Surface & Coatings Technology,  205 (2010) 1697-1701.

[14]   Zhang P, Nie X, Hu H and Liu Y. TEM analysis and tribological properties of plasma electrolytic oxidation (PEO) coating on a magnesium engine AJ62 alloy. Surface & Coatings Technology, 205 (2010) 1508-1514.

[15]   Revie RW, Uhlig's Corrosion Handbook, 2nd ed, John Wiley & Sons, New York, 2000.

[16]   Ryu HS and Hong S.-H, Corrosion resistance and antibacterial properties of Ag-containing MAO coatings on AZ31 magnesium alloy formed by microarc oxidation. J of the Electrochemical Society, vol. 157, 2010, p.C131-C136.

[17]   Shi Z, Liu M and Atrens A, Measurement of the corrosion rate of magnesium alloys using Tafel extrapolation. Corrosion Science 52 (2010) 579–588.

[18]   Song GL and Atrens A, Corrosion mechanisms of magnesium alloys. Advanced Engineering Materials, 1 (1) (1999) 11-33

[19]   Zhang P, Nie X and Northwood DO, Influence of coating thickness on the galvanic corrosion properties of Mg oxide in an engine coolant. Surface & Coatings Technology, 203 (2009) 3271-3277.

[20]   Zeng L, Yang S, Zhang W, Guo Y and Yan C, Preparation and characterization of a double-layer coating on magnesium alloy AZ91D. Electrochimica Acta 55 (2010) 3376–3383.

[21]   Cakmak E, Tekin K, Malayoglu U and Shrestha S, The effect of substrate composition on the electrochemical and mechanical properties of PEO coatings on Mg alloys. Surface & Coatings Technology 204 (2010) 1305–1313.

[22]   Duan H, Yan C, and Wang F, Effect of electrolyte additives on performance of plasma electrolytic oxidation films formed on magnesium alloy AZ91D. Electrochimica Acta, 52 (2007) 3785-3793.

[23]   Nocedal J and Wright SJ, Numerical Optimization, Springer, New York, 1999.

[24]   EC-Lab®  Software User's Manual, 2010, http://www.bio-logic.info/.

[25]   Hwang DY, Kim YM and Shin DH, Corrosion Resistance of Plasma-Anodized AZ91 Mg Alloy in the Electrolyte with/without Potassium Fluoride. Material Transaction, 50(3) (2009) 671-678.

[26]   Zhang Y, Yan C, Wang F. and Li W, Electrochemical behavior of anodized Mg alloy AZ91D in chloride containing aqueous solution. Corrosion Science, 47 (2005) 2816-2831.

[27]   Jorcin JB, Orazem M E, Pébère N and Tribollet B, CPE analysis by local electrochemical impedance spectroscopy. Electrochimica Acta, 51 (2006) 1473-1479.

[28]   Ryu HS, Ryu J, Park D and Hong S.-H, Electrochemical Corrosion Properties of Nanostructured YSZ Coated AZ31 Magnesium Alloy Prepared by Aerosol Deposition. J of the Electrochemical Society, 158 (2) (2011) C23-C28.

[29]   Makar G L, Kruger J, Corrosion of Magnesium. International Materials Reviews, 38 (1993)138-153.

[30]   Song G, Atrens A, Dargusch M, Corr. Sci. 1999, 41, 249.

# CHAPTER 5

# PROCESSING-MICROSTRUCTURE RELATIONSHIPS IN THE PLASMA ELECTROLYTIC OXIDATION (PEO) COATING OF A MAGNESIUM ALLOY.

## Published in:

## 5.1 Introduction

The PEO method can be used to form a thick, hard and adherent ceramic coating on the surface of Mg alloys, as well as other light weight metals Al and Ti, and their alloys [1-3]. Many processing parameters can affect the PEO process, including electrolyte composition [4], substrate material [5], and electrical parameters, mainly current mode and current density [6]. Different current modes have been utilized in the PEO treatment including, DC, AC, unipolar and bipolar current modes [2] which play important roles in the consequent voltage breakdown, local melting and oxidation of the substrate, quenching and re-crystallization processes. Hence, the formation mechanisms for the coatings are complex due to the involvement of electro-, thermal-, and plasma- chemical reactions in the electrolyte [3,7,8].

It has been recognized that when using either DC or pulsed unipolar modes of PEO processing for Mg [9], the resulting oxide coating is porous, contains other defects, and is only partially adherent. Varying the current mode produces changes in the PEO discharge events both in terms of discharge intensity (how strong they are) and discharge density (number of discharges). The differences in the nature of the discharges have a profound effect on the coating microstructure, thickness, roughness, porosity, hardness, and the corrosion resistance of the coated magnesium alloy. PEO coatings formed using a bipolar current mode have been reported to have a more compact structure with fewer defects, and a more uniform coating thickness compared to coatings formed using a unipolar mode [8,10,11].

As noted by Dunleavy et al [12], methodologies to obtain quantitative data on the PEO discharge events and the associated plasmas, which are integral to the growth mechanism and strongly affect both the microstructure and properties of the coating, fall into three categories- optical, spectral and electrical. Optical measurements can provide information on the duration, size (spatial extent) and spatial distribution of the discharges. Optical measurements on Mg have shown discharge event durations of 50 to 1100 μs [8]. Electrical measurements can provide information on discharge currents, which are typically in the range of 1 to 100 mA [12]. Current density values can also be obtained if the discharge diameters are estimated using optical measurements [12]. Spectral analysis can provide information on the temperatures, densities and chemical compositions of plasmas [13].

The spectral diagnostic technique is an effective way to study the physical phenomenon in the PEO process by investigating the emission spectra of plasma. Optical emission spectroscopy (OES) has previously been applied to the PEO process for the detection and analyses of light that is emitted from the plasma species for Al [13,14], Mg [8,15,16] and Ti [17] alloys. OES has also been used in the study of coating mechanisms in the PEO process [15-18]. The optical emission spectra were recorded and plasma temperature profile versus processing time was constructed [13]. In these previous studies, the collective behavior of the plasma discharge over the entire surface, rather than the individual discharges, was reported. Based on the OES results, and with an assumption of local thermodynamic equilibrium (LTE) [19], plasma electron temperatures can be calculated using the relative intensities of spectral lines of the same atomic or ionic species [19]. Evaluations based on the spectroscopic method for an Al 1100 alloy show the electron temperatures to be in the range of 4000 - 7000 K for the unipolar current mode and 4000 - 5500 K for the bipolar current mode [15].

In this chapter, the plasma-microstructure relationships in the PEO processing of magnesium alloy AM60B are studied by optical emission spectroscopy (OES). The acquisition system for the plasma spectrum is described, and the effect of hybrid current modes (combination of bipolar and unipolar) on the plasma is analyzed through a comparison of the plasma spectra and plasma electron temperatures for two different hybrid current modes, unipolar followed by bipolar and bipolar followed by unipolar. The

single modes, unipolar and bipolar were, used for comparison purposes. The temporal characterizations of the lines for Hβ, Hα, Na I and Mg I are used in the analysis. These OES observations are then related to the microstructure of the resultant PEO coatings.

## 5.2 EXPERIMENTAL ARRANGEMENT AND DIAGNOSTIC METHODS

### 5.2.1. Material and PEO process

Due to good ductility and toughness with reasonable yield and tensile properties, AM60B magnesium alloy (mass fraction: Al 5.6–6.4%, Mn 0.26–0.4%, Zn ≤ 0.2%, balance Mg) disc coupons (Φ25×5mm) were used as the test samples in this study. The coupons were manually ground and polished on 240, 400,600, and 1200 grit silicon carbide (SiC) waterproof abrasive papers. The coating was obtained in an alkaline electrolyte containing 7 g/l $K_4P_2O_7$, and 3g/l $Na_2Al_2O_4$ and potassium hydroxide (1 g/l KOH). A cooling system maintained the electrolyte at a temperature below 25 $^oC$ during the process.

The PEO coating system used to produce the oxide coatings consists basically of a stainless steel water cooled container with the alkaline electrolyte and a powerful electrical source (output 300-1000 V). The stainless steel container acts as a counter-electrode (cathode) with the coupons as the anode. The electrodes are connected to two pulsed DC power supplies (with an amplitude in the range of 0-5 A and 0-15 A) operating under a constant current control function (after the initial transitory regime) to generate different current waveforms. During the coating process, the voltage was increased gradually with process time so as to maintain a preset current density as the coating thickness increased. These power supplies were specially designed to allow independent control over the main pulse parameters, such as pulse duration, amplitude and duty cycle, during both positive and negative biasing using a Spik 2000A controller.

To examine the effects of current mode on the resultant properties of the coatings, the PEO coating process was carried out using different current modes. Four different sets were prepared, with each set consisting of four coated samples. The process parameters are listed in Table 5.1.

- Set U (a unipolar pulsed-DC mode) for 30 minutes.
- Set B (a bipolar current mode) for 30 minutes.

- Set H1 used a combined unipolar (H11 for only 15 min) followed by bipolar (H12 for another 15 min) current mode for a total of 30 minutes.
- Set H2 switched the sequence for the unipolar and bipolar modes compared with Sample H1 (H21 treated firstly using bipolar current mode; H22 completed the treatment using unipolar mode for second 15 minutes) as shown in Fig. 5.1 (a and b).

Scanning electron microscopy (FEI Quanta 200 FEG with solid state backscattered detector operated at 10 KV) in both the secondary electron (SE) and back-scattered electron (BSE) modes was used to observe both the coating surface morphology and, through observation of sample cross sections, coating thickness and integrity. The samples were first sputtered with a gold film to make them conductive for SEM analysis.

Table 5.1  PEO Process parameters for coating AM60B Mg alloy.

| Sample | | Current mode | Time (min) | $I^+$ (A) | $I^-$ (A) | $T^+_{on}$ (µs) | $T^+_{off}$ (µs) | $T^-_{on}$ (µs) | $T^-_{off}$ (µs) | $C_R$ |
|---|---|---|---|---|---|---|---|---|---|---|
| U | | Unipolar | 30 | 0.7 | N/A | 400 | 100 | N/A | N/A | N/A |
| B | | Bipolar | 30 | 0.7 | 0.63 | 400 | 100 | 400 | 100 | 0.74 |
| H1 | Hybrid | Unipolar H11 | 15 | 0.7 | N/A | 400 | 100 | N/A | N/A | N/A |
| H1 | Hybrid | Bipolar H12 | 15 | 0.7 | 0.63 | 400 | 100 | 400 | 100 | 0.74 |
| H2 | Hybrid | Bipolar H21 | 15 | 0.7 | 0.63 | 400 | 100 | 400 | 100 | 0.74 |
| H2 | Hybrid | Unipolar H22 | 15 | 0.7 | N/A | 400 | 100 | N/A | N/A | N/A |
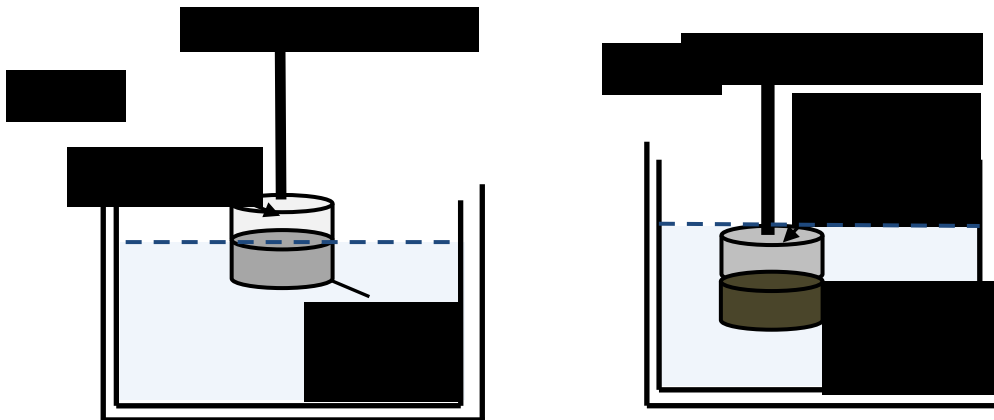


Figure 5.1. Schematic representation of the experimental set-up for PEO coatings using (b) single current mode and (b) two current modes (hybrid).

### 5.2.2 Optical Emission Spectroscopy

Passive spectroscopy diagnostics, in which light emitted from the plasma itself is recorded, are well established in plasma physics since they are non-destructive, and consequently do not affect the plasma. Radiating atoms, molecules and ions can provide an insight into plasma processes and plasma parameters, with the possibility of performing real time observations. In the passive method, one of the basic underlying processes is the excitation of particles (atoms, molecules, ions) by electron impact from level q to level k and the decay to level i by spontaneous emission with the transition probability $A_{ki}$ resulting in line emission $\varepsilon_{ki}$.

The importance of the population models is to determine the quantity of emitted photons and its dependency on the plasma parameters. In thermal equilibrium in a plasma, the population density of excited states is described by a Boltzmann distribution. However this equilibrium is essentially never achieved in laboratory plasmas. Therefore a less complete form of thermal equilibrium, known as Local Thermal Equilibrium (LTE), is considered [19].

The observed spectral range was from 200 to 775 nm. A specially designed PC2000-UV-VIS Fiber Optic Spectrometer (Ocean Optics Company) was used. A 1200 line holographic UV for bandwidth 200-500 nm and 1200 line holographic VIS for bandwidth 450-770 nm gratings with the spectral resolution of 1.0 nm at mid to high sensitivity, were used to acquire the total spectrum from 200 nm to 770 nm. The spectral signals were then acquired by Sony ILX511B silicon CCD detector which consists of a 2048-element linear CCD-array (a charge- coupled device array detector). As only relative intensities have to be measured, the intensity is in arbitrary units. The intensity of spectrum is the cumulative result of an acquiring cycle. Since the discharges occur randomly (the source does not always emit equally over the whole sample area), an integrated signal was used which was collected from the total sample surface facing the fiber optic. Before the experiments, a cross-check of the manufacturer's spectrometer wavelength calibration was done using two different laser beams (He-Cd with $\lambda$= 442 nm and He-Ne with $\lambda$= 632.816 nm). An intensity sensitivity calibration was also performed using SL2 calibrated Lamp (StellarNet Inc.): excellent matching was found.

The emission intensities of the plasma species were monitored as a function of both time and current mode using the OES system. Six different spectral lines were recorded simultaneously, which eliminates discrepancies that may otherwise happen if the spectra are recorded at different times or with different samples.
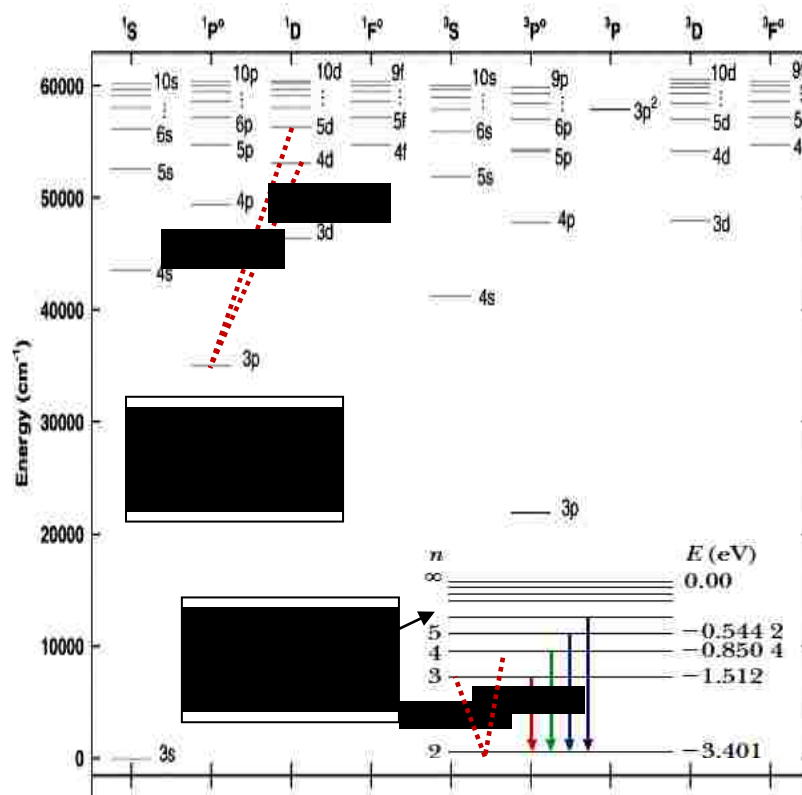


Figure 5.2. Atomic level configuration of H- Balmer series and Mg I.

## 5.3 Diagnostic method

Plasma emission intensities were measured and analyzed by using optical emission spectroscopy to determine the plasma compositions and to calculate the electron temperature. The plasma electron temperature $T$e, can be determined from the relative intensities of spectral lines of the same atomic species [19]. This method is valid if the level populations of the lines in question are populated according to the Boltzmann law: in other words, at least local thermodynamic equilibrium (LTE) must exist for these levels. Figure 5.2a shows the atomic level for hydrogen Balmer series whereas Figure 5.2b shows the atomic level configuration for magnesium which is a two electron system.

The levels are separated into two multiplet systems: a singlet and a triplet system. Optically allowed transitions (used in this calculation) which are excited from the same energy level are indicated by an arrow and labeled with the corresponding wavelength. Energy is measured relative to the ground state 3s $^1$S.

## 5.4 Experimental Results

## 5.4.1 Voltage behavior

The voltage behaviour has been shown to be a limiting factor on the intensity of plasma discharges during PEO processing [12,20]. Fig. 5.3 shows the average output anodic voltage as functions of PEO processing time using four combinations of current modes. The average voltage–time profile for PEO process is highly reproducible.
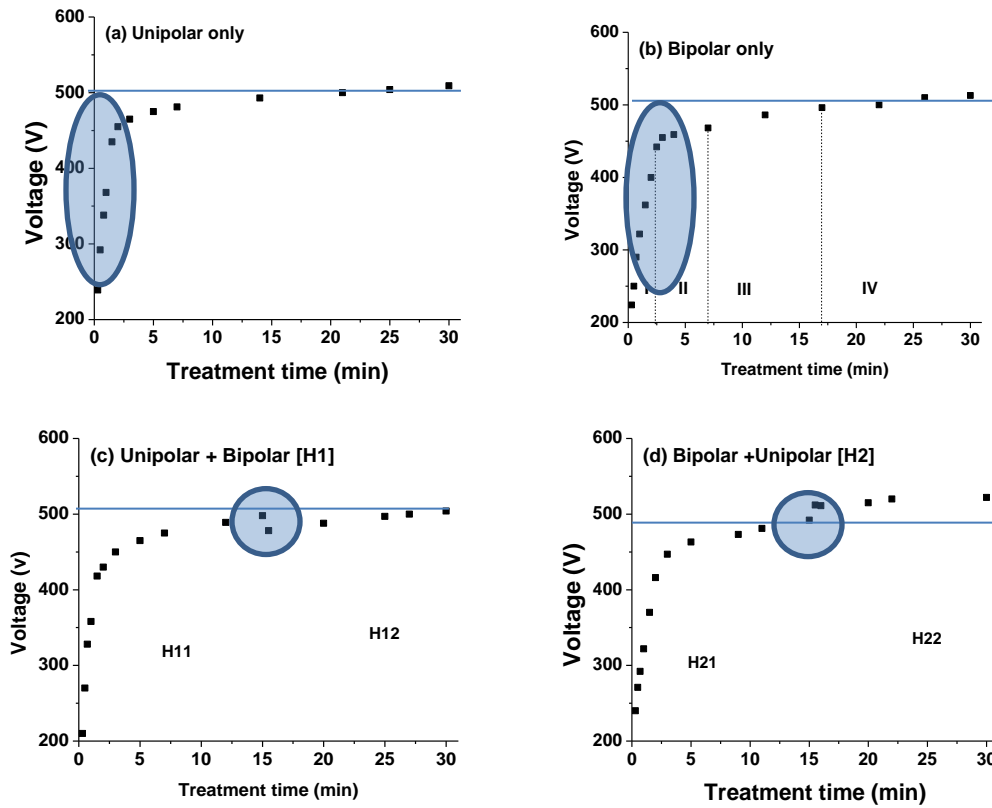


Figure 5.3. Plots of anodic voltage vs. treatment time during the PEO process using: (a) unipolar U, (b) bipolar B. (c) hybrid1 H1, and (d) hybrid2 H2 current modes.

Clear differences were seen between the curves for the four current modes. For the unipolar current mode, Figure 5.3a the anodic potential raises quicker than that for the bipolar current mode, Figure 5.3b. It then continues to rise gradually, reaching ~510 V

after 30 minutes. For H1 current mode when changing the mode from unipolar (H11) to bipolar (H12) current mode after 15 minutes, the voltage drops from 500 to 480 V then rise gradually to 504V, Fig 5.3c. However, for the H2 when the current mode changes from bipolar (H21) to unipolar (H22) after 15 minutes the voltage increased from 490 to 510 V and then further increased gradually to 520 V (Fig. 5.3d).

According to the evolution of voltage (for example Fig. 5.3b), the PEO process can be divided into four discharge stages, which have been described in detailed by Hussein et al [13]. In the early stage of the process, which mainly involves the rapid electrochemical formation of an initial insulating oxide film, a sharp increase in the voltage was seen where the breakdown voltage is not yet reached. Then the rate of voltage change starts to decreases. However, numerous sparks moving rapidly over the whole sample surface area start to appear, which indicates a start of the breakdown of the oxide layer. After that the rate of voltage increase becomes slower and concentrated discharges appear as relatively large and long lasting sparks. Finally, for the last stage, stage IV, the distribution of discharge is non-uniform and there are small variations in the voltage values. For hybrid1 (H1) current mode, the changing of current mode delays the transaction from stage III to stage IV (see Fig. 5.3c) however, for H2 mode the current mode change accelerates the transition from stage III to the stage IV, which is dominated by the relatively strong discharges.

### 5.4.2 Acquisition of the PEO Plasma Spectra

The plasma spectrum from 200 to 775 nm for PEO using a unipolar current mode is shown in Fig. 5.4. It is found that the plasma spectrum includes both continuous and line spectra. The continuous spectrum is generated by free-to-free transitions (Bremsstrahlung) of thermo electrons and recombination radiation of electrons and ions (free-to-bound transitions). The line spectrum consists of both atomic spectra and ionic spectra which may emitted from different plasma regions [16]. Fig. 5.4 shows typical emitted spectra in the NUV and visible regions of the plasma discharge, and show that the PEO plasma contains magnesium, aluminum and Mn (from substrate, but no spectral lines of other alloying elements, such as Zn, due to their low concentrations), silicon, oxygen, sodium, potassium, hydrogen α and β Balmer lines (from the electrolyte). The

phosphorus lines from the electrolyte were not seen, since P emission in the 270–775 nm range comes from energy levels that required 9.5 eV (110000 K) and therefore cannot be recorded at the relatively low PEO plasma temperature, ≈ 0.5 eV (5800 K).
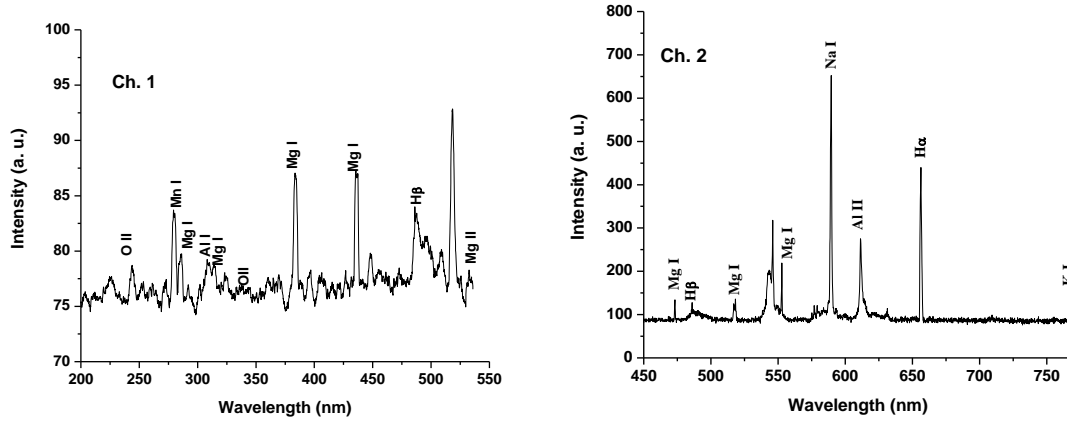


Figure 5.4.  Typical emission spectrum using two channels of the spectrometer.

### 5.4.3. Temporal Characterization of Line Spectrum

In order to study the influence of the current modes on the PEO plasma, it is necessary to investigate the changes in plasma spectrum with time. The acquisition frequency is about 3 Hz. The intensity of spectrum is corresponds to the cumulative result of all discharge events during the acquisition period. An OES spectrometer was used to record the key spectral lines at 383.8 nm (Mg I), 518.3 nm (Mg I), 470.3 nm (Mg I), 552.8 nm (Mg I), 486.1 nm (Hβ), 589.5 nm (Na I), and 656.2 (Hα) (see Table 5.2) [21], and their variation with time.

The spectra of the PEO plasma for different species of PEO coatings using H1 and H2 current modes are shown in Figs. 5.5 and 5.6 for a total coating process time of 30 min. The characteristic peaks that were observed are the result of excitation of these specific elements during the PEO process. Figs. 5.5 and 5.6 show that the discharges are from the components of the electrolyte (Na and Hβ) and the substrate (Mg) which are excited during the process. The emission line intensity results indicate that most of the species in the plasma exhibited similar trends over the treatment time. This confirms that during the discharges the local plasma temperature is high enough to excite all the species that exist in those locations at that particular time. The line intensities produced using unipolar

current mode, U, were higher than the intensities of the samples produced using a bipolar current mode, B. By using the bipolar current mode, there will be a balance of the discharge effects. The cathodic component of the bipolar current mode, as well as the longer $T_{off}$ duration, has a significant effect on the discharge behavior [18].
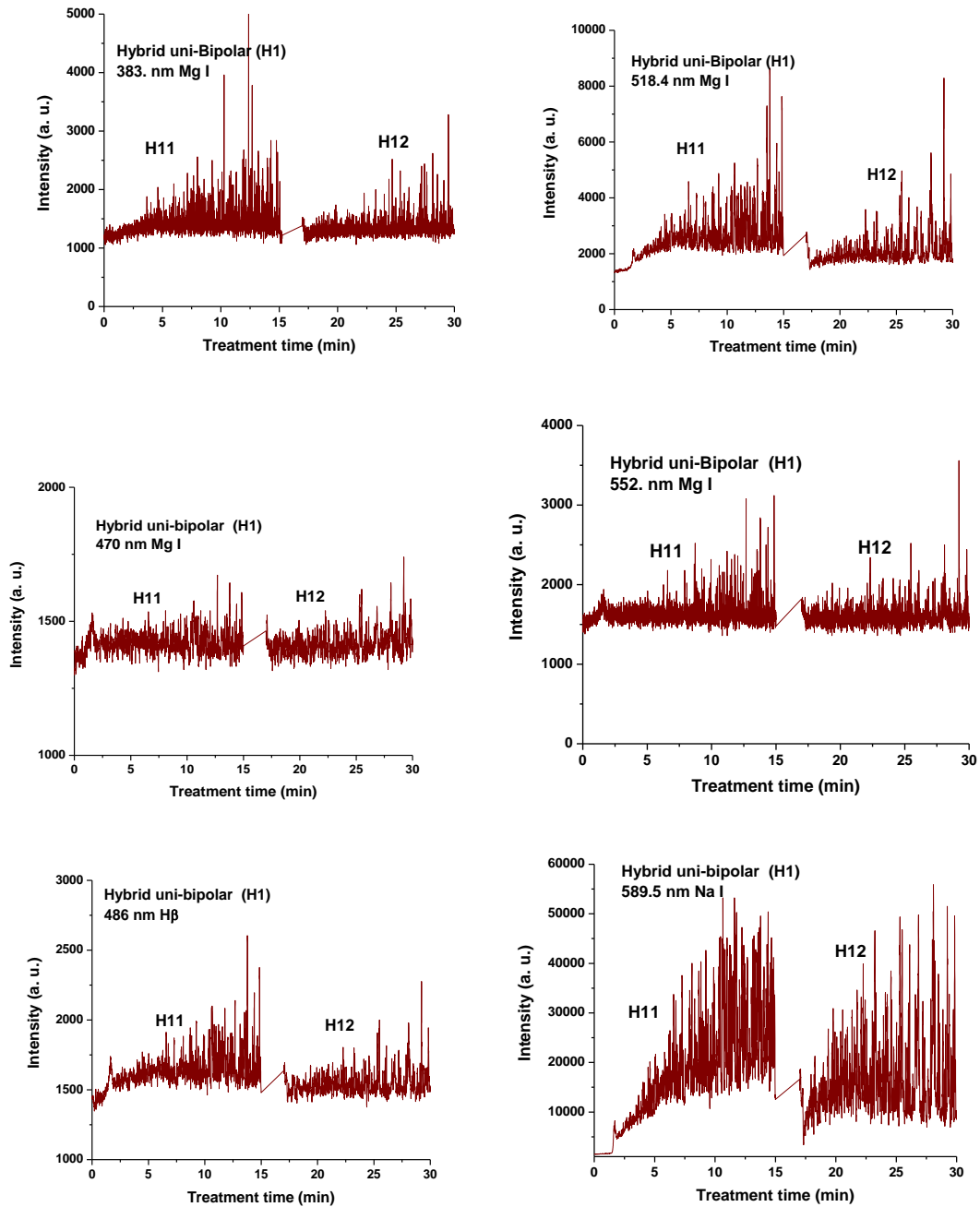


Figure 5.5. Typical time variation of the emission line intensity during the PEO process using hybrid current mode, unipolar followed by bipolar.

For the singlet spectral lines of Mg I 470.3 nm and 552.8 nm, the intensity does not increase as much as that of the triplet Mg I lines (518.3 nm and 383.8 nm), because these singlet lines require a higher excitation energy.
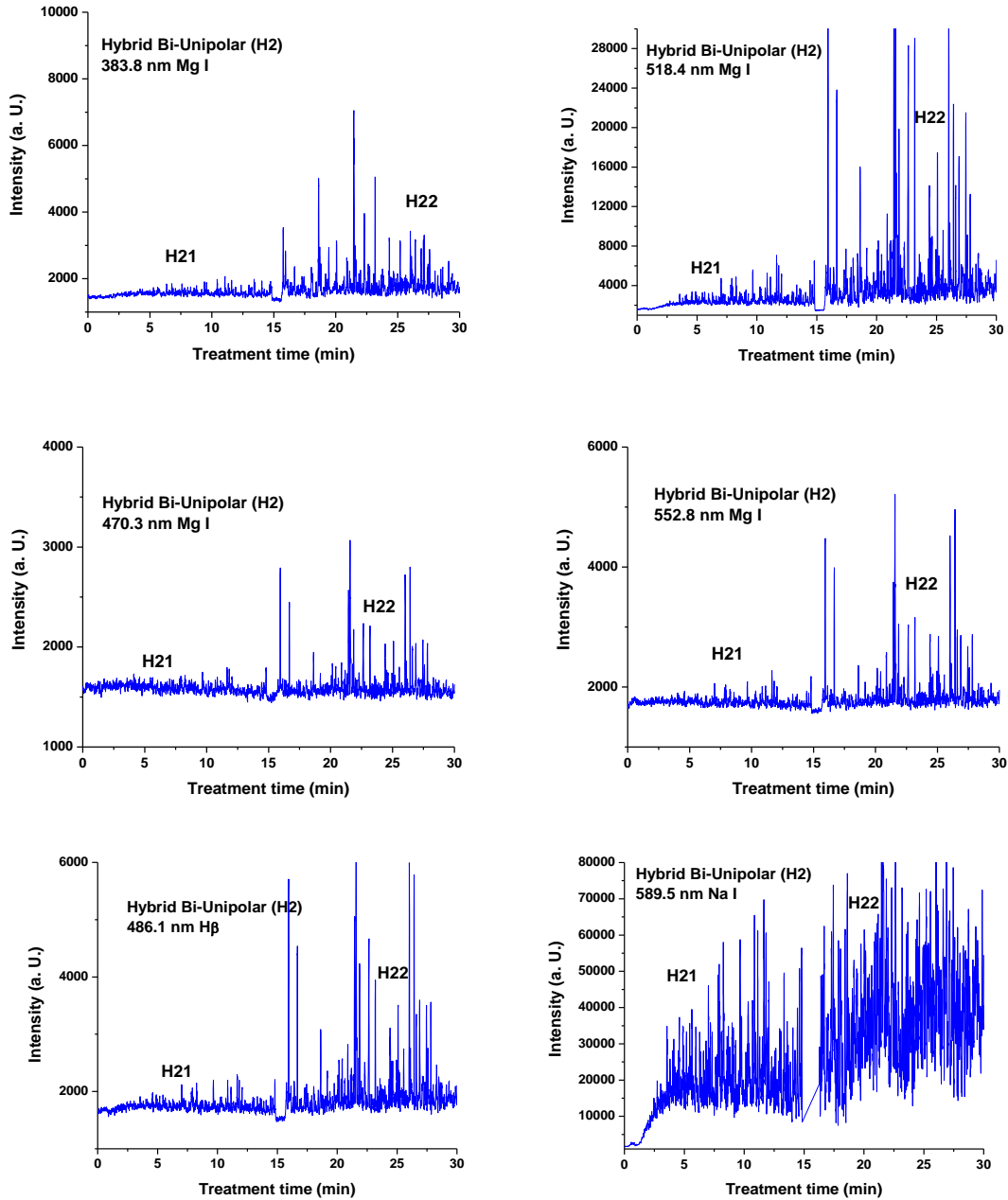


Figure 5.6. Typical time variation of the emission line intensity during the PEO process using hybrid current mode, bipolar followed by unipolar.

The observed strong excitation of sodium seems not contribute to the coating structure, since the EDX analysis of the coatings in a previous study [22] demonstrated that Na was not incorporated into the coating. This suggests that the PEO plasma discharges provide the required energy for the coating formation but all the elements excited by the plasma do not get incorporated into the coating.

Table 5.2 Spectral lines observed in this experiment with the wavelength ($\lambda$), transition, statistical weight of the upper and lower state $g_k$ and $g_i$ (respectively), photon energy ($\Delta E$) and the transition probabilities ($A_{ki}$) [21].

| Line | $\lambda$ nm | Transition | $g_k$ | $g_i$ | $\Delta E$ eV | $A_{ki}$ $\times 10^8$ S$^{-1}$ |
|---|---|---|---|---|---|---|
| Mg I | 383.8 | 3s3d $^3$D $\rightarrow$ 3s3p $^3$P | 7 | 5 | 3.22 | 1.68 |
| Mg I | 518.3 | 3s4s $^3$S $\rightarrow$ 3s3p $^3$P | 3 | 5 | 2.38 | 0.57 |
| Mg I | 470.3 | 3s5d $^1$D $\rightarrow$ 3p$^1P_1^0$ | 3 | 5 | 2.63 | 0.22 |
| Mg I | 552.8 | 3s4d $^1$D$\rightarrow$3p$^1P_1^0$ | 3 | 5 | 2.24 | 0.14 |
| H$_\beta$ | 486.1 | 4d $^2$D $\rightarrow$ 2p $^2$P | 4 | 2 | 2.55 | 0.172 |
| Na I | 589.5 | 3p $^2$P $\rightarrow$ 3s $^2$S | 3 | 3 | 1.36 | 0.614 |
| H$\alpha$ | 656.2 | 3d $^2$D $\rightarrow$ 2p $^2$P | 4 | 2 | 1.89 | 0.539 |

For the hybrid current mode starting with unipolar followed by bipolar (H1), Fig. 5.5, distinctive intensity spikes of Mg 518 nm can be seen in the period between 7 to 15 minutes from the start of the process. These spikes may be attributed to the strong discharges as well as to the particular discharge stages (I-IV) as described in [18]. On the other hand, the intensity of the same Mg I 518 nm line shows fewer spikes with lower intensities in the bipolar current mode period indicating weaker discharge events. Also the spikes only start to appear during the last six minutes of the processing time. For the hybrid current mode (H2), Fig. 5.6 shows that by starting with a bipolar current mode the Mg I 518.0 nm emission intensity signals are weak. When the current mode was switched

to the unipolar mode, the intensity of the spectral lines increase rapidly and, although the spark sizes were small, they later grow to a larger size.

### 5.4.4. LTE Analyses and Self-Absorption

The LTE model describes a state of plasma in which a population distribution is determined by the law of statistical equilibrium except that radiation processes are not in a detailed balance. The population distribution of LTE plasmas can be described by Boltzmann and Saha equations [19] and free electrons have a Maxwellian energy distribution [19]. The LTE state is often found in laboratory plasmas of relatively high density and relatively low temperature when collisional processes are far more important than radiative processes. Even in non-LTE plasmas, it is always possible to find levels for which collisional transitions are dominant compared with radiative transitions depending on plasma conditions. Those levels said to be in *partial* LTE. The Boltzmann and Saha equations can be conveniently applied for the relative population distributions among the levels in partial LTE. The partial LTE state occurs when the collisional de-excitation rate from the upper level to the lower level greatly exceeds the spontaneous decay rate. The assumption of LTE is fulfilled when the electron density is high enough so that:

$$N\text{e} \geq 1.6 \times 10^{18} Te^{1/2} (\Delta E)^3 \ (\text{m}^{-3}) \qquad \textbf{5.1}$$

where $\Delta E$ (in eV) is the largest energy gap in the atomic energy level system and $T$e (in K) is the electron temperature of plasma [19]. When the electron temperature is 6 000 K, the threshold value of electron density to fulfill the LTE assumption is about $5.4 \times 10^{22}$ m$^{-3}$. Plasma electron densities of the PEO plasmas from our previous measurements [13] are lower than the threshold value. Therefore partial LTE should be considered where the concentration yield is given by [23]:

$$N_e \geq 7.0 \times 10^{24} \frac{Z^7}{n^{17/2}} (\frac{kT}{Z^2 E_H})^{1/2} (m^{-3}) \qquad \textbf{5.2}$$

where $kT$ is the electron temperature in (eV), $E_H$ (eV) is the ionization potential for the corresponding element , $z$ is the ionization stage (z =1 for neutral atoms) and $n$ is the principle quantum number of the lowest quantum level included in the partial LTE (for the H, $z$ =1 and $n$=2). The plasma electron concentration obtained from our previous work [13], which is in good agreement with the results of [16], were $(0.7 - 1.2) \times 10^{22}$ m$^{-3}$

which is higher than the minimum plasma electron concentration for partial LTE, $N_e >$ $0.4 \times 10^{22}$ m$^{-3}$, and therefore partial LTE exists, and the electron temperature estimated by Boltzmann assumption and Stark broadening effect reflect the characteristics of the plasma correctly.

Dunleavy et al [20] has discussed the opacity problem in the PEO plasma. Following their discussion which is based on the results presented in ref. [24] on the effect of the absorption coefficient for water on the Balmer line intensity ratio, as a function of wavelength in the range of 580-790 nm, it can be estimated that the fraction of trapped photons in passage through up to about 10 cm of water would be less than 12% which is negligible for the present purposes. Consequently, the PEO plasma was assumed to be optically thin, i.e. none of the observed lines emitted from the plasma were affected by self-absorption.

### 5.4.5 Plasma electron temperature

The intensity ratio of the recorded 656.2 nm (H$_\alpha$) to 486.1 nm (H$_\beta$) spectra $I_{H\ (3d\ ^2D\ \rightarrow\ 2p\ ^2P)}$ / $I_{H\ (4d\ ^2D\ \rightarrow\ 2p\ ^2P)}$ (from the same ionization stage) (Te1) and the ratio of 552.8 nm (Mg I) to 470.3 nm (Mg I) $I_{Mg\ (3s4d\ 1D\rightarrow3p1}P_1^0)$ / $I_{Mg\ (3s5d\ 1D\ \rightarrow\ 3p1}P_1^0)$ (Te2) were used to determine plasma electron temperature ($T_e$). The Te results for experiments carried out using four different current modes are presented in Fig. 5.7. The average temperatures of each two curves are also shown in Fig. 5.7. It can be seen that the average measured temperature of the two ratios are in the range of 5800 - 6800 K for the unipolar case, 6100 - 6700 K for bipolar case, 6300 – 6600K for H1 case and in the range 5900 – 6700 K for H2 case. These results are in good agreement with the Te results for Mg AJ62 alloy [15].

Fig. 5.7a shows plasma temperature profile for the unipolar current mode (U). Te1 is initially around 7000 K which corresponds to the early stage discharges where the density of the discharges is very high. Te then drops to about 5000 K after about three minutes and then fluctuated around 5600 K for the reminder of the time. Electron temperatures measured using the second pair of lines Te2 (552.8 nm to 470.3 nm) are slightly higher than those obtained from the first pair of lines Te1 (656.2 nm to 486.1 nm) particularly after the first two min. The curve started to show a high number of closely-spaced temperature spikes some of them reaching up to 7000 K. These spikes corresponded to

relatively strong discharges initiated from the sample surface-coating interface, the so-called B-type discharge [13], whereas the base line average is at ~6000 K.
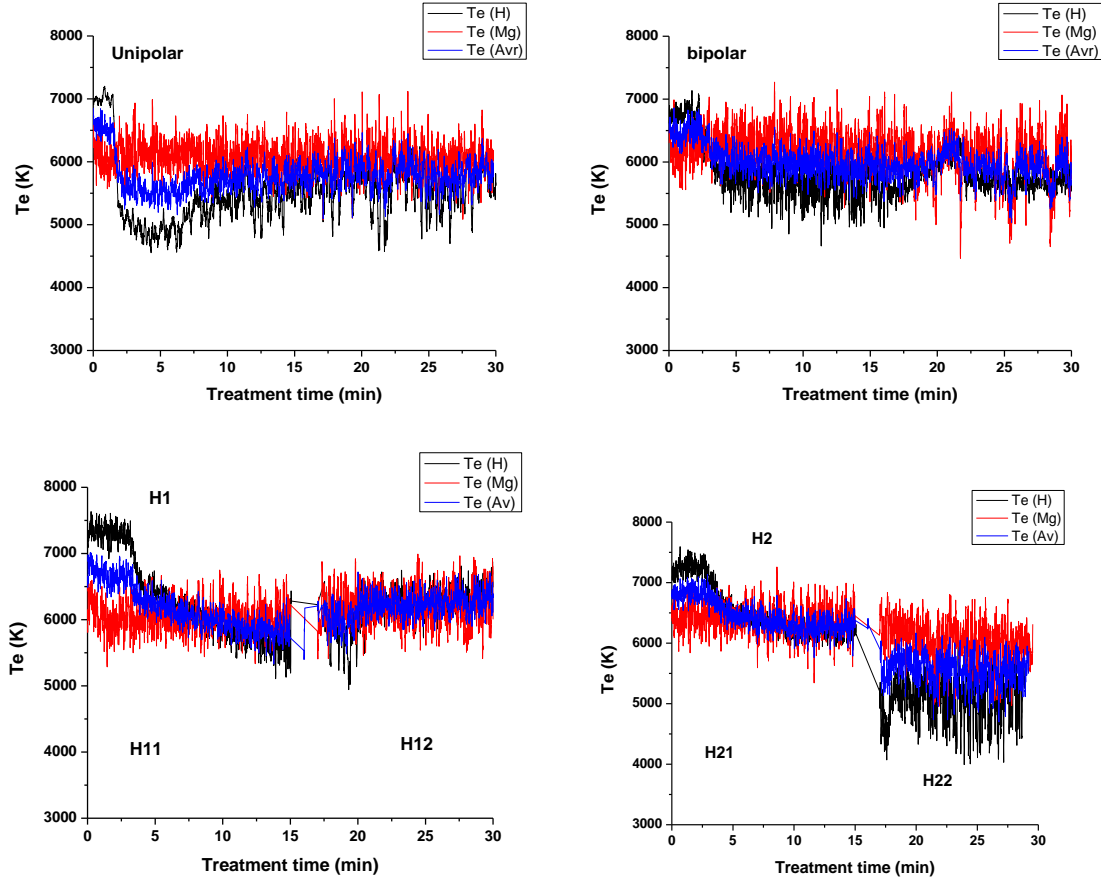


Figure 5.7. Plasma temperature as a function of treatment time (min) determined from the intensity ratio of (Te1) $I_{H\ (3d\ ^2D\ \rightarrow\ 2p\ ^2P)}$ / $I_{H\ (4d\ ^2D\ \rightarrow\ 2p\ ^2P)}$ (656.2 nm/486.1 nm) and (Te2) $I_{Mg\ (3s4d\ 1D\rightarrow3p1P_1^0)}$ / $I_{Mg\ (3s5d\ 1D\ \rightarrow\ 3p1P_1^0)}$ (552.8 nm/470.3 nm), for the samples U at unipolar, B at bipolar, H1 and H2 at Hybrid current mode.

For the bipolar case B, Fig. 5.7b shows that the base line average is ~5500 K for the first 20 min and then spike around 21 min to 6100 K and then fluctuates around 5900 K. Electron temperatures measured using the second pair of lines Te2 shows relatively higher temperature than those obtained from the first pair of lines Te1 during the entire treatment time after 4 min. Temperature spikes start to appear after 8 min. However, these spikes are less frequent and cooler than that for the unipolar samples.

Applying a hybrid current mode, sample H1, treated using a unipolar mode first followed by a bipolar mode, clearly shows the effect of current mode on the plasma temperature

76

where the average temperatures of the plasma during the bipolar mode were higher than those during the unipolar mode (Fig 5.7c). This is attributed to the fact that when suppressing the strong B-type discharges the number of other discharges, A-, C- and mild B- types, will increase which will then increase the base line temperature. Fig 5.7c also shows that the Te1 results are in very good agreement with the Te2 results for the bipolar treatment period. The use of a hybrid current mode, sample H2, where the sample was coated first using a bipolar current mode followed by the unipolar current mode, shows almost the same trends as for H1 samples, in terms of the bipolar period having higher average electron temperatures, and the good agreement between Te1 and Te2.

Table 5.3  Spike and average plasma electron temperatures for the four different current modes.

| Sample # | Plasma electron temperature: K |
|---|---|
| Unipolar (U) | 5000-7000 [5700] |
| Bipolar (B) | 5200-6600 [6100] |
| H1 (H11+H12)) | 5500-7500 [6000]/[6500] |
| H2 (H21+H22) | 4200-7500 [6500]/[5500] |

Table 5.3 summarizes the average background temperature and maximum spike temperatures for the four sets of samples. We therefore conclude that the $T_e$ – time profile depends strongly on the type of discharge and on the current mode, as a result of the competition between both the current phases (positive and negative) and the pulse timing. When using a bipolar current mode, the strong temperature spikes (due to B-type discharge) are suppressed, or only appear at later times, and since the total number of all types of discharge (A-, C- and mild B-type discharges) will be increased, it has the largest effect on the average (background) plasma temperature and hence on the coating microstructure and surface morphology.

## 5.5 Discharge behaviour and coating microstructure

The fluctuations in signal intensities and temperature during the coating process (i.e. weak and strong signals) reflect differences in location of both the discharge initiation,

77

and discharge type. Based on our discharge model described in detail in [13], the Mg emission intensity signals were due to three different types of discharge that are differentiated according to the origins of such signals. The B-type discharge is due to dielectric breakdown in a strong electric field occurring through the oxide layer. The A- and C- types of discharge are due to gas discharges occurring in micropores of the oxide film. Type A are from the surface pores, while the C- type are from discharges on relatively deep pores. While the high intensity spikes mainly correspond to the B-type discharge, the background intensity profile was related to the A-type and C-type discharges. The observed differences in the intensity: time trends between unipolar, bipolar, and the hybrid current modes suggest that the current mode plays a significant role in the coating process [11].

Fig. 5.8 (i) shows the SEM micrographs of the coating surfaces obtained using secondary electron mode (SE): H11 treated using unipolar current mode only for 15 minutes, H12 by completing the treatment of H11 using bipolar current mode for another 15 minutes; H21 treated firstly using bipolar current mode; H22 completed the treatment using unipolar mode for second 15 minutes. Fig. 5.8 (ii) which are SEM micrographs of the coating cross-sections also obtained using the secondary electron mode. As can be seen from Fig. 5.8 c and d for unipolar followed by bipolar compared with Fig. 5.8 a and b for unipolar only, the addition of a bipolar part improves the coating quality compared with the unipolar current mode, in terms of surface morphology where the porosity levels were reduced significantly and the cross-sectional microstructure for the H12 shows a coating with fewer-defects that is more adherent to the substrate compared to the H11 sample, which was treated using a unipolar mode only. Therefore, the bipolar part seems to act as a repair mode for the coatings.

The coating surface morphology and cross-sectional microstructure that are obtained can be linked to the plasma discharge behavior. Fig. 5.9 a is a schematic diagram of the discharge process for a Mg-alloy sample, and shows the influence of the discharges on the intensity profile, Fig. 5.9 c, as well as on the coating microstructure (Fig. 5.9b and d). The high intensity spikes correspond to the strongest discharges (B-type discharge) which significantly affect the microstructure and morphology of the coating [25]. These strong discharges produce a more porous coating. Strong discharges can be reduced, or

eliminated, by appropriately adjusting the bipolar current and the on and off time interval of the pulses as can be seen in Figs. 5.5 and 5.6. Elimination of the B-type discharges leads to denser microstructures with less porosity.

A modified growth model that not only includes Type A, B and C discharges but also discharges that occur in large pores near the interface between the inner and outer layers (type D) and those which may form the pancake-structures that occur mainly within the outer coating layer (type E) has been proposed by Cheng et al [26]. However, according to our discharge model [13], the pancake-structures are due to strong Type B discharges initiated close to the substrate surface. Fig. 5.9b is a SEM micrograph of a coating prepared using a unipolar current mode and shows a large number of 'pancake'-like features and discharge pores which irregularly arranged on the coating surface: This is a common characteristic of PEO coatings.  Fig. 5.9b, shows that some of the regions on the coating surface were covered with freshly solidified magnesium oxide, leaving the adjacent regions uncovered.

The relatively large holes in the center of the pancake suggest that they were produced by strong discharges and such holes might penetrate deep in to the coating. Some micro-cracks were present on the coating surface, which could have resulted from thermal stresses generated during the rapid solidification of the molten oxide product in the strong discharge channel [27]. The stronger the discharge, the larger is the molten mass produced by a single discharge. When this molten mass erupts from the discharge channel, it rapidly solidifies around the discharge channels, thus, giving rise to the 'pancake-like' features and randomly distributed discharge pores on the coating surface. Both of these features cause an increase in the surface roughness. The micro-pores are due to gas bubbles ejected from surface discharges and are referred to as A- and C- type discharges.
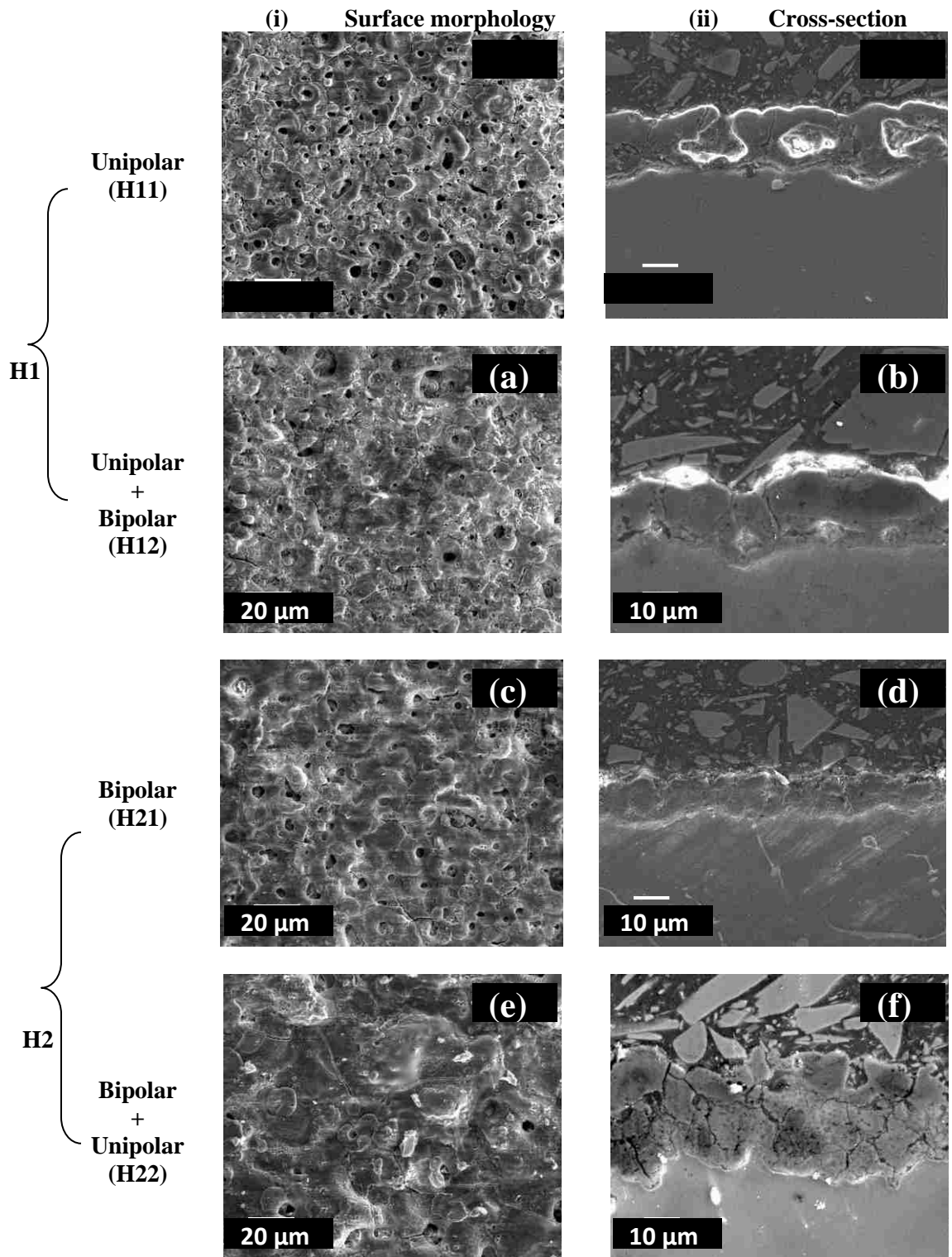
Figure 5.8. (i) morphology of oxide coatings on an Mg AM60B alloy using secondary electron mode (SE) (ii) SEM micrographs of polished sections of coatings using secondary electron mode (SE) and for: (a, b) unipolar H11, (c, d) hybrid1 (uni + bipolar), (e,f) bipolar H21 and (g , h) hybrid2 (bi + unipolar) current modes.

Fig. 5.9d is a SEM micrograph of the cross-section of a sample produced using the unipolar current mode (U). The coating has a significant amount of connected porosity, holes and other structural defects both within the coating and near the coating/substrate interface. Such defects and porosity were likely caused by the strong B- type discharges and gas trapping in the vicinity of electrical discharges at such an area due to a fast solidification process. The average coating thickness after the 30 min treatment time for H1 was about 25-30 μm and 33-40 μm for H2. The coating-substrate interfaces had a wavy-jagged appearance, which may be the result of dissolution of the substrate during the treatment time and/or the presence of intermetallics at the grain boundaries. Also, there is evidence of a network of through-coating defects (microcracks). One of major concerns is the substrate/coating interface, where the very strong B-type discharge is initiated.

The main effect of the bipolar current mode is a discharge disturbance, which prevents the development of long lived, very large microdischarges. By using the bipolar current mode there will be a balance of the discharge effects [15]. A unipolar current mode produces a thicker coating than the bipolar: see Fig. 5.8 b compared with Fig. 5.8 f. Coatings prepared using a combination of unipolar followed by bipolar modes (H1) had a dense inner layer with fewer defects with lower growth rate compared with coatings prepared using reverse order i.e. bipolar followed by unipolar (H2) as can be seen from comparing Figs. 5.8 d and h.

X-ray diffraction (XRD) analysis was used to further investigate the changes in composition of PEO coatings due to the changes of the current mode. XRD analysis results of the substrate Mg alloy (uncoated) and the PEO-coated samples are shown in Fig. 5.10. The PEO coatings formed on AM60B in a mixed phosphate-silicate electrolyte consist mainly of MgO together with smaller amounts of $Mg_2SiO_4$, $MgAlPO_5$ and $MgAl_2O_4$. However, there are some differences in phase contents. The bipolar mode seems to promote the formation of MgO phase. A unipolar mode is more likely to promote the formation of the $Mg_2SiO_4$ and $MgAl_2O_4$ phases. Higher intensity MgO peaks are seen in samples prepared using bipolar and hybrid current modes compared to ones prepared using the unipolar mode, while the intensities of the $Mg_2SiO_4$ and $MgAl_2O_4$ peaks were higher when the unipolar and hybrid current modes were used.  MgO is

formed via substrate metal oxidation during PEO treatment, while the $Mg_2SiO_4$ and $MgAlPO_5$ phases are derived from the co-deposition of the alkaline electrolyte components into the coating structure.
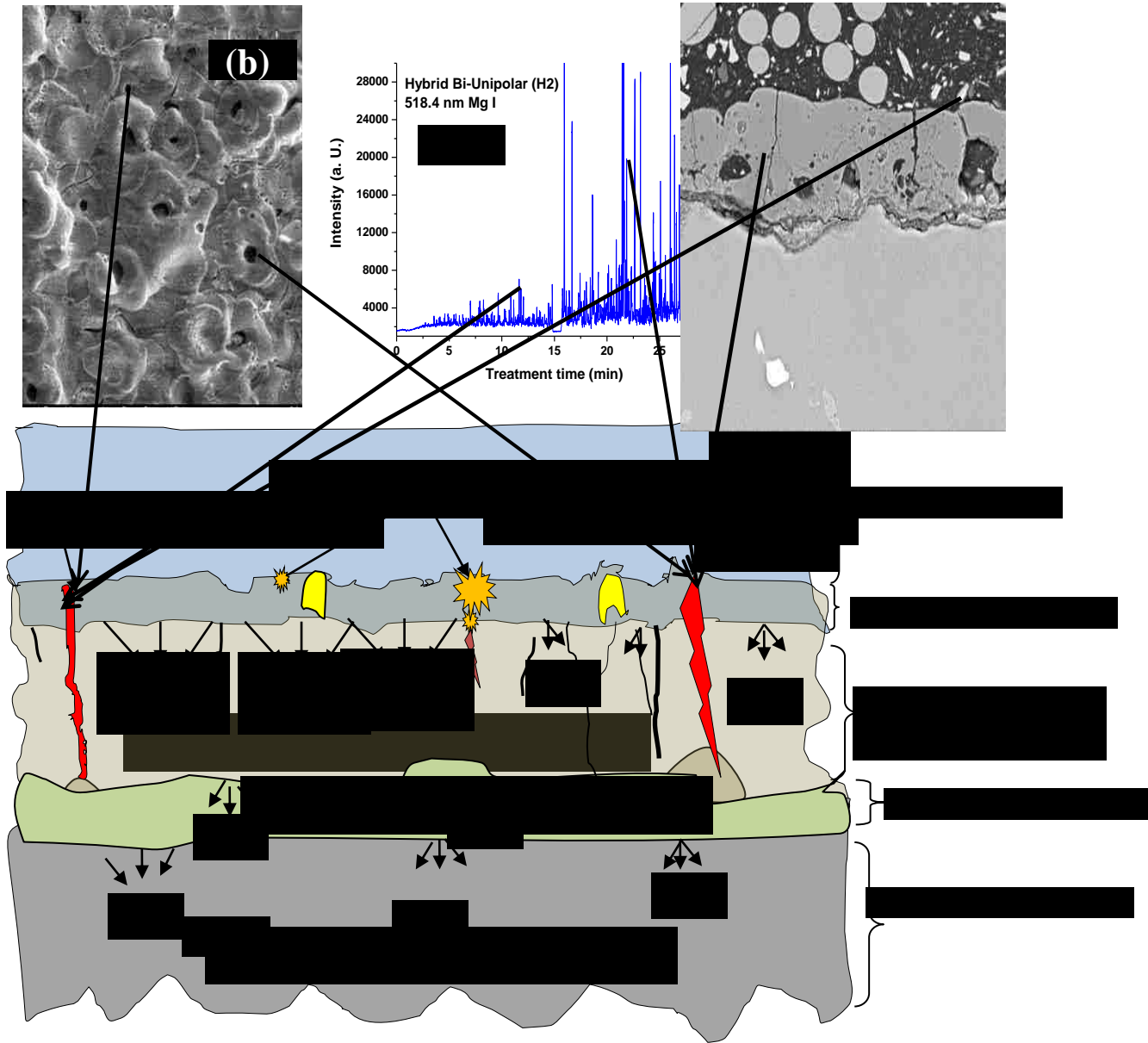


Figure 5.9. Schematic diagram of the discharge model showing the influence of B-type discharges on plasma temperature profile, surface morphology and on the cross section of the oxide coating.
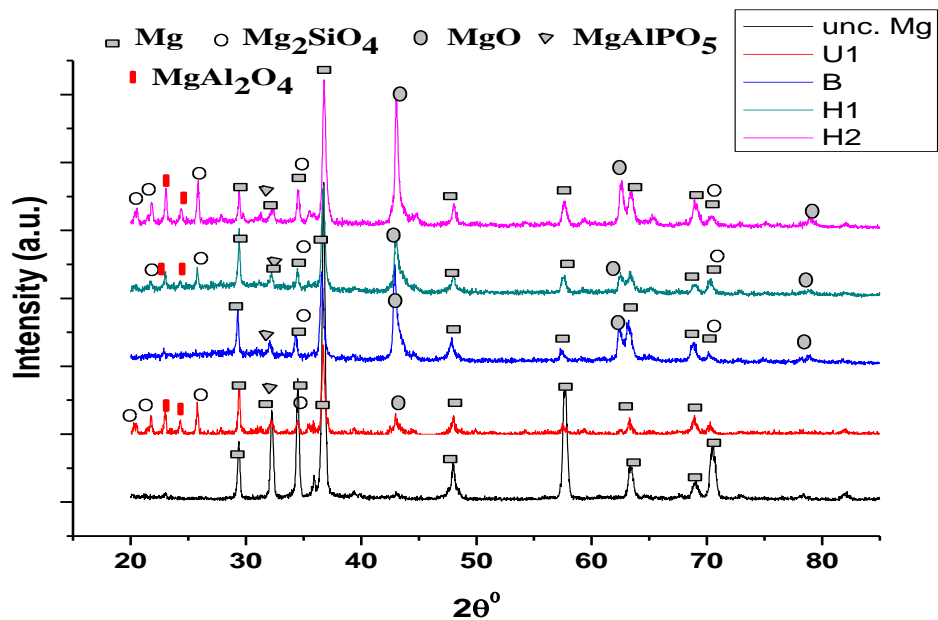
Fig. 5.10. XRD patterns of (unc. Mg) uncoated and coated samples using (U) unipolar, (B) bipolar and (H1 and H2) hybrid current modes.

## 5.6 Porosity and pore size analysis

Fig. 5.11a shows relatively low magnification SEM images which were image-processed for porosity analysis. The surfaces of the coatings were dominated by many randomly arranged donut-shaped projections with open or sealed microporosities in the center. The large microporosities are considered as footprints of the plasma discharge channels, through which the Mg and $Mg^{2+}$ from the substrate were likely ejected and reached the coating/electrolyte interface during the plasma-induced melting, then combined with the electrolyte anion including $Al_2O_4^{2-}$ or $OH^-$ and reacted with $O_2$ generated due to electrolysis, and finally sintered and deposited on the coating surface, contributing to the coating growth. Fig. 5.11 gives the average porosities (which represent the percentage of the surface areas of black spots relative to the total image area) for each of the four cases. The averaged porosities of each sample, was determined from SEM images for a typical surface area of 620 by 675 μm. The pores varied in size from very small diameters (<1

µm) through medium size (few µm) to large pores (>10 µm). Pore sizes can be linked with the discharge type described in detail by Hussein et al [13].
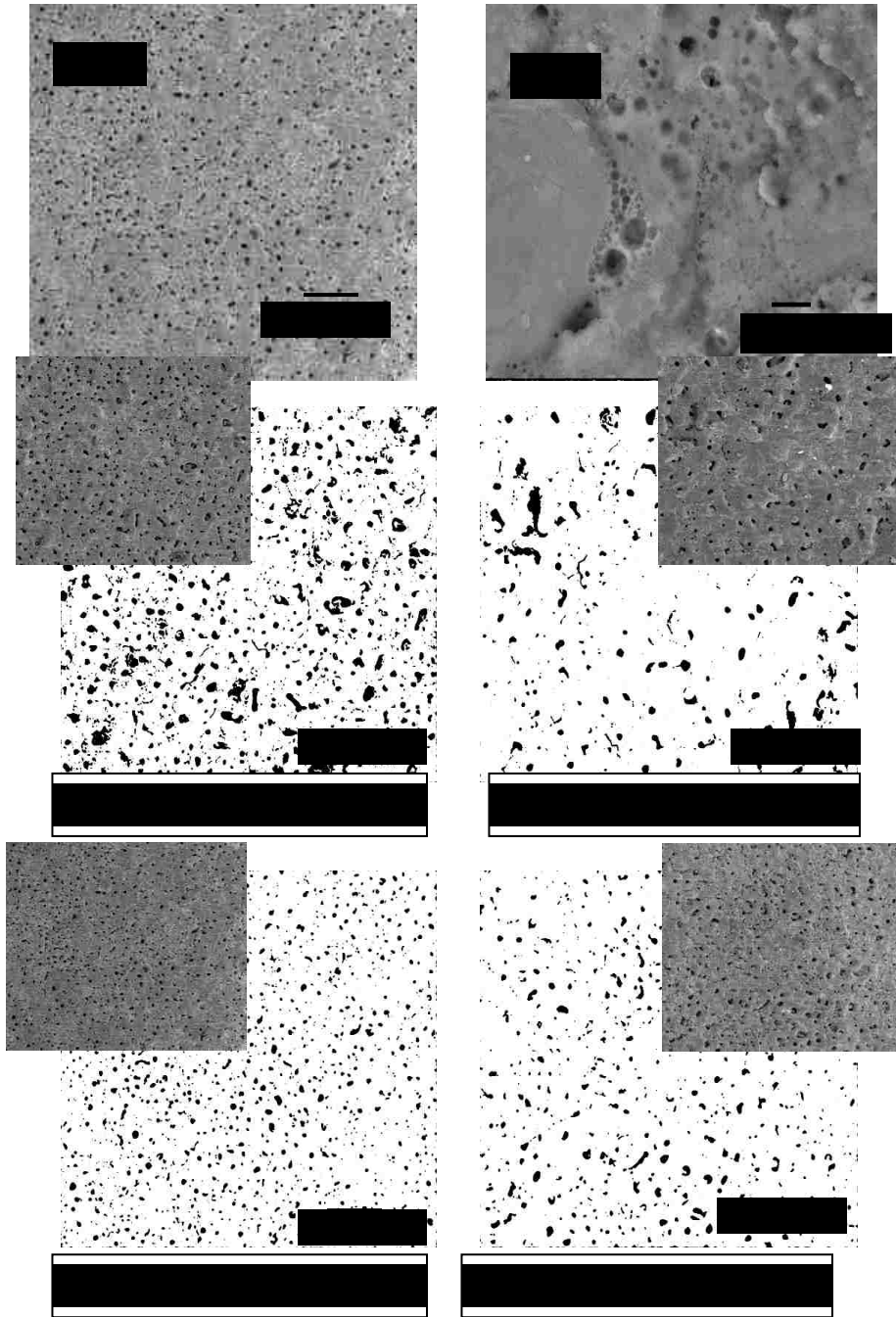


Figure 5.11. (a) Low and (b) high magnification SEM images and the processed images with corresponding porosities distribution chart for (c) H11, (d) H12, (e) H21 and (f) H22.

Sample H11 (unipolar for 15 minutes only) with an average porosity of 14.4% exhibited a large number of pores with diameter <10 µm. H12 (unipolar followed by bipolar)

showed a lower porosity (4.3 %) than H11 but, some large pores were also present on the surface. The porosity of H21 and H22 are 8.4% and 7.2% respectively, with medium pore sizes. H11 (only unipolar) showed the highest level of porosity which may be attributed to the large number of the strong and irregularly distributed B-type discharges which are generally associated with the unipolar current mode [10,14]. However after applying a bipolar current mode for the second 15 minutes, H12, the porosity was reduced to the lowest value of all four modes. Such morphology was expected since both the number and intensity of the strong B-type discharges [15] are reduced by using a bipolar current mode. Porosity has a significant effect on the mechanical properties of ceramic coatings, mainly hardness and stiffness: 20% of porosity can reduce the hardness by 60-70% from the fully dense value [29], and may also reduce the stiffness by 30% [30].

According to Curran and Clyne [26], the porosity of the PEO coatings should be higher than the measured values for H11, H12, H21 and H22 due to the existence of very fine scale porosity (< 100 nm). Such fine scale porosity although detectable using techniques such as mercury porosimetry, densitometry and BET adsorption measurements as used by Curran and Clyne [31], cannot be seen on the low magnification SEM micrograph. However, examination of the coating surface at a higher magnification, Fig. 5.11b, reveals the presence of such fine scale, interconnected porosity. In addition of the very fine scale porosity, Fig 5.11b also shows different sizes of pores, tiny and very small sizes which are related to the discharge behaviors, A-, and C- type discharges however the medium and large pore sizes are related to the mild and strong B- type discharges, shown in Fig 5.9.

## 5.7 Corrosion resistance of the coatings

Fig. 5.12 shows the potentiodynamic polarization curves of the uncoated AM60B Mg alloy (unc. Mg) and the PEO coated specimens using either unipolar, bipolar or hybrid current modes (curves U, B and H1-H2 respectively). A summary of the results of the potentiodynamic corrosion test in a 3.5% NaCl solution is given in Table 5.4. Compared to the uncoated AM60B, all PEO-coated samples exhibited a higher polarization resistance, a lower corrosion current density and a higher (more noble) corrosion potential. The more porous coating on samples U leads to the poorer corrosion

resistance. Comparatively, coating H1 (U+B), having thick and relatively dense oxide layers, has a higher polarization resistance and lower corrosion current densities than the other PEO coatings.

Table 5.4  Potentiodynamic polarization corrosion test results in a 3.5%wt NaCl solution

| | Uncoated AM60B (S0) | U | B | H1 | H2 |
|---|---|---|---|---|---|
| $E_{corr}$ (V) | -1.51 | -1.46 | -1.43 | -1.48 | -1.421 |
| $I_{corr}$ ($\mu A/cm^2$) | 100 | 0.316 | 0.072 | 0.0071 | 0.100 |
| $\beta_a$ (mV) | 26.7 | 59.4 | 398.6 | 114.6 | 55.1 |
| $\beta_c$ (mV) | 139.5 | 149.0 | 211.8 | 210.0 | 191.3 |
| $R_p$ ($\Omega \cdot cm^2$) | 97.4E+02 | 5.84E+04 | 8.35E+05 | 4.54E+06 | 1.86E+05 |
| Pi ($\mu m/year$) | 2285 | 7.2 | 1.6 | 0.16 | 2.3 |
| PEF % | N/A | 209 | 3015 | 16,450 | 673 |

The use of a hybrid current mode, sample H2, where the samples were coated using a bipolar current mode first, followed by a unipolar current mode, the corrosion current density was  $1.00\times10^{-7}$ A/cm$^2$ while the corrosion potential increased to (-1.42 V) with polarization resistance of $1.86\times10^{+8}$  $\Omega$ cm$^2$. Applying a hybrid current mode, sample H1, treated using unipolar mode first followed by a bipolar mode, gives the highest polarization resistance compared with other samples with a value  of $4.54\times10^{+9}$  $\Omega$ cm$^2$ and the lowest corrosion current density of $7.10\times10^{-9}$ A/cm$^2$, but the corrosion potential decreased to (-1.48 V). Use of an unipolar current mode sample U, gives the lowest polarization resistance compared with other samples with a value  of $5.11\times10^{+7}$  $\Omega$ cm$^2$ and corrosion current density of $5.65\times10^{-7}$ A/cm$^2$ and the corrosion potential of (-1.44 V). Sample H1 with a coating thickness of 24 to 36μm appeared to have the best corrosion resistance of the coated AM60B coupons. Potentiodynamic polarization corrosion test results showed that these PEO coatings significantly increased the corrosion resistance of AM60B alloy. The ranking for corrosion resistance in 3.5% NaCl medium was Mg uncoated < sample U < sample H2 < sample B < sample H1.
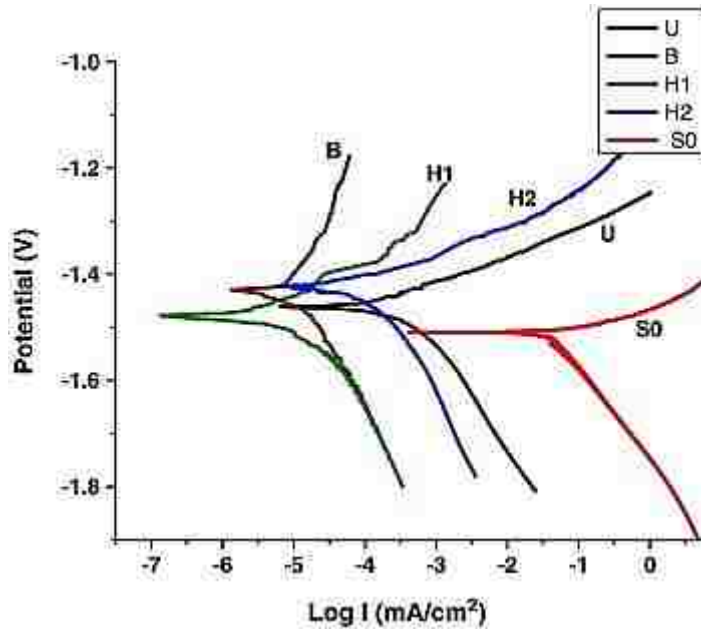
Fig. 5.12. Potentiodynamic polarization curves of the uncoated (S0) and coated samples using unipolar (U), bipolar (B) and Hybrid (H1 and H2) current modes.

There are three main parameters that can have a significant effect on the corrosion properties of the PEO coatings. These parameters are: coating phase composition; porosity level and other coating defects; and, to some extent, the coating thickness. Since the bipolar current mode produces a dense coating with minimum defects, while the unipolar mode gives the more chemically stable $Mg_2SiO_4$ spinel phase, a combination of the two modes has improved the coating properties in terms of both microstructure and corrosion resistance, as is shown for sample H1. The order of the applied current modes (unipolar and bipolar modes) has a significant effect on the coating characteristics as can be seen from a comparison of the morphology, phase structure, cross section and corrosion resistance of samples H1 and H2. For sample H1, which was unipolar followed by bipolar, the unipolar mode produced an inner layer containing the more corrosion resistant spinel phase plus a top layer that was dense and corrosion resistant.

It is generally expected that a thicker coating gives rise to better corrosion resistance. However, as the microcrack, defect and porosity levels in the unipolar sample coating U was quite high, it exhibited a lower corrosion resistance compared to other samples even though it was thicker. Therefore, for better localized corrosion resistance the coating needs to be not only thicker, but also should be free from defects such as porosity. The

87

substrate-coating interface layer seems to have an important effect on the corrosion resistance; it acts as a barrier layer from the corrosion medium. The significant amount of connected porosity, holes and other structural defects both within the coating, and near the coating/substrate interface, for sample U2, treated using a longer off-time unipolar mode, causes the corrosion resistance to be the lowest of the coated samples.

It is illustrative to compare the corrosion protection properties afforded by the PEO-coatings for different Mg-alloys. In the potentiodynamic polarization method for measuring the corrosion rate of Mg alloys, the corrosion current density, $i_{corr}$ ($\mu A/cm^2$) can be related to the average corrosion rate, $P_i$ (mm/year) by the Stern–Geary equation [32] (chapter 4, equation 4.4). The calculated values for $P_i$ and the protection efficiency ($P_{EF}$ %) afforded by the coating are also given in Table 5.4. It should be stressed that these values of $P_i$ are for specimens that were not subjected to impact–sliding. Generation of craters and cracks during impact–sliding wear would degrade the corrosion resistance [33].

## 5.8 Conclusions

Four different current modes (unipolar, bipolar and hybrid (unipolar-bipolar and bipolar-unipolar)) were used in the PEO processing of Mg-alloy AM60B in a mixed aluminate and phosphate electrolyte. The effects of current mode on the plasma parameters were investigated and the following conclusions are made:

-Plasma electron temperatures (Te) were determined by the line intensity ratios of two pairs of H and Mg lines, the 656.2 nm to 486.1 nm (Te1) and the 552.8 nm and 470.3 nm (Te2) lines respectively. Plasma electron temperatures were found to in the range of 5000 - 7000 K for the unipolar case, 5200 - 6600 K for the bipolar case, 5500 – 7500K for the unipolar + bipolar case and 4200 – 7500 K for bipolar + unipolar case.

- Controlling or reducing the strong discharges had a significant positive effect on the plasma temperature profiles and leads to denser inner layer microstructures with less porosity.

- A careful examination of the plasma characterization results obtained by OES analysis and the SEM results of the coating morphology and microstructure, highlights clear differences between samples coated using unipolar, bipolar or hybrid current modes. A

hybrid (H12) current mode improves the coating quality compared to the unipolar mode (H11) in terms of having a dense inner layer with fewer defects due to the combination effects of the two current modes. The fluctuations in the measured line intensities (different spike) support the discharge model and the resulting coating microstructures.

- Where the bipolar current mode produces a dense coating with minimum defects, while the unipolar mode gives more chemically stable Mg2SiO4 spinel phase, a combination of the two modes has improved the coating properties in terms of microstructures and corrosion resistance.

- The corrosion performance is more closely related to the protective nature of the dense oxide layer at the coating–substrate interface. In this regard, the most protective oxide is formed by using the H1 current mode [unipolar + bipolar]. The protection efficiency of the H1 coating is approximately 25 times more than for the H2 [bipolar + unipolar] coating. In the H1 case, the bipolar mode appears to repair the damage produced during the unipolar cycle.

**References**

[1]     Yerokhin AL, Nie X, Leyland A,  Matthews A, Dowey J, Plasma electrolysis for surface engineering. Surface & Coatings Technology, 122 (1999) 73-93.
[2]     Walsh FC, Low CTJ, Wood RJK, Stevens KT, Archer J, Poeton AR, Ryder A, Review. Plasma electrolytic oxidation (PEO) for production of anodised coatings on lightweight metal (Al, Mg, Ti) alloys. Transactions of the Institute of Metal Finishing, 87 (2009) 122-135.
[3]     Hussein RO, Nie X, Northwood DO, The Application of Plasma Electrolytic Oxidation (PEO) to the Production of Corrosion Resistant Coatings on Magnesium Alloys: A Review. Corrosion and Materials, 38(1) (2013) 55-65.
[4]     Liang J, Bala Srinivasan J P, Blawert C, Störmer M, Dietzel W, Electrochemical corrosion behaviour of plasma electrolytic oxidation coatings on AM50 magnesium alloy formed in silicate and phosphate based electrolytes. Electrochimica Acta 54 (2009) 3842–3850.
[5]     Cakmat E, Tekin KC, Malsyooglu U and Shrestha S, The effect of substrate composition on the electrochemical and mechanical properties of PEO coatings on Mg alloys.  Surface & Coatings Technology,` 204 (2010) 1305-1313.
[6]     Wei CB, Tian XB, Yang SQ, Wang XB, Fu RKY, Chu PK, Anode current effects in plasma electrolytic oxidation. Surface & Coatings Technology, 201 (2007) 5021-5024.

[7] Curran, JA, Clyne TW, Thermo-physical properties of plasma electrolytic oxide coatings on aluminium. Surface & Coatings Technology, 199(2-3) (2005) 168-176.

[8] Arrabal R, Matykina E, Hashimoto T, Skeldon P, Thompson GE, Characterization of AC PEO coatings on magnesium alloys. Surface & Coatings Technology, 203 (2009) 2207-2220.

[9] Gnedenkov SV, Khrisanfova OA, Zavidnaya AG, Sinebryukhov SL, Egorkin VS, Nistratova MV, Yerokhin A, Matthews A, PEO coatings obtained on an Mg–Mn type alloy under unipolar and bipolar modes in silicate-containing electrolytes. Surface & Coatings Technology, 204 (2010) 2316-2322.

[10] Hussein RO, Northwood DO, Su JF, Nie X, A study of the interactive effects of hybrid current modes on the tribological properties of a PEO (plasma electrolytic oxidation) coated AM60B Mg-alloy. Surface & Coatings Technology, 215 (2013) 421-430.

[11] Hussein RO, Northwood DO and Nie X, The influence of pulse timing and current mode on the microstructure and corrosion behaviour of a plasma electrolytic oxidation (PEO) coated AM60B magnesium alloy. J. of Alloys and Compounds, 541 (2012) 41-48.

[12] Dunleavy CS, Curran JA, Clyne TW, Self-similar scaling of discharge events through PEO coatings on aluminium. Surface & Coatings Technology, 206 (2011) 1051-1061.

[13] Hussein RO, Nie X, Northwood DO, Yerokhin A, Matthews A (2010), Spectroscopic study of electrolytic plasma and discharging behaviour during the plasma electrolytic oxidation (PEO) process. Journal of Physics D: Applied Physics, 43, 105203.

[14] Klapkiv MD, Nykyforchyn HM, Posuvailo VM, Spectral analysis of an electrolytic plasma in the process of synthesis of aluminium oxide. Materials Science, 30 (1994) 333-343.

[15] Hussein R.O., Zhang P., Northwood D.O. and Nie X. Improving the corrosion resistance of magnesium alloy AJ62 by a plasma electrolytic oxidation (PEO) coating process Corrosion and Materials 36 (3) (2011) 38-49.

[16] Dunleavy CS, Golosnoy I O, Curran J A and Clyne T W, (2009) Characterisation of discharge events during plasma electrolytic oxidation. Surface & Coatings Technology, 203(22), 3410-3419.

[17] Hussein R., Nie X, Northwood DO, A spectroscopic and microstructural study of oxide coatings produced on a Ti–6Al–4V alloy by plasma electrolytic oxidation. Materials Chemistry and Physics., 134 (2012) 484-492.

[18] Hussein RO, Nie X, Northwood DO, An investigation of ceramic coating growth mechanisms plasma electrolytic oxidation (PEO) processing. Electrochimica Acta 112 (2013) 111– 119

[19] H.R. Griem: Principles of Plasma Spectroscopy. Cambridge, Cambridge University Press; 1997.

[20] Dunleavy CS, Curran JA, Clyne TW, Time dependent statistics of plasma discharge parameters during bulk AC plasma electrolytic oxidation of aluminum. Applied Surface Science, 268 (2013) 397-409.

[21]     Sansonetti JE and Martin WC, Handbook of Basic Atomic Spectroscopic Data. Journal of Physical and Chemical Reference Data, 34 [4] (2005) 1559-2260.

[22]     Lianga J, Guoa B, Tiana J, Liua H, Zhoua J, Liua W, Xu T, Effects of NaAlO2 on structure and corrosion resistance of microarc oxidation coatings formed on AM60B magnesium alloy in phosphate–KOH electrolyte. Surface & Coatings Technology, 199 (2005) 121-126.

[23]     Griem HR, Plasma Spectroscopy. Cambridge, McGraw-Hill; 1964.

[24]     Sullivan SA, 'Experimental Study of the Absorption in Distilled Water, Artificial Sea Water, and Heavy Water in the Visible Region of the Spectrum. Journal of the Optical Society of America, 53 (1963) 962-968.

[25]      Cheng Y, Wu F, Matykina E, Skeldon P, Thompson GE, The influences of microdischarge types and silicate on the morphologies and phase compositions of plasma electrolytic oxidation coatings on Zircaloy-2. Corrosion Science 59 (2012) 307-315

[26] Cheng Y, Xue Z, Wang Q, Wu X, Matykin E, Skeldon P, Thompson GE, 'New findings on properties of plasma electrolytic oxidation coatings from study of an Al–Cu–Li alloy.  Electrochimica Acta, 107 (2013) 358– 378.

[27]     Curran J A, Clyne T W, Porosity in plasma electrolytic oxide coatings. Acta Materialia, 54 (2006) 1985–1993.

[28]     Zhang P, Nie X and Northwood DO, Influence of coating thickness on the galvanic corrosion properties of Mg oxide in an engine coolant. Surface & Coatings Technology, 203 (2009) 3271-3277.

[29]     MacKenzie JK, 'The Elastic Constants of a Solids Containing Spherical Holes, Proceedings of the Physical Society, B63 (1950) 2-11.

[30]     McColm IJ,  Ceramic hardness. New York, NY: Plenum Press; 1990.

[31]     Bockris J, Reddy K N, Modern Electrochemistry. New York: Plenum; 1973. p. 622.

[32]     Stem N., Geary A, Electrochemical polarization. Journal of The Electrochemical Society, 104 (1957) 56-63.

[33]     Berg G, Friedrich C, Broszeit E, Berger C, Fresenius, scratch test measurement of tribolojical hard coating in practice. Journal of Analytical Chemistry, 358 (1997) 281-285.

# CHAPTER 6

# A STUDY OF THE INTERACTIVE EFFECTS OF HYBRID CURRENT MODES ON THE TRIBOLOGICAL PROPERTIES OF A PEO (PLASMA ELECTROLYTIC OXIDATION) COATED AM60B MG-ALLOY

**Published in:**

## 6.1 Introduction

Recent developments in the plasma electrolytic oxidation (PEO) process allow the production of oxide layers on magnesium alloys with excellent tribological properties, and the potential to be used in many applications [1]. While the tribological properties of these coatings have been extensively studied, there is little information available on coating failure mechanisms. The tribological properties of PEO-coated Mg alloys have been evaluated by a number of research groups under dry sliding conditions [2-5]. The PEO-coated materials show a higher coefficient of friction (COF) but a lower wear rate than the uncoated alloy. It has also been found that the wear resistance increased with increasing coating thickness due to an enhanced load-bearing capability. The wear properties of PEO coatings on Mg AM60B alloy under boundary lubrication conditions were studied by Guo et al. [6]. It was found that the micro-porosities at the coating surfaces acted as oil reservoirs and were beneficial to the oil-lubricated wear performance. The effects of the PEO process parameters (electrolyte concentration, current density, current frequency and treatment time) on the tribological properties of the coatings under boundary lubrication conditions have also been studied by Zhang et al. [6]. The treatment time is one of the most significant factors affecting the COF [7], since roughness increased with treatment time which leads to an increased COF. The wear rate is influenced by many factors including, in decreasing order of importance, current

density, electrolyte concentration, frequency and treatment time. Yerokhin et al. [8] reported that PEO coatings may reduce the fatigue limit of magnesium alloys by no more than 10%, which is substantially lower than the effect of anodizing.

For applications which involve repetitive impact and sliding motions at relatively high contact loads or sudden impact (defense, biomedical implant, or electronic device covers) the coated components usually have to withstand high contact loads and the effect of scratches. To do this, the coatings must have good adhesion to the base material in order to withstand high loads and shearing forces without chipping or peeling, and a low coefficient of friction to reduce wear [9]. Many testing methods, including the pin-on-disk test, impact test and scratch test have been used to study coating failures on various substrates [10-12]. For applications where dynamic repetitive loadings are applied, a vertical ball-on-plate impact test was first introduced to evaluate the adhesive and cohesive failures of hard coatings [13]. Bantle and Matthews [14] pointed out that three failure regions are involved in the impact indent: a central region with cohesive failure; an intermediate region with cohesive and adhesive failures; and a peripheral region with circular crack failure plus piling up of the material. The general effect of repetitive dynamic impact is the degradation of the coating due to fatigue [9] and [15]. However, there was still a need for a testing method to study the coating wear properties under a combination of impact and sliding motions (repetitive impact–sliding motions). For repetitive impact–sliding motions, impact–fatigue wear testing methodology has been developed and used to study coating failure behavior under vertical impacting motions (vertical ball-on-plate) [16]. Also an inclined impact–sliding fatigue test method, which uses a combination of impact force and compression force [17] has been developed.

Changing the current mode produces changes in the PEO process characteristics, including the breakdown voltage and discharge events, both in terms of discharge intensity and density. The discharges have a profound effect on the coating microstructure, thickness, roughness, porosity, hardness, and coating growth rate, and hence affect the corrosion and wear resistance of the coated magnesium alloy. In this chapter we investigated the effect of current mode (unipolar, bipolar or hybrid (combination of both)) on the corrosion and wear properties of PEO coatings formed on an AM60B magnesium alloy. The tribological properties were determined by both a pin-

on-disk method and an inclined impact–sliding fatigue test method. The corrosion resistance was determined by potentiodynamic polarization testing. The structure is related first to the discharges produced by using the different current modes and then to the tribological and corrosion performance.

## 6.2. Materials and experimental methods

### 6.2.1. PEO coating preparation

AM60B magnesium alloy specimens with a disk shape ($25 \times 7$ mm) was used as the test coupons for the coating process. For reasonable coating growth rates, the electrolyte used for the PEO process was composed of potassium phosphate (7 g/l $K_4P_2O_7$), sodium aluminate (3 g/l $Na_2Al_2O_4$) and potassium hydroxide (~ 1 g/l KOH to keep the pH value at 12) in distilled water. The electrolyte bath capacity was 3 l. The temperature of the electrolyte was kept at $25 \pm 2$ °C using a water cooling system.

Three different sets were prepared with each set consisting of four coated samples. Sample U was coated using a unipolar current mode for 30 min. Sample B was coated using a bipolar current mode for 30 min. Sample H1 was coated using a combined unipolar (for 15 min) followed by bipolar (for 15 min) current mode for 30 min in total. For sample H2 the sequence for unipolar and bipolar was reversed compared with sample H1. The process parameters are listed in Table 6.1. All samples were processed using the same current density (50 mA/cm2) and the voltage was increased gradually with time, as the coating thickness increased.

Table 6.1. PEO process parameters for coating depositions on an AM60B Mg alloy.

| Sample | Current mode | Time (min) | $I^+$ (A) | $I^-$ (A) | $T_{on}^+$ (µs) | $T_{off}^+$ (µs) | $T_{on}^-$ (µs) | $T_{off}^-$ (µs) | $C_R$ |
|---|---|---|---|---|---|---|---|---|---|
| U | Unipolar | 30 | 0.7 | N/A | 400 | 100 | N/A | N/A | N/A |
| B | Bipolar | 30 | 0.7 | 0.63 | 400 | 100 | 400 | 100 | 0.74 |
| H1 | Unipolar | 15 | 0.7 | N/A | 400 | 100 | N/A | N/A | N/A |
| | Bipolar | 15 | 0.7 | 0.63 | 400 | 100 | 400 | 100 | 0.74 |
| H2 | Bipolar | 15 | 0.7 | 0.63 | 400 | 100 | 400 | 100 | 0.74 |
| | Unipolar | 15 | 0.7 | N/A | 400 | 100 | N/A | N/A | N/A |

### 6.2.2. Characterization of PEO coatings

Scanning electron microscopy (FEI Quanta 200 FEG with a solid state backscattered detector operated at 10 kV) in both the secondary electron (SE) and back-scattered electron (BSE) modes was used to observe both the coating surface morphology and, by observation of sample cross sections, the coating thickness and integrity. For the energy dispersive X-ray analysis (EDX) the SEM was operated at 15 kV with an electron beam spot size of 3 nm. A Mitutoyo SJ-201P surface profiler with precision of 0.01 μm was used to measure the surface roughness of all samples.

### 6.2.3. Tribological testing

### 6.2.3.1. Pin-on-disk

The wear resistance of coated and uncoated samples was evaluated using a pin-on-disk tester (FALEX ISC tribometer) under dry conditions with a 10 mm AISI 52100 steel ball as the wear medium (pin) and the samples as the disk. The steel ball was used, rather than the normal WC ball, so as to make the testing comparable to that of the inclined impact–sliding test. The coated samples were lightly polished using sand papers up to 2500 grit prior to wear testing to ensure a relatively smooth surface with minimum roughness. The tests were conducted at room temperature (20 °C), ~ 50% humidity, using a 2 N applied load and a rotation speed of 75.0 mm/s with the sample running on a 4 mm radius track. The tests were stopped after reaching a total wear distance of 100 m. After wear testing, the samples were cleaned in acetone, and dried in air. The wear tracks of the samples were characterized using a WYKO NT1100 optical profiler. The volume loss due to wear of the samples was calculated based on geometries (width and depth) of the wear tracks [18].

### 6.2.3.2. Inclined impact–sliding wear instrument

A schematic diagram of the inclined impact–sliding wear tester can be found in Ref. [19]. In this method, a hard ball (10 mm AISI 52100 steel ball) is mounted on the shaft of a double-way air cylinder with the piston driven by compressed air producing vertical oscillatory motions. A steel ball is used in this test rather than a ceramic ball, since a ceramic ball could potentially fracture on the initial impact loading. The sample is set on an inclined sample holder which is returned to its position by a spring.

An OMEGA LCKD-500 load cell is placed on the sample holder to record the normal force on the sample surface during the impact–sliding movement. The desired normal impact and compression forces were obtained by adjusting the pre-strain of the spring and the pressure in the air cylinder. For all tests, the impact and compression loads were set as 325 N and 210 N, respectively. The impact/compression forces were recorded and a typical load cycle is presented in Fig. 6.1(a) which shows the force curve in one impact cycle. The load cell was removed and the coated samples were placed on the sample holder for impact tests. The load curve demonstrates the three stages in each impact cycle, i.e. impact force $F_i$, vibrating stage and compression force $F_c$ as shown in Fig. 6.1(a). When the counterpart ball contacts the impacted sample surface for the first time, the first peak in the load occurs, which is defined as the effective impact force $F_i$. According to the Hertzian contact stress equation [20] for a sphere-on-plane contact condition, when $F_i$ = 325 N, the maximum and mean contact pressures in the impact crater for the first impact should be around 3.24 GPa and 2.16 GPa, respectively, which are larger than the yield strength (130 MPa) and compression strength of the AM60B Mg alloy. After the counterpart ball completed the first full contact with the coating surface and formed a deep impact crater, a series of rebounds and impacts occurred. After the vibration stage, the load continues to change gradually until the pre-setup compression load ($F_c$) is reached, and then the ball starts to move up. This is named as the compression force stage, in which a tail with sliding failures was formed.
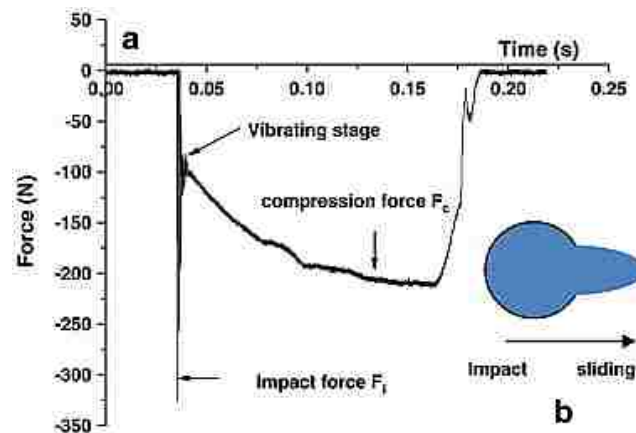


Fig. 6.1. The force curve in one impact cycle under $F_i/F_c$ = 325 N/210 N at a 2.5 Hz impact frequency.

The distance d between the steel ball and the sample is fixed at 1.3 mm which is the same distance between the load cell and the ball. The impact frequency used in this study was 2.5 Hz, which gives a total impact time, including the up and down motion, of 400 ms. The static air pressure, P was set around 0.12 MPa. Each coated sample was scheduled to be impacted 2000 cycles. Coating failure mechanisms of samples U, B, H1 and H2 were investigated. After a test, a crater head and a sliding wear track could be seen on the coating surface as illustrated in Fig. 6.1(b).

## 6.3. Results and discussion

### 6.3.1. Microstructure of the coatings

Fig. 6.2(a,c,e,g) shows the SEM micrographs of the U, B, H1 and H2 samples, obtained using a back-scattered electron mode (BSE). Projections and microporosities were observed in all the coated samples. However, the size and the shape of the projections and the microporosity were different. The surfaces of the coatings were dominated by many randomly arranged donut-shaped projections with open or sealed microporosities in the center. The microporosities are considered as footprints of the plasma discharge channels, through which the Mg and Mg2 + from the substrate were likely ejected and reached the coating/electrolyte interface during the plasma-caused melting, then combined with the electrolyte anions including Al2O42 − or OH− and reacted with O2 generated due to electrolysis, and finally deposited and sintered on the coating surface, contributing to the coating growth. Fig. 6.2(c and e) for the bipolar and H1 current mode respectively, shows a reduction in pore size (with an average pore size of ∼ 9.5–10 μm) relative to the unipolar and H2 modes (with an average pore size of ∼ 13.5–15 μm) (Fig. 6.2(a and g)). Such morphology was expected since both the number and intensity of the strong B-type discharges [9] are reduced by using a bipolar current mode. The average pore size for the H2 mode is ∼ 13.5 μm which may be attributed to the current mode for the last cycle, which in this case with the unipolar coming after the bipolar mode, causes some strong B-type discharges and, hence, relatively large pores are produced. Nevertheless, the four current modes show relatively similar surface morphology since such morphologies reflect the very last discharge events before the process was ended. Some microcracks appear on the coating surface. Thermal stresses are one source of

residual stress and can be categorized as: (i) stresses caused by differential thermal contraction between the coating and the substrate and (ii) stresses caused by temperature gradients within the coating during treatment.

The PEO coatings have an outer porous layer and an inner dense layer which exhibits excellent mechanical properties, as shown in Fig. 6.2(b,d,g,h) which are SEM micrographs of cross-sections using a secondary electron mode. Coating growth rate, structure and composition of the regions are substantially influenced by substrate composition, electrolyte composition and treatment regime [21]. Plasma discharge channels were found in the porous top layers. These channels went through the porous layer but stopped at the inner layer, and thus could be categorized as C-type plasma discharges, which occur in the micropores under the relatively deep surface [22]. The oxide coating morphology and microstructure were also significantly different under different current operating modes. The bipolar current mode could improve the coating quality compared with the unipolar current mode, in terms of surface morphology and cross-sectional microstructure.

The average surface roughness of all the coated samples is listed in Table 6.2, together with the coating thickness and pore size. A unipolar current mode gives rise to thicker, more porous (amounted size) coatings with a higher surface roughness than those produced using a bipolar current mode.
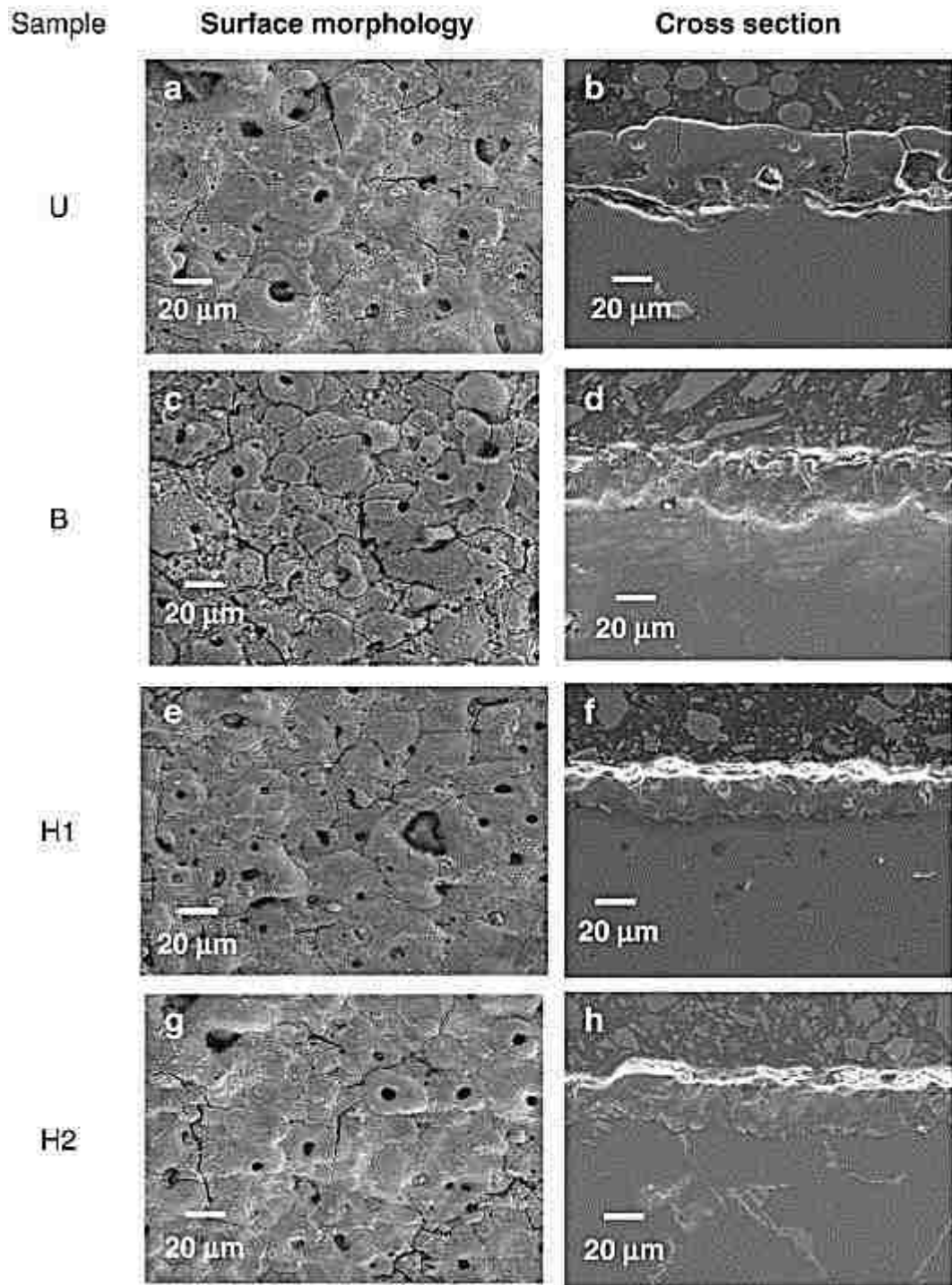
Fig 6.2. (L) SEM micrographs of polished sections of coatings using secondary electron mode (SE) and (R) morphology of oxide coatings on an Mg AM60B alloy using back-scattered electron mode (BSE) for: (a, b) unipolar, (c, d) bipolar and (e, f, g and h) hybrid current modes.

Table 6.2. Characterization of coated samples and dry sliding wear results.

| Sample | Coating thickness (µm) | Surface roughness Rz (µm) | Level of porosity and other defects | Average pore sizes (µm) | COF | Wear rate $\times 10^{-4}$ mm$^3$/N m |
|---|---|---|---|---|---|---|
| U | 40 to 55 | 44.3 ± 1.6 | Porous with many microcracks | 15.0 | 0.72 to 0.8 | 6.24 ± 2.0 |
| B | 31 to 42 | 31.3 ± 0.7 | Low level of porosity and microcracks | 9.5 | 0.55 to 0.6 | 1.78 ± 0.4 |
| H1 | 22 to 38 | 34.2 ± 0.5 | Low level of porosity and microcracks | 10.0 | 0.55 to 0.6 | 4.14 ± 1.0 |
| H2 | 21 to 39 | 37.1 ± 1.2 | Intermediate level of microcracks and porosity | 13.5 | 0.65 to 0.7 | 4.96 ± 1.2 |
| S0 | NA | 2.6 ± 0.2 | NA | NA | 0.4 to 0.5 | 9.0 ± 2.7 |

## 6.3.2. Tribological properties

Fig. 6.3 presents optical micrographs of the wear tracks on the uncoated and coated samples using the pin-on-disk method. Severe worn grooves were found on the uncoated sample under a 2 N load (Fig. 6.3 (S0)). As noted previously, during the wear tests the maximum compressive stresses exerted on the uncoated Mg sample are estimated to be about 590 MPa for a 2 N load [23]. Thus, the compressive stress is much larger than the yield strength of the Mg alloy (about 130 MPa according to the datasheet from Meridian Lightweight Technology Inc. [23]). Therefore, during the wear test, a large amount of plastic deformation occurred in the Mg alloy, resulting in severe plowing wear. Under a 2 N normal load, sample B showed the smallest wear tracks of all coated samples. Coating H1 had the second best wear rate among all coatings. Under 2 N load only coating U exhibited deep but not penetrating wear tracks. The dark areas seen on the wear tracks in optical micrographs of the coated samples are due to material transfer from the AISI 52100 steel ball during sliding.
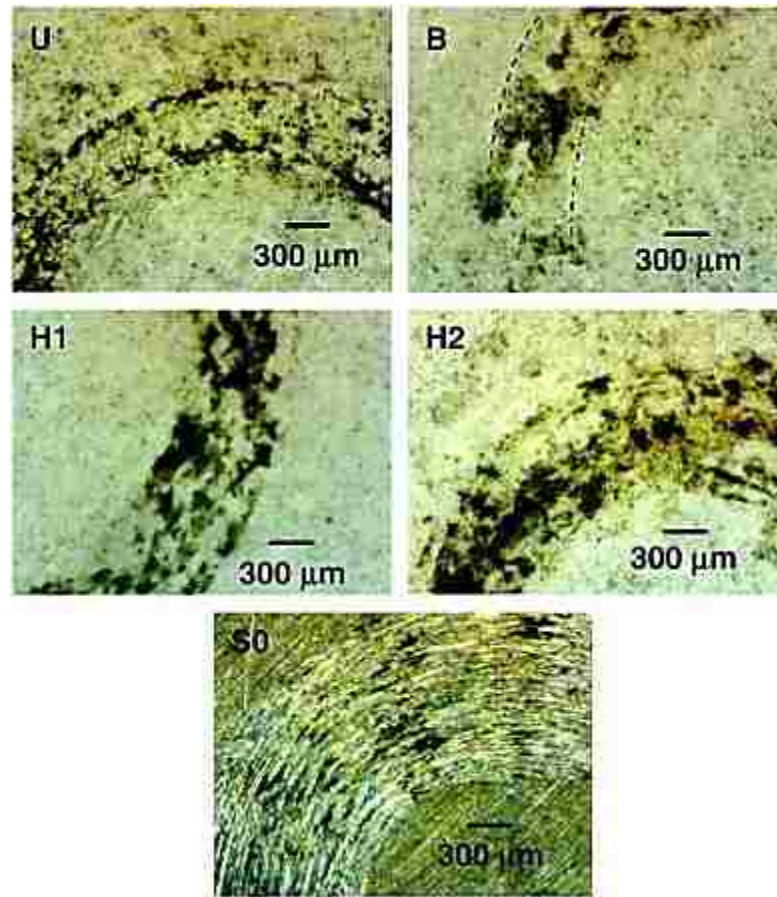
Fig. 6.3. Optical micrographs of the wear tracks after pin-on-disk tests for the uncoated AM60B Mg alloy (S0), and the coated substrate using unipolar (U), bipolar (B), and the hybrid current modes (H1 and H2).

Fig. 6.4 gives the COF versus sliding distance plots for all coated samples (U, B, H1 and H2) and the uncoated sample (S0). Compared with the S0, the four coated samples exhibited higher COFs when slid against the ASTM E52100 steel ball under dry (un-lubricated) conditions: see Table 6.2. The differences in coefficients of friction between the four samples are attributed to the different morphologies and surface roughness as shown in Fig. 6.5 for the roughness parameter Rz. A higher surface roughness and a less dense (more porous) coating lead to a higher COF. Based on the data presented in Fig. 6.4, Fig. 6.5 and Fig. 6.6 shows a linear relation between Rz and COF. Fig. 6.7 shows the wear rates, calculated using a volume loss method, of the uncoated Mg alloy and the four coated samples. The uncoated Mg alloy has a high wear rate of $(8.99 \pm 2.7) \times 10^{-4}$ mm$^3$/N m. The sample coated using unipolar current mode has a wear

rate of $(6.24 \pm 2.0) \times 10^{-4}$ mm$^3$/N m while the wear rates of samples coated using the bipolar current mode (sample B) are $(1.78 \pm 0.43) \times 10^{-4}$ mm$^3$/N m. Using the hybrid current mode (H1 and H2) wear rates are in the range of $(4.14 \pm 1.0)$–$(4.96 \pm 1.2) \times 10^{-4}$ mm$^3$/N m, which indicates that the PEO coatings have much better wear resistance than the Mg alloy substrate. Furthermore, samples B, H1 and H2 have better wear resistance than sample U, which is consistent with the measured COF during the sliding period. The enhancement of the wear resistance can be attributed to the enhancements of the microstructure of coatings prepared using hybrid or bipolar current modes which have a more compact structure than that of sample U. In addition, the different phase composition of the coating might also partly account for the higher wear resistance of samples B and H1. Previous work [24] has shown that the bipolar mode seems to promote the formation of MgO phase. The unipolar is more likely to promote the formation of the $Mg_2SiO_4$ and $MgAl_2O_4$ phases. Since a hybrid mode is a combination of unipolar and bipolar modes, MgO, $Mg_2SiO_4$ and $MgAl_2O_4$ phases were detected [24], but with different intensities, for the H1 and H2 modes. The H1 mode shows lower $Mg_2SiO_4$ and $MgAl_2O_4$ phase contents compared to the H2 mode. This is consistent with the fact that the "final" layer on H1 was produced using a bipolar mode. The wear resistance of the coated samples is a complex process that involves surface roughness and hardness which are controlled by phase contents and porosity levels. In the unipolar mode where type B-discharges are dominant, plasma temperatures can reach 7000 K [21] and the formation of $Mg_2SiO_4$ and $MgAl_2O_4$ phases is more likely. The hardness of these phases is high in the fully dense form. However, the unipolar mode or H2 mode (finished with unipolar) generates relatively large pores thus would reduce the overall hardness and hence, reduces the wear resistance of the coated samples.
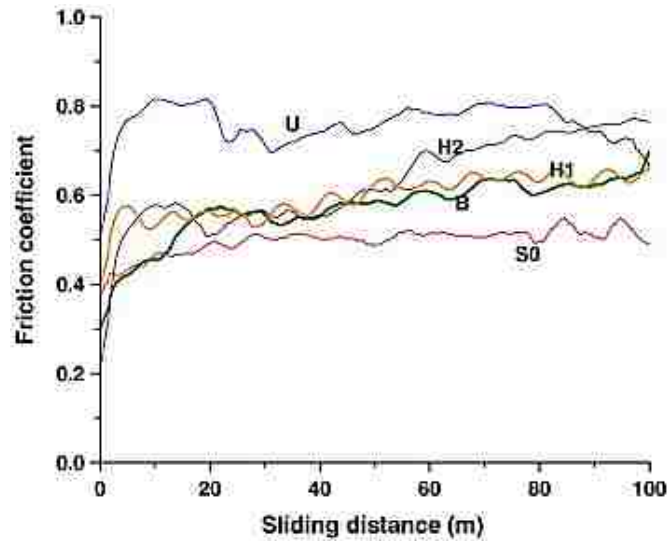
Fig. 6.4. Coefficients of friction vs. sliding distance for samples U, B, H1, and H2 and the S0 uncoated Mg alloy substrate.
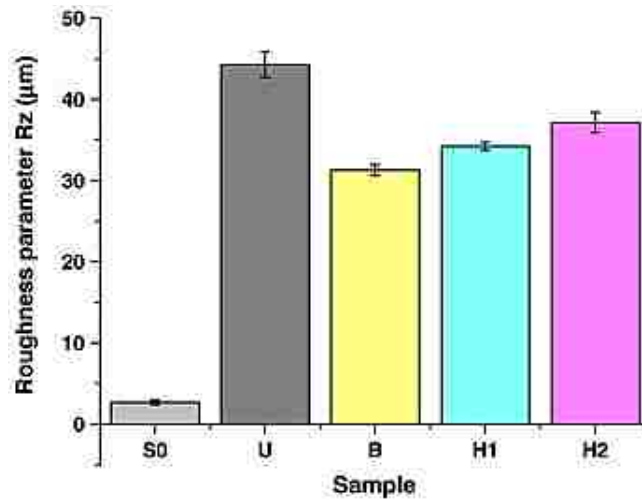


Fig.6.5. Roughness parameter Rz of the oxide coatings formed using different current modes and the uncoated Mg alloy substrate.
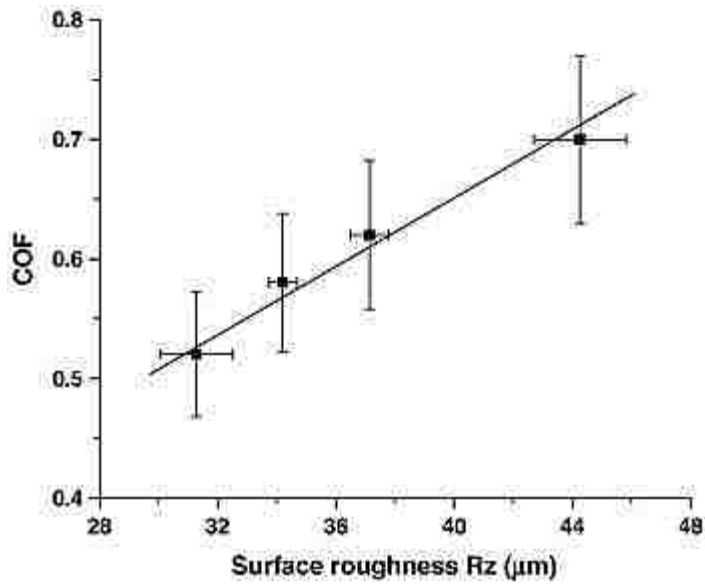
Fig. 6.6. Coefficients of friction vs. roughness parameter Rz of the oxide coatings on an Mg alloy substrate.
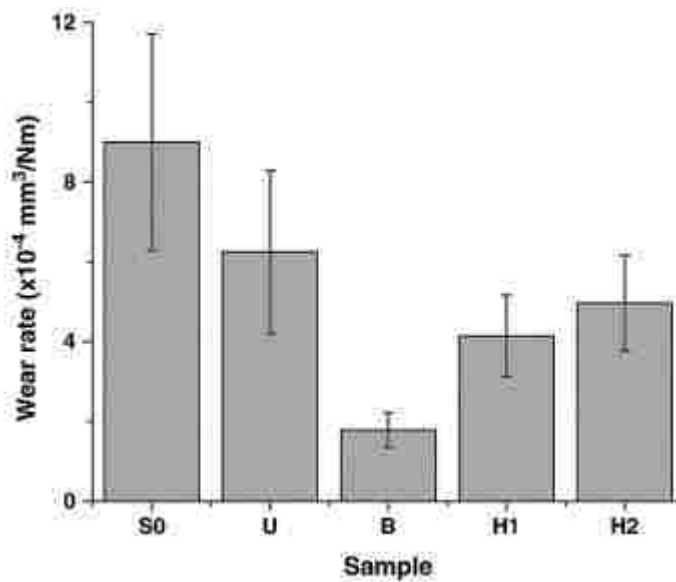


Fig. 6.7. Wear rates of the oxide coatings formed using different current modes and the uncoated Mg alloy substrate.

### 6.3.3. Inclined impact–sliding wear

Before discussing the results, caution should be exercised when using surface observations to interpret failure mechanisms. It is always possible that the damage observed at the surface is not representative of that occurring at the sub-surface. Fig. 6.8

shows SEM images of the impact–sliding tracks of the U sample, EDX spectrum showing the material transferred from the steel ball to the remaining coating, and a schematic illustration of the failure modes. Of the four principal failure mechanisms detailed in Refs. [16 and 17], namely cohesive failures (mainly chipping); adhesive failures (mainly peeling); material transfer; and fatigue cracks, only peeling was not detected in the PEO coated specimens. Material transfer, which is the dark area in the SEM micrograph and the schematic diagram of Fig. 6.8, was more severe at spots where the surface had become rougher due to other failure mechanisms.
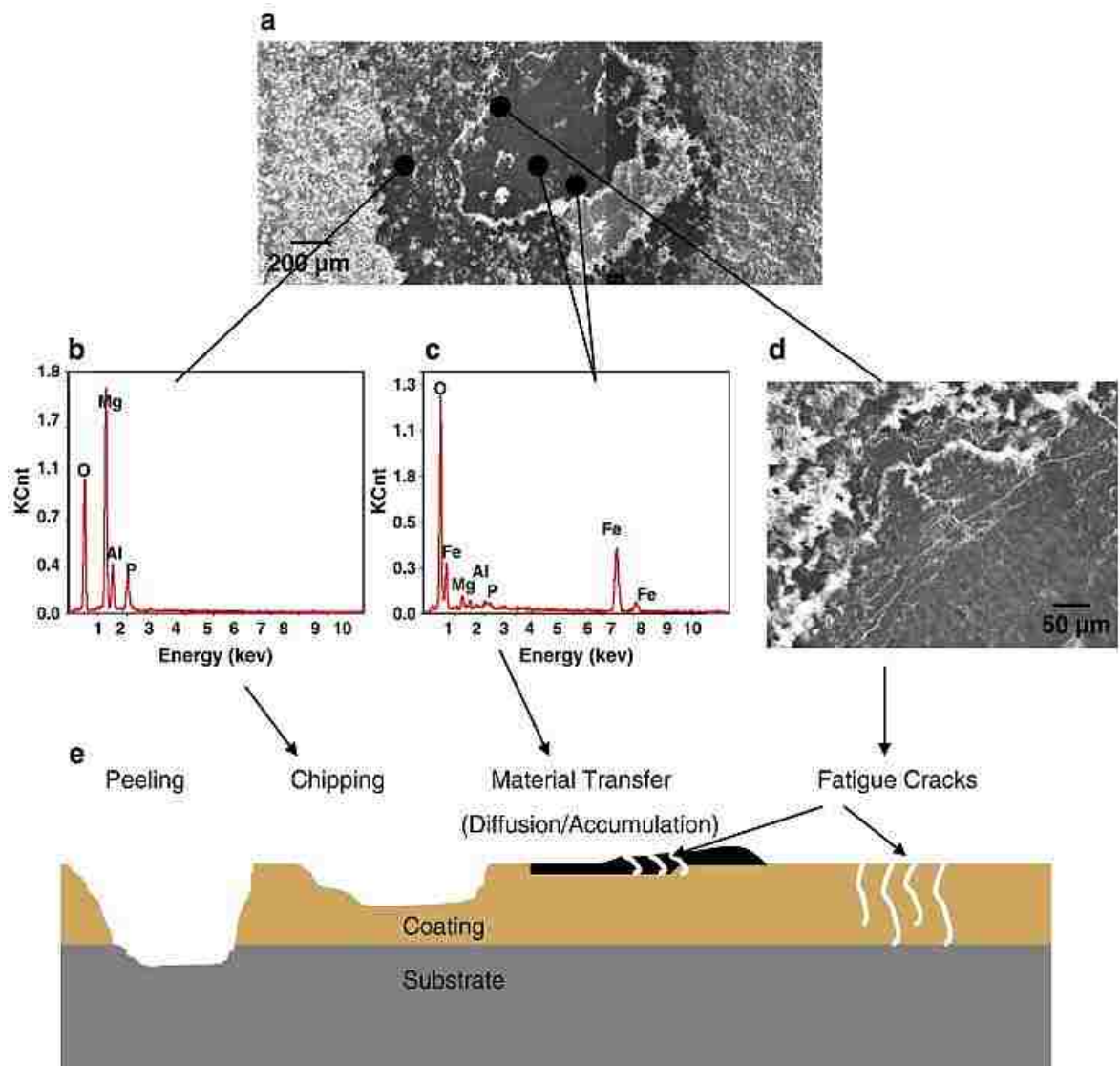


Fig. 6.8. (a, d) SEM images of the PEO coating using U current mode, (b, c) EDX spectrum showing the material transferred from the steel ball to the remaining coating and (e) illustration of failure modes.

Fatigue cracks were found at the impact-induced crater. The coating was still present at the center of the crater together with Fe transferred from the steel ball. Fatigue cracks appeared at the boundary of the crater (Fig. 6.8(d)), in the coating itself and on the sliding track. Peeling where the substrate was exposed (no coating) was not observed at the applied impact force used in this work. Chipping occurred without penetrating the coating through to the substrate–coating interface (Fig. 6.8(a and e)).

Fig. 6.9 shows the optical micrographs of the impact–sliding tracks of all samples after 2000 impact cycles. By using Photoshop and Image-Pro Plus software on the optical images shown in Fig. 6.9, the total track area and the crater area of the coated samples were calculated and are shown in Table 6.3. Compared to samples U and H2 samples B and H1 show the smallest crater area. PEO-coated samples showed better resistance to impact than S0. Samples B and H1 show relatively smaller crater areas compared with samples U and H2. Although a coating (such as a ceramic oxide) with a high hardness and large thickness could reduce the plastic deformation of the coated substrate at a low impact load, the effect was limited at a high impact load. It should be noted that the craters are created by the impact dynamic energy during the impact hammering.

Table 6.3. Impact–sliding track area and crater area of coated samples.

| Sample | Total track area ($mm^2$) | Crater area ($mm^2$) |
|---|---|---|
| S0 | 4.95 | N/A |
| U | 3.81 | 0.86 |
| B | 2.43 | 0.65 |
| H1 | 3.53 | 0.63 |
| H2 | 3.63 | 0.91 |
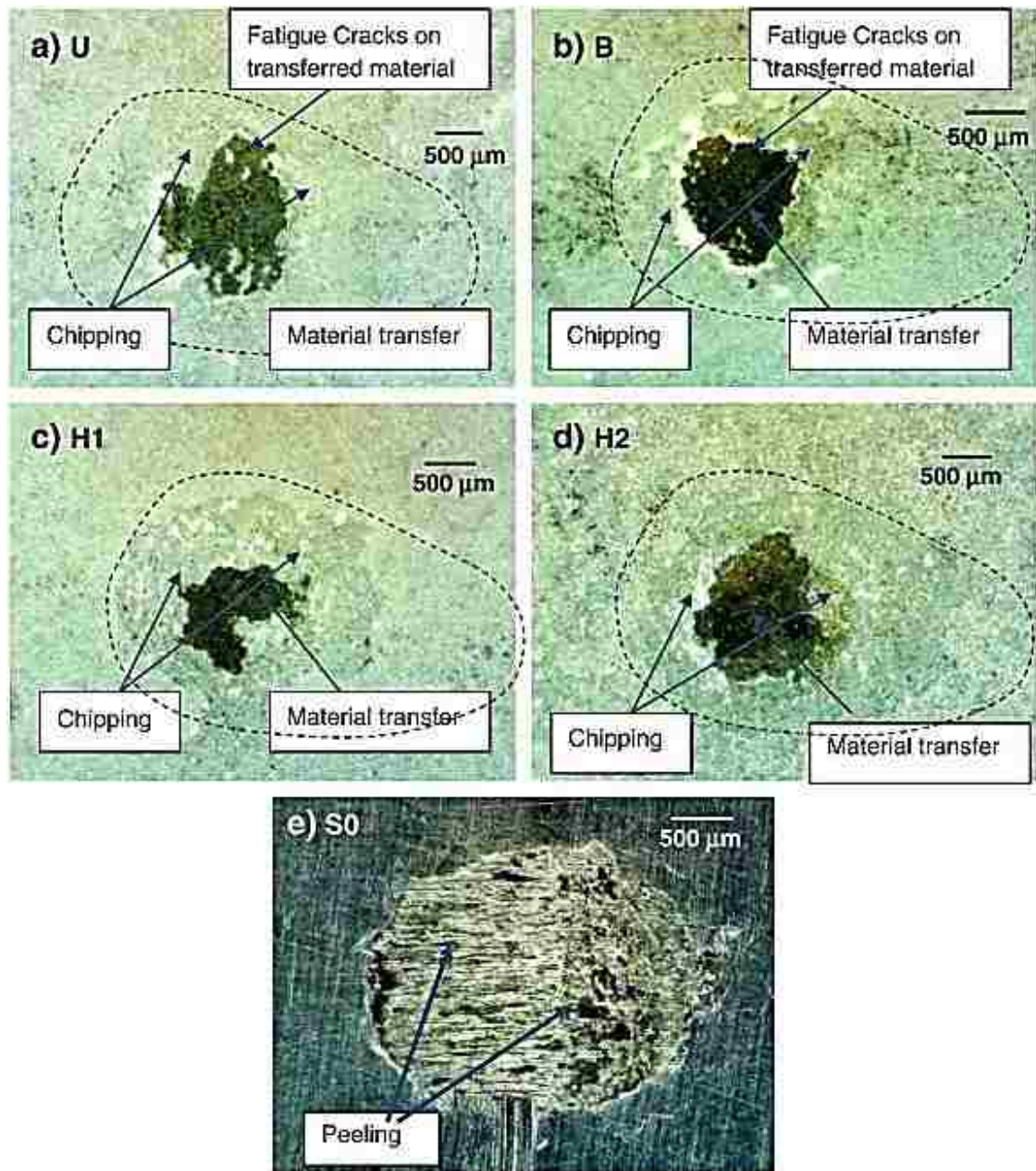
Fig. 6.9. Optical micrographs showing the craters (after 2000 impact cycles) of the PEO coatings prepared using (a) unipolar, (b) bipolar, (c) hybrid 1, and (d) hybrid 2 current modes and (e) the uncoated sample.

Fig. 6.10(a) is a SEM image showing the three layers of PEO coated specimen H2 after the impact–sliding test. There is an outside unaffected top layer, a slightly affected second layer which represents the inner dense layer, and the third layer corresponding to a very dense interface layer. Fig. 6.10(b) is a schematic of these three layers. The dark layer is due to the material transfer (Fe) from the steel ball due to the impact force.
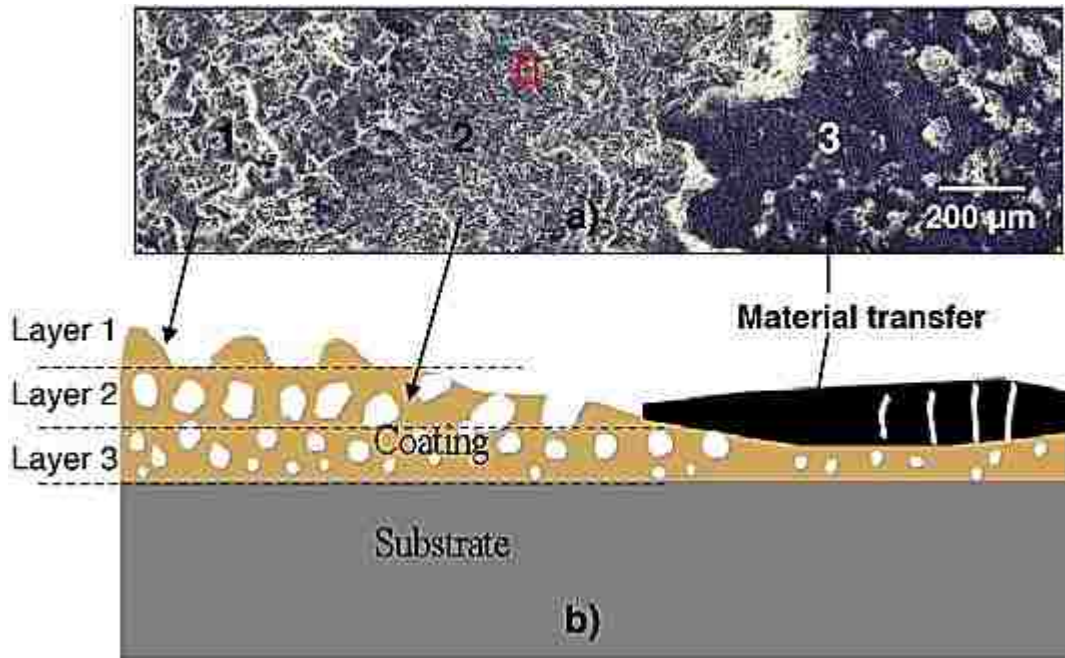
Fig. 6.10. (a) SEM images and (b) schematic showing the three layers exposed after impact testing.

Fig. 6.11a shows a typical EDX line scan across the impact crater of sample U. A back-scattered electron image of the coating is also given in Fig. 6.11b which shows the existence of a high Z element (Fe) as a white area near the center of the crater. Looking at the EDX line scans from location A (undamaged coating at the left side of Fig. 6.11(a)) to location B (undamaged coating at the right side of Fig. 6.11(a)), the following observations can be made. The Mg intensity is relatively constant, except that it increases in what is layer 2 (Fig. 6.10) where the coating has peeled off the porous outer layer. The O signal increases at the edge and center of the crater area. The line scan for Fe shows a significantly higher Fe content at the center of the crater. This increase in iron and oxygen at the center of the crater is confirmed by the area EDX scan given in Fig. 6.11(c). Thus Fe was transferred from the steel ball during the impact and sliding processes to the PEO coating. Although the coating was still intact, this kind of material transfer could result in enhanced adhesive wear.

108
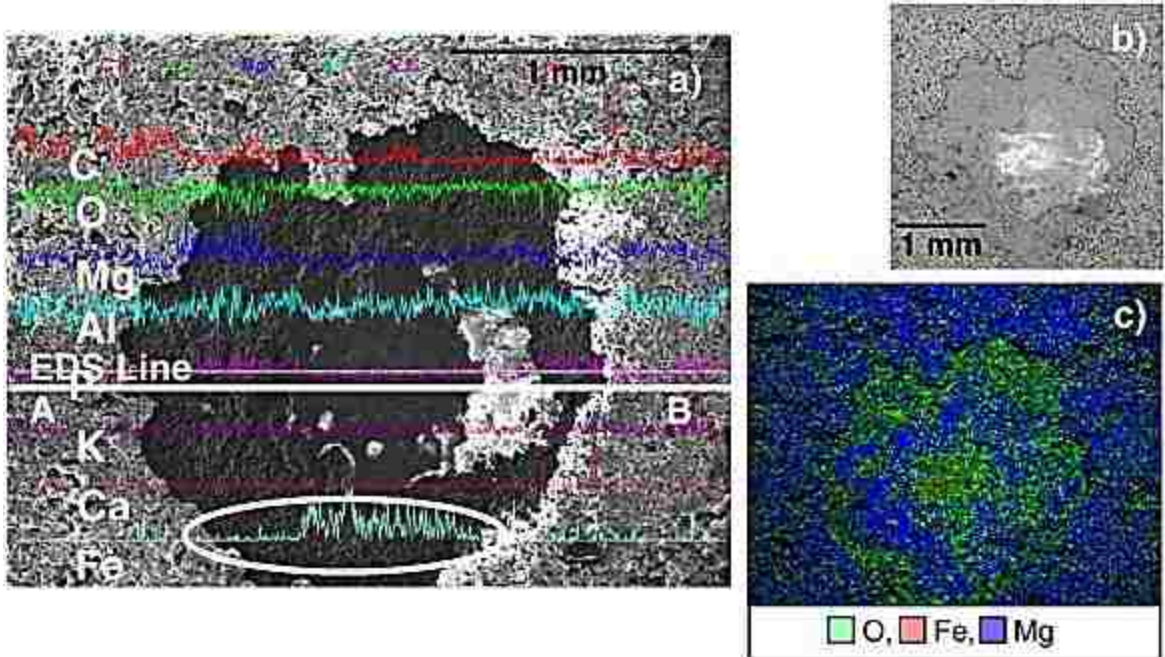
Fig. 6.11. SEM image showing the crater of the PEO U coating with a typical EDX. (a) Line scan EDX from location A to B, (b) backscattered electron image of the crater and (c) area scan of the crater for the Mg, O and Fe.

## 6.4. Conclusions

1.The growth rate, porosity level and microstructure (including phase content) of PEO coatings formed on an AM60B magnesium alloy are significantly influenced by the current mode. The thickness, porosity, defect level and roughness are increased by using a unipolar or hybrid 2 (finished with unipolar) current mode, where type B-discharges are dominant, compared to coatings prepared using a bipolar or hybrid 1, finished with bipolar current mode.

2.The denser coatings with lower surface roughness that are produced by the B and H1 current modes compared to the U and H2 modes lead to improved tribological performance in both pin-on-disk and inclined impact–sliding tests.

3.In the pin-on-disk tests, the COF is shown to be directly dependent on the surface roughness, Rz.

**References**

[1]     Li X, Liu X, Luan BL, Corrosion and wear properties of PEO coatings formed on AM60B alloy in NaAlO2 electrolytes. Applied Surface Science, 257 (2011) 9135–9141.

[2]     Arrabal R, Matykina E, Hashimoto T, Skeldon P, Thompson GE, Characterization of AC PEO coatings on magnesium alloys. Surface & Coatings Technology, 203 (2009) 2207-2220.

[3]     Liang J, Hu L, Hao J, Characterization of microarc oxidation coatings formed on AM60B magnesium alloy in silicate and phosphate electrolytes. Applied Surface Science, 253 (2007) 4490-4496.

[4]     Wang S, Yang Z, Zhao Y, Wei M, Tempering Temperature Effect on Sliding Wear at High Temperatures in Mottled Cast Iron. Tribology Letters, 38 (2010) 39-45.

[5]     Bala Srinivasan P, Liang J, Blawert C, Dietzel W, Dry sliding wear behaviour of magnesium oxide and zirconium oxide plasma electrolytic oxidation coated magnesium alloy. Applied Surface Science, 256(10) (2010) 3265-3273.

[6]     Guo J, Wang L, Liang J, Xue Q, Yan F, Tribological behavior of plasma electrolytic oxidation coating on magnesium alloy with oil lubrication at elevated temperatures. Journal of Alloys and Compounds, 481 (2009), 903–909.

[7]     Zhang P, Nie X, Hu H, Wear and Galvanic Corrosion Protection of Mg alloy via Plasma Electrolytic Oxidation Process for Mg Engine Application. in SAE 2009 World Congress. 2009.

[8]     Yerokhin AL, Shatrov A, Samsonov V, Shashkov P, Leyland A and Matthews A, Fatigue properties of Keronite coatings on a magnesium alloy. Surface & Coatings Technology, 182 (2004) 78-84

[9]     Voevodin A A, Schneider J M, Rebholz C, Matthews A, Multilayer composite ceramic-metal-DLC coatings for sliding wear applications. Tribology International, 29 (1996), 559–570.

[10]    Bouzakis KD, Asimakopoulos A, Michailidis N, Kompogiannis S, Maliaris G, Giannopoulos G, Pavlidou E, Erkens G, The inclined impact test, an efficient method to characterize coatings' cohesion and adhesion properties. Thin Solid Films 469 (2004) 254-262.

[11]    Bantle R, Matthews A, Investigation into the impact wear behavior of ceramic coatings. Surface & Coatings Technology, 74/75 (1995), 857-868.

[12]    Berg G, Friedrich C, Broszeit E, Berger C, Fresenius, scratch test measurement of tribolojical hard coating in practice. Journal of Analytical Chemistry, 358 (1997) 281-285.

[13]    Knotek O, Bosserhoff B, Schrey A, Leyendecker T, Lemmer O, Esser S, A new technique for testing the impact load of thin films: the coating impact test. Surface & Coatings Technology, 54–55 (1992) 102-107.

[14]    Bantle, R. and Matthews, A. (1995), Investigation into the impact wear behavior of ceramic coatings. Surface & Coatings Technology, 74/75, 857-868

[15]    Bouzakis KD, Vidakis N, Leyendecker T, Erkens G, Wenke R, Determination of the fatigue properties of multilayer PVD coatings on various substrates, based on

the impact test and its FEM simulation. Thin Solid Films 308–309 (1997) 315-322.

[16] Su J F, Nie X, Mulholland T, Combinative Influence of Impact and Pressing Forces on Coating Failure Behaviour. Surface & Coatings Technology, 205 (2010) 1520-1526.

[17] Su JF, Yu D, Nie X, Hu H, Inclined impactsliding wear tests of TiN/Al2O3/TiCN coatings on cemented carbide substrates. Surface & Coatings Technology, 206 (2011) 1998-2004.

[18] Chattopadhyay R, Surface Wear Analysis, Treatment, and Prevention, ASM-International, OH, USA, 2001.

[19] Chen Y, Nie X, Study on fatigue and wear behaviors of a TiN coating using an inclined impact-sliding test. Surface & Coatings Technology, 206 (2011) 1977-1982.

[20] Lingaiah K, in: Machine Design Databook, 2nd ed., McGraw-Hill, New York, 2003, p. 2.20.

[21] Hussein RO, Zhang P, Xia Y, Nie X, Northwood DO. The effect of current mode and discharge type on the corrosion resistance of plasma electrolytic oxidation (PEO) coated magnesium alloy AJ62. Surface & Coatings Technology, 206 (2011) 1990-1997.

[22] Hussein RO, Nie X, Northwood DO, Yerokhin A, Matthews A (2010), Spectroscopic study of electrolytic plasma and discharging behaviour during the plasma electrolytic oxidation (PEO) process. Journal of Physics D: Applied Physics, 43, 105203.

[23] http://www.meridian-mag.com/magnesium/datasheet.pdf.

[24] Hussein RO, Northwood DO and Nie X, The influence of pulse timing and current mode on the microstructure and corrosion behaviour of a plasma electrolytic oxidation (PEO) coated AM60B magnesium alloy. J. of Alloys and Compounds, 541 (2012) 41-48.

# CHAPTER 7

# AN INVESTIGATION OF CERAMIC COATING GROWTH MECHANISMS IN PLASMA ELECTROLYTIC OXIDATION (PEO) PROCESSING.

**Published in:**

## 7.1 Introduction

Besides the process technology, the growth mechanisms of the PEO coating, and the coating's microstructure and properties, are gaining more and more attention [1,2]. To further our understanding of the Plasma Electrolytic Oxidation (PEO) process, and to aid in the optimization of the process, it is important to identify the mechanisms of coating formation. During plasma electrolytic oxidation, complex physical and chemical process occurs near the interface between electrolyte and the electrode. Several micro-discharge formation models have been proposed [3-7]. In the first model [4], the micro-discharges appear as a result of the oxide film dielectric breakdown in a strong electric field. The second group of models considers each micro-discharge as a gas/glow discharge occurring in a micropore of the oxide film [5]. The formation of a gas phase in the pore (and discharge ignition in it) is believed to be induced by an initial dielectric breakdown of a barrier layer in the bottom of the micropore [3]. The third model [7] assumed the possibility of free electron generation and glow discharge ignition in the gaseous media at the oxide-electrolyte interface, which leads to heating, melting and quenching the underlying oxide layer. Any other model considers the formation of the micro-arc discharge as an electronic 'avalanche', or due to an electronic tunneling effect [6]. Yerokhin et al [3] found that the above models [4-7] do not fit the spatial, temporal and electrical characteristics of micro-discharge phenomena which were observed in their investigation. They suggested a new model based on the analogy with contact glow discharge electrolysis. The model assumes the possibility of free electron generation and

glow discharge ignition in the gaseous media at the oxide-electrolyte interface, which leads to heating, melting and quenching of the underlying oxide layer.

Recently, optical emission spectroscopy (OES) has been used to investigate the plasma discharge behavior during the PEO process [8,9]. Due to the extreme nonlinearity of plasma discharge, monitoring the evolution of spectral signals and microstructure is helpful in understanding the mechanism underlying PEO process. Species from the substrate (Mg, Al and Ti) and the electrolyte (H, OH, Na and K) were found to be involved in the plasma discharge during the PEO process. The evolution of the spectra is considered to reflect the change in mechanism that initiated the plasma discharge, from bound-bound transitions of electrons between atomic level to collision–radiative recombination of electrons (bound-free transitions) and Bremsstrahlung radiation (free-free transitions).  According to Dunleavy et al [9], the plasma emission spectra indicated that there were two distinct regions of the plasma, a central core of high temperature (~16, 000 $\pm$ 3500 K), with a high electron density (Ne ~5$\times$ $10^{17}$ cm-3) and a peripheral region, probably extending into the surrounding electrolyte, which was much cooler (~3000-4000 K) and less dense (Ne ~5$\times$ $10^{15}$ cm-3). Hussein et al studied the evolution of the emission spectra of plasma discharge during the PEO process [10]. The fluctuations in plasma intensities and temperatures during the plasma discharging as well as the coating morphology were found to be due to the different types of discharge, which originated at the metal/coating interface (type B), within the coating upper layer (type C), or at the coating surface/electrolyte interface (type A) [8]. Type B discharges are responsible for the high temperature spikes (up to 10 000K) present in the electron temperature profiles. On the other hand, type A and C discharges produce the base temperature profile and any small fluctuations around this base line (~ 4500K). Hussein et al. [10] have described the coating development during PEO processing based on a general theory of the breakdown of a metal/dielectric system in an electric field, optical emission spectroscopy observations and SEM/EDX analysis of the coatings. Their general coatings mechanisms can be applied to the PEO processing of any of the light-weight metals (Mg, Al, Ti or Zr). However process parameters including electrolyte composition or electrical parameters (DC, AC, unipolar, bipolar, constant current or voltage) have a significant effect on such mechanisms.

The AJ62 Magnesium alloy (MgAl6Mn0.3Sr2) is a die castable alloy that has good creep resistance and has been used in the mass production of an automotive powertrain crankcase. Magnesium alloy AJ62 has recently been developed as a structural automotive powertrain material. This alloy is characterized not only by a high strength-to-weight ratio synonymous with magnesium alloys but also by relatively good properties at elevated temperatures [11-13]. Its high temperature performance has led engineers to use this alloy as an engine block material initially with an Al-Si alloy liner [14]. AJ62 is the only Mg–Al alloy thus far to have been used in the mass production of an automotive power train crankcase [14].

The main objective of this work is to develop a correlation between the oxide ceramic layer formation processes and the growth rate during PEO coating. To do this, we examine the production and diffusion of oxygen and its effect on the coating formation. In this chapter, coatings up to 110 μm thick were produced on a AJ62 Mg-alloy substrate using the PEO process. Optical emission spectroscopy (OES) was employed to follow the microdischarges and substrate and electrolyte elements present in the plasma discharge during the coating growth, and to determine plasma electron temperatures.

## 7.2. Experimental procedures

### 7.2.1 Materials and PEO processing method

A PEO coating system as described in Chapter 3 was used to produce the oxide coating on the samples. The PEO coating process was carried out using a bipolar current mode which consists of two components, a positive component and a negative component. During the coating process, the positive $I^+$ and negative $I^-$ current density was maintained at 0.07 and 0.06 A/cm$^2$ respectively and the voltage was increased gradually with time, as the coating thickness increased, process parameters for PEO treatment are listed in Table 7.1.

The AJ62 Magnesium alloy disc coupons (Φ25×5mm) were used as the test samples in this study. The coupons were manually ground and polished on 240, 400,600, and 1200 grit silicon carbide (SiC) waterproof abrasive papers. The coating was obtained in an alkaline electrolyte containing sodium aluminate (10g/l $Na_2Al_2O_4$) and potassium hydroxide (1 g/l KOH). The temperature of the electrolyte was kept below 25 $^o$C by a

water cooling system. The PEO processing parameters for the coated Mg samples are listed in Table 7.1.

**Table 7.1  PEO Process parameters for coating AJ62 Mg alloy.**

| Sample | Current mode | Time (min) | $I^+$ (A) | $I^-$ (A) | $T_{on}^+$ (μs) | $T_{on}^-$ (μs) | $T_{off}^+$ (μs) | $T_{off}^-$ (μs) | $C_R$ |
|--------|-------------|-----------|-----------|-----------|-----------------|-----------------|------------------|------------------|-------|
| S1-S9 | Bipolar | 3-120 | 0.7 | 0.6 | 400 | 100 | 400 | 100 | 0.77 |

## 7.2.2 Optical emission spectroscopy

The main characterization of the micro-discharges was performed by means of optical emission spectroscopy (OES). Four different spectral lines were recorded simultaneously, which eliminates discrepancies that may otherwise happen if the spectra are recorded at different times. The spectral lines (Table 7.2) at 285.2 nm (Mg I), 486.1 nm (H$_\beta$), 656.2 nm (H$\alpha$), and 777.2 nm (O I) were recorded.

**Table 7.2 Spectral lines used in this experiment together with their wavelength ($\lambda$), transition, statistical weight of the upper and lower state g$_k$ and g$_i$ (respectively), photon energy ($\Delta$E) and the transition probabilities (A$_{ki}$) [15].**

| Line | $\lambda$ (nm) | Transition | $g_k$ | $g_i$ | $\Delta E$ (eV) | $A_{ki} \times 10^8$ S$^{-1}$ |
|------|----------------|------------|-------|-------|-----------------|-------------------------------|
| Mg I | 285.2 | $3s3p\ ^1P \rightarrow 3s^2\ ^1S$ | 3 | 1 | 4.33 | 5.0 |
| H$_\beta$ | 486.1 | $4d\ ^2D \rightarrow 2p\ ^2P$ | 4 | 2 | 2.55 | 0.172 |
| H$\alpha$ | 656.2 | $3d\ ^2D \rightarrow 2p\ ^2P$ | 4 | 2 | 1.89 | 0.539 |
| O I | 777.2 | $3p\ ^5P \rightarrow 3s\ ^5S$ | 7 | 5 | 1.59 | 0.369 |

## 7.2.3 Coating characterization

The samples were cut to be about 4-mm-thick sections normal to the Tangential-Radial surface and mounted with resin and polished to a mirror finish then sputtered with a gold film to make them conductive before SEM analysis. The coating thicknesses for different treatment times were determined using a PosiTector 6000 coating thickness meter with N type probes: this instrument uses the eddy current principle to measure the thickness of

non-conductive coating (ceramic) on non-ferrous metal (magnesium). The dimensions of the magnesium alloy sample before and after oxidation were measured using a Mitutoyo Absolute ID-S112 spiral "Absolute Position" digital micrometer, from which the inner and outer thickness values at different treatment time were calculated. The meter was set to zero-position for the uncoated substrate then the total outer thickness measured after the coating, which represents twice the thickness of the sample dimension changes.

## 7.3 Results

### 7.3.1 Voltage behavior.

Fig. 7.1 show a typical output anodic ($V_A$) and cathodic ($-V_C$) voltage change during the 120 min of PEO treatment. By combining the output voltage results with the OES emission intensities and plasma temperatures, four discharge stages can be identified in the PEO process, namely: **Stage I:** In the early stage of the process which mainly involves the rapid electrochemical formation of an initial insulating oxide film, a sharp increase in the voltage was seen. In this stage the breakdown voltage is not yet reached. **Stage II:** The rate of the voltage change decreases in this stage, which is characterized by numerous sparks moving rapidly over the whole sample surface area. This indicates a start of the breakdown of the oxide layer, an increase in temperature and, therefore, melting of the substrate metal. **Stage III:** In this stage the rate of voltage increase becomes slow; this stage is characterized by larger but slower moving discharges. As the oxide layer grows, its electrical resistance increases, therefore the nature of the plasma changes. **Stage IV:** In this stage the rate of voltage variation is even slower than that in stage III and concentrated discharges appear as relatively large and long lasting sparks. However the occurrence of the strong discharges is less frequent than that in stage III due to the thicker coating causing more difficulty in the initiation of such discharges. For some cases, such strong discharges may cause irreversible damage to the coatings in stage IV.
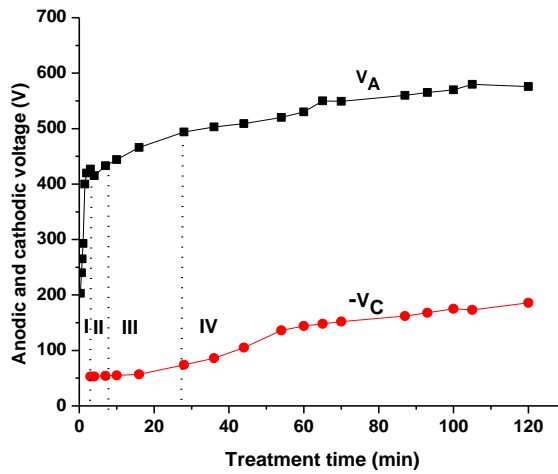
**Fig. 7.1.** Plots of anodic and cathodic voltage vs. treatment time during the PEO process using bipolar current mode.

### 7.3.2 Optical emission characterization.

As the plasma coating process proceeds, the discharge appearance changes and the plasma emission intensities varied as shown in Fig. 7.2. Fig. 7.2 shows the optical emission intensity profile of the Mg line (285.2 nm) for a bipolar current mode for a total treatment time of 120 min: this illustrates the time evolution of a substrate element present in the plasma discharge during the coating growth.
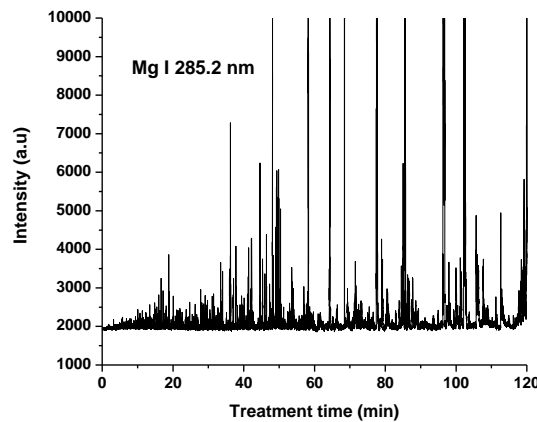


**Fig. 7.2.** Typical time variation of the emission line intensity of Mg I during the PEO process.

As the PEO process preceded, relatively strong variations in the microdischarges were observed, indicated by many separated spikes in Fig.7.2. These spikes correspond to the relatively strong discharges (B-type discharge) [16-17], which are initiated from the

117

magnesium surface-coating interface. The spike height increases as the process proceeds, particularly after 40 minutes processing time. Optical emission spectra of oxygen line at 777.2 nm spectral line were used to follow the time evolution and the behavior of the oxygen in the plasma discharge during the coating growth. The intensity spectrum of O I for three different treatment times 30, 50 and 120 min respectively are shown in Fig. 7.3(a-c).
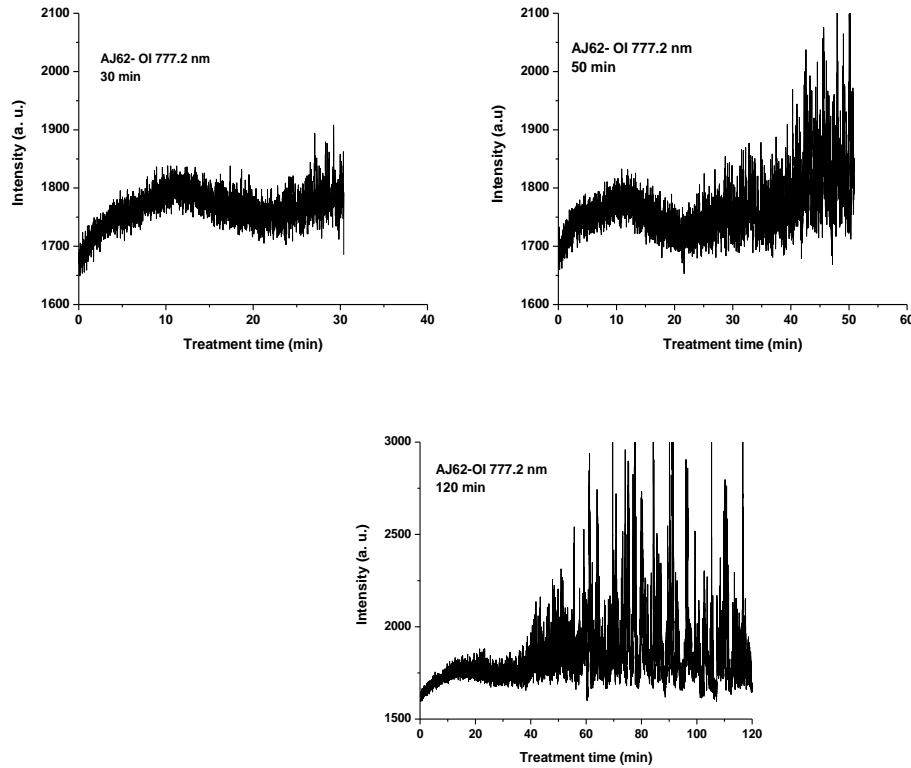


**Fig. 7.3.** Typical time variation of the emission line intensity of O I during the PEO process at three different treatment times.

For the 30 min treatment time relatively low O I intensity signals are observed as shown in Fig. 7.3(a). The oxygen signal started to be noticeable for the period 40 to 50 min, see Fig. 7.3(b). As the coating process proceeds, the oxygen (O I) intensity signal generally increased with the treatment time (Fig 7.3(c)); this is likely due to the increased amount of oxygen evolution as the process preceded, as has been previously observed for aluminum by Snizhko et al [18]. By comparing the optical emission intensity of oxygen Fig. 7.3(c) with Fig. 7.2 for Mg, the evolution of oxygen is related to the intensity of the microdischarges, where after 40 minutes processing time, both the O and Mg signals

increase due to the existence of B-type discharges. However, the O signal densities are larger than that of Mg due to its relatively low excitation energy (1.59 eV) compared to that of Mg (4.33 eV) [15].

### 7.3.3 Plasma electron temperature

The spectral lines selected for the calculation should belong to the same atomic or ionic species and are emitted in the same ionization stage. In this case, the intensity ratio of the recorded 656.2 nm ($H_\alpha$) to 486.1 nm ($H_\beta$) spectra $I_{H\,(3d\,^2D\,\rightarrow\,2p\,^2P)}$ / $I_{H\,(4d\,^2D\,\rightarrow\,2p\,^2P)}$ were used to determine plasma electron temperature ($T_e$) which is presented in Fig. 7.4. The average temperatures are also shown in Fig. 7.4.
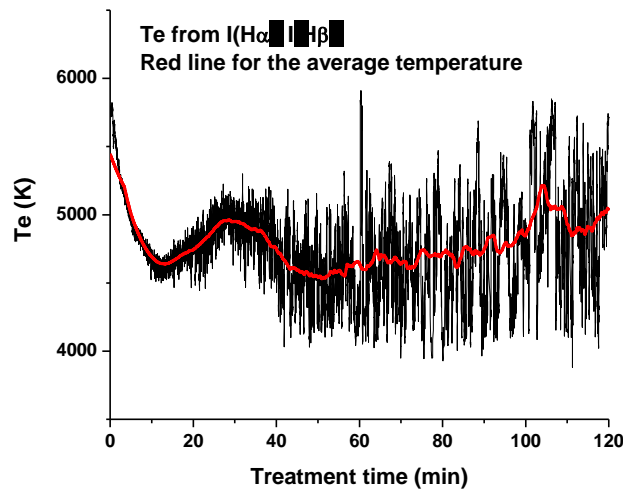


**Fig. 7.4.** Plasma temperature as a function of treatment time (min) determined from the intensity ratio of Hα (656.3 nm)/Hβ (486.1 nm)

It is commonly accepted that the discharge in PEO occurs when the applied voltage reaches a certain critical value corresponding to the breakdown of the oxide layer (or at least of the barrier part of it) formed on the sample surface: this leads to the development of intense light emission generated at the numerous micro-discharge sites. Fig. 7.4 shows plasma temperature is initially around 5500 K which corresponds to the early stage discharges where the density of the discharges is very high (accumulation of the individual discharge temperatures). Te then drops to about 4500 K after about ten minutes and then increased to about 5000 K at 25 min after that drops to around 4500 K at 40 min. Then the average electron temperatures curve started to gradually increase to

reach up to 5000 K. There were a high number of closely-spaced temperature spikes some of them reaching up to 5800 K. These spikes corresponded to relatively strong discharges initiated from the sample surface-coating interface, the so-called B-type discharges.

### 7.3.4 Microstructure of the coatings.

Figs. 7.5 (a-f) present SEM micrographs of the surface morphologies of coatings produced using different processing times. Projections and microporosity with different sizes and shapes were observed on all the coated samples. Curly projections were found to be dominant on the surfaces of coatings.
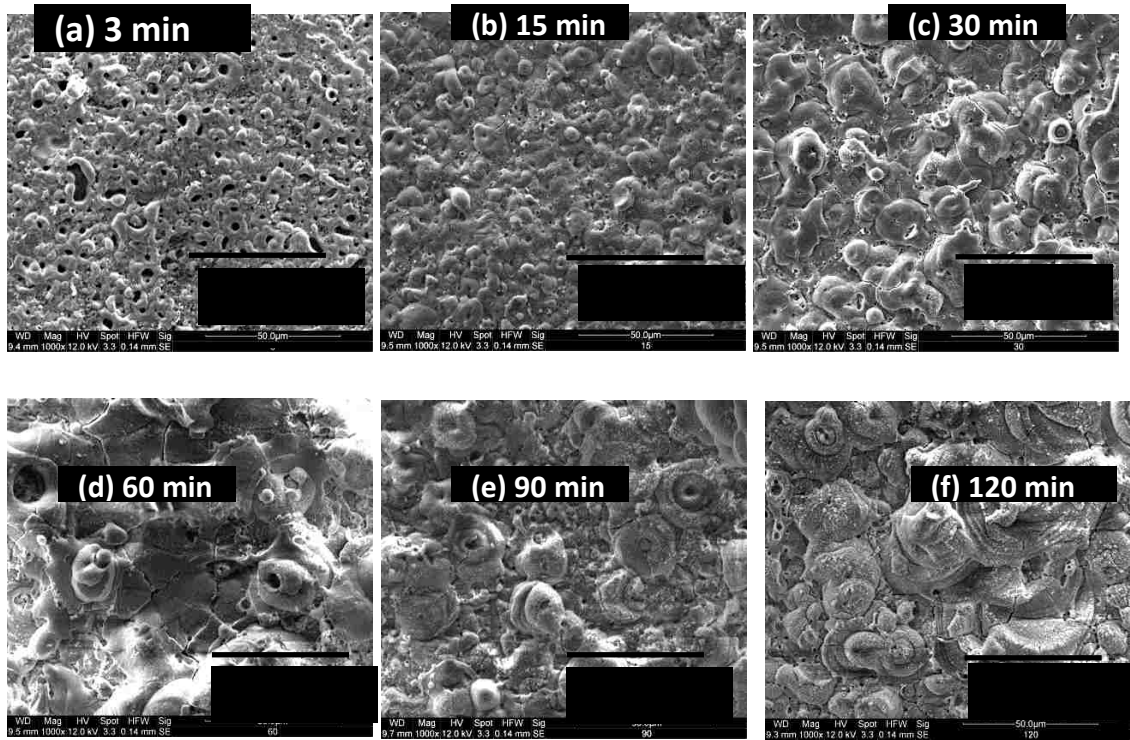


**Fig. 7.5** SEM micrographs showing the surface morphology of oxide coatings on AJ62 for different treatment times.

The surfaces of the coatings were dominated by a 'pancake' shaped projections with open or sealed microporosity in the center. Short processing times, eg 3 minutes (Fig. 7.5(a)), show the highest density of open (un-sealed) channels at the centers of the 'pancake' structures. The microporosity is considered to be "footprints" of the plasma discharge channels, through which the Mg and $Mg^{2+}$ from the substrate were likely ejected and reached the coating/electrolyte interface during the plasma-generated melting. The Mg

and $Mg^{2+}$ then reacted with $O_2$ generated by electrolysis, and finally sintered and deposited on the coating surface, thus contributing to coating growth.

Figs. 7.6 (a-f) present SEM micrographs of cross-sections of coated samples using different treatment times. The dashed-line on the micrograph indicates the approximate position of the original surface of the magnesium alloy specimens before PEO treatment. All coating-substrate interfaces had a wavy-jagged appearance, which may be the result of dissolution of the substrate in the early stages of processing and/or the presence of intermetallic phases at the grain boundaries. The α-Mg grain boundaries in the AJ62 alloy are often decorated with the $(Al, Mg)_4Sr$ and $Al_3Mg_{13}Sr$ intermetallics [117]. During the total PEO processing time, the coating is composed of two distinct layers, namely, an outer layer with a significant amount of connected porosity, cracks and other structural defects and a more compact inner layer. The distributions of porosity and other defects were inhomogeneous in both layers but was more evident in the outer layer . However, the relative proportions of the two layers change with PEO processing time. It should also be emphasized again that the PEO processing parameters were chosen to produce a compact and adherent coating.

During plasma discharges, processes including melting, melt-flow and re-solidification continuously occur in the outer layer thus causing a fluctuating repetitive increase and decrease in surface temperature which leads to a porous structure.  The inner layer was dense and adhered well to the substrate and exhibits excellent mechanical properties. A thin and very dense coating/substrate interface layer is clearly shown for coatings with processing times longer than 15 minutes. The oxide coating on the sample treated for 3 min, Fig 7.6(a), was 5 to 8 µm thick and was almost completely composed of a porous outer layer. This is consistent with the surface morphology, Fig. 7.5(a), which showed a high density of open (un-sealed) channels at the center of the 'pancake' structures, which could extend to the coating substrate interface. As the processing time increases, the coating thickness increases. The thickness of the oxide layer was in the range of 70-90 µm and 100-115 µm for the samples treated for 90 and 120 min, respectively.
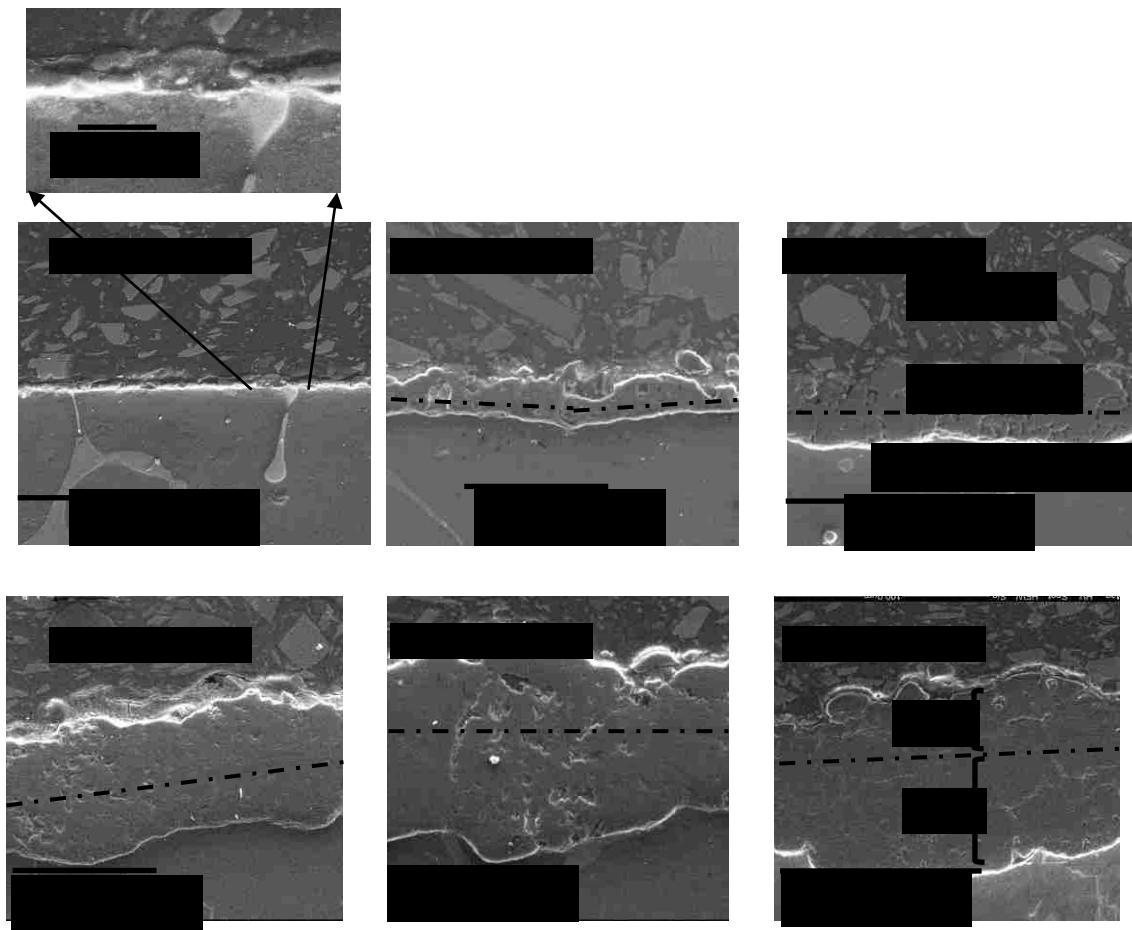
 **Fig. 7.6** SEM micrographs of cross-sections of coatings on AJ62 for different treatment times.

### 7.3.5. PEO coating thickness.

The results shown in Figs.7.7 and 7.8 for the variation of the total coating thickness with treatment time, as well as the results of the outwards growing part (Lo) towards the coating surface and the inward (Li) part towards the original magnesium surface, are in good agreement with the results of [1]. Thus, there is a combination of two growth mechanisms: growth of an outer layer onto the surface of the coated sample away from the surface by microdischarges, ejection of melting Mg which then oxidizes and solidifies, and growth of an inner layer into the substrate by an oxygen diffusion process. The variation of the average total coating thickness, Lt, obtained by two different techniques, SEM cross section and Eddy current, with PEO processing time is shown in

Fig. 7.7. There is good agreement between the two methods and that the total thickness of coatings increases linearly with processing time.

The slope of the $L_T$ vs. time plot, which is determined by the positive current density [19], gives an average growth rate of $0.9 \pm 0.1$ µm/min: a coating with a thickness of $110 \pm 5$ µm is obtained after 120 min coating. The total thickness (Lt) is composed of an outer Lo and an inner Li layer, where Lo is the coating thickness above the original surface of the sample before oxidation and, Li is the coating thickness below the original surface towards the magnesium alloy substrate. The variations of Lo and Li with PEO processing time are shown in Fig. 7.8(a). In the initial stages up to about 45 minutes, the coating growth towards the coating surface, Lo, is larger than that towards the magnesium alloy substrate, Li. After about 50 minutes, the value of Li dramatically increases compared to Lo, indicating that the coating growth rate towards the magnesium alloy substrate is greater than that towards the coating surface.
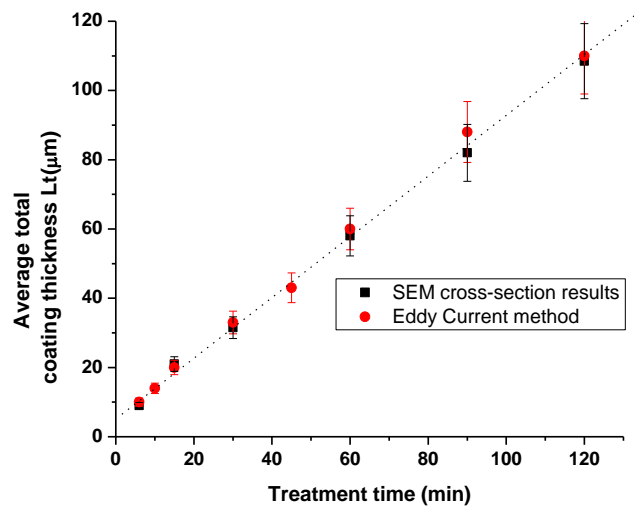


**Fig. 7.7** Average coating thickness variation with PEO processing time.

Fig. 7.8(b) shows the variation with processing time of the ratios, Lo/Lt and Li/Lt. The ratio Lo/Lt gradually decreases from 0.75 and finally reaches 0.4, which indicates that in the initial stages the PEO coating grows mainly outwards. On the other hand, the Li/Lt ratio increases from 0.2 to 0.6 with increasing processing time: this may indicate oxygen diffusion through the coating.
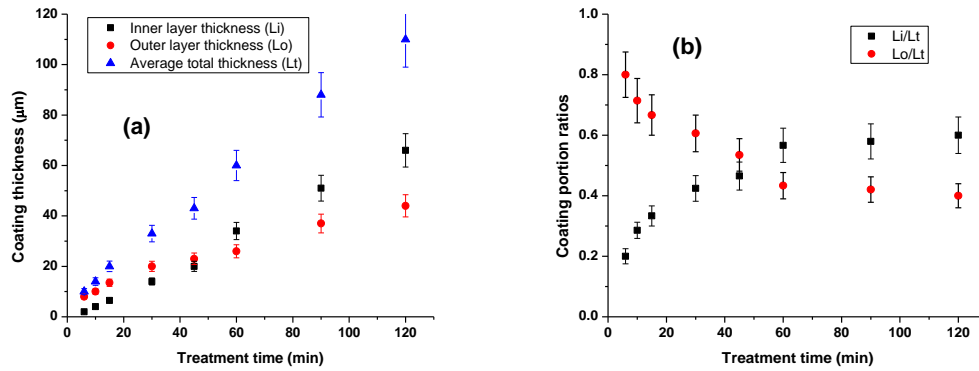
**Fig. 7.8** Inwards and outwards coatings portion during PEO coatings (a), coatings portion ratios to the total thickness (b) vs. treatment time.

## 7.4. Discussion

### 7.4.1. PEO-Coating mechanisms.

Fig. 7.9 is a schematic of a PEO coating process on a magnesium alloy substrate. For PEO an appropriate electrical potential is applied to magnesium to increase the thickness of the thin oxide MgO layer on the surface of the magnesium (Fig. 7.9(a)). This natural outer layer is not dense, because it's Pilling- Bedworth ratio, ~ 0.81<1, indicates that the underlying metal cannot be completely covered. As the surface has been passivated by non-conductive oxide coating, the voltage between the substrate and the electrolyte rapidly rises as the native oxide thickens (Fig 7.9(b)) and within a few minutes the voltage reaches several hundred volts. It increases until it has becomes too high for the dielectric coating and a microscopic plasma discharge breaks the coating and generates a large number of very short-lived, very small plasma discharges (Fig 7.9(c)). These discharges result in localized plasma reactions, with conditions of high temperature and pressure which modify the growing oxide. This breakdown results in the formation of a slightly thicker coating, which will be broken again in the course of the next cycle, under a slightly higher potential difference. Processes including melting, melt-flow, re-solidification; diffusion, sintering and densification of the growing oxide are parts of the PEO coating process.

For the coating growth, there are three simultaneous processes taking place, namely the electrochemical reactions, the plasma chemical reactions [18,20,21] and thermal diffusion. The main electrochemical reactions occur at the coating/electrolyte interface.

124

During the PEO process different types of discharge take place [16]. An important consequence of the occurrence of those discharges is the development of metallurgical processes in the growing oxide layer, which are induced by the heat liberated in discharge channels from electron avalanches. Molten oxide is ejected from the coating/substrate interface into the coating surface where it is rapidly solidified and re-crystallized by the electrolyte, Fig 7.9(d). As a result, decomposition of metal hydroxide to oxide and formation of complex compounds can occur, Fig 7.9(e). The direction and intensity of these processes depend on the density and power of the discharges which are known to be defined by thickness of the oxide layer. Therefore, the thicker the layer, the less frequent, yet more powerful and extended, the discharges become [18].
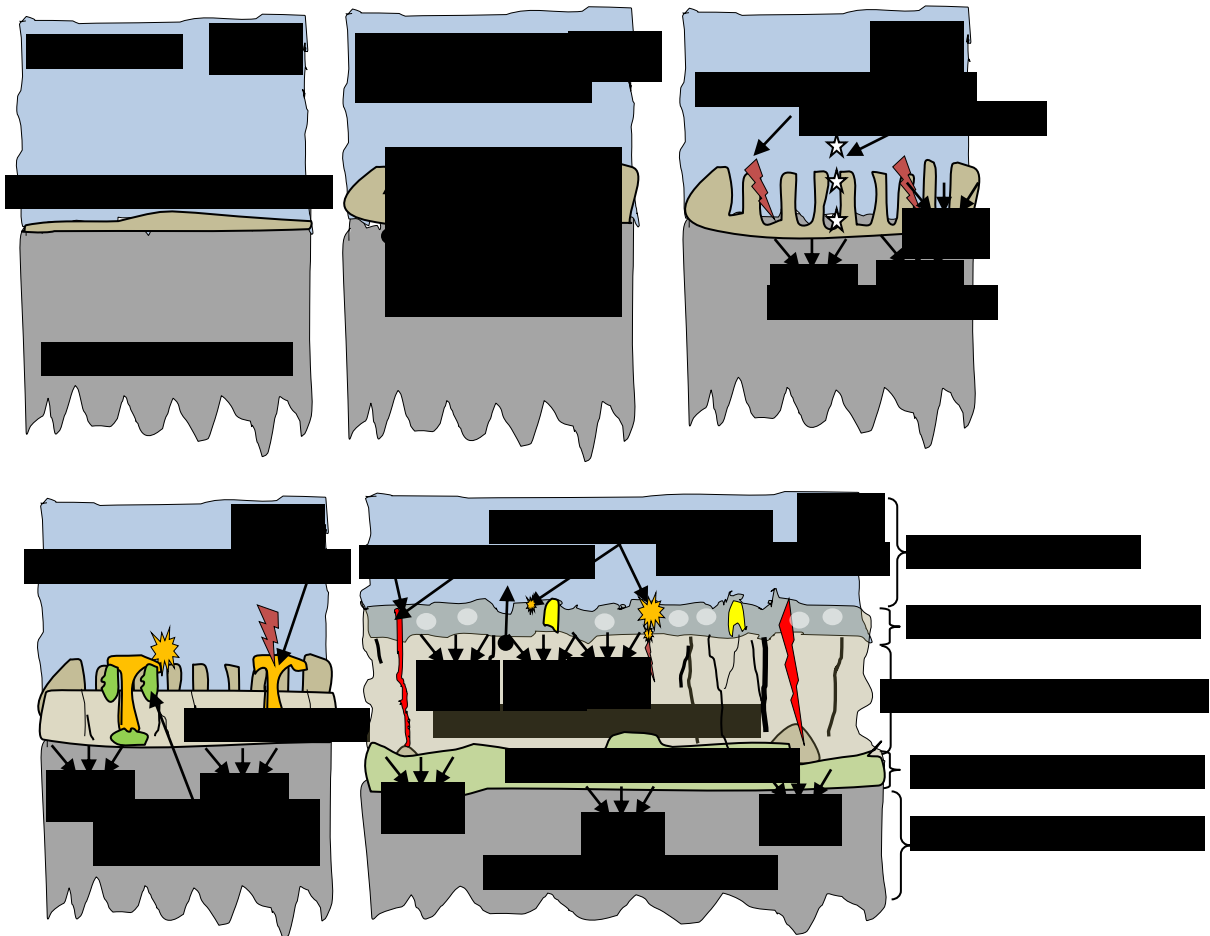


**Fig. 7.9** Schematic of the coating process during PEO treatment.

The PEO coating thickness depends on current mode type and density, electrolyte composition and concentration and treatment time. The PEO coatings of Mg alloys are comprised of amorphous and crystalline phases such as MgO, $Mg_2SiO_4$, $Mg_3(PO_4)_2$ or $Mg_2AlO_4$, depending on the electrolyte [21]. While the temperature of the electrolytes should be kept below 20 $^o$C, normally using a water cooling system, the local plasma temperature in the discharge channels is higher than 4000 K (see Fig. 7.4), which leads to the formation of oxide coatings. For the PEO process on Mg alloys, the main electrochemical reactions occurring at the coating/electrolyte interface using an aluminate-containing electrolyte are given by equations 2.1 - 2.6.

### 7.4.2 Growth mechanisms

The plasma chemistry of the surface discharges is quite complex in nature, involving, on one hand, charge transfer at the substrate/electrolyte interface, and on the other hand, strong ionization and charge transfer effects between the substrate surface and the electrolyte through the oxide layer with the aid of the plasma [22]. Generally, the discharge event tends to occur in the coating–substrate interface or regions near the interface, which are responsible for the thermal and chemical conditions at the metal surface, thus playing an important role in formation, composition, and structure and stress state of phases formed. However, it is worth mentioning that the discharges induce no changes of substrate microstructure or texture. Processes such as melting, melt-flow, re-solidification; sintering and densification of the growing oxide take place during the PEO coating process.

1- **Linearity of the growth rate:** Most PEO studies indicate that the coating thickness increases linearly with coating time [1,19]. However, some research [9,20-21] shows that such linearity could break down at longer treatment times. According to Sundararajan et al.'s proposed growth mechanism [1,23], the growth of oxide layers results only from molten substrate elements which are oxidized when flowing out through the discharge channels that are created due to the oxide layer breakdown . In this way, an oxide is formed which contributes to the layer when being ejected from the channels and rapidly cooled at the surface–electrolyte interface. Discharge channels are continuously formed and move on the coating surface and since they have a finite life, they are formed

and closed continuously through the coating process and contribute to the coating thickness.

2-      **Inward and outwards coating growth:** The variation in geometrical dimensions during PEO processing is an important issue for understanding the coating growth mechanisms [20]. The growth mechanism of the ceramic coating layer is a combination of inwards to the alloy substrate (inner layer) and outwards to the coating surface (outer layer) simultaneously. During the early stages, the coating grows mainly outwards. After the coating reaches a certain thickness the inner layer grows faster than the outer layer. However, at this time, the coating thickness continues to increase in both directions. The inner growth is attributed to the growth of the compact layer at the film/substrate interface by diffusion or transport of oxygen, while the growth of outer layer onto the surface are due the electrochemical and the plasma chemical reactions.

3-      **Growth of compact layer at film/substrate interface by diffusion or transport of oxygen**: At longer processing times, the inward coating growth rate increases. This change may be connected to the increase of thermally-activated diffusion. For PEO process, both thermally-activated diffusion and ions transformation have an important contribution leading the coating growth [23]. Inward oxygen diffusion plays a key role in coating growth, and the growth rate of the PEO process coating is controlled by the rate of transferring oxygen towards the magnesium substrate as shown in the schematic diagram of Fig. 7.9(b-e).

4-      **Growth rate dependence on the process parameters:** The rates of growth of the outer and inner oxide layers are process parameter dependent. They result from a combination of three processes namely, (i) discharge processes causing the substrate to melt and oxidize when flowing out through the discharge channels and being rapidly cooled at the surface–electrolyte interface, (ii) partial destruction of the outer layer due to strong discharges and (iii) diffusion of oxygen process from the electrolyte towards the substrate through the coating.

Fig. 7.10 is a schematic diagram of the coating development during PEO. The dashed line between Lo and Li in Fig. 7.10 represents the position of the original surface of magnesium alloy before PEO treatment.
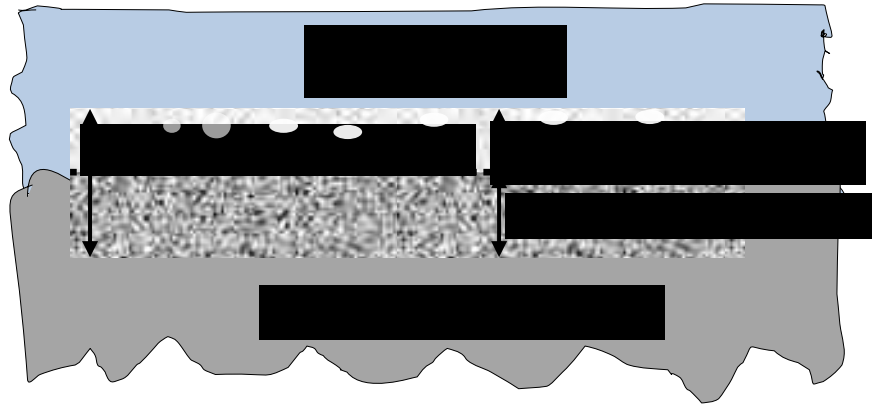
**Fig. 7.10** Schematic diagram of dimension changes of magnesium alloy before and after PEO treatment

It can be seen in Fig. 7.7 that the total thickness of coatings (Lt) increases linearly with increasing oxidation time which is the common observation in PEO treatments.

In this work for processing times higher than 45 min, the inward coating growth rate increases. This change may be connected to the increase of thermally-activated diffusion. As shown in the schematic diagram of Fig. 7.9(b) and during PEO of magnesium, the metal cations that transfer away from the metal substrate react with anions to form a ceramic coating. On the other hand, oxygen anions transfer into magnesium substrate due to the high electric field of $10^6$ V/cm [24] in the discharge channels and react with $Mg^{2+}$ cations to form a ceramic coating. Fig 7.3 shows the intensity distribution of oxygen ion (777.2 nm) as a function of treatment time. The amount of oxygen that is excited due to the high plasma temperature increases significantly after 45 minutes processing time. The high oxygen signal spikes shown in Fig. 7.3(c) are due to B-type plasma discharges which may enhance the delivery of oxygen into the internal layer of the coating through the discharge channels. Therefore, inward oxygen diffusion plays a key role in coating growth, and the growth rate of the PEO process coating is controlled by the rate of transferring oxygen towards the magnesium substrate as shown in the schematic diagram of Fig. 7.9(b-e).

According to Fick's first law of diffusion, the rate at which atoms or ions diffuse in a material directly depends on the diffusivity or diffusion coefficient D. The kinetics of diffusion is strongly temperature dependent, where D ($cm^2$/s) is related to temperature by equation (3.2) [25]:

$$D = D_0 \exp(\frac{-Q}{RT})$$

<div align="right">**7.1**</div>

where $D_o$ (cm$^2$/s) is a constant for a given system (0.000043 cm$^2$/s for O diffusion in MgO [25]), T (K) is the temperature, R is the gas constant (1.987 cal / mole·K), and Q (cal/mol) is the activation energy for a given system (82100 cal/mol for O diffusion in MgO [25]). By using the average time variation of the plasma temperature results shown as a red line in Fig. 7.4, together with equation (7.1), the temporal variation of the diffusivity was calculated and is presented in Fig. 7.11. As the temperature of the plasma process increase, the diffusion coefficient D increases and, therefore the flux of oxygen towards the substrate increases as well. The instantaneous high temperature and high pressure in the discharge zone greatly enhance inter diffusion between the oxygen anions and magnesium cations in the coating near the discharge zones. At higher plasma temperatures, the thermal energy supplied to the diffusing ions ($O^{2-}$) allows the ions to overcome the activation energy barrier and more easily move and interact with the magnesium cations $Mg^{2+}$ produced during the discharges to form MgO.  Hence, the inner oxide layer (Li) is the major contributor to the total coating thickness Lt. At the very early stage of the process, the number of very small discharges are extremely large and each of them contributes to the overall plasma temperature. Hence, Te is high and then decreases due to the changes in the number of small discharges. However, as shown in Fig. 7.3, the concentration of oxygen is relatively low, and hence the diffusion effect during the first 45 minutes of processing time is lower than that after 45 min where the plasma temperature and oxygen concentration start to increase. This appears to explain the variation of the Lo and Li with time. On the other hand, the diffusion processes are controlled by the increase in thickness of ceramic coating, which may slow down the growth rate of the coating.

In PEO process, the formation of the new coating and the dissolution of the previously formed coating occur simultaneously [21]. In the present study, a strong alkaline electrolyte was employed (ph=13) and the ceramic coating is mainly composed of $MgAl_2O_4$ and the MgO phases [26], which do not readily dissolve in a strong alkaline electrolyte [27]. Therefore the process of dissolution of outer oxide layer in the electrolyte is significantly reduced, while the magnesium substrate is oxidized. The three

types of discharges (A,B and C) contribute to the oxide layer growth as described earlier, but strong B discharges may destroy some of the formed layer. This may explain the reduction in outer oxide layer thickness after 45 min, which is where the strong discharges start to appear as shown in Fig. 7.2. Therefore, change in thickness of the oxide layer results from a competition between three processes, namely oxide growth due to plasma discharging processes, partial destruction of oxide and diffusion of oxygen into substrate.
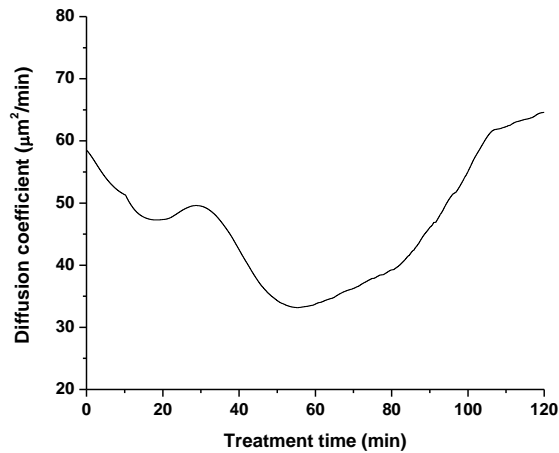


**Fig. 7.11** Diffusion coefficient (D) of O in MgO as a function of treatment time, during PEO processing of AJ62 Mg alloy.

## 7.5 Conclusions.

- In PEO process, the ceramic coating grows inwards to the alloy substrate (inner layer) and outwards to the coating surface (outer layer) simultaneously. During the early stages, the coating grows mainly outwards. After the coating reaches a certain thickness the inner layer grows faster than the outer layer. However, at this time, the coating thickness continues to increase in both directions.

- The rates of growth of the outer and inner oxide layers are process parameter dependent. They result from a combination of three processes namely, (i) discharge processes causing the substrate to melt and oxidize when flowing out through the

discharge channels and rapidly cooled at the surface–electrolyte interface, (ii) partial destruction of the outer layer due to strong discharges and (iii) diffusion process.

- Oxygen diffusion into the Mg-alloy substrate plays a leading role in coating growth. The growth rate of the coating is influenced by the plasma temperature, which enhances the rate of oxygen transfer into the magnesium substrate.

**References**

[1]   Sundararajan G, Krishna LR. Mechanisms underlying the formation of thick alumina coatings through the MAO coating technology. Surface & Coatings Technology, 167 (2003) 269-277.

[2]   Qiu Z, Wang R, Zhang Y, Qu Y, Wu X. Study of Coating Growth Behavior During the Plasma Electrolytic Oxidation of Magnesium Alloy ZK60, Journal of Materials Engineering and Performance, 24 (2015) 1483–1491.

[3]   Yerokhin L, Snizhko LO, Gurevina NL, Leyland A, Pilkington A, Matthews A. Discharge characterization in plasma electrolytic oxidation of aluminium. Journal of Physics. D, Applied Physics, 36 (2003) 2110-2120.

[4]   Albella J M, Montero I and Martinez-Duart J M, Parkhutik V, Dielectric breakdown processes in anodic Ta2O5 and related oxides. J. Materials Science, 26 (1991) 3422-3432.

[5]   Epelfeld A V, Lyudin V B, Dunkin O N and Nevskaya O S. Bulletin of the Russian Academy of Sciences Physics,  64 (2000), 610

[6]   Ikonopisov S, Girginov A and Machkova A, Theory of electrical breakdown during formation of barrier anodic films. Electrochemical Acta, 22(10) (1977) 1077–1082.

[7]   Hickling A and Ingram M D, Contact glow-discharge electrolysis. Transactions of the Faraday Society, 60 (496, part 4) (1964) 783-793.

[8]   Hussein RO, Nie X, Northwood DO, Yerokhin A, Matthews A, Spectroscopic study of electrolytic plasma and discharging behaviour during the plasma electrolytic oxidation (PEO) process. Journal of Physics D: Applied Physics, 43 (2010) 105203.

[9]   Dunleavy CS, Golosnoy I O, Curran J A and Clyne T W, Characterisation of discharge events during plasma electrolytic oxidation. Surface & Coatings Technology,  203(22) (2009) 3410-3419.

[10]   Hussein RO, Nie X and Northwood DO, Influence of process parameters on electrolytic plasma discharging behavior and  aluminum oxide coating microstructure. Surface & Coatings Technology, 205 (2010) 1659-1667.

[11]   Kunst M, Fischersworring-Bunk A, L'Esperance G, Plamondon P and Glatzel U, Microstructure and dislocation analysis after creep deformation of die-cast Mg–Al–Sr (AJ) alloy. Material Science and Engineering A, 510-511 (2009) 387-392.

[12]   Pekgulayuz M and Celikin M, Creep resistance in magnesium alloys. International Materials Reviews, 55 (4) (2010) 197-217.

[13]   L'Esperance G, Plamondon P, Kunst M and Fischersworring-Bunk A, Characterization of intermetallics in Mg-Al-Sr AJ62 alloys. Intermetallics, 18 (2010) 1-7.

[14]   Fischersworring-Bunk A, Kunst M and Dietsche A, High temperature fatigue and creep-automotive power train application perspectives. Materials Science and Technology, 32(12) (2007) 1389-1395.

[15]   Sansonetti JE and Martin WC, Handbook of Basic Atomic Spectroscopic Data. Journal of Physical and Chemical Reference Data, 34 [4] (2005) 1559-2260.

[16]   Hussein RO, Nie X, Northwood DO, Yerokhin A, Matthews A (2010), Spectroscopic study of electrolytic plasma and discharging behaviour during the plasma electrolytic oxidation (PEO) process. Journal of Physics D: Applied Physics, 43, 105203.

[17]   Hussein RO, Zhang P, Xia Y, Nie X, Northwood DO. The effect of current mode and discharge type on the corrosion resistance of plasma electrolytic oxidation (PEO) coated magnesium alloy AJ62. Surface & Coatings Technology, 206 (2011)1990-1997.

[18]   Snizhko LO, Yerokhin AL, Pilkington A, Gurevina NL, Misnyankin DO, Leyland A, Matthews A, Anodic processes in plasma electrolytic oxidation of aluminium in alkaline solutions. Electrochimica Acta, 49[13] (2004) 2085-2095.

[19]   Mécuson F, Czerwiec T, Belmonte T, Dujardin L, Viola A, Henrion G. Diagnostics of an electrolytic microarc process for aluminum alloy oxidation. Surface & Coatings Technology, 200 (2005) 804-808.

[20]   Xue W, Deng Z, Chen R, Zhang T. Growth Regularity of Ceramic Coatings Formed by Microarc Oxidation on Al-Cu-Mg alloy. Thin Solid Films, 372 (2000) 114-117.

[21]   Chang L. Growth regularity of ceramic coating on magnesium alloy by plasma electrolytic oxidation. Journal of Alloys and Compounds. 468 (2009) 462–465.

[22]   Rakoch AG, Khokhlov VV, Bautin VA, Lebedeva NA, Magurova YV, Bardin IV, Model concepts on the mechanism of microarc oxidation of metal materials and the control over this process. Protection of Metals and Physical Chemistry of Surfaces, 42 (2006) 158-169.

[23]   Krishna LR, Somaraju KRC, Sundararajan G, The tribological performance of ultra-hard ceramic composite coatings obtained through microarc oxidation. Surface & Coatings Technology, 163 –164 (2003) 484–490.

[24]   Yerokhin AL, Nie X, Leyland A, Matthews A, Dowey S J. Plasma electrolysis for surface engineering. Surface & Coatings Technology, 122 (1999) 73-93.

[25]   Askeland D. R. and Fulay P. P., Essentials of Materials Science & Engineering, Toronto, Canada, Cengage Learning, Second edition 2009

[26]   Zhang P, Nie X and Northwood DO, Influence of coating thickness on the galvanic corrosion properties of Mg oxide in an engine coolant. Surface & Coatings Technology, 203 (2009) 3271-3277.

[27]   Guo HF, An MZ, Huo HB, Xu S, Wu LJ. Microstructure characteristic of ceramic coatings fabricated on magnesium alloys by micro-arc oxidation in alkaline silicate solutions. Applied Surface Science, 252 (2006) 7911-7916.

# CHAPTER 8

# THE EFFECT OF PROCESSING PARAMETERS AND SUBSTRATE COMPOSITION ON THE CORROSION RESISTANCE OF PLASMA ELECTROLYTIC OXIDATION (PEO) COATED MAGNESIUM ALLOYS.

**Published in:**

## 8.1 Introduction

When magnesium is exposed to an aqueous solution, both $Mg(OH)_2$ and $MgO$ can be formed: $Mg(OH)_2$ is in contact with the metal, and on top of the hydroxide layer is a $MgO$ layer that has direct contact to the aqueous solution [1]. For pure Mg, this layer is not protective at pH values below 10.5, unless additional alloying elements are added to pure Mg. Due to a multi-phase microstructure, the corrosion mechanism for the Mg alloys is more complex than that for pure magnesium. Generally the two important factors that influence the corrosion performance of a multi-phase magnesium alloy are hydrogen evolution and the stability of the corrosion film [2]. The corrosion performance of magnesium alloys largely depends on the alloying elements and impurity elements. Song et al. [3] described the interface of several Mg-Al-Zn alloys after exposure at the corrosion potential. For the AZ91-alloy there are three layers in the oxide film: enriched $Al_2O_3$, $MgO$ and $Mg(OH)_2$. Marker et al. performed a test with fourteen elements alloyed with pure magnesium, and measured the corrosion rate with immersion tests in 3% sodium chloride solution [4]. They concluded that elements such as Fe, Ni, Cu and Co have the greatest effect in accelerating the corrosion rate even at a very low concentration. Ag, Ca and Zn have smaller effect in the accelerating corrosion rate, while Al, Sn, Cd, Mn, Si and Na have little or no effect at concentrations below 5%. The

most common alloying element used in magnesium is aluminum [5]. Since Mg is a soft metal, aluminum can improve its strength. The major secondary phase, which can greatly increase the corrosion resistance in this system, is $MgAl_{12}$. Zn is another important alloying element that is usually added along with aluminum with the maximum amount of 1.5-2%. Manganese has no direct effect to improve or reduce the corrosion resistance of Mg alloys; however, it can reduce the detrimental effects of impurities when their concentration exceeds the tolerance limits [6]. Atrens and Song summarized the mechanism of galvanic corrosion in magnesium. If the alloy contains elements such as Fe, Cu or Ni, galvanic corrosion becomes a significant factor for overall corrosion. If the alloy contains alloying elements such as Al, Mn, Zn, or Cd, the galvanic corrosion is less harmful.

Electrochemical impedance spectroscopy (EIS) can provide valuable information about surface treatment layers on PEO-coated magnesium, and the interfaces between electrolyte/coating/substrate [8,9]. It also allows the kinetics of heterogeneous electron-transfer reactions, coupled chemical reactions, or adsorption processes to be studied [10], and can provide information about pitting and crevice corrosion [11]. In this study the effect of substrate composition on the electrochemical properties of PEO coatings on Mg and Mg alloys (AM60B, AJ62, and AZ91D) was investigated. The coatings morphologies were also investigated to assess the relationship to their intrinsic alloy corrosion rate.

## 8.2. Experimental Procedures

Disc-shaped coupons ($25\times7$mm) cut from Mg and Mg alloys (AM60B, AJ62, and AZ91D) (Table 8.1) bars were used as the test samples in this study. The coupons were ground and polished with up to 600 grit SiC abrasive papers. The coating was obtained in an alkaline electrolyte containing sodium aluminate ($10$g/l $Na_2Al_2O_4$) and potassium hydroxide (~1 g/l KOH) added to balance the pH at 12. The electrodes are connected to two pulsed DC power supplies operating under a constant current control function to generate a bipolar current mode. Process parameters, are listed in Table 8.2. All samples were processed using the same current density ($50$ mA/cm$^2$). Scanning electron microscopy in the back secondary electron (SE) mode was used to observe both the

coating surface morphology and, through observation of sample cross sections, coating thickness and integrity. The coating thicknesses of coated pure Mg and Mg alloy for different treatment times were determined using a PosiTector 6000 coating thickness meter with N type probes: this instrument uses the eddy current principle to measure the thickness of non-conductive coating (ceramic) on non-ferrous metal (magnesium).

Table 8.1 Nominal composition of alloying elements in Mg alloys.

| Mg Alloys | Composition (wt.%) | | | | | |
|---|---|---|---|---|---|---|
| | Al | Mn min. | Zn | Si | Sr | Mg |
| AM60B | 5.5 to 6.5% | 0.25% | 0.22% | 0.10% | N/A | balance |
| AJ62 | 6.1% | 0.34% | N/A | N/A | 2.1% | balance |
| AZ91D | 8.3-9.7% | 0.15% | 0.35-1.0% | 0.10% | N/A | balance |

Table 8.2.  PEO Process parameters for coating  AJ62 Mg alloy.

| Sample | Current mode | Time (min) | $I^+$ (A) | $I^-$ (A) | $T_{on}^+$ ($\mu s$) | $T_{on}^-$ ($\mu s$) | $T_{off}^+$ ($\mu s$) | $T_{off}^-$ ($\mu s$) | $C_R$ |
|---|---|---|---|---|---|---|---|---|---|
| All | Bipolar | 0-30 | 0.7 | 0.6 | 400 | 100 | 400 | 100 | 0.77 |

To determine the corrosion resistance of the PEO coating, electrochemical impedance spectroscopy (EIS) were performed for uncoated and coated samples at $25\pm2$ $^o$C using a Solartron 1285 Potentiostat with Corrware software, through a frequency response analyzer. Measurements were performed three times to ensure reproducibility of the results. Electrochemical impedance spectroscopy (EIS) measurements were performed at the open circuit corrosion potential on the PEO coatings after 30 minute of initial delay to stabilize the open-circuit potential (OCP)

## 8.3 Results and discussion
### 8.3.1. PEO coating thickness.
The variations of the average total coating thickness (at different positions) for pure Mg and AJ62,AM60B and AZ91D Mg alloys with PEO treatment time are shown in Fig.

8.1(a), which shows that the coating thickness increases linearly with coating time which is in good agreement with most of the PEO experiments [12]. The slope of the linear variation of the layer thickness as a function of the treatment time which is determined, for bipolar current mode, by the positive current density [13] gives an average growth rate of 0.9 ± 0.05 µm/min. However AZ91D Mg alloy shows relatively higher coating thickness compared with other samples.

To cross check the coating thickness results, the variation of the average total coating thickness of AJ62 Mg alloy with the treatment time from two different techniques, SEM cross section results and from Eddy current method are presented in Fig. 8.1(b). It shows good agreement between the two methods and that the total thickness of coatings gradually increases with oxidation time.
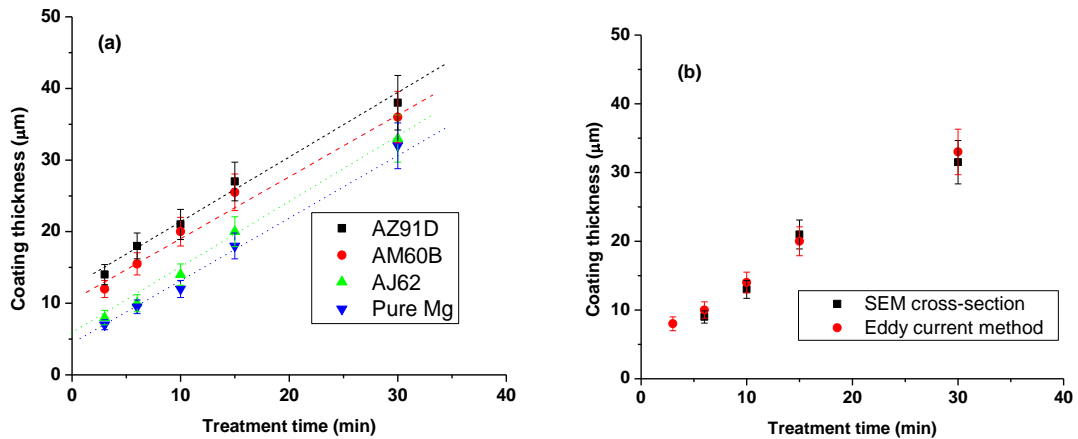


Fig. 8.1(a) Average coating thickness variation with PEO processing time for different Mg alloys and (b) a comparison of the coating thickness from two different methods

### 8.3.2 Microstructure of the coatings.

Fig. 8.2 presents the SEM micrographs of the surface morphologies of coatings produced for different processing times using different alloys. The average porosities (which represent the percentage of the surface areas of porous relative to the total image area) measured by Image software are also given in Fig. 8.2.The averaged porosities of each sample, was determined from SEM images for a typical surface area of $620 \times 675$ µm$^2$. The coatings has a large number of micropores mainly due to oxygen gas trapping and evolution and/or electrolyte vapors. Zhou et al [14] point out that the main reason for

high porosity of PEO coatings on magnesium alloys is the low Pilling–Bedworth ratio of magnesium.

The back scattered electron micrographs in Fig. 8.2 show a large number of 'pancake'-like features and discharge pores which irregularly arranged on the coating surface: This is a common characteristic of PEO coatings. The relatively large holes in the center of the pancake suggest that they were produced by strong discharges and such holes might penetrate deep in to the coating. Some micro-cracks were present on the coating surface, which could have resulted from thermal stresses generated during the rapid solidification of the molten oxide product in the strong discharge channel [15]. The stronger the discharge, the larger is the molten mass produced by a single discharge. The micro-pores are due to gas bubbles ejected from surface discharges and are referred to as A- and C-type discharges in ref [16].

It can readily be observed that the morphology of each coating is, to some extent, different from coating to coating and all the coatings exhibit different levels of porosity. The pores varied in size from very small diameter (<1 μm) through medium size (few μm) to large pores (>10 μm). Pore sizes can be linked with the discharge type described in detail by Hussein et al [16]. For 3 and 6 minutes treatment times, alloy AM60B with average porosities of 11.5%, and 7.6% respectively, exhibited a large number of pores with diameters <1 μm to >10 μm. Alloys AJ62 also contained large pore sizes. For pure Mg, the average porosities are around 6% for all treatment times. While the porosity levels generally decreases with treatment time for Mg alloys, alloy AJ62 shows high average porosity values with some large pores (~ 10 μm) for the 30 minutes case. AM60B and AZ91D alloys showed a lower porosity (2- 4. %) for treatment times of 10 minutes and longer than AJ62 and pure Mg. AJ62 is one of the typical alloys comprised of two or more phases, which are deadly seen in the SEM micrographs of Fig. 8.2 for treatment time of 3 min. The microstructure of this alloy consists of α-Mg matrix and interdendritic compounds distributed at grain boundaries (the grey white region) which are the phase Al4Sr [17].
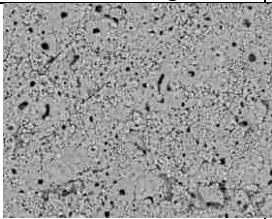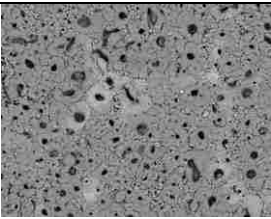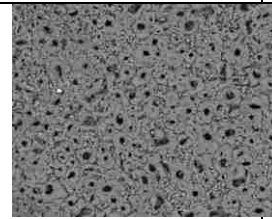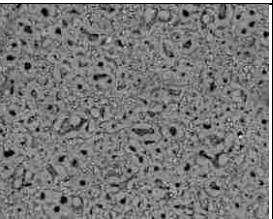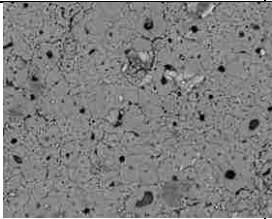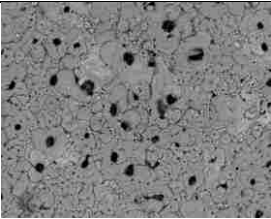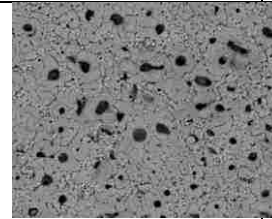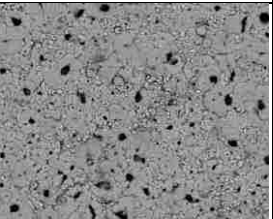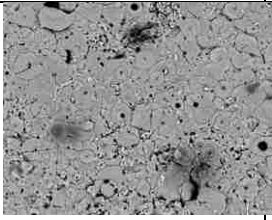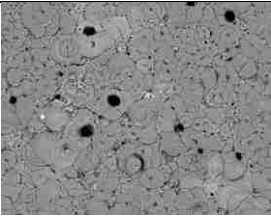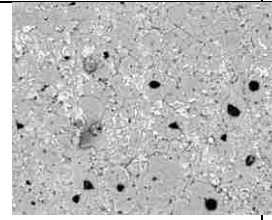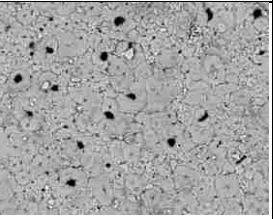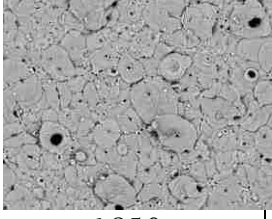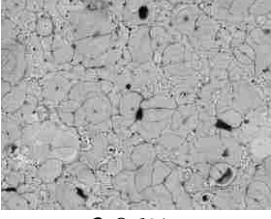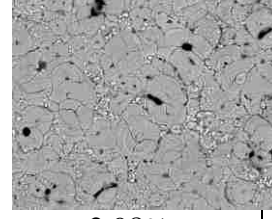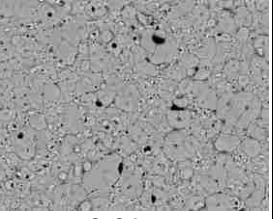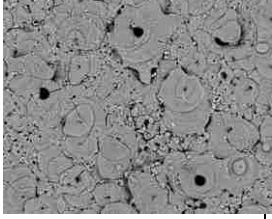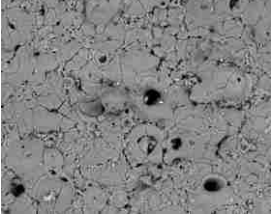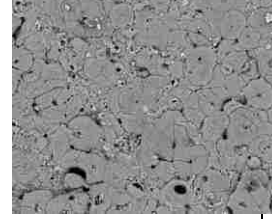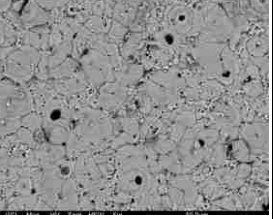
| | Pure Mg | AJ62 | AM60B | AZ91D |
|---|---|---|---|---|
| 3 min | 6.11% | 7.85% | 11.53% | 10.39% |
| 6 min | 5.87% | 5.55% | 7.63% | 5.67% |
| 10 min | 6.22% | 4.39% | 4.04% | 3.02% |
| 15 min | 6.85& | 3.96% | 2.98% | 2.29% |
| 30 min | 6.81% | 5.54% | 2.14% | 3.59% |

Fig. 8.2 SEM micrographs showing the surface morphology of PEO coated Mg and Mg alloys at different treatment times showing the data of pore analysis (Percentage area of porosity,%).

### 8.3.3 Electrochemical Impedance Spectroscopy (EIS) Measurements

In order to obtain a physical picture of the corrosion processes of the coatings at the electrode/electrolyte interface, the processes occurring due to the changes of the electrode surface and in the coatings layer, experimental EIS data were modeled using nonlinear

least-squares fit analysis software and the electrical equivalent circuits representing the various elements of the coatings.The Nyquist and the Bode (frequency dependencies of impedance modulus |Z| and phase angle theta) diagrams from the EIS analysis of experimental and fitted curves of different Mg alloys treated by PEO at five different coating treatment times are given in Figs. 8.3-8.6. Taking both the physical structure of the PEO coatings and their impedance responses into account, and based on previous studies [8,18], equivalent circuits employed for curve fitting of the untreated, PEO-treated pure Mg and PEO-treated AJ62, AM60B and AZ91D Mg alloys were developed and are illustrated in Fig. 8.7 a, b and c, respectively. Different combinations of elements in different sequences were tried. The results shown in Fig. 8.8 for the uncoated and in Figs. 8.3-8.6 for PEO-coated Mg and Mg alloys show different EIS behavior, and the difference was present for all of the frequency range of the EIS plots. It is evident from these plots that these different materials have different corrosion behaviour which is summarized in sections 8.3.3.1 and 8.3.3.2.
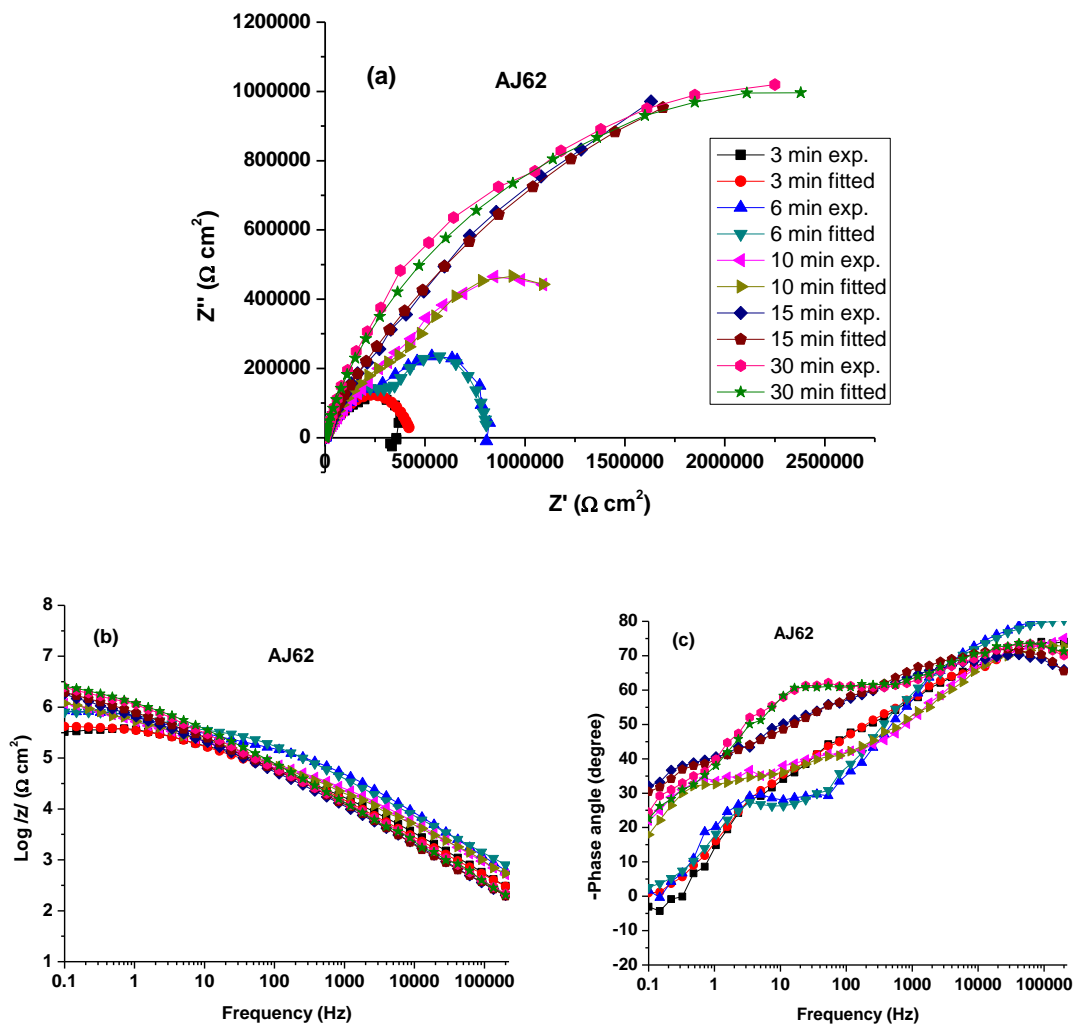
Fig. 8.3 EIS plots of coated AJ62 Mg alloy at different treatment time ((a) Nyquist, (b) Impedance and (c) angles plots) (equivalent circuit is shown in Fig8.7(a))
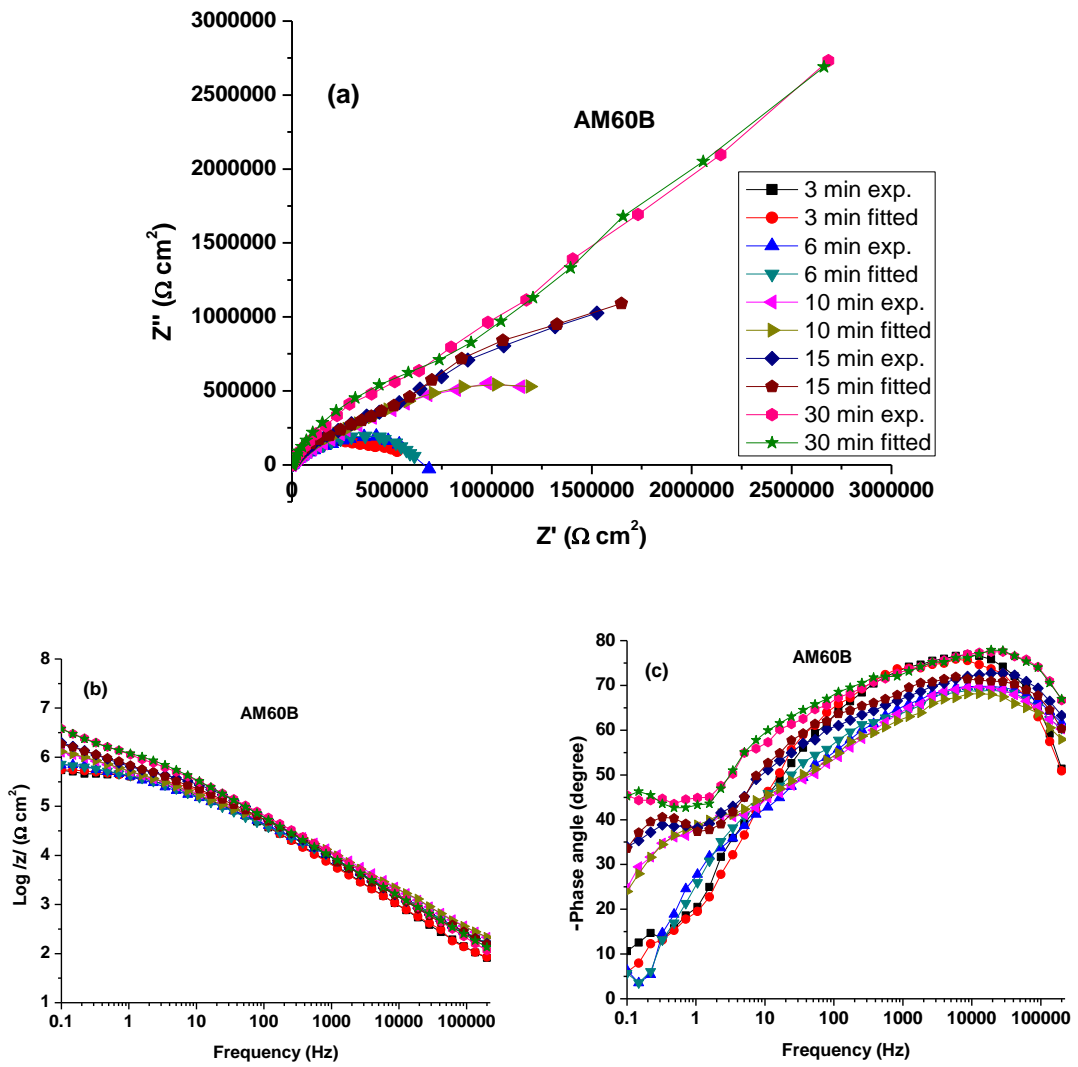
Fig. 8.4 EIS plots of coated AM60B Mg alloy at different treatment time ((a) Nyquist, (b) Impedance and (c) angles plots) (equivalent circuit is shown in Fig8.7(a))
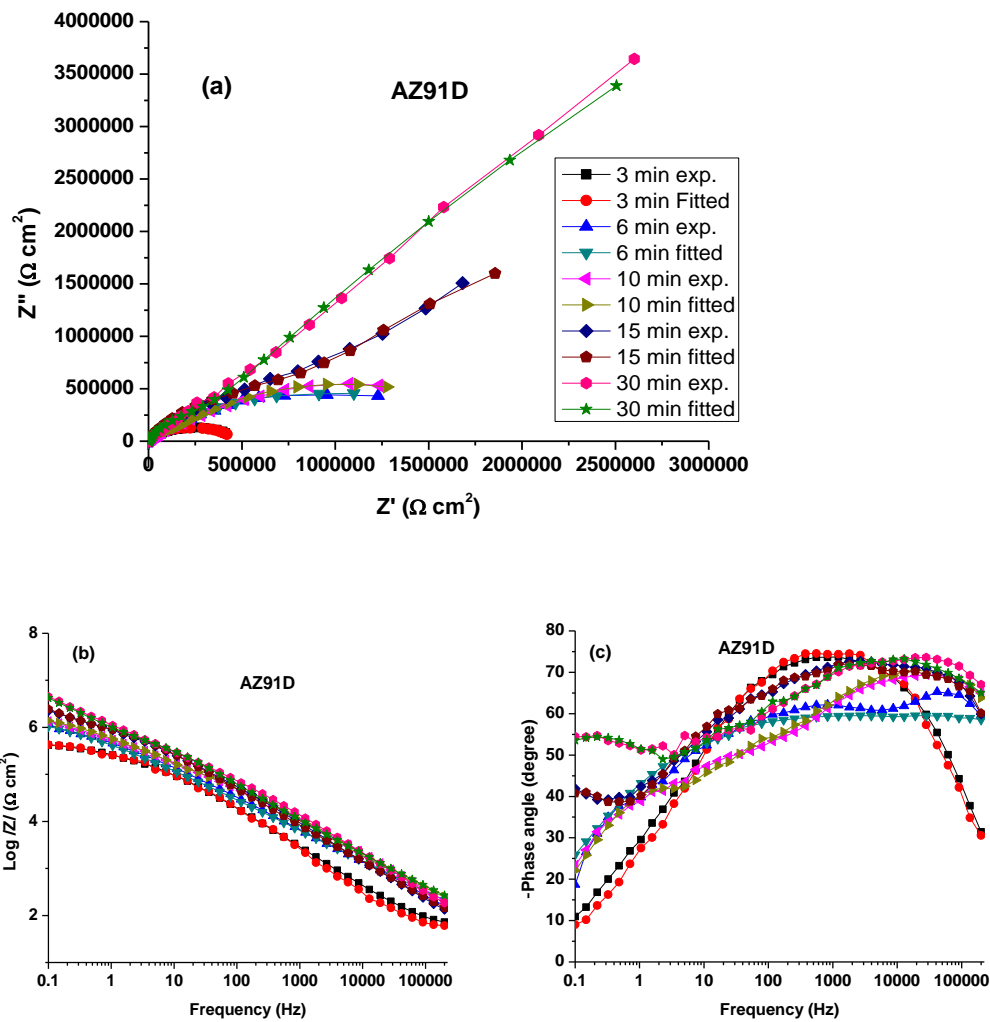
Fig. 8.5 EIS plots of coated AZ91D Mg alloy at different treatment time ((a) Nyquist, (b) Impedance and (c) angles plots) (equivalent circuit is shown in Fig8.7(a))
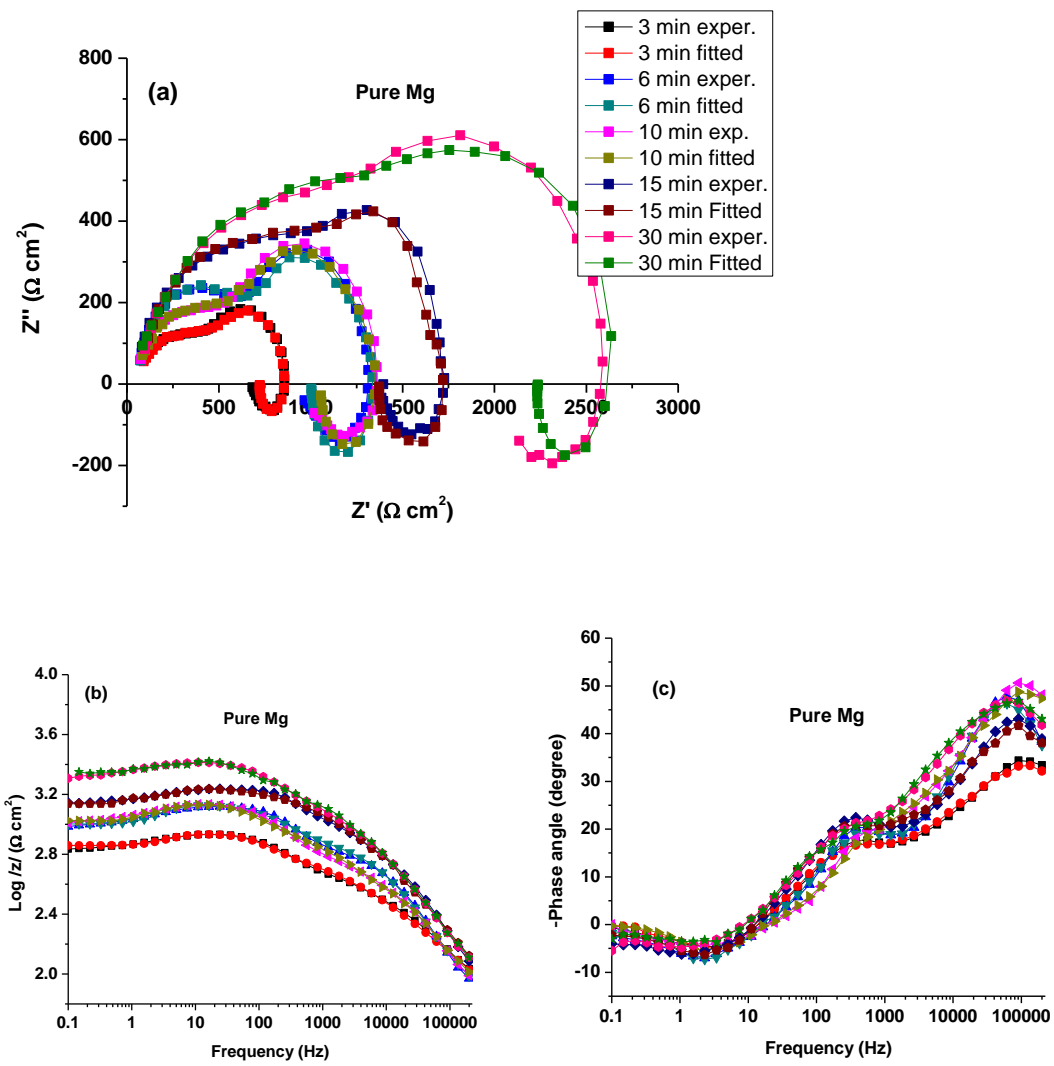
Fig. 8.6 EIS plots of coated Pure Mg alloy at different treatment time ((a) Nyquist, (b) Impedance and (c) angles plots) (equivalent circuit is shown in Fig8.7(b))
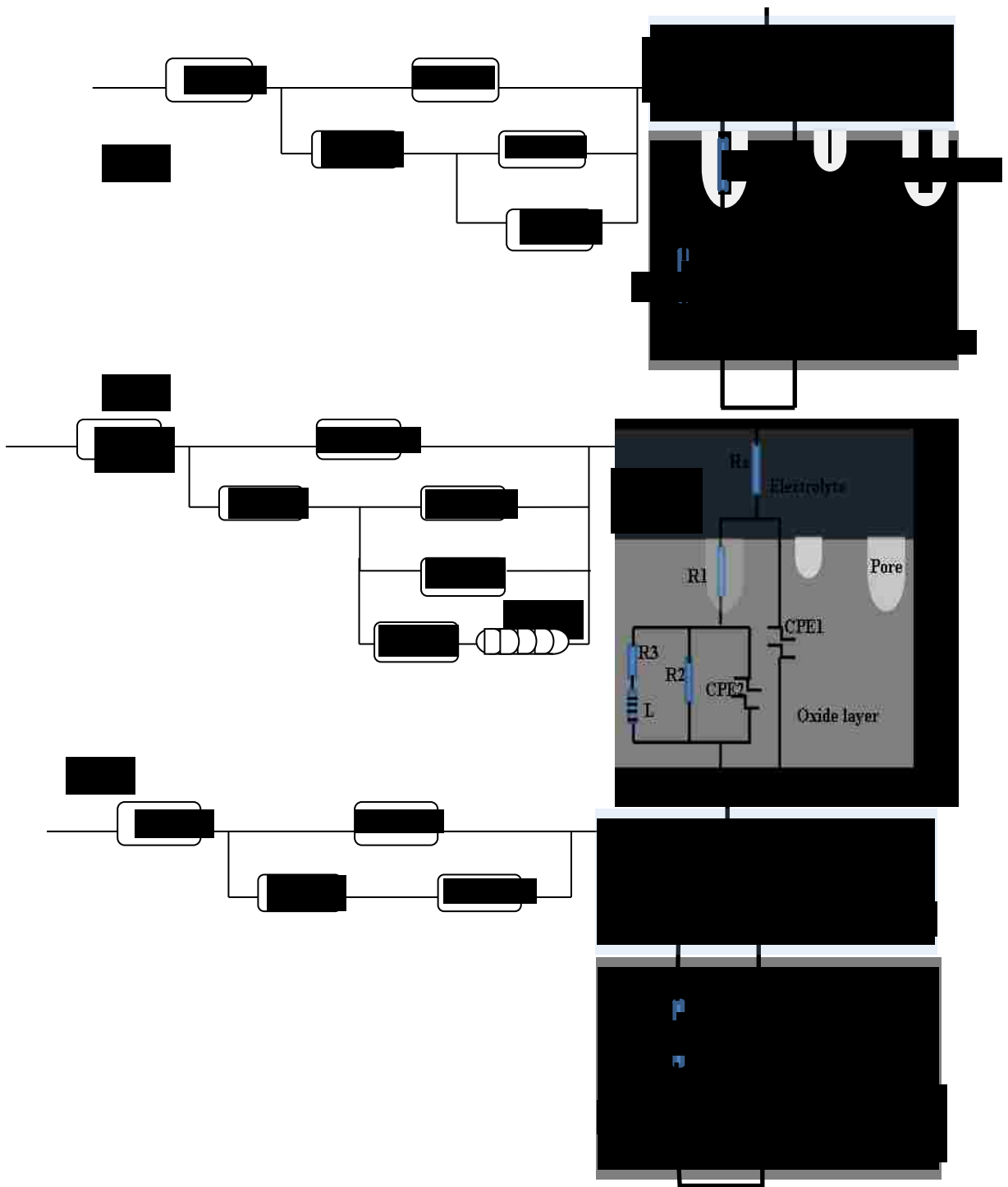
Fig. 8.7 The equivalent circuit models for (a) coated Mg alloy, (b) coated pure Mg and (c) uncoated Mg alloys.

### 8.3.3.1 PEO coated samples

The PEO coatings studied in this work were obtained using regimes that are different not only in terms of Mg alloys used, but also in coating treatment time. Hence, with increasing coating treatment time, the corrosion protection performance of PEO coatings is directly dependent on their thickness, uniformity and amount of porosity and other defects as indicated by the significant decrease in average porosity values with coating treatment time (Fig. 8.2). In order to get a quantitative measure of the alloying elements effect, the EIS spectrum of the coated Mg alloy was modeled using the same equivalent circuit presented in Fig. 8.7(a). Again, an agreement between the experimental and modeled data is excellent, thus justifying the use of the proposed equivalent circuit.

### 8.3.3.1.1 PEO coated AJ62

Fig. 8.3 shows the Nyquist and Bode plots of experimental and fitting curves of the coated AJ62 Mg alloy as a function of coating time. The model chosen for the fitting of the PEO-treated Mg alloy was a commonly used model for PEO [19,20]. It is recognized that any electrode process is complex and usually consist of a many different sub-processes. The sub-processes include both mass transfer and charge transfer and can be in series or parallel with each other [8]. The proposed equivalent circuit used describes the behavior of a process characterized by two time constants, namely the high-frequency (HF) time constant (CPE1−R1) and low-frequency (LF) time constant (CPE2−R2), where the low frequency data are on the right side of the Nyquist plot and higher frequencies are on the left. In all of the applied equivalent circuits in this work, $R_S$ represent the resistance of the solution between reference and working electrodes. $R_S$ has nothing to do with the electrode process and its value depends mainly on the geometry of employed cell and the conductivity of the test solution. $R_1$ is the coating resistance which is parallel with a constant phase element *CPE1* (*CPE_1* in the model of Ryu et al [21]). *CPE2* is the constant phase element for the double layer capacitance of the interface electrical double layer at, or near, the coating/substrate interface. $R_2$ represent the polarization resistance which is the Faradic charge transfer resistance related to electrochemical reactions in the same coating/substrate interface region [19]. Therefore, the high frequency (HF) range of impedance diagrams can be associated with the properties of the coating/electrolyte

interface, while the low frequency (LF) range characterizes the mass-transport processes through the formed dense substrate/coating interface layer or an (activation-controlled step.

A good fit was observed between the experimental data and the simulated values (Fig. 8.3 (a,b and c)). The values of the circuit elements calculated from the fitting for the spectrum recorded on the coated AJ62 Mg alloys surfaces are summarized in Tables 8.3. The fitting quality was evaluated by the chi-squared ($x^2$) values [22], which were in the range of $1\times10^{-3}$–$1\times10^{-4}$ indicating good agreement between the experimental and equivalent circuit data.

Table 8.3. Fitting results of EIS diagrams of PEO treated AJ62 Mg alloy using different coating times. Equivalent circuit is Rs+CPE1/(R1+CPE2/R2)

| sample | R1 ($\Omega\cdot cm^2$) | CPE1-Q ($\mu F/cm^2\ s^{1-n}$) | CPE1-n | R2 ($M\Omega\cdot cm^2$) | CPE2-Q ($\mu F/cm^2\ s^{1-n}$) | CPE2-n | R3 ($M\Omega\cdot cm^2$) |
|---|---|---|---|---|---|---|---|
| 3 min | 20.48 | 0.452 | 0.610 | 0.261 | 0.980 | 0.208 | 0.256 |
| 6 min | 20.22 | 0.387 | 0.566 | 0.472 | 0.905 | 0.852 | 0.512 |
| 10 min | 20.05 | 0.254 | 0.620 | 0.800 | 0.622 | 0.971 | 0.810 |
| 15 min | 20.59 | 0.252 | 0.679 | 1.025 | 0.547 | 0.825 | 1.981 |
| 30 min | 20.41 | 0.055 | 0.751 | 1.970 | 0.465 | 0.515 | 2.191 |

According to the data obtained for the AJ62 coating the magnitudes of R1 and R2 are increasing with coating time where they start from 0.26, 0.25 M $\Omega$ cm$^2$ for short treatment time reaching almost 2, 2.2 M $\Omega$ cm$^2$ for 30 min treatment time, respectively, implying that the two layers contributed almost equally to the anti-corrosion performance of the coatings. Bode phase angle diagram shown in Fig. 8.3(c) shows that as the for the low frequency the phase angle is shifted to lower angle as the coating time increased whereas at the HF range, phase angles becomes closer to each other around -60$^o$. Whereas Bode impedance diagram (Fig. 8.3(b)) shows the impedance modulus at the LF range, vary from $10^{5.5}$ to $10^{6.5}$ $\Omega$ cm$^2$ with the coating time.

### 8.3.3.1.2 PEO coated AM60B

The Nyquist and Bode plots of experimental and fitting curves as a function of PEO time of coated AM60B are shown in Fig. 8.4. In the LF range, the phase angle is shifted to lower angle as the coating time increased reaching -45$^o$ for the sample coated for 30 min.

The impedance modulus ranges from $10^{5.7}$ to $10^{6.6}$ Ω cm$^2$. As shown in Table 8.4, significantly larger values of R2 compared to that of R1 suggests that the corrosion protection is provided predominantly by the inner barrier layer where R2 reaches 8.8 M Ω cm$^2$ compared to R1 of 1.9 M Ω cm$^2$ for the 30 min sample. Also, the relatively lower value of CPE1 ($9.4 \times 10^{-8}$ F/cm$^2$ s$^{n-1}$) reflects the lower double layer capacitance resulting from the relatively low porosity of the coating. A low R1 and a much higher R2 value point to the fact that the porous layer of the coating was not able to provide high resistance against corrosion and the total resistance of the coating was mainly derived from the inner layer which is directly adjacent to the metal surface, and acts as a barrier to prevent the corrosive electrolyte from reaching the substrate.

Table 8.4. Fitting results of EIS diagrams of PEO treated AM60B Mg alloy using different coating times. Equivalent circuit is Rs+CPE1/(R1+CPE2/R2)

| Time (min) | Rs (Ω·cm$^2$) | CPE1-Q (μF/cm$^2$ s$^{1-n}$) | CPE1-n | R1 (MΩ·cm$^2$) | CPE2-Q (μF/cm$^2$ s$^{1-n}$) | CPE2-n | R2 MΩ·cm$^2$ |
|---|---|---|---|---|---|---|---|
| 3 | 20.31 | 1.995 | 0.882 | 0.209 | 0.109 | 0.833 | 0.370 |
| 6 | 20.67 | 0.429 | 0.678 | 0.218 | 0.497 | 0.811 | 0.392 |
| 10 | 20.88 | 0.581 | 0.674 | 0.679 | 0.573 | 0.804 | 1.042 |
| 15 | 20.55 | 0.190 | 0.727 | 0.71 | 0.580 | 0.551 | 5.070 |
| 30 | 20.52 | 0.094 | 0.804 | 1.875 | 0.320 | 0.819 | 8.796 |

### 8.3.3.1.3 PEO coated AZ91D

In spite of the fact that the PEO- coated AZ91D exhibits a much higher corrosion rate than the coated AJ62-alloy and the n values are close to 0.5 for CPE1, the Nyquist plot does not show a clear Warburg behaviour (slope of a 45$^o$ between Z' and Z''). This is primarily due to the fact that current (flow of ions) can pass relatively easily through the coating layer due to the existence of pores. The Nyquist and Bode plots of experimental and fitted curves for the coated AZ91D presented in Fig. 8.5 are similar to coated AJ62. Therefore, the analysis of the equivalent circuit and corresponding mechanism of corrosion process is similar to that of AJ62. However, when compared to AJ62, the values of R2 are higher ranging from 0.38 to 12 M Ω cm$^2$ and CPE1 ($1.1 \times 10^{-7}$ F/cm$^2$ s$^{n-1}$), nevertheless CPE2 is 3 times lower for AZ91D than AJ62 (Tables 8.5 and 3). As a result, R2 of coating AZ91D was much higher compared with the R1 value of AJ62, and

hence the dense layer of the coating was able to provide high resistance against the corrosion and the total resistance of the coating was mainly derived from the inner layer which was dense. The Bode diagrams of Fig. 8.5 (b and c) shows that in the LF range, the phase angle is shifted to -55$^o$ for the sample coated for 30 min compared to -10$^o$ for the 3 min coated sample and the impedance modulus changing from $10^{5.6}$ to $10^{6.8}$ $\Omega$ cm$^2$. In comparison with the other coatings, AZ91D exhibited higher values of R2 and lower value of CPE2 (Table 8.5) which indicates that the coating has high corrosion resistance.

Table 8.5. Fitting results of EIS diagrams of PEO treated AZ91D Mg alloy using different coating times. Equivalent circuit is Rs+CPE1/(R1+CPE2/R2)

| sample | Rs ($\Omega \cdot$cm$^2$) | CPE1-Q ($\mu$F/cm$^2$ s$^{1-n}$) | CPE1-n | R1 (M$\Omega \cdot$cm$^2$) | CPE2-Q ($\mu$F/cm$^2$ s$^{1-n}$) | CPE2-n | R2 (M$\Omega \cdot$cm$^2$) |
|---|---|---|---|---|---|---|---|
| 3 min | 20.19 | 0.786 | 0.709 | 0.186 | 0.960 | 0.021 | 0.376 |
| 6 min | 20.21 | 0.533 | 0.651 | 0.564 | 0.723 | 0.660 | 1.281 |
| 10 min | 20.88 | 0.240 | 0.692 | 0.611 | 0.693 | 0.713 | 1.523 |
| 15 min | 20.15 | 0.186 | 0.755 | 1.576 | 0.668 | 0.888 | 5.069 |
| 30 min | 20.47 | 0.116 | 0.753 | 1.188 | 0.162 | 0.994 | 12.142 |

In summary, analysis of equivalent circuits of all the above coatings demonstrates a two layered structure of the films as characterized by the presence of two time constants. However, the values of the circuit components vary. This is because an equivalent circuit is based on a possible physical model which represents the physicochemical process that occurs in the system under investigation. Depending on factors such as film characteristics, and whether the charge transfer process is affected by diffusion limitations, the features of EIS spectra and their corresponding equivalent circuits may vary

### 8.3.3.1.4 PEO coated pure Mg

It is obvious that the Nyquist results for the coated pure Mg presented in Fig. 8.6 exhibit a distinctly different behaviour compared to that of the PEO-coated Mg alloy samples. In the low frequency range, the curve attains negative values forming a curve known as an inductive loop [20]. This loop may be attributed to decomposition of metal to ions

leading to the formation of corrosion products, and then to the adsorption of electro-active species of the electrolyte, which leads to localized corrosion followed by the formation of pits on the surface [20,23].

Table 8.6. Fitting results of EIS diagrams of PEO treated Pure Mg using different coating times. Equivalent circuit Rs+CPE1/R1+CPE2/R3/(R3+L)

| T Min | Rs $\Omega\cdot cm^2$ | CPE1-Q $\mu F/cm^2\ s^{1-n}$ | CPE1 -n | R1 $\Omega\cdot cm^2$ | CPE2-Q $\mu F/cm^2\ s^{1-n}$ | CPE2- n | R2 $\Omega\cdot cm^2$ | R3 $\Omega\cdot cm^2$ | L (H) |
|---|---|---|---|---|---|---|---|---|---|
| 3 | 20.44 | 2.540 | 0.602 | 213.5 | 11.15 | 0.575 | 944.3 | 2337 | 99.9 |
| 6 | 20.61 | 0.337 | 0.765 | 417.3 | 8.011 | 0.801 | 646.3 | 696.1 | 34.8 |
| 10 | 20.76 | 0.335 | 0.751 | 541.1 | 5.529 | 0.804 | 874.2 | 1097 | 60.0 |
| 15 | 20.13 | 0.310 | 0.744 | 810 | 3.475 | 0.666 | 2238.2 | 2978 | 13.4 |
| 30 | 20.84 | 0.291 | 0.768 | 1127 | 3.422 | 0.791 | 1575.3 | 2014 | 60.0 |

Fig. 8.7 (b) and Table 8.6 shows the equivalent circuit giving the best fit for the impedance data of the coated pure Mg samples. The circuit consists of two time constants together with an inductor (with inductance L) and a resistor (RL) which are parallel with one of the time constant components. It is clear that the equivalent circuit has an additional inductive element compared to that of the coated Mg alloys. The inductor represents the negative loop of the Nyquist curve. Fig. 8.1 shows that the thicknesses of the coating on pure Mg during all 5 treatment time are lower than that on the Mg-alloys. Furthermore, the SEM micrographs revels that the porosity levels are high in the coated pure Mg allowing the electrolyte to pass through the coating easily and reach the substrate. The diffusion of electrolyte species into the pores will be easier at higher frequencies thereby resulting in adsorption at the inner barrier layer. Due to this adsorption, the Nyquist curve shows an inductive behavior in the LF range [24]. For the PEO coated pure Mg, relatively small R2 values indicated a relatively open access of the electrolyte into the coating region due to the defects in this layer. Figs. 8.3-8.6 show that the impedance modulus of the coated pure magnesium increases with the coating treatment time from 630 $\Omega$ cm$^2$ for 3 min coating time reaching 2000 $\Omega$ cm$^2$ for 30 min treatment time these values are higher than those for the uncoated pure Mg, but still lower than for all the coated Mg alloys.

### 8.3.3.2 Uncoated Mg alloys

The impedance response of the uncoated Mg alloys is somewhat different from that of the coated specimens. The equivalent circuits employed, a metal/solution system, is illustrated in Fig. 8.7(c). This circuit models a cell where polarization is due to a combination of kinetic and diffusion processes. The shape and magnitude of impedance in the Nyquist and Bode plots of the pure Mg and Mg alloys are in very good agreement with previously reported results [8,21]. The experimental Nyquist diagram recorded shows a semicircular trend, characterized by a one-time-constant behavior (single peak of the phase angle Bode diagram with maximum angle of $70^{o}$). The impedance modulus of the pure magnesium is far less than all other samples. The differences in the impedance may be related to the corrosion protection mechanisms of the alloys provided by the naturally formed oxide layer which is very thin (about few nm) and easily corroded by the corrosive electrolyte.

Table 8.7. Fitting results of EIS diagrams of untreated Mg alloys. Equivalent circuit Rs+CPE1/(R1+CPE2)

| sample | $R_S$ $(\Omega \cdot cm^2)$ | CPE1-Q $(F/cm^2\ s^{1-n})$ | CPE1-n | R1 $(\Omega \cdot cm^2)$ | CPE2-Q $(F/cm^2\ s^{1-n})$ | CPE2-n |
|---|---|---|---|---|---|---|
| Pure Mg | 42.21 | 6.528e-6 | 0.925 7 | 650.5 | 0.193 5 | 8.475e-3 |
| AJ62 | 41.78 | 13.79e-6 | 0.811 9 | 4 748 | 0.048 8 | 5.812e-6 |
| AM60B | 40.85 | 4.742e-6 | 0.929 9 | 2 632 | 7.283e-3 | 0.183 4 |
| AZ91D | 41.68 | 4.823e-6 | 0.946 5 | 2 470 | 0.359 6e-3 | 0.383 6 |

The CPE2 is in the range from 0.2 $F/cm^2\ s^{n-1}$ for pure Mg and $3.6 \times 10^{-4}$ $F/cm^2\ s^{n-1}$. CPE1 values were in the range of 4.8-13.8 $\mu F/cm^2\ s^{n-1}$, which is equivalent to a double layer capacitance, where n~1 (Table 8.7). The charge-transfer resistance, R1, has a minimum value of 650 $\Omega$ $cm^2$ for pure uncoated Mg to 4750 $\Omega$ $cm^2$ for uncoated AJ62 alloy while Rs value is 41 $\Omega$ $cm^2$. The Nyquist plot for the uncoated AZ91D Mg alloy shows a different behavior than for other alloys but is similar to previous reports [18,25] and is characterized by two capacitive loops (Fig. 8.8). At low frequencies (i.e. higher real impedance values, $Z'$) the circle is distorted due to the contribution of the second

capacitance. The Nyquist diagrams, shows first a semicircle which can be fitted to an Rs+R1//CPE1, Randles Cell circuit, while the next part requires a second constant phase element Q2 for the fitting routine, Fig. 8.7 (c). It was reported that the first loop was associated with the charge transfer and the smaller capacitive loop was attributed to the corrosion products formed on the surface of AZ91D Mg alloy [8].
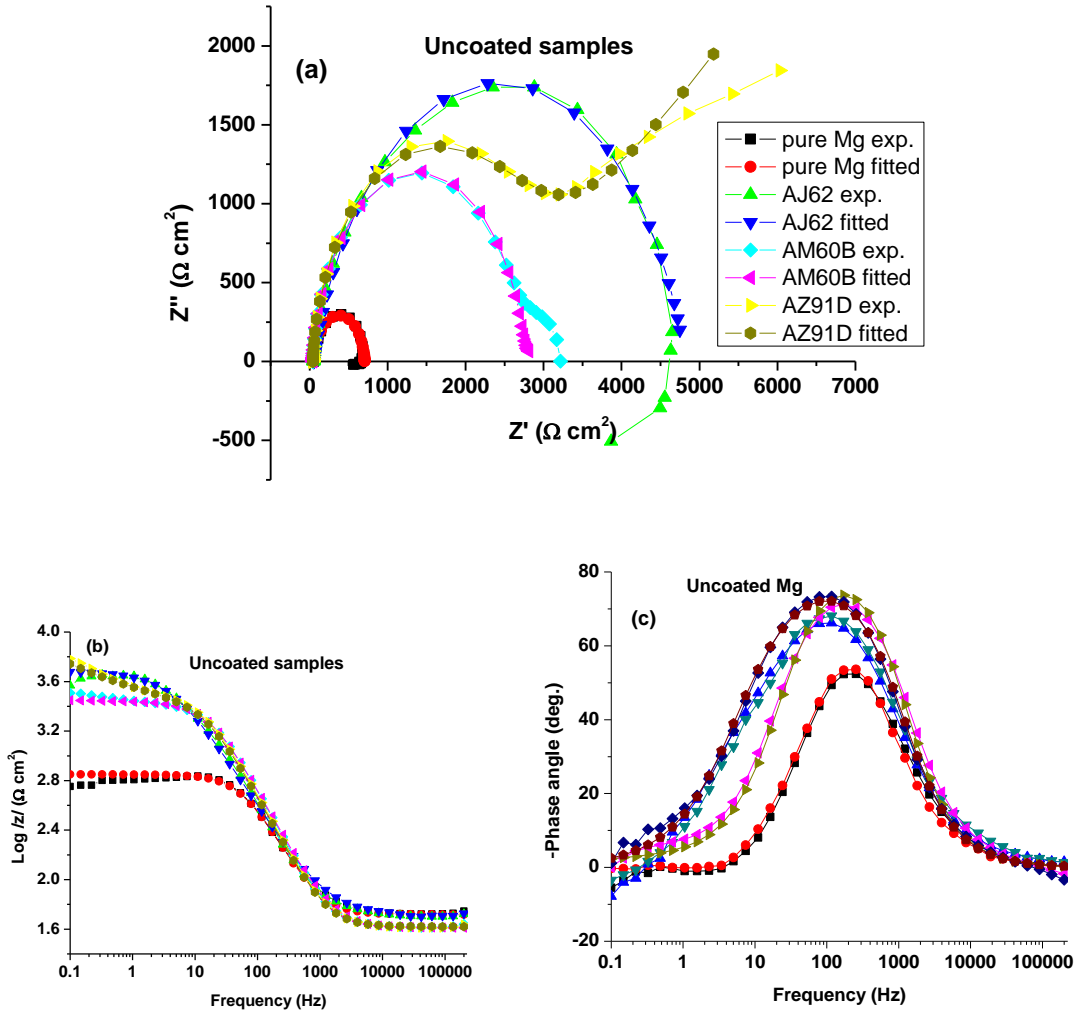


Fig. 8.8 EIS plots of uncoated Mg alloys at different treatment time ((a) Nyquist, (b) Impedance and (c) angles plots) (equivalent circuit Fig8.7(c))

Based on the electrochemical results, the total resistance ($R_T = \sum_{n=2}^{n} R_n$) of the coating is listed in Table 8.8, and it can be summarized that EIS measurements showed poor

corrosion resistance of all uncoated sampled as indicated by relatively low $R_T$. The corrosion resistance of the coated Mg alloys improved substantially by PEO-coating however, the corrosion resistance of the coated pure Mg improved slightly.

Table 8.8. The total resistance ($R_T$) ($M\Omega{\cdot}cm^2$) of the uncoated and coated different Mg alloys.

| Sample | Pure Mg | AJ62 | AM60B | AZ91D |
|---|---|---|---|---|
| uncoated | $6.50{\times}10^{-4}$ | $4.75{\times}10^{-3}$ | $2.63{\times}10^{-3}$ | $2.47{\times}10^{-3}$ |
| 3 min | $3.50{\times}10^{-3}$ | 0.52 | 0.58 | 0.562 |
| 6 min | $1.76{\times}10^{-3}$ | 0.98 | 0.61 | 1.85 |
| 10 min | $2.51{\times}10^{-3}$ | 1.61 | 1.72 | 2.13 |
| 15 min | $6.02{\times}10^{-3}$ | 3.06 | 5.78 | 6.65 |
| 30 min | $4.71{\times}10^{-3}$ | 4.161 | 10.67 | 13.33 |

## 8.4 Conclusion

- The results showed that surface morphologies, coating thickness and porosity level were affected by both the alloying elements and coating treatment time.
- As the time of coating increased, the corrosion protection performance of PEO coatings is directly dependent on their thickness, uniformity and amount of porosity and other defects as indicated by the significant decrease of average porosity values with coating treatment time which could slow down the penetration rate of the electrolyte into the PEO coating. Therefore, the total impedance also increased.
- Each coating has a different phase composition and surface morphology due to the effect of different alloying elements. This in turn affects the corrosion mechanism of these coatings which is reflected in their respective EIS curves. Thus, different types of equivalent circuits have been modeled to best fit these curves.
- Electrochemical impedance spectroscopy data indicate that the bipolar PEO coated AZ91D Mg alloy demonstrates a higher corrosion resistance when compared to coated AM60B, AJ62 and pure Mg. The ranking for corrosion resistance in 3.5% NaCl medium was Mg uncoated < coated pure Mg < coated AJ62< coated AM60B < coated AZ91D which is consistent with the coating

average thickness results. That may be attributed to the discharging behaviors, coating structure, thickness and amount of porosity.

## References

[1]     Fournier V, Marcus P, Olefjord I, Oxidation of magnesium. Surface Interface Analysis, 34 (2002) 494-497.
[2]     Shrestha S, Magnesium and Surface Engineering-Technology Vision. Editorial in Surface Engineering, 26 (2010), 313-316.
[3]     Song G, Atrens A, Wu X, Bo Z, Zhang B, Corrosion behaviour of AZ21, AZ501 and AZ91 in sodium chloride. Corrosion Science, 40 (1998) 1769-1791.
[4]     Makar G L, Kruger J, Corrosion of Magnesium. International Materials Reviews, 38 (1993)138-153.
[5]     Kojima Y, Platform science and technology for advanced magnesium alloys. Materials Science Forum, 3 (2000) 350–351.
[6]     Hillis J E, (1983) The Effects of Heavy Metal Contamination on Magnesium Corrosion Performance. SAE Technical Paper #830 523, Detroit.
[7]     Song G L, Atrens A, Corrosion mechanisms of magnesium alloys. Advanced Engineering Materials, 1 (1999) 11–33.
[8]     Zhang Y, Yan C, Wang F, Li W, Electrochemical behavior of anodized Mg alloy AZ91D in chloride containing aqueous solution, Corrosion Science, 47 (2005) 2816–2831
[9]     Arrabal R, Mota JM, Criado A, Pardo A, Mohedano M, Matykina E, Assessment of duplex coating combining plasma electrolytic oxidation and polymer layer on AZ31 magnesium alloy. Surface & Coatings Technology, 206 (2012) 4692–4703.
[10]    Huang VM, Wua S-L, Orazema ME, Pébèreb N, Tribollet B, Vivier V, Local electrochemical impedance spectroscopy: A review and some recent developments. Electrochimica Acta, 56 (2011) 8048– 8057.
[11]    Mansfeld F, Lin S, Kim K, Shih H, Pitting and Surface Modification of SiC/Al. Corrosion Science, 27 (1987) 997-1000.
[12]    Sundararajan G, Krishna LR. Mechanisms underlying the formation of thick alumina coatings through the MAO coating technology. Surface & Coatings Technology, 167 (2003) 269-277.
[13]    Mécuson F, Czerwiec T, Belmonte T, Dujardin L, Viola A, Henrion G. Diagnostics of an electrolytic microarc process for aluminum alloy oxidation. Surface & Coatings Technology, 200 (2005) 804-808.
[14]    Zhou X, Thompson GE, Skeldon P, Wood GC, Shimizu K, Habazaki H, Film formation and detachment during anodizing of Al–Mg alloys.  Corrosion Science, 41 (1999) 1599–1613.
[15]    Hussein RO, Northwood DO and Nie X, The influence of pulse timing and current mode on the microstructure and corrosion behaviour of a plasma electrolytic oxidation (PEO) coated AM60B magnesium alloy. J. of Alloys and Compounds, 541 (2012) 41-48.
[16]    Hussein RO, Nie X, Northwood DO, Yerokhin A, Matthews A (2010), Spectroscopic study of electrolytic plasma and discharging behaviour during the

plasma electrolytic oxidation (PEO) process. Journal of Physics D: Applied Physics, 43, 105203.

[17]   Kielbus A**,** Rzychon T, Microstructure and creep properties of aj62 and ae44 diecasting magnesium alloys. Materials Science Forum, 638-642 (2010) 1546-1551

[18]   Jorcin J-B, Orazem M E, Pe´be`re N, Tribollet B, CPE analysis by local electrochemical impedance spectroscopy. Electrochimica Acta, 51 (2006) 1473-1479.

[19]   Hussein RO, Zhang P, Xia Y, Nie X, Northwood DO. The effect of current mode and discharge type on the corrosion resistance of plasma electrolytic oxidation (PEO) coated magnesium alloy AJ62. Surface & Coatings Technology, 206 (2011)1990-1997.

[20]   Ghasemi A, Raja VS, Blawert C, Dietzel W, Kainer KU, The role of anions in the formation and corrosion resistance of the plasma electrolytic oxidation coatings. Surface & Coatings Technology, 204 (2010) 1469-1478.

[21]   Ryu HS, Ryu J, Park D and Hong S.-H, Electrochemical Corrosion Properties of Nanostructured YSZ Coated AZ31 Magnesium Alloy Prepared by Aerosol Deposition.  Journal of Electrochemical Science, 158 (2) (2011) C23-C28.

[22]   EC-Lab$^{®}$  Software User's Manual, 2010, http://www.bio-logic.info/.

[23]   Duan H, Du K, Yan C, Wang F, Electrochemical corrosion behavior of composite coatings of sealed MAO film on magnesium alloy AZ91D. Electrochimica Acta, 51 (2006) 2898–2908.

[24]   Sreekanth D, Rameshbabu N, Venkateswarlu K, Effect of various additives on morphology and corrosion behavior of ceramic coatings developed on AZ31 magnesium alloy by plasma electrolytic oxidation. Ceramics International, 38 (2012) 4607–4615

[25]   Brunelli K, Dabala M, Calliari I, Magrini M, Effect of Hcl pre-treatment on corrosion resistance of cerium-based conversion coatings on magnesium and magnesium alloys. Corrosion Science, 47 (2005) 989–1000.

# CHAPTER 9

# EFFECT OF CATHODIC CURRENT DENSITY ON THE CORROSION PROTECTION OF THE OXIDE COATINGS FORMED ON AZ91D MAGNESIUM ALLOY BY PLASMA ELECTROLYTIC OXIDATION.

**Published In:**

Hussein R. O., Nie X. and Northwood D. O. (2013) Effect of cathodic current density on the corrosion protection of the oxide coatings formed on AZ91D magnesium alloy by plasma electrolytic oxidation. Corrosion and Prevention 2013", Australia 2013, paper no. 112.

## 9.1 Introduction.

Magnesium is one of the most attractive materials for lightweighting, and has seen a sharp rise in industrial consumption. However, since magnesium and its alloys are very active chemically, corrosion protection is a critical factor which can decreased mechanical stability and an unattractive appearance. There are generally two possible ways to improve the corrosion behavior of Mg and Mg alloys. These are either to change the chemical composition, phase constituents and distribution, and thereby modify the microstructure [1], which is often difficult and would be a long-term goal [2], or by surface treatments or form coatings [3], which produce an independent protective ceramic, polymer or composite layers on the Mg alloys [4].

The corrosion performance of magnesium alloys largely depends on the alloying and impurity elements. In order for a coating to provide adequate corrosion protection for Mg and Mg alloys, the coating must be uniform, pore free, well adhered and self-healing in case there is physical damage to the coating. Plasma electrolytic oxidation (PEO) has been used to rapidly and economically produce oxide coatings on magnesium alloy components of almost any shape and size. A promising approach to produce high-quality oxide coatings with good corrosion and wear resistance on magnesium alloys is to use the PEO process.

The effects of electrical parameters mainly current density [5] and current mode [6] on the microstructure and corrosion behaviour of PEO coatings on Mg alloys have been

widely investigated. Increasing the current density and/or voltage led to an increase in layer thickness, as well as enlargement of the surface craters. Changing the current mode produces changes in the PEO process characteristics, including the breakdown voltage and discharge events, both in terms of discharge intensity and density [7]. The discharges have a profound effect on the coating microstructure, thickness, roughness, porosity, hardness, and coating growth rate, and hence affect the corrosion resistance of the coated magnesium alloy. PEO coatings formed using a bipolar current mode have been reported to have a more compact structure with fewer defects, and uniform coating thickness compared to coatings formed using a unipolar mode [8]. However, the unavoidable porous structures in the PEO coatings decrease the corrosion resistance, which may restrict any future potential applications for Mg alloys.

In this study the role played by current density using bipolar current modes on the microstructural characteristics of oxide coatings produced by a PEO process on a AZ91D Mg alloy is investigated. The coatings morphologies were also investigated to assess the relationship to their intrinsic alloy corrosion rate. Corrosion resistance is used as the measure of change in coating properties.


**9.2. Experimental Procedures**

Due to its excellent combination of mechanical properties and castability and reasonable corrosion resistance, AZ91D magnesium alloy disc coupons ($\Phi25\times5$mm) were used as the test samples in this study. 8 g/l Na2Al2O4and 1 g/l KOH were dissolved in de-ionized water and was used as the electrolyte in PEO processing. Process parameters are listed in Table 9.1. Scanning electron microscopy (FEI Quanta 200 FEG with solid state backscattered detector operated at 10 KV) in the back scattered secondary electron (BSE) mode was used to observe both the coating surface morphology and, through observation of sample cross sections, coating thickness and integrity.

**Table 9.1. PEO Process parameters for coating AZ91D Mg alloy.**

| S | Current mode | Time (min) | $I^+$ (A) | $J^+$ (A/cm$^2$) | $I^-$ (A) | $T_{on}^+$ ($\mu s$) | $T_{on}^-$ ($\mu s$) | $T_{off}^+$ ($\mu s$) | $T_{off}^-$ ($\mu s$) | $C_R$ |
|---|---|---|---|---|---|---|---|---|---|---|
| S1 | Bipolar | 30 | 0.68 | 0.05 | 0.5 | 400 | 100 | 400 | 100 | 0.9 |
| S2 | Bipolar | 30 | 0.95 | 0.07 | 0.7 | 400 | 100 | 400 | 100 | 0.9 |
| S3 | Bipolar | 30 | 1.5 | 0.11 | 1.1 | 400 | 100 | 400 | 100 | 0.9 |

To determine the corrosion resistance of the PEO coating, potentiodynamic polarization in a 3.5% NaCl solution tests were carried out for uncoated and coated samples at 25 $^o$C using a Solartron 1285 Potentiostat with Corrware software (Chapter 3). Electrochemical impedance spectroscopy (EIS) was also used for uncoated and coated samples, through a frequency response analyzer which enabled the scan to be generated automatically under computer control. Measurements were performed three times to ensure reproducibility of the results. Electrochemical impedance spectroscopy (EIS) measurements were performed at the open circuit corrosion potential on the PEO coatings after 30 minute of initial delay to stabilize the open-circuit potential (OCP).

## 9.3 Results and Discussion.

### 9.3.1 Microstructure of the Coatings.

The surface morphologies of the three sets of PEO coatings, prepared under the process parameters listed in Table 9.1 for treatment times of 30 min obtained using back-scattered electron mode (BSE) are shown in Fig. 9.1(a-c). All samples show micro-pores, micro-cracks and a 'pancake' structure wherein the center of each pancake was a discharge channel through which the molten magnesium surged out of the channel and quickly solidified leaving distinct boundaries that define each pancake. The micro-cracks are attributed to internal stresses in the PEO coatings formed as a result of complex interactions between the stress generation and stress relaxation processes [8]. Figure 9.1(c) is a SEM micrograph of Sample S3, fabricated with the current density of 0.11 A/cm2, and shows a number of pancake features and relatively large pores in the coating. The relatively large holes in the center of the pancake suggest that there are strong discharges and such holes may penetrate deep into the coating thickness: these discharges are called B- type discharges by Hussein et al [9] in their discharge model.

SEM micrographs showing the cross-sections of the PEO coated samples for the three different current densities are also presented in Fig. 9.1.
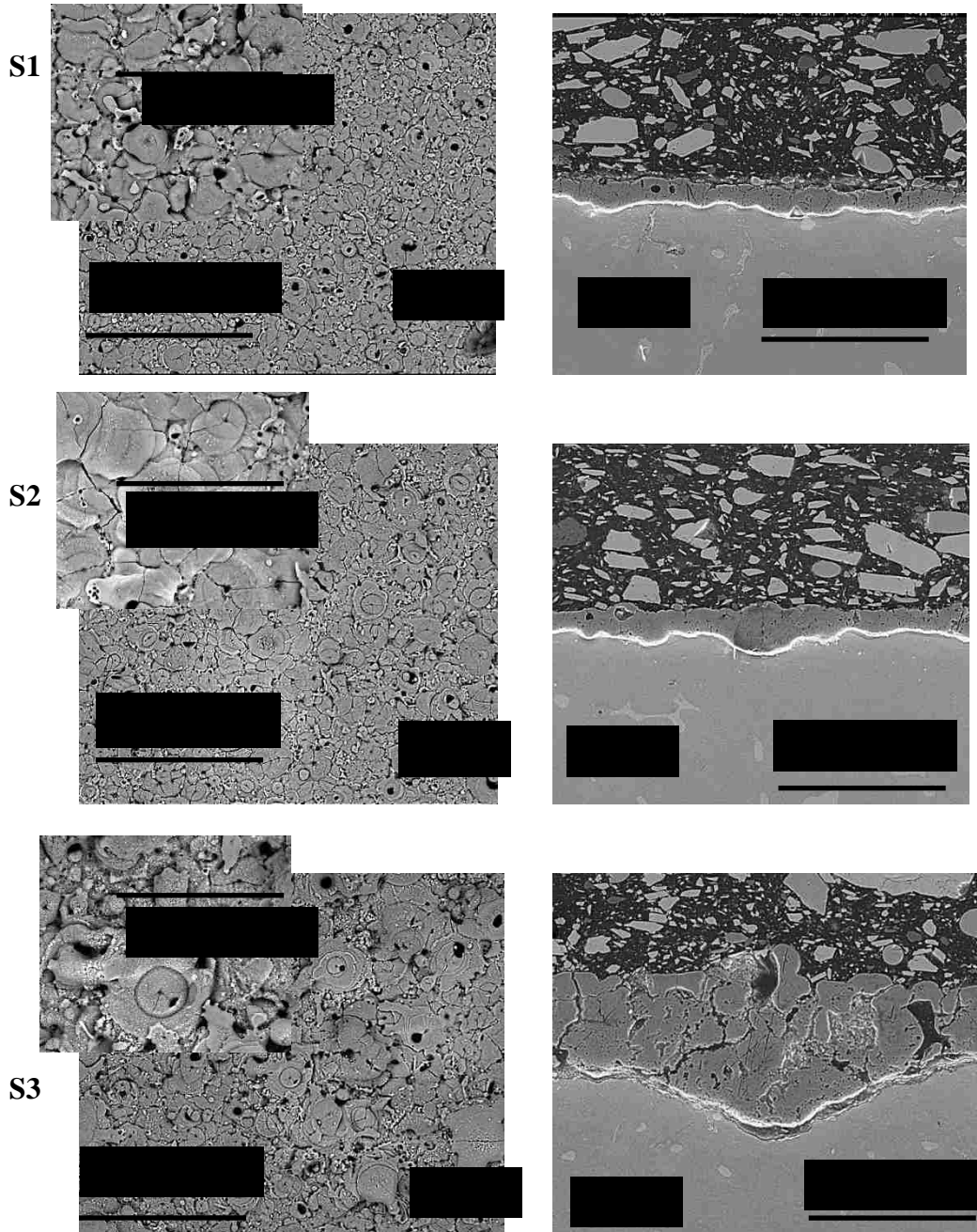


Figure 9.1. SEM micrographs showing the surface morphology and cross section of oxide coatings on AZ91D alloy for (a,d) S1(J=0.05 A/cm$^2$) , (b,e) S2(J=0.07 A/cm$^2$)  and (c,f) S3(J=0.11 A/cm$^2$)  samples respectively. The insert figures are micrographs at higher magnifications.

The micro-pores are due to gas bubbles ejected from surface discharges and are referred to as A and C discharges [9]. In the specimen processed using current density of 0.07

A/cm2, Fig. 9.1(b), the pore density is reduced, and the size of the pores is smaller relative to the S3. However, sample S1 shows some holes in the center of the relatively smaller pancake diameter compared to S2 and S3 pancake diameter, indicating a reduction of the strength of the discharges. Stronger discharges have greater energy inputs which cause a larger amount of substrate and its oxide to melt down, and eventually the molten material is ejected onto the surface, forming larger pancake features when it is rapidly cooled by the electrolyte.

All coating-substrate interfaces had a wavy-jagged appearance, which may be the result of dissolution of the substrate in the early stages of the treatment and the substrate intermetallic phases. Figure 9.1(f) shows the cross section of a ceramic coating for the S3 sample.

The coating showed significant porosity, holes and other defects within the coating and near the coating/substrate interface. Such defects would have a detrimental effect on the coatings corrosion resistance. The average coating thickness was in the range of 50-70 μm. Current density plays an important role during the formation of PEO coatings.

When the current density increases, the strength of the discharges increases, hence discharge channels and the amount of ejected molten oxide become larger which leads to thicker coating quicker, combined with relatively larger holes and more coating defects. For the S2 case, Fig. 9.1(e), the oxide layer was thinner than for the S3 case, 23 - 50 μm. Ii was clear that besides the improvement of the surface morphology, the cross sections show the coating improvement in terms of porosity and other defects. The PEO coating on S1 samples had an average thickness in the range of 18-26 μm and were composed of a network of through-coating defects (micro cracks).

### 9.3.2 Corrosion Resistance

### 9.3.2.1 Potentiodynamic Polarization

It is illustrative to compare the corrosion protection properties afforded by the PEO-coatings for different current densities using a bipolar current mode. The potentiodynamic polarization curves of the uncoated AZ91D Mg alloy and the PEO coated specimens after immersion in a 3.5% NaCl solution for different times up to 24 h are shown in Fig. 9.2. Compared to the uncoated AZ91D, all PEO-coated samples

exhibited a higher polarization resistance, a lower corrosion current density and a higher (more noble) corrosion potential. The first point to note is that the variation of corrosion resistance with current density is not linear. Some of the polarization curves eg. S3 at 0.5h, and S1 at 24h, exhibit evidence of a "passive behaviour". However, this passive behaviour dose not lead to significant reductions in corrosion current densities, particularly at longer immersion times.

It is generally expected that a thicker coating gives rise to better corrosion resistance. However, a thicker coating obtained using a higher current density (S3) offered less protection than coatings obtained using lower current densities (S1 and S2). This indicates that the defect density is the dominating influence rather than the coating thickness. Increasing the coating thickness did not reduce the amount of open defects that provided access for the electrolyte to the magnesium alloy substrate. Sealing the coating would appear to be necessary to protect against long term exposure in aggressive environments. Comparatively, coating S2, having relatively thick and dense oxide layers, has a higher polarization resistance and lower corrosion current densities than the other PEO coatings (Table 9.2). Hence, with increasing current density, the corrosion protection performance of PEO coatings is directly dependent on their uniformity and amount of porosity and other defects.
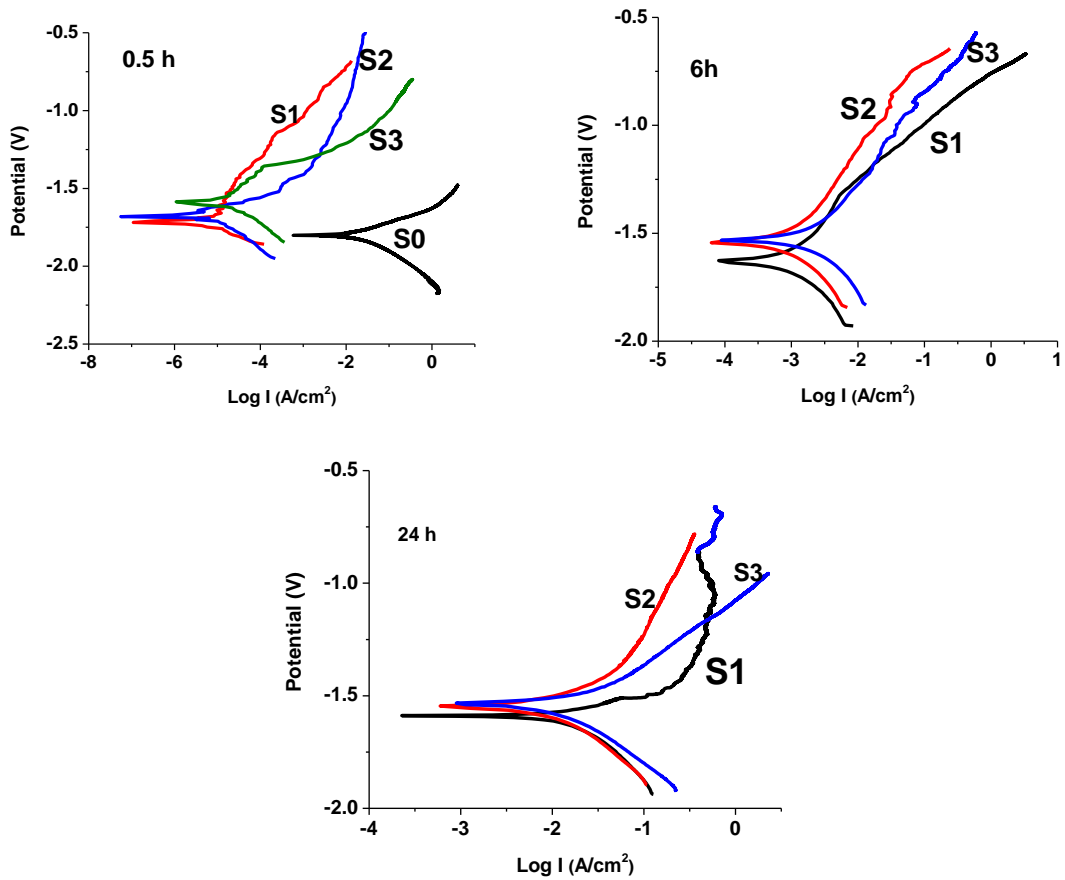
**Fig. 9.2.** Potentiodynamic polarization curves of the uncoated (S0) and PEO-coated samples using different current densities (S1-S3) after three different immersion times.

**Table 9.2. Potentiodynamic polarization corrosion test results in3.5%wt NaCl solution**

| Immn. time | S | $E_{corr}$ (V) | $i_{corr}$ $\mu A/cm^2$ | $\beta a$(mV) | $\beta c$(mV) | $R_p$ (K$\Omega$/cm$^2$) | $P_i$ (mm/year) |
|---|---|---|---|---|---|---|---|
| 0.0 h | S0 | -1.797 | 22.43 | 110.0 | 168.3 | 1.29 | $5.12\times10^{-1}$ |
| 0.5 h | S1 | -1.717 | 0.005 | 173.0 | 91.8 | 5214.0 | $1.14\times10^{-4}$ |
| | S2 | -1.673 | 0.004 | 96.2 | 126.9 | 5947.7 | $9.14\times10^{-5}$ |
| | S3 | -1.586 | 0.011 | 216.0 | 134.1 | 3270.2 | $2.51\times10^{-4}$ |
| 6 h | S1 | -1.632 | 1.05 | 414.2 | 334.2 | 76.52 | $2.40\times10^{-2}$ |
| | S2 | -1.541 | 0.801 | 348.0 | 304.3 | 88.12 | $1.83\times10^{-2}$ |
| | S3 | -1.525 | 2.12 | 387.0 | 353.6 | 37.93 | $4.84\times10^{-2}$ |
| 24 h | S1 | -1.585 | 14.39 | 111.2 | 308.5 | 2.47 | $3.29\times10^{-1}$ |
| | S2 | -1.547 | 10.93 | 261.5 | 330.0 | 5.80 | $2.50\times10^{-1}$ |
| | S3 | -1.536 | 10.85 | 169.1 | 273.8 | 4.19 | $2.48\times10^{-1}$ |

In the potentiodynamic polarization method for measuring the corrosion rate of AZ91D Mg alloys, the corrosion current density, $i_{corr}$ ($\mu$A/cm$^2$) can be related to the average corrosion rate, $P_i$ (mm/year) by the Stern-Geary equation [10], the calculated values for $P_i$ are also given in Table 9.2. Potentiodynamic polarization corrosion test results showed that these PEO coatings significantly increased the corrosion resistance of AZ91D alloy. The ranking for corrosion resistance in 3.5% NaCl medium was Mg uncoated < sample S3 < sample S1 < sample S2 for 0.5h and 6h immersion times. However for 24h immersion time the ranking is sample S1 < sample S2 and S3 which may attributed to the smaller coating thickness of S1coating that may be partially dissolved during the immersion period compared to S2 and S3 coatings.

## 9.3.2.2 Electrochemical Impedance Spectroscopy (EIS) Measurements

The Nyquist and the Bode diagrams from the EIS analysis of experimental and fitted curves of AZ91D Mg alloy treated by PEO at three different current densities during three different immersion times are given in Figs. 9.3-9.5. Taking both the physical structure of the PEO coatings and their impedance responses into account, and based on previous studies [11,12], equivalent circuits employed for curve fitting of the untreated and PEO-treated AZ91D at different treatment time are listed in the Tables 9.3-9.5 and are illustrated in Figs. 9.6 (a) and (b). The choice of the circuit was a balance between a reasonable fitting of the experimental values and a good description of the electrochemical system by keeping the number of circuit elements at a minimum. For the uncoated samples the presence of Warburg element and its resistance R3 is an evidence for a diffusion control processes.

The results shown in Fig. 9.3 are for AZ91D alloy without and with PEO treatment after immersion in 3.5 % NaCl solution for 0.5h. Nyquist plots of untreated AZ91D alloy were characterized by an inductive loop in the low frequency (LF) region (enlarged part of Fig. 9.3). Figs. 9.4-9.5 for PEO-coated Mg alloy immersed for 6h and 24h respectively shows different EIS behavior, and the difference was present for all of the frequency range of the EIS plots. As shown in the Bode plot (Fig. 9.4), the impedance modulus at low

frequencies decreased during the first 6 h of immersion, indicating continuous dissolution of the magnesium matrix.

### 9.3.2.2.1 0.5h Immersion Time.

In order to get a quantitative measure of the current density and immersion time effects, the EIS spectrum of the coated Mg alloy was modeled using the equivalent circuit presented in Fig. 9.6. An excellent agreement between the experimental and modeled data was obtained. Fig. 9.3 shows the Nyquist and Bode plots of experimental and fitting curves of the coated AZ91D Mg alloy as a function of current density after immersion in 3.5 % NaCl solution for 0.5h.

The values of the circuit elements calculated from the fitting for the spectrum recorded on the coated AZ91D Mg alloys surfaces are summarized in Table 9.3. The fitting quality was evaluated by the chi-squared ($x^2$) values [13], which were in the range of $1\times10^{-3}$ to $1\times10^{-4}$ indicating good agreement between the experimental and equivalent circuit data. According to the data obtained for the PEO-coated AZ91D coating immersed for o.5h in the solution, exhibits a much higher corrosion rate than those for 6 and 24h immersion time, and the magnitudes of R1for the coated samples are varying with current density, however it is in the range (0.167-0.23 M $\Omega$ cm$^2$), and Q1 values increases from 0.14 for S1 to 0.24 $\mu F/cm^2$ s$^{n-1}$ for S3. Bode impedance diagram (Fig. 9.3(b)) shows the impedance modulus at the LF range, vary from $10^{5.5}$ $\Omega$ cm$^2$ for S3 to $10^{6.5}$ $\Omega$ cm$^2$ for S1and S2. The Nyquist curves for the uncoated AZ91D Mg alloy presented in Fig. 9.3 exhibit, a negative values in the low frequency range forming a curve known as an inductive loop [12]. This loop may be attributed to decomposition of metal to ions leading to the formation of corrosion products. The impedance modulus at the LF range for uncoated sample is $10^{3.1}$ $\Omega$ cm$^2$ (Fig. 9.3(b)).
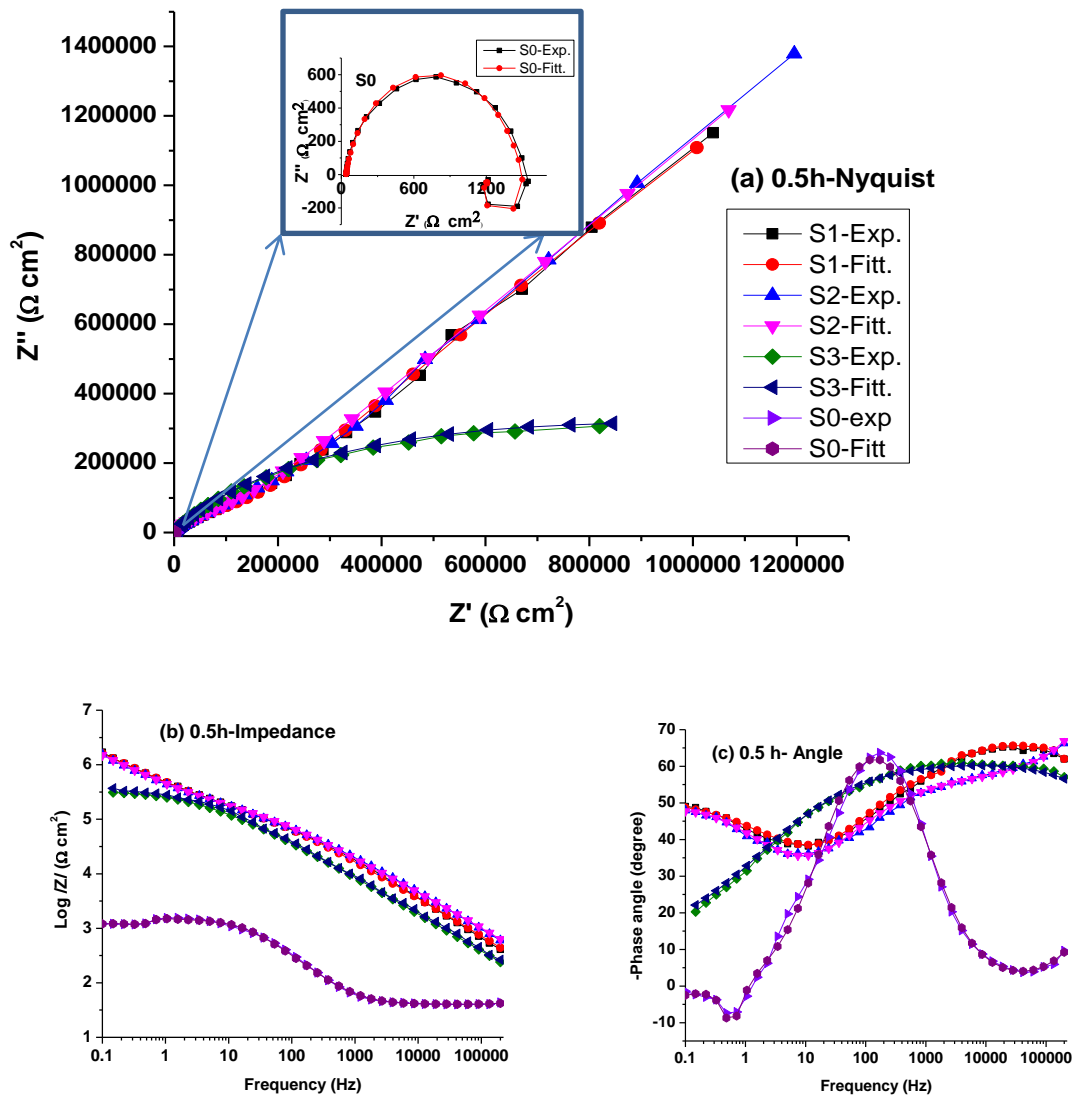
Fig. 9.3. EIS plots of coated and uncoated AZ91DMg alloy at different current densities for 0.5 h immersion time ((a) Nyquist, (b) Impedance and (c) angles plots)

### 9.3.2.2.2 6h Immersion Time.

The Nyquist and Bode plots of experimental and fitting curves as a function of current density of coated AZ91D for 6h immersion time are shown in Fig. 9.4. Although, the same equivalent circuit was used as for the 0.5h immersion time, PEO-coated Mg alloy immersed for 6h shows different EIS behavior, and the difference was present for all of the frequency range of the EIS plots. The experimental Nyquist diagram recorded shows

a semicircular trend with diameters (which reflects the corrosion resistance of the sample) in the range of 29-60 k$\Omega$ cm$^2$. This loop may be attributed to decomposition of metal to ions leading to the formation of corrosion products, and then to the adsorption of electro-active species of the electrolyte [12,14].

**Table 9.3. Fitting results of EIS diagrams of PEO treated AZ91D Mg alloy using different current densities.**

| Immn. time | S | Rs $\Omega \cdot cm^2$ | CPE1-Q $\mu F/cm^2 \, s^{1-n}$ | CPE1-n | R1 $(\Omega \cdot cm^2)$ | CPE2-Q $\mu F/cm^2 \, s^{1-n}$ | CPE2-n | R2 $(\Omega \cdot cm^2)$ |
|---|---|---|---|---|---|---|---|---|
| 0.5h | S1 | 70 | 0.14 | 0.68 | $1.67 \times 10^5$ | 0.70 | 0.55 | $2.5 \times 10^{23}$ |
| | S2 | 70 | 0.20 | 0.63 | $2.30 \times 10^5$ | 0.70 | 0.60 | $2.2 \times 10^7$ |
| | S3 | 67 | 0.24 | 0.68 | $2.00 \times 10^5$ | 0.74 | 0.74 | $2.0 \times 10^6$ |
| 6h | S1 | 70 | 1.1 | 0.67 | $3.97 \times 10^4$ | 9.2 | 0.78 | $1.7 \times 10^4$ |
| | S2 | 70 | 0.75 | 0.61 | $5.81 \times 10^4$ | 25.7 | 0.99 | $2.0 \times 10^3$ |
| | S3 | 70 | 1.1 | 0.62 | $7.87 \times 10^2$ | 0.0059 | 0.93 | $2.8 \times 10^3$ |

In the LF range, the phase angle is shifted to lower angle around 0 to -7$^o$ for S3 and (S1&S2) samples respectively. The impedance modulus ranges from $10^{4.5}$ to $10^{4.75}$ $\Omega$ cm$^2$. As shown in Table 9.3, the values of R1 ranging from 5.8 $\times 10^2$  $\Omega$ cm$^2$ for S3 to 7.9 $\times 10^4$ M $\Omega$ cm$^2$ for s1 sample. The values of CPE1 are about 1.0 $\mu F/cm^2$ s$^{n-1}$.
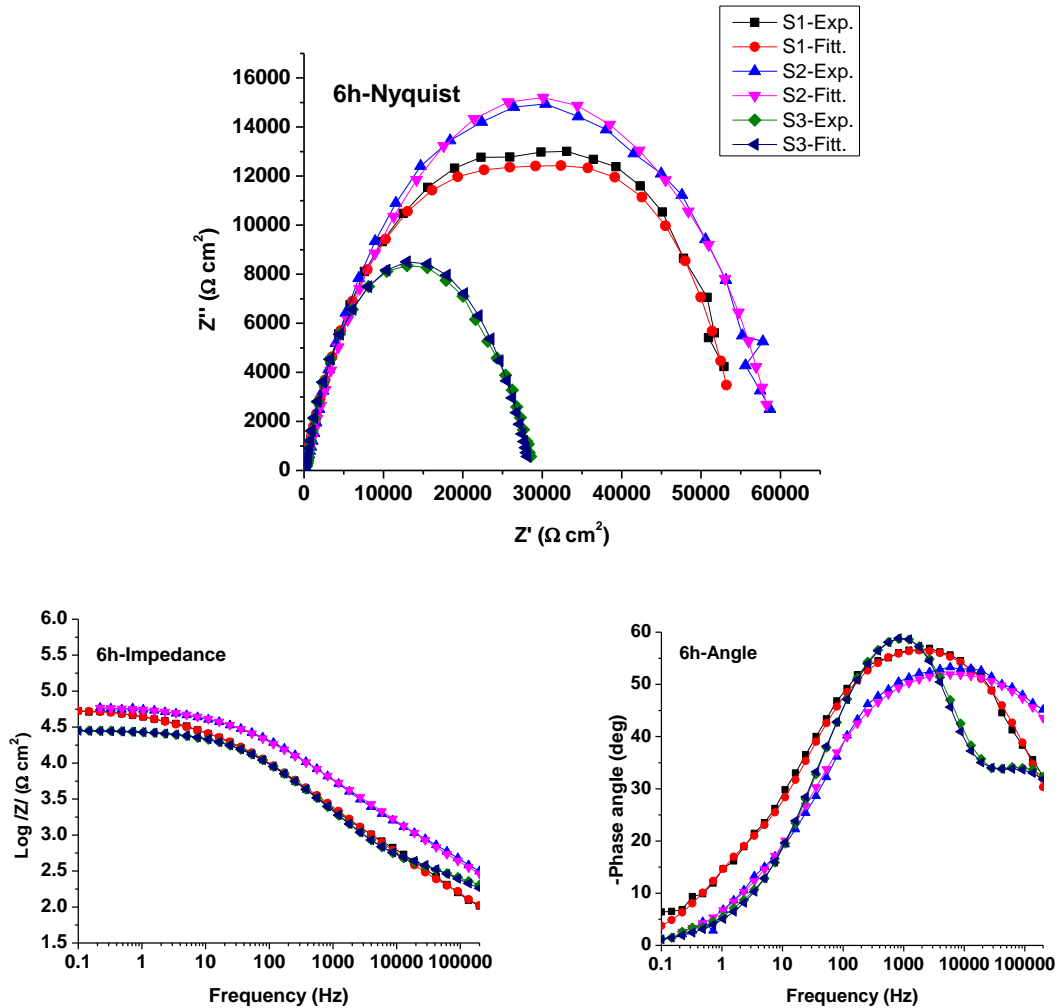
Fig. 9.4. EIS plots of coated and uncoated AZ91DMg alloy at different current densities for 6 h immersion time ((a) Nyquist, (b) Impedance and (c) angles plots).

### 9.3.2.2.3  24 h Immersion Time.

The impedance response of the coated AZ91D Mg alloys immersed for 24h is somewhat different from that of the 0.5h and 6h immersion samples. This circuit models a cell where polarization is due to a combination of kinetic and diffusion processes. The experimental Nyquist diagram recorded shows a semicircular trend, with much smaller diameter compered to 6h case which in the range of 2.8-8 k$\Omega$ cm$^2$. Fitting results of EIS diagrams of PEO treated samples immersed for 24h, reveals some negative values of the elements which has no physical meaning hence the semi-circle diameter were used as an indicator of the corrosion resistance. In the low frequency range, the curve attains

negative values forming an inductive loop curve [12]. The longer immersion time allows the electrolyte to pass through the coating easily and reach the substrate. The diffusion of electrolyte species into the pores will be easier at higher frequencies thereby resulting in adsorption at the inner barrier layer. Due to this adsorption, the Nyquist curve shows an inductive behavior in the LF range [15]. Fig. 9.5 (b) and Table 9.4 show the equivalent circuit giving the best fit for the impedance data of the 24h immersion time. The magnitude of impedance modulus /Z/ was reduced to the range of $10^{3.5}$ to $10^{3.9}$ $\Omega$ cm$^2$ for S1 and (S2 and S3) respectively, which can be attributed to the electrolyte penetration through the PEO coating after the coating degradation, however /Z/ is still higher than that of the uncoated Mg alloy with 0.5h immersion time.
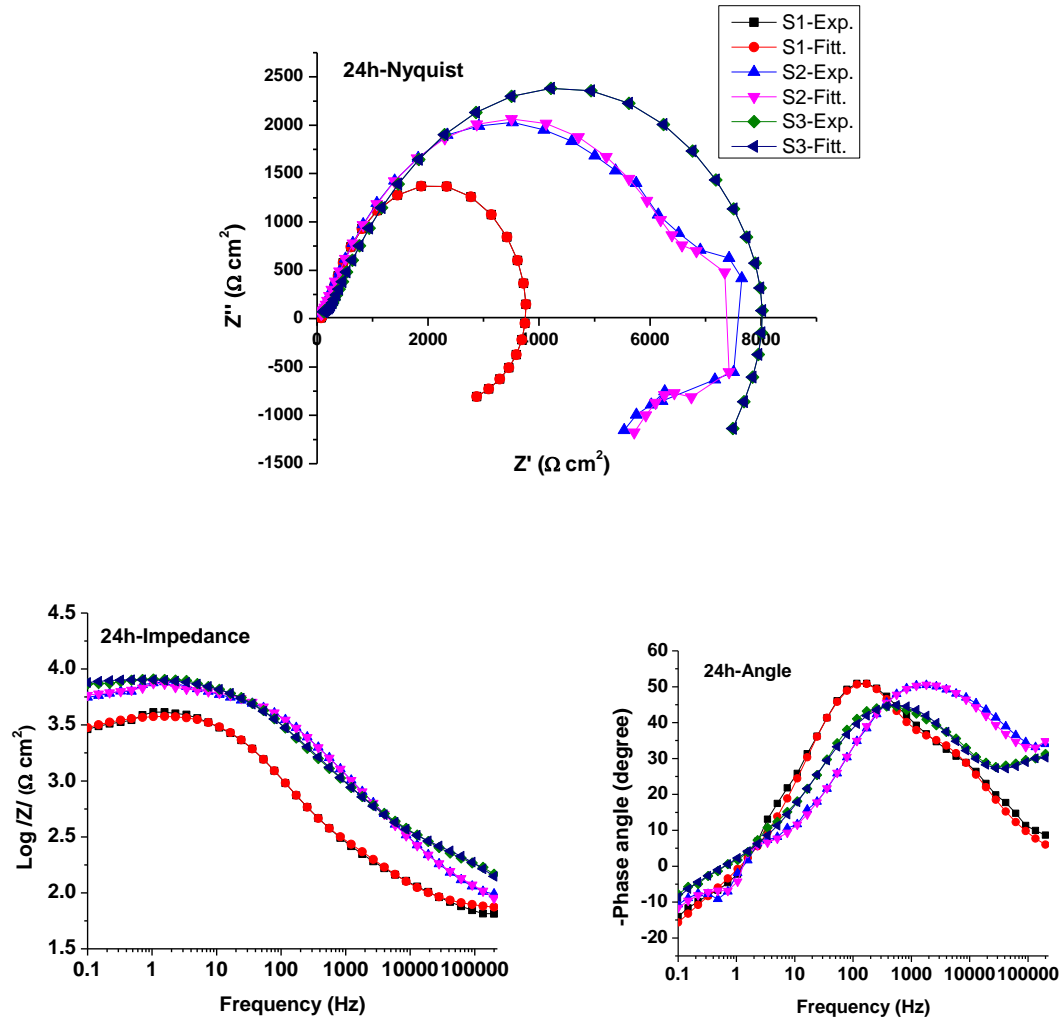
Fig. 9.5. EIS plots of coated and uncoated AZ91DMg alloy at different current densities for 24 h immersion time ((a) Nyquist, (b) Impedance and (c) angles plots)

**Table 9.4. Fitting results of EIS diagrams of PEO treated AZ91D Mg alloy using different current densities for 24h immersion time.**

| S | Rs $\Omega \cdot cm^2$ | CPE1-Q F/cm$^2$ s$^{1-n}$ | CPE 1-n | R1 $\Omega \cdot cm^2$ | CPE2-Q $\mu$F/cm$^2$ s$^{1-n}$ | CPE2 -n | R2 $\Omega \cdot cm^2$ | CPE3-Q $\mu$F/cm$^2$ s$^{1-n}$ | CPE3-n | R3 $\Omega \cdot cm^2$ |
|----|------|------|------|------|------|------|------|------|------|------|
| S1 | 70 | $1.5 \times 10^{-5}$ | 0.63 | $1.56 \times 10^4$ | 17.4 | 1 | 40 | -26.8 | 0.22 | -21740 |
| S2 | 70 | $2.3 \times 10^{-6}$ | 0.67 | -95 | 1.8 | 0.4 | 5537 | 300 | 0.002 | -11.81 |
| S3 | 70 | $4.5 \times 10^{-8}$ | 0.86 | 185 | 0.82 | 1 | -5.6 | 3.8 | 0.64 | 8563 |

168

**Table 9.5. Fitting results of EIS diagrams of untreated AZ91D Mg alloy (S0) for 0h immersion time.**

| S | Rs $\Omega \cdot cm^2$ | CPE1-Q F/cm$^2$ s$^{1-n}$ | CPE 1-n | R1 $\Omega \cdot cm^2$ | CPE2-Q $\mu$F/cm$^2$ s$^{1-n}$ | CPE2 -n | R2 $\Omega \cdot cm^2$ | CPE3-Q F/cm$^2$ s$^{1-n}$ | CPE3 -n | R3 $\Omega \cdot cm^2$ |
|---|---|---|---|---|---|---|---|---|---|---|
| S0 | 70 | $6.0 \times 10^{-9}$ | 1 | -30 | 10.16 | 0.88 | 1433 | 0.057 | 0.55 | 0.98 |
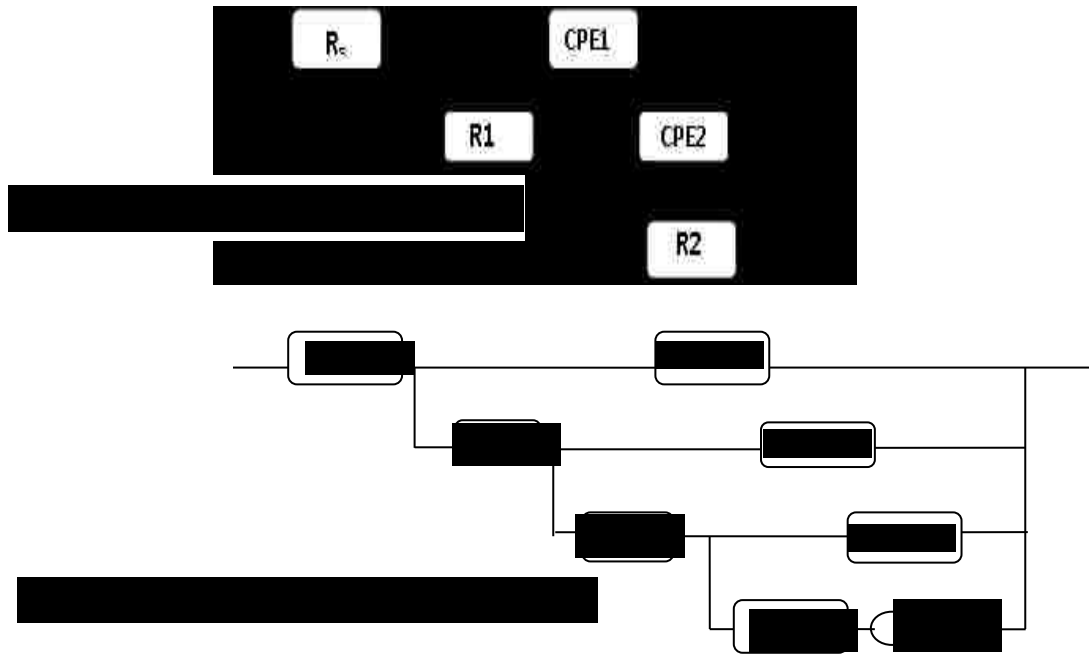


**Fig. 9.6** The equivalent circuit model for (a) coated AZ91DMg alloy for 0.5, 6h immersion time, (b) coated Mg alloy for 24h immersion time and uncoated Mg alloys.

## 9.4 Conclusions

- It is concluded that the corrosion protection performance of the PEO coatings is indirectly dependent on the current density and is controlled by the amount of porosity and other coating defects which could slow down the penetration rate of the electrolyte through the PEO coating. Although, increasing the cathodic current density during the PEO processing of AZ91D magnesium alloy from 0.05 A/cm$^2$ to 0.11A/cm$^2$ produced a thicker coating (thickness increased from 22µm to 60

μm), there was a corresponding increase in coating defects, including porosity and microcracks, which affected the overall corrosion performance.

- Based on the potentiodynamic polarization and EIS results, it was found that all PEO coated offered significant corrosion protection to the AZ91D alloy for short immersion times (0.5 hour) prior to corrosion testing. Compared to uncoated alloy, the corrosion rate from potentiodynamic polarization was reduced by at least three orders of magnitude. The high impedance and R2 values in the EIS results demonstrated that the PEO coating did not undergo any significant degradation and that the coating at the metal-substrate interface was providing significant protection.

- As the immersion time prior to corrosion testing was increased from 0.5 hours to 6 hours and finally to 24 hours, the protective properties of the PEO coatings were greatly reduced such that for the 24 hour immersion samples, the corrosion rates for the PEO-coated samples were comparable to those for the uncoated alloy with no immersion before corrosion testing. [N.B. 24 hour immersion of the uncoated alloy would have substantially degraded the alloy]. Sealing of the PEO coating would appear to be necessary for long-term exposure in aggressive environments.

**References**

[1]     Kaesel VT, Tai PT, Bach FW, Haferkamp H, Witte F, Windhagen H. Approach to control the corrosion of magnesium by alloying. In: Proceedings of the Sixth International Conference on Magnesium Alloys and their Applications. New York: Wiley VCH, 2004. p. 534–539.

[2]    Song G, Atrens A, Recent insights into the mechanism of magnesium corrosion and research suggestions. Advanced Engineering Materials, 9(3) (2007) 177–183.

[3]     Gray JE, Luan B. Protective coatings on magnesium and its alloys – a critical review. J Alloys and Compounds, 336 (2002) 88–113.

[4]     Hussein R.O., Zhang P., Northwood D.O. and Nie X. Improving the corrosion resistance of magnesium alloy AJ62 by a plasma electrolytic oxidation (PEO) coating process. Corrosion and Materials, 36 (3) (2011) 38-49.

[5]  Gnedenkov SV, Khrisanfova OA, Zavidnaya AG, Sinebryukhov SL, Egorkin VS, Nistratova MV, Yerokhin A, Matthews A, PEO coatings obtained on an Mg–Mn type alloy under unipolar and bipolar modes in silicate-containing electrolytes. Surface & Coatings Technology, 204 (2010) 2316-2322.

[6]     Curran, JA, Clyne TW, Thermo-physical properties of plasma electrolytic oxide coatings on aluminium. Surface and Coatings Technology, 199(2-3) (2005) 168-176.

[7]     Huang VM, Wua S-L, Orazema ME, Pébèreb N, Tribollet B, Vivier V, Local electrochemical impedance spectroscopy: A review and some recent developments. Electrochimica Acta, 56 (2011) 8048– 8057.

[8]     Hussein RO, Nie X, Northwood DO, The Application of Plasma Electrolytic Oxidation (PEO) to the Production of Corrosion Resistant Coatings on Magnesium Alloys: A Review. Corrosion and Materials, 38(1) (2013) 55-65.

[9]     Hussein RO, Nie X, Northwood DO, Yerokhin A and Matthews A, Spectroscopic study of electrolytic plasma and discharging behaviour during the plasma electrolytic oxidation (PEO) process. Journal of Physics D: Applied Physics, 43 (2010) 105203.

[10]     Stem N, Geary A, Electrochemical Polarization, A Theoretical Analysis of the Shape of Polarization Curves. Journal of The Electrochemical Society, 104 (1957) 56-63.

[11]     Hussein RO, Zhang P, Xia Y, Nie X and Northwood DO, The effect of current mode and discharge type on the corrosion resistance of plasma electrolytic oxidation (PEO) coated magnesium alloy AJ62. Surface & Coatings Technology, 206 (7) (2011) 1990-1997.

[12]   Ghasemi A, Raja VS, Blawert C, Dietzel W, Kainer KU, The role of anions in the formation and corrosion resistance of the plasma electrolytic oxidation coatings. Surface & Coatings Technology, 204 (2010) 1469-1478.

[13]     EC-Lab®   Software User's Manual, 2010, http://www.bio-logic.info/.

[14]   Ghasemi A, Raja VS, Blawert C, Dietzel W, Kainer KU, The role of anions in the formation and corrosion resistance of the plasma electrolytic oxidation coatings. Surface & Coatings Technology, 204 (2010) 1469-1478.

[15]     Duan H, Yan A, Wang F, Growth process of plasma electrolytic oxidation films formed on magnesium alloy AZ91D in silicate solution. Electrochimica Acta, 52 (2007) 5002−5009.

[16]     Sreekanth D, Rameshbabu N, Venkateswarlu K, Effect of various additives on morphology and corrosion behavior of ceramic coatings developed on AZ31 magnesium alloy by plasma electrolytic oxidation. Ceramics International, 38 (2012) 4607–4615

# CHAPTER 10

# THE ROLES OF THE ELECTROLYTE COMPOSITION AND CONCENTRATION ON THE CORROSION RESISTANCE OF THE OXIDE COATINGS FORMED ON AZ91D MAGNESIUM ALLOY BY PLASMA ELECTROLYTIC OXIDATION.

**Published in:**

## 10. Introduction.

Energy efficiency is currently one of the top concerns in industry. For the automotive and aerospace sectors, a reduction in the weight of vehicles will reduce the consumption of gas and, hence, promote environmental friendliness. Magnesium is the lightest of all the engineering metals. This combined with a high strength-to-weight ratio, recyclability, good castability and weldability, makes magnesium alloys one of the most promising materials for many future applications [1]. However, magnesium and its alloys are not without their disadvantages which include: low elastic modulus, limited strength and creep resistance at elevated temperature and high chemical reactivity with associated poor corrosion resistance [1]. The protective properties of passive films on Mg are low, so they are less able to protect this very active metal against environmentally induced degradation. The idea of "stainless magnesium" is attractive. If we try to mimic the development of stainless steel, where the addition of greater than 12%Cr led to the replacement of native (non-protective) oxide with a passive (protective) oxide, we run into a number of "problems". As pointed out by Birbilis et al [2], most elements have limited solubility in Mg and therefore it is impossible to reach the critical alloying content to form the passive oxide. However, Birbilis et al [2] were able to produce "stainless magnesium" through the development of a low strength Mg-3.7wt%As alloy.

Rather than forming a passive oxide, arsenic acts as an inhibitor, by inhibiting hydrogen atom recombination. The Mg-As exhibited filiform corrosion in tests 0.1M NaCl, instead of uniform corrosion. Consequently, one of the major methods for improving the corrosion resistance of magnesium alloys is an appropriate surface treatment [3]. Coatings have found wide usage for corrosion protection of magnesium alloys and the plasma electrolytic oxidation (PEO) method has demonstrated a particular effectiveness in producing coatings with not only corrosion protection but also enhanced wear properties, hardness and toughness with better thermal stability and dielectric properties [4]. PEO-coated Mg alloys have found application in automotive engineering, electronic technology and aerospace industries. One of the earlier successful applications of PEO coated magnesium was the improvement of the corrosion resistance of helicopter gear box housings [5].

Plasma Electrolytic Oxidation (PEO), is a high voltage plasma-assisted oxidation process that transforms the magnesium metal surface, as well as other light weight metals Al and Ti, into thick, ultra-hard ceramic oxides by a plasma discharge in an electrolytic bath [6-7]. The PEO process can be considered as a combination of anodizing (electrolytic oxidation) and plasma discharging processes. The main similarities between the PEO and anodizing processes, is that both of them involve oxidation of substrate using an electrolytic bath and the first stage of the PEO process is an anodization process. Generally, for better protection of magnesium alloys from corrosion, the coatings should be compact and sufficiently thick with minimum defects, so as to isolate the magnesium alloy surface from the surrounding environment. They also should be hard enough to resist scratches and have a high dielectric strength, so that the flow of current between dissimilar metals can be reduced, thus minimizing contact corrosion. The majority of magnesium components are die-cast products, so the coating processes should be able to cope with some surface imperfections of the die-cast components, such as pores, impurities, and composition and microstructure variations. One of the main advantages of PEO process is that it can be applied to treat samples with complex shapes, and surfaces with different composition and microstructure.

The structures of the oxide layer produced by the PEO process depend on various processing parameters, including chemical composition and concentration of the

electrolyte, substrate composition and the electrical parameters including: current density, current mode and processing time [3]. In particular, the electrolyte chemistry (concentration and composition) has a significant influence on the electrochemical reactions, discharge characteristics and breakdown voltage. This, in turn, affects the microstructure, the density of porosity and other defects, thickness, and hence, the corrosion resistance of PEO coatings. Therefore, the selection of the proper electrolyte composition is important for improving the corrosion resistance of PEO-coated Mg alloys.

PEO coatings on Mg alloys and other lightweight alloys are normally produced using environmentally friendly base electrolytes (NaOH/KOH) with the addition of silicate, aluminate, phosphate or polyphosphate-containing alkaline electrolytes to increase the conductivity of the electrolyte solution. The coatings formed using only KOH at different concentrations, consist of the unstable and easily degradable MgO phase [8,9]. Addition of $Na_2SiO_3$ and $NaAlO_2$ to the KOH electrolyte, produces spinel phases, $Mg_2SiO_4$ or $MgAl_2O_4$, in the PEO coatings which provide better corrosion resistance, higher hardness and better wear properties [3, 10,11]. Increasing the amount of $Na_2SiO_3$ [10,11] or $NaAlO_2$ [3] in the electrolyte, increases the amount of the spinel phases relative to the MgO, thus further improving the corrosion properties.

There has been a significant research interest in the addition of polyvalent metal anions, such as chromate, tungstate and vanadate, to the electrolyte in the PEO processing of aluminum, titanium and magnesium alloys. With respect to a tungstate addition, the majority of the studies have been on aluminum alloys [12-17] with a more limited amount of data on titanium alloys [14,15,18-20] and magnesium [21-25]. With the exception of the study by Zhao et al [22], it was generally found that incorporation of tungstate into the electrolyte produced a more compact coating with improved corrosion and wear resistance.

Figure 10.1 schematically illustrates the parameters that affect the coating quality. During PEO coating, there are three simultaneous processes taking place, namely the electrochemical reactions, the plasma chemical reactions and thermal oxygen diffusion [3]. The PEO process of light-weight metals is strongly influenced by such parameters as electrolyte composition and concentration, current or voltage applied and substrate alloy.

Generally, these parameters have a direct influence on the discharging behavior: type, size, duration, population density and temperature. The discharges play an essential role in the formation and resulting composition of the 3-layer oxide structure, by influencing phase transformations, crystallization and sintering. This, then, affects the physical, mechanical and chemical properties of the coating. A detailed knowledge of the coating mechanisms is extremely important in order to produce a desired coating quality to reach the best performance of the PEO coatings in terms of corrosion resistance and tribological properties (wear rate, COF).

In this study PEO coatings were formed on an AZ91D magnesium alloy using a base KOH electrolyte with additions of an aluminate ($Na_2Al_2O_4$) and tungstate ($Na_2WO_4$) to increase the electrolyte conductivity. The effects of modifying the electrolyte on the surface morphology, microstructure and chemical composition of PEO coatings were determined using scanning electron microscopy (SEM) and energy dispersive analysis (EDS). The corrosion resistance was determined using potentiodynamic polarization in a 3.5% NaCl solution and is then related to the coating structure.
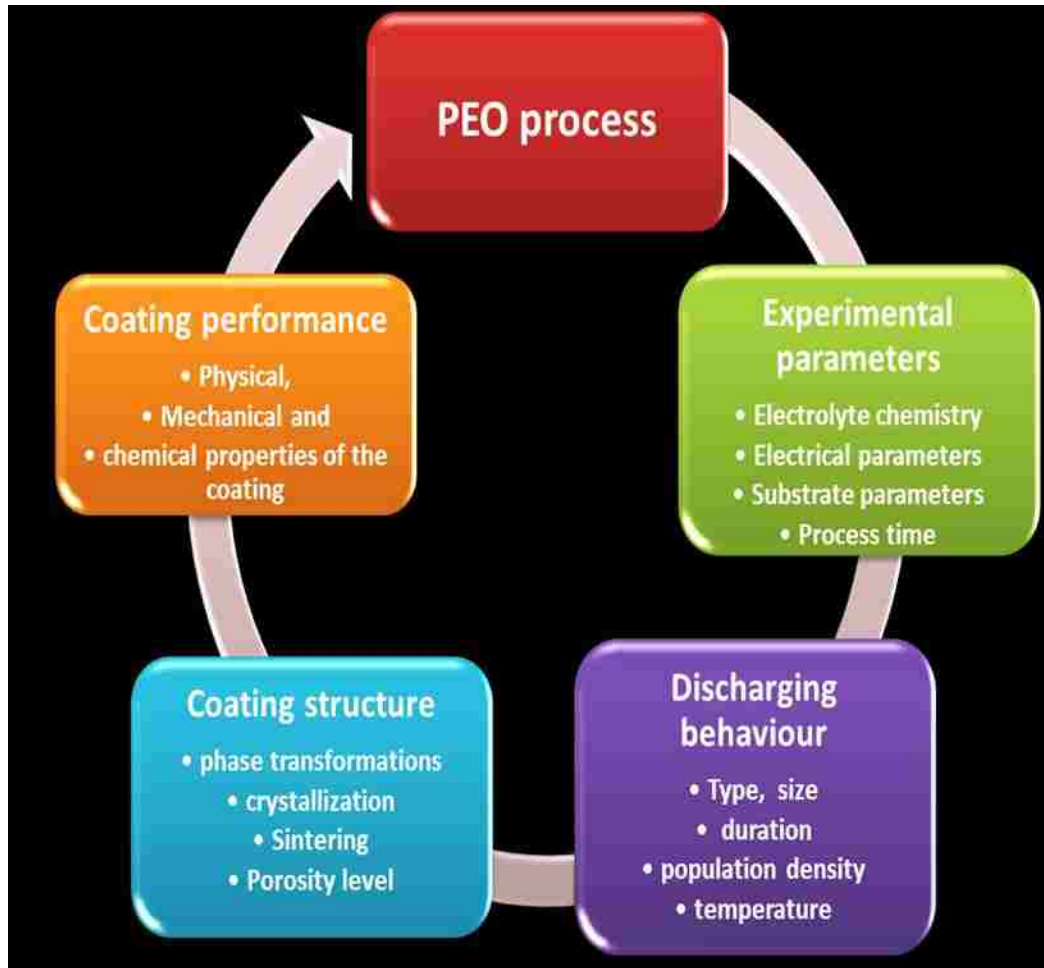
Fig. 10.1 PEO process properties, mechanisms and performance

## 10.2. Experimental Procedures

### 10.2.1 Materials and PEO Processing Method

Disc-shaped coupons (25×7mm) cut from AZ91D bar was used as the substrate. The coating was obtained in an alkaline electrolyte containing different concentrations of $Na_2Al_2O_4$, KOH and $Na_2WO_4.2H_2O$, as shown in Table 10.1. The processing parameters for the coated Mg samples are listed in Table 10.2. The PEO coating process was carried out under a constant current using a bipolar current mode. Process parameters, are listed in Table 10.2.

Scanning electron microscopy (FEI Quanta 200 FEG with solid state backscattered detector operated at 10 KV) in the secondary electron (SE) mode was used to observe

both the coating surface morphology and, through observation of sample cross sections, coating thickness and integrity. To identify the phases generated during the PEO coating, analytical X-ray diffraction (XRD) was performed on all coated samples. Copper Kα radiation (wavelength k = 0.15406 nm) was employed at a tube current of 45 mA and a voltage of 45 kV. For phase identification, the scan range varied from 10 to 80° (in 2θ) with a step size of 0.05o and 1.5s in each step.

Table 10.1 Electrolyte composition for PEO processing of AZ91D

| Sample | KOH (g/l) | $Na_2Al_2O_4$ (g/l) | $Na_2WO_4.2H_2O$ (g/l) |
|--------|-----------|---------------------|------------------------|
| S1 | 2 | 8 | 0.0 |
| S2 | 2 | 8 | 1.0 |
| S3 | 2 | 8 | 2.0 |
| S4 | 2 | 8 | 6.0 |
| S5 | 2 | 15 | 0.0 |

Table 10.2.  PEO processing parameters for coating  AZ91D Mg alloy.

| Sample | Current mode | Time (min) | $I^+$ (A) | $I^-$ (A) | $T_{on}^+(\mu s)$ | $T_{on}^-(\mu s)$ | $T_{off}^+(\mu s)$ | $T_{off}^-(\mu s)$ | $C_R$ |
|--------|--------------|------------|-----------|-----------|-------------------|-------------------|--------------------|--------------------|-------|
| All | Bipolar | 15 | 1.0 | 0.8 | 400 | 100 | 400 | 100 | 0.83 |

To determine the corrosion resistance of the PEO coating, potentiodynamic polarization tests were carried out for uncoated and coated samples at 25 $^o$C using a Solartron 1285 Potentiostat with Corrware software. A three electrode cell with the coated samples as the working electrode, an Ag/AgCl/sat KCl reference electrode, and platinum as a counter electrode, was used in the experiments. When the corrosion potential remained stable the potential were scanned from -0.15V versus open circuit potential up to -2.0 V versus the reference electrode at a rate of 1.0 mV/s.

## 10.3. Results

### 10.3.1 Voltage Behavior.

Figure 10.2(a) shows plots of the anodic output voltage versus treatment time for the 5 electrolyte compositions. Such plots are typical for the PEO process [27] except that only

three stages, I, II, III, are seen. The normal stage IV was not seen since the PEO treatment time used, namely 15 minutes, was too short for stage IV to be attained. The three stages seen were as follows: Stage I:  In the early stage of the process, which mainly involves the rapid electrochemical formation of an initial insulating oxide film corresponding to the traditional anodizing stage, a sharp increase in the voltage was seen. Stage II: The rate of the voltage change decreases in this stage, which is characterized by numerous sparks moving rapidly over the whole sample surface area. This indicates the start of the breakdown of the oxide layer and corresponds to the moment when the surface of the alloy becomes totally covered by the PEO film. Stage III: In this stage the voltage remains relatively stable and characterized by larger but slower moving discharges.

The slope of the curve at initial stages (region I) depends strongly on the electrolytic composition. This behavior is more clearly observed in the inset, Fig. 10.2(b). For the S1 and S5 samples which were coated in an electrolyte containing no tungstate, the time required to reach the breakdown voltage (the point on the curve where the slope drastically changes and the initiation of sparks occurs) is longer than that for samples coated in electrolytes which contain tungstate (S2,S3 and S4): see Table 10.3. Also, as the aluminate concentration increases, S1 to S5, the slope increases. Samples coated in an electrolyte containing tungstate (S2,S3 and S4) show sharper increases in V-t slope compared with S1 and S5 and as the concentration of the tungstate increases, the slope also increases, indicating that the time to reach breakdown voltage is shorter for sample S4 compared with S1, S2  and S3. Looking at the breakdown voltages for the different electrolytes, Table 10.3, compared to the breakdown voltage (390 V) for the base aluminate/KOH electrolyte, S1, there is a decrease in breakdown voltage on increasing either the aluminate concentration or adding tungstate.
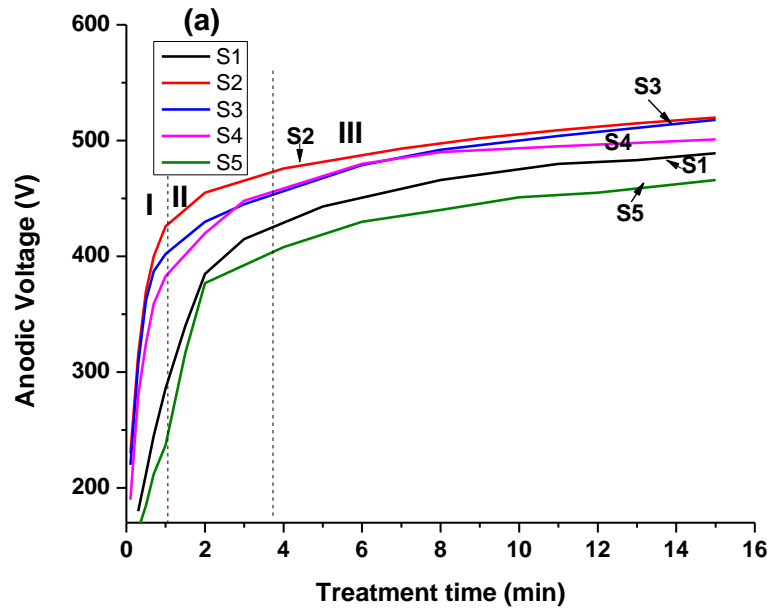
Fig. 10.2 Plots of anodic voltage vs. treatment time during the PEO process using bipolar current mode: the three discharge stages I, II and III are identified with respect to sample S2.

Table 10.3 Breakdown voltage and time, thickness, color and composition of coating.

| Sample | Break down | | Coating thickness (μm) | Color | Composition (wt%[*]) | | | |
|---|---|---|---|---|---|---|---|---|
| | v(V) | t(min) | | | O | Mg | Al | W |
| S1 | 390 | 2.0 | 25.2±2.5 | gray | 37.33 | 33.3 | 29.08 | 0.0 |
| S5 | 360 | 1.5 | 22.8±2.3 | gray | 38.28 | 26.9 | 34.71 | 0.0 |
| S2 | 375 | 0.50 | 30.0±3.0 | gray/light green | 37.44 | 33.4 | 26.85 | 2.3 |
| S3 | 360 | 0.40 | 28.5±2.9 | gray/medium green | 36.13 | 30.7 | 30.06 | 3.1 |
| S4 | 280 | 0.25 | 43.4±4.5 | Green with black spots | 35.18 | 29.3 | 26.91 | 8.6 |

**\* As neasured at the surface of the coatings using EDS**

The results for the effect of the NaWO$_4$ addition on the breakdown voltage are consistent with those of Ding et al [24] for an AM60B Mg-alloy in a silicate-KOH electrolyte, namely as the tungstate content increases, there is a corresponding decrease in the breakdown voltage. Ding et al [24] relate this decrease in the breakdown voltage to the

increase in electrolyte conductivity with increasing tungstate concentration as predicted theoretically by Ikonopisov [28].


**10.3.2 Coating Microstructure, Morphology and Composition.**

A summary of the coating microstructures, morphology and compositions is given in Table 10.3 and Fig. 10.3. Figure 10.3 contains three sets of information on the PEO coatings obtained using the five different electrolytes. Figs. 10.3(b,e,h,k and n) are SEM micrographs of the surface morphology. Figs. 10.3 (a,d,g,j and m) are SEM micrographs of cross-sections of the coatings. The coating thickness values listed in Table 10.3 were obtained from these cross-sections. Figs. 10.3(c,f,i,l and o) are the EDS spectra obtained from the surface of the coatings. The quantitative compositional analysis obtained using these spectra are given in Table 10.3.

The SEM micrographs of the coating surfaces, Figs. 10.3(b,e,h,k and n) show that all surfaces consist of a number of 'pancake-like' features and discharge pores which are irregularly arranged on the coating surface. Because of the local high temperature and the strong electric field, molten oxide is ejected from the coating/substrate interface into the coating surface where it is rapidly solidified and re-crystallized by the electrolyte which may also cause micro-cracks which are present on the coating surface. Sample S5 produced with a concentrated aluminate electrolyte shows a relatively smoother surface compared with S1 produced with a more dilute aluminate electrolyte. Samples S2,S3,S4 coated with a tungstate-containing electrolyte show relatively larger 'pancake-like' features indicating strong discharges and thereby increase the roughness of the surface.

The cross-sectional micrographs, Figs. 10.3(a, d, g and m), show that all coatings are composed of a porous outer layer, an intermediate layer that is relatively dense and a thin inner dense (barrier) layer that is well adhered to the substrate. Such a multilayer structure is common for PEO coatings on magnesium alloys [3] but the relative thickness, microstructure and composition of the layers depends on both the material and the PEO processing parameters. If we first compare the coatings produced without a tungstate addition, we can see that the coating prepared in the dilute (8g/l) aluminate electrolyte, S1, is about 25 μm thick but contains a significant amount of connected porosity and other defects both within the coating and near the coating/substrate interface, Fig. 10.3(a).

Large pores were also evident on the surface of the coating, Fig. 10.3(b). Increasing the aluminate concentration to 15 g/l, S5, produced a slightly thinner coating (≈22μm) but the coating was denser and contained less micro-scale defects and cracks, Figure 10.3(d). Also compared to S1 there were fewer large pores visible on the surface, Figure 10.3(e). As an increasing amount of tungstate was added to the 8g/l aluminate, there was a general increase in thickness, Figs. 10.3(g,j,m). However, it is important to note a key change in the barrier layer at the substrate/coating interface which becomes thicker and is clearly visible in Figs. 10.3(j) and (m). It is this barrier layer that is particularly important in determining the corrosion resistance [3].

Turning now to the composition of the coatings, as given Table 10.3 and obtained from the EDS spectra given in Figs. 10.3(c,f,i,l,o), we can readily see that the main components af all coatings are O, Mg and Al. It is instructive to examine any changes in composition relative to sample S1, i. e. lower aluminate concentration (8g/l) and no tungstate addition.

Increasing the aluminate concentration to 15g/l (S5), gives a small increase in O content, a significant increase in Al content and matching decrease in Mg content. This is consistent with previous studies that showed that increasing the amount of $NaAlO_2$ in the electrolyte lead to an increase in the amount of the spinel phase, $MgAl_2O_4$, relative to MgO. The addition of tungstate to the base aluminate (8g/l) electrolyte produced a somewhat different result: see S2, S3 and S4. The O and Mg contents were reduced, relative to S1, for higher tungstate additions, namely 2.0 and 6.0g/l. The Al content fluctuated but generally decreased with increasing tungstate addition. The W content of the coating increased with increasing tungstate addition to electrolyte, indicating the incorporation of tungsten into the oxide. This is also reflected in a color change of the PEO coating from gray to green to green with black spots: Table 10.3. Thus in the higher tungstate electrolytes, rather than forming more spinel phase, as in the high aluminate electrolyte, a tungsten-containing oxide is formed, possibly $WO_3$ [24,29].
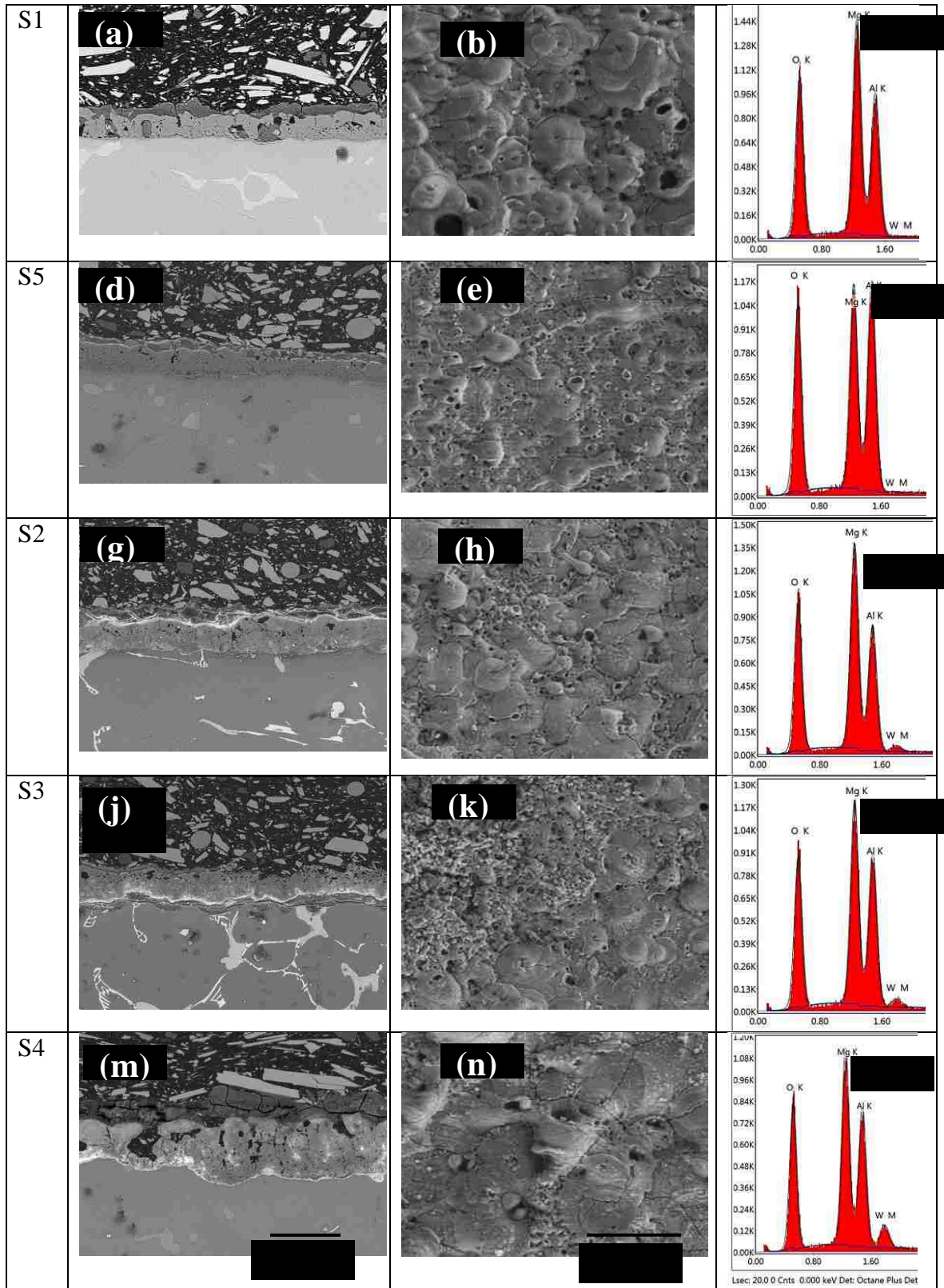
Fig. 10.3 EDS and SEM micrographs showing the surface morphology and cross section of oxide coatings on AZ91D alloy for different electrolyte concentration and compositions.

| (a) S1 | (b) S5 | (c) S4 |
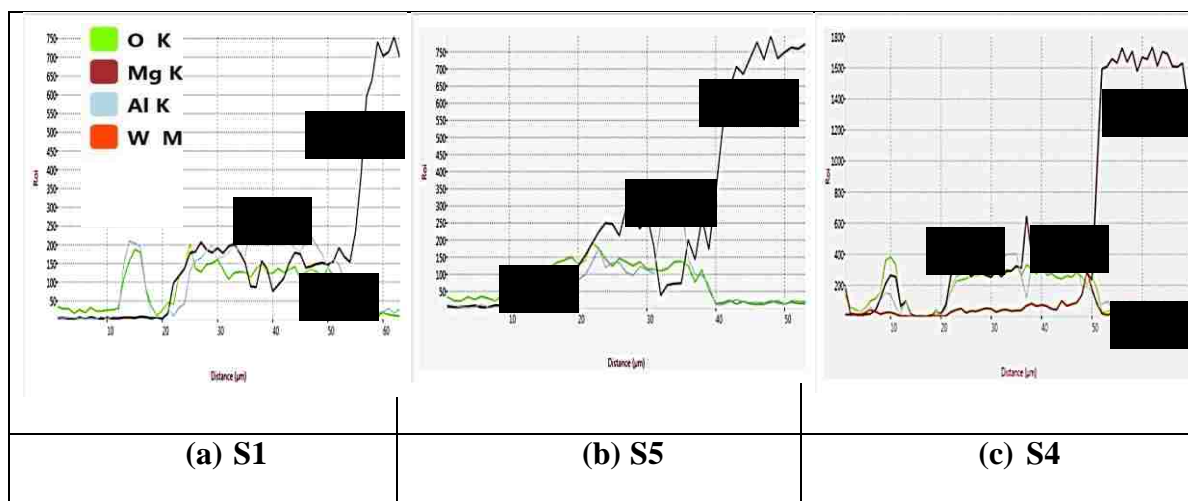
Fig. 10.4 Elements linear scanning analysis of the PEO coating formed in electrolyte containing (a) 0 g/l ($Na_2WO_4$) to the base 8g/l $Na_2Al_2O_4$/KOH electrolyte (b) 0 g/l ($Na_2WO_4$) to the 15g/l $Na_2Al_2O_4$/KOH electrolyte and (c) 6 g/l ($Na_2WO_4$) to the base electrolyte by EDX.

To identify the generation of phases during the PEO, energy dispersive spectroscopy (EDS) element line scanning analysis has also been performed across the entire cross section as shown in Fig. 10.4. The result of EDS shown in Fig 10.4(a) indicates that Mg, O, and Al elements were the major components and distributed almost regularly across the thickness of the coating formed in an electrolyte containing 8g/l g/l $Na_2Al_2O_4$ with no tungstate added to the electrolyte: sample S1. The results for S5, 15 g/l $Na_2Al_2O_4$ with no tungstate added, show that the aluminum concentration increases close to the coating/substrate interface, Fig. 10.4(b). However Fig. 10.4(c) shows that for the coating formed in an electrolyte containing 6 g/l $Na_2WO_4$ addition to the base $Na_2Al_2O_4$/KOH electrolyte, Mg, O, Al and W were the major components and the W concentration gradually increases with the coating depth reaching a maximum value near the coating/substrate interface.

### 10.3.3 The XRD patterns of the coatings

X-ray diffraction (XRD) analysis was used to further verify the above microstructural phase identification, and to investigate the changes in composition and phase analysis of PEO coatings due to the changes of the electrolytic composition and concentration. XRD spectra of all PEO-coated samples are shown in Fig. 10.5(a). Detailed identification of the phases present for samples S1 and S4 are given in Fig. 10.5(b) and (c), respectively.

183

For the oxide coatings formed on AZ91D in a KOH-NaAl$_2$O$_4$ electrolyte without the addition of tungstate, the periclase phase MgO, together with the spinel phase MgAl$_2$O$_4$, are the main phases present in the coatings, regardless of the aluminate concentration. Some amorphous phase was also observed, which appears on the XRD pattern as a broad peak at 2$\Theta$ values less than 17$^o$. However, the treatment of AZ91D Mg alloy in the electrolyte containing concentrated aluminate sample S5 increases the amount of MgAl$_2$O$_4$. Based on the intensities of the strongest peaks corresponding to MgAl$_2$O$_4$ at 2$\Theta$ values of 19$^o$, 31$^o$ and 45$^o$, the relative amount of MgAl$_2$O$_4$ in the coating was increased by 1.3 to 1.7 times, when comparing S1 and S5 see Fig. 10.5(a). These observations are consistent with those of an earlier study of PEO-coating formed on a AM60B Mg-alloy [24] which showed that when the aluminate concentration increased, the relative amount of the spinel MgAl$_2$O$_4$ phase to the MgO phase also increased. For coatings produced using mixed aluminate-tungstate electrolytes (S2, S3, S4) as well as MgO, and an increased amount of MgAl$_2$O$_4$, the tungsten containing phases WO$_3$ and MgWO$_4$ are also present. The addition of 1g/l tungstate to the base electrolyte (S2) increases the intensity of the spinel phase MgAl$_2$O$_4$ relative to the MgO phase. The intensity of the amorphous phase also increases and the MgWO$_4$ phase starts to appear in the XRD pattern. Fig. 10.5(a) shows that the addition of 2g/l tungstate to the base electrolyte (S3) further increases the fraction of spinel phase MgAl$_2$O$_4$ and decrease the fraction of periclase MgO. The addition of 6g/l tungstate (S4), Fig. 10.5(c), causes the amorphous phases to disappear leaving the hard spinel MgAl$_2$O$_4$ phase, and creates the new phases, WO$_3$ and MgWO$_4$ which cause the greenish color with some black spots on the samples. The peaks due to the substrate Mg decrease dramatically indicating that the coating gets thicker and more compact. The addition of the tungstate to the base electrolyte influences the PEO discharge processes due to the changes in electrolyte conductivity characteristics which then influence the deposition growth rate and phase composition of the oxide coatings. Hwang et al [30] have shown that the presence of WO$_3$ in the oxide layers will significantly improve the adhesion strength between the substrate and the oxide coating.

Fig. 10.5 XRD patterns of oxide coatings formed in aluminate-KOH electrolyte with addition of different concentrations of $Na_2WO_4$: (a) all samples (b)0 g/l $Na_2WO_4$, and (c) 6.0 g/l $Na_2WO_4$.

## 10.3.4 Electrochemistry of Plasma Electrolytic Oxidation (PEO)

The growth of the oxide coating mainly occurs due to three different, yet simultaneous, processes, namely: the electrochemical reactions; the plasma chemical reactions; and thermal diffusion [27]. The electrochemical formation of surface oxide layers can occur through different mechanisms depending on the electrolyte, eg. silicates, aluminates, tungstate. The main electrochemical reactions occur at the coating/electrolyte interface. The plasma chemistry of the surface discharges involves, on one hand, charge transfer at the substrate/electrolyte interface, and on the other hand, strong ionization and charge transfer effects between the substrate surface and the electrolyte through the oxide layer

185

with the aid of the plasma. During the PEO process different type of discharges will take place [3]. An important consequence of the occurrence of those discharges is the development of metallurgical processes in the growing oxide layer, which are induced by the heat liberated in discharge channels from electron avalanches.

The increase in conductivity of the electrolyte may cause an increase in the deposition growth rate of PEO coatings. Complex compounds (oxides of both the substrate material (Mg) and electrolyte-base elements (Al and W)) can be created inside the discharge channels formed during PEO process across the growing oxide layer. During the PEO coating of magnesium alloys in the electrolyte contains aluminates, the aluminate ions enter into the film through the main electrochemical reactions that occurs at the metal/oxide and oxide/electrolyte interfaces are as follows [3]:

$$Mg \rightarrow Mg^{2+} + 2e^- \qquad\qquad \textbf{10.1}$$

$$Mg^{2+} + 2OH^- \rightarrow Mg(OH)_2 \qquad\qquad \textbf{10.2}$$

$$Mg(OH)_2 \rightarrow MgO \downarrow + H_2O \qquad\qquad \textbf{10.3}$$

$$Mg^{2+} + 2AlO_2^- \rightarrow MgAl_2O_4 \downarrow \qquad\qquad \textbf{10.4}$$

The cation released from the metal (reaction (10.1)) combines with the anion in the electrolyte to form compounds $Mg(OH)_2$ and/or $Mg_2AlO_4$. As the concentration of $Na_2Al_2O_4$ increase, more aluminate ions participate in coating formation which results in an increase in the volume fraction of the $MgAl_2O_4$ phase and an increase in corrosion resistance. The unstable hydroxide $Mg(OH)_2$ dehydrates to MgO by the high temperature (reaction (10.3)), resulting in the discharge channels from the plasma discharge.

The existence of $Na_2WO_4.2H_2O$ in the electrolyte will cause some of the $WO_4^{2-}$ ions to lose the electrons forming the black $WO_3$ compound. The main electrochemical reactions occurring during the PEO process in tungstate-containing electrolytes are as follows [29]:

$$2WO_4^{2-} - 4e^- \rightarrow 2WO_3 + O_2 \uparrow \qquad\qquad \textbf{10.5}$$

$$WO_3 + 3Mg \rightarrow 3MgO + W \qquad\qquad \textbf{10.6}$$
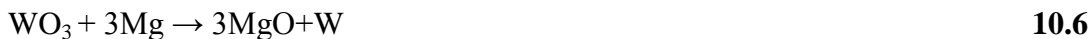
As noted in section 10.3.2, the ceramic layer which was formed in the electrolyte with addition of $Na_2WO_4.2H_2O$ exhibit different colors. The greenish color with some black spots may be related to the presence of $WO_3$ and $Na_2WO_4$ in the coating.

## 10.3.5 Corrosion Resistance of the Coatings

The potentiodynamic polarization curves at room temperature of uncoated AZ91D Mg alloy and PEO-coated materials at two different aluminate concentrations and four different tungstate concentrations after immersion in a 3.5% NaCl solution for 0.33h immersion time are shown in Figs. 10.6(a) and (b) respectively, and the associated electrochemical data are listed in Table 10.4. The corrosion potentials (Ecorr), corrosion current density (Icorr) and anodic/cathodic Tafel slopes $\beta a$ and $\beta c$ were derived from the test data. Based on the approximately linear polarization at the corrosion potential, the linear polarization resistance (Rp) values were calculated. The average corrosion rate, $P_i$ (mm/year) can be calculated from the corrosion current density, $i_{corr}$ ($\mu A/cm^2$) using the equation 4.4 (chapter 4). The protection efficiency ($P_{EF}$ %) afforded by the coating has also been calculated using the equation 3.5:
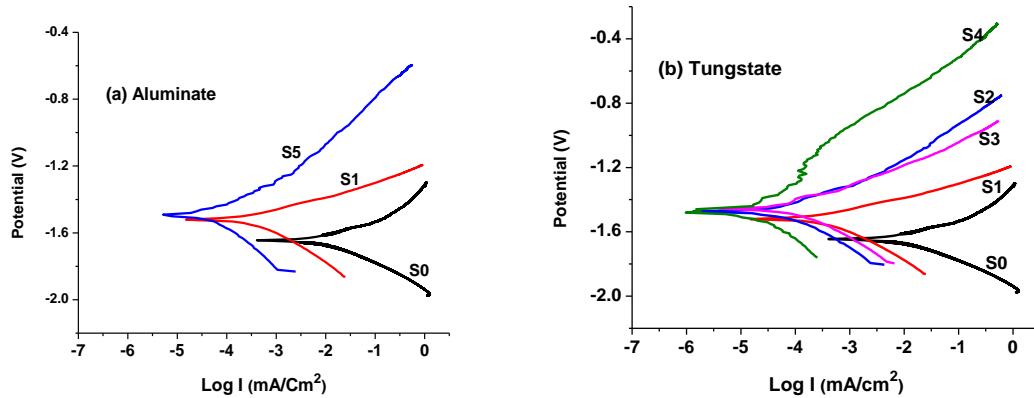


Fig. 10.6 Potentiodynamic polarization curves of the uncoated (S0) and coated samples with (a) different aluminate concentrations (S1 and S5) and (b) different tungstate concentrations (S1 – S4), for 0.33h immersion time.

Compared to the uncoated AZ91D, all samples with PEO-coatings exhibited a higher polarization resistance, a lower corrosion current density and a higher (more noble) corrosion potential, regardless of the composition or concentration of the electrolyte. For the uncoated AZ91 Mg alloy, the corrosion current density (Ecorr), associated corrosion potential (Icorr), and corrosion resistance Rp were determined to be -1.64 vs. Ag/AgCl/sat KCl., 7.97 $\mu A/cm^2$, 3.0 K$\Omega$/cm2, respectively. The differences in the level of protection observed for the five samples are considered to be related to differences in coating

compactness, thickness, porosity and density of other defects. The changes in the curves caused by an increase in the aluminate content in the electrolyte (Fig. 10.6(a)) are to shift the polarization curves to a lower corrosion current density and a higher (more noble) corrosion potential. By changing the concentration of tungstate from 0g/l to up to 6g/l in the electrolyte, the corrosion current density decreased from $1.56 \times 10^{-1}$ $\mu A/cm^2$ to $9.00 \times 10^{-3}$ $\mu A/cm^2$, the corrosion potential increased from (-1.52 V) to (-1.47 V) and the polarization resistance increased from 120   $k\Omega/cm^2$ for S1 to 3640 $k\Omega/cm^2$ for S4, as shown in Fig. 10.6(b) and Table 10.4.

**Table 10.4.  Potentiodynamic polarization corrosion test results in3.5%wt NaCl solution**

| Sample | Immersion time | $E_{corr}$ (V) | $I_{corr}$ ($\mu A/cm^2$) | $\beta_a$ (mV) | $\beta_c$ (mV) | Rp ($K\Omega/cm^2$) | $P_i$ (mm/year) | $P_{EF}$ % |
|---|---|---|---|---|---|---|---|---|
| S0 | 0.33 h | -1.64 | 7.97 | 100 | 123.6 | 3.0 | 1.82E-01 | N/A |
| S1 | 0.33h | -1.52 | 0.156 | 73.1 | 104.9 | 120 | 3.56E-03 | 39 |
|  | 24h | -1.53 | 4.60 | 90.3 | 271.1 | 6.4 | 1.05E-01 | 1.1 |
| S3 | 0.33h | -1.46 | 0.006 | 122.2 | 133.5 | 462 | 1.37E-3 | 237 |
|  | 24h | -1.48 | 3.100 | 221.8 | 261.8 | 16.8 | 7.08E-02 | 4.5 |
| S4 | 0.33h | -1.47 | 0.0009 | 150.7 | 150.8 | 3640 | 2.06E-04 | 153 |
|  | 24h | -1.48 | 0.386 | 225.3 | 247.4 | 133.3 | 8.82E-03 | 43 |
| S5 | 0.33 h | -1.49 | 0.043 | 153.3 | 211.3 | 898 | 9.83E-4 | 1212 |
|  | 24 h | -1.49 | 2.12 | 309.1 | 330.9 | 32.8 | 4.84E-02 | 10 |

This significant improvement of the corrosion resistance of S4 relative to S1 is attributed to the two factors. First, the coating is more compact with lower porosity/defects density. Secondly, the coating contains the W-containing phases, $WO_3$ and $MgWO_4$, and a higher $MgAl_2O_4$ spinel content than coatings produced using dilute aluminate-only electrolyte (S1). Hence, for short immersion time, it is suggested that the aggressive Cl⁻ ions penetrate through the larger pores in the outer layer, possibly through the intermediate dense layer, but are prevented from reaching the Mg-alloy substrate by the dense interface layer, where the tungsten content is highest (see Fig 10.4(c)), and it is possible

that $WO_3$ or $MgAl_2O_4$ may act in the manner of an inhibitor. These results showing an improvement in corrosion resistance with increased tungstate additions to an aluminate-based electrolyte are in agreement with the results of previous studies [23,24] for tungstate additions to a silicate-based electrolyte, which were also obtained at short immersion times.

Figure 10.7 shows the relationship between polarization resistance (Rp) and coating thickness. If we look only at the data for coatings produced with an electrolyte containing 8g/l aluminate and 0-6g/l tungstate, a cursory examination of the data would suggest, as indicated in Fig. 10.7, that there is a linear relationship between Rp and the thickness of the PEO coating. However, as described in Sections 10.3.2 and 10.3.3, a change in the electrolyte composition and concentration produces not only a change in thickness (growth rate) of the coating but also a change in the multilayer structure of the coating, including porosity and phase composition. This is further reinforced when comparing S1 with S5, where the aluminate concentration in the electrolyte has been increased from 8g/l to 15 g/l. Although Rp for the coating has been increased seven-fold, from 120 to 898 $k\Omega/cm^2$, the coating thickness (growth rate) was slightly decreased. This increased corrosion resistance is due to a lower level of porosity and defects in the coating and the partial replacement of MgO with the spinel phase $MgAl_2O_4$. These observations are consistent with other studies [31,32] of anodic films formed on a Mg-Al alloy which have shown that as the aluminate concentration increased, the solution conductivity increased, the breakdown voltage decreased, and the relative amount of the spinel $MgAl_2O_4$ phase to MgO phase increased.
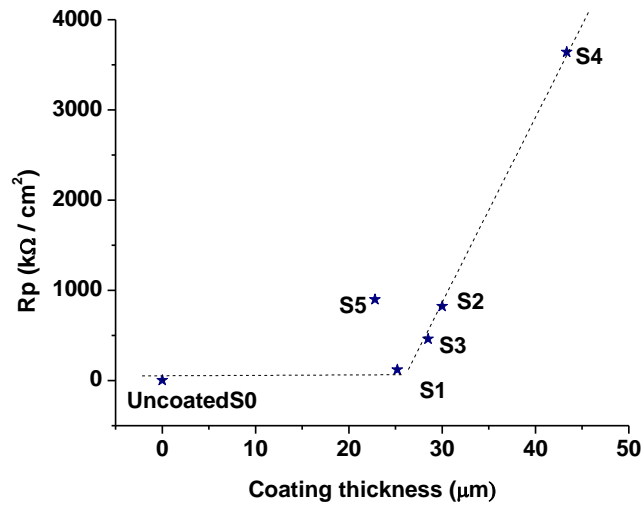
Fig. 10.7. Polarization resistance (Rp) as a function of coating thickness

The potentiodynamic polarization curves of the uncoated AZ91D Mg alloy (S0) for 0.33h and PEO-coated samples as a function of aluminate concentration and tungstate concentration in the electrolyte for a 24h immersion time are shown in Figs. 10.8(a) and (b), respectively. As shown in Fig. 10.8(a) and Table 10.4, the potentiodynamic polarization corrosion test results for the coated AZ91D Mg alloys after 24 hours immersion prior to corrosion testing are significantly different from those of the 0.33h immersion. The experimental polarization diagram recorded for the 24h immersion time shows a significant increase in Icorr compared to the 0.33h immersion. There is a corresponding reduction in polarization resistance from 120 to 6.4 KΩ cm2 for the coating formed in a dilute aluminate electrolyte (S1*) and from 898 to 33 KΩ/cm2 for the coating formed in concentrated aluminate electrolyte (S5*). The longer immersion time allows the electrolyte to penetrate through the coating via the interconnected micro-pores and reach the substrate. There may also be partial dissolution during the immersion period. The magnitude of Pi was increased to the range of 0.1 to 0.05 mm/year for S1* and S5* respectively. However, Rp, at least for the high aluminate coating, was still 10 times higher than that of the uncoated Mg alloy. Sealing the coating would appear to be necessary to protect against long term exposure in aggressive environments.
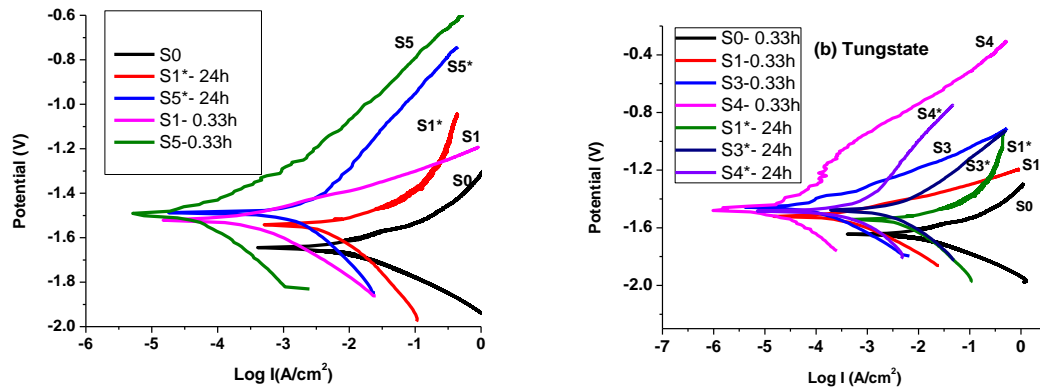
Fig. 10.8 Potentiodynamic polarization curves of the uncoated (S0) for 0.33h and coated samples with (a) two aluminate concentration (S1 and S2) and (b) different tungstate concentrations (S1, S3 and S4). (*) for 24h immersion time.

The effect of tungstate addition to the electrolyte on the corrosion properties of the coated samples immersed for 24 h is shown in Fig. 10.8(b) and Table 10.4. Due to the relatively thicker and more compact coatings on S4 treated with the addition of 6g/l tungstate to the electrolyte, the value of the polarization resistance after 24h immersion time is 133 KΩ/cm2 which is higher than the corrosion resistance of the other coated samples immersed for 24h and is 50 times better than the uncoated sample immersed for 0.3h. The magnitude of Pi was increased to the range of 0.1 to 0.009 mm/year for S1* and S4* respectively. As shown in Table 10.4, the values of Rp ranging from 6.4  kΩ cm2 for S1 to 900 kΩ cm2 for S4 sample. According to the change of the potentiodynamic polarization curves and corrosion behavior with immersion time, the protective properties of the PEO coatings in aggressive environment can be severely degraded after 24 hours immersion prior to corrosion testing. This can be attributed to the high levels of connected porous (microcracks and residual pores from plasma discharges). With increasing of immersion time, not only the outer porous layer but also the interface dense layer was also partially penetrated by the aggressive $Cl^-$ ions by thinning MgO, MgAl2O4 and MgWO4 of the interface layer, reaching the substrate. Sealing the outer porous layer using techniques such as simple sealing using sodium silicate (water glass), or by boiling in hot water, or using a multi-layer system (painting or sol-gel coating) seems to be a useful solution for further improving the service life [33].

Returning to the coatings formed in a tungstate-containing electrolyte (S2, S3, S4), as well as the enhanced formation of the spinel phase, there is a higher growth rate of the coating, i. e. thicker coatings, and the incorporation of a tungsten-containing oxide (WO3) into the coating. There is also a thicker barrier layer at the coating-substrate interface in S3 and S4, Figs. 10.3(j,m). It is this barrier layer and the relatively dense intermediate layer, rather than the outer porous layer that is easily penetrated by the electrolyte that are the main contributors to any enhanced corrosion resistance. There is the open question as to whether the tungsten-containing oxide acts like the spinel in improving corrosion resistance or whether it has some inhibitive effect. Although there is not a linear relationship between Rp and the tungstate concentration in electrolyte or wt% W in coating, our results showing an improvement in corrosion resistance with increased tungstate additions to an aluminate-based electrolyte are in agreement with those by Li et al [23] and Ding et al [24] for tungstate additions to a silicate-based electrolyte.

## 10.4. Conclusions

Potentiodynamic polarization corrosion testing of an AZ91D Mg-alloy PEO coated in a base electrolyte containing 2g/l KOH together with varying levels of $Na_2Al_2O_4$ (8 or 15 g/l) and $Na_2WO_4 . 2H_2O$ (0, 1, 2, 6 g/l) show that the electrolyte concentration and composition directly influences the surface morphology, coating microstructure, porosity level, thickness and phase composition of the coatings, which, in turn, affects the corrosion performance.

- Increasing the aluminate concentration in the electrolyte from 8 to 15 g/l, produces a coating that is denser and contains a higher amount of the spinel phase relative to MgO. This produces a more corrosion resistant coating.
- The addition of tungstate to an electrolyte containing 8g/l aluminate, increases the conductivity of the electrolyte, lowers the break-down potential, lowers the porosity/defect density of the coatings, increases the coating growth rate and producing thicker substrate/coatings interface layer, increases the $MgAl_2O_4$ spinel phase content and leads to the formation of the tungstate-containing phases $WO_3$ and $MgWO_4$..

- The corrosion resistances of the W-containing coatings, at least at the highest tungstate addition to the aluminate electrolyte, are much improved over those produced using only the aluminate electrolyte.

- According to the change of the potentiodynamic polarization curves and corrosion behavior with immersion time, the protective properties of the PEO coatings in aggressive environment can be severely degraded after 24 hours immersion prior to corrosion testing. Sealing of the porous outer layer of the coating is suggested as a mean of increasing the overall service life.

## References

[1] Mordike BL, Ebert T, Magnesium properties-applications-potential. Materials Science and Engineering, A302 (2001) 37-45.

[2] Birbilis N, Williams G, Gusieva K, Samaniego A, Gibson MA, McMurray HN, Poisoning the corrosion of magnesium. Electrochemistry Communications, 34 (2013) 295-298.

[3] Hussein RO, Nie X, Northwood DO. The application of plasma electrolytic oxidation (PEO) to the production of corrosion resistant coatings on magnesium alloys: a review. Corrosion and Materials, 38 (1) (2013) 54-65.

[4] Hussein RO, Zhang P, Xia Y, Nie X and Northwood DO, The effect of current mode and discharge type on the corrosion resistance of plasma electrolytic oxidation (PEO) coated magnesium alloy AJ62. Surface & Coatings Technology, 206 (7) (2011) 1990-1997

[5] Blawert C, Dietzel W, Ghali E and Song G, Anodizing Treatments for Magnesium Alloys and Their Effect on Corrosion Resistance in Various Environments. Advanced Engineering Materials, 8 (2006) 511-533.

[7] Yerokhin AL. Nie X, Leyland A, Matthews A and Dowey S J, Plasma electrolysis for surface engineering. Surface & Coatings Technology, 122 (1999) 73-93.

[7] Hussein R.O., Zhang P., Northwood D.O. and Nie X, Improving the Corrosion Resistance of Magnesium Alloy AJ62 by a Plasma Electrolytic Oxidation (PEO) Coating Process. Corrosion and Materials, 36 (3) (2011) 38-49.

[8] Ma Y, Nie X, Northwood DO and Hu H, Systematic study of the electrolytic plasma oxidation process on a Mg alloy for corrosion protection. Thin Solid Films, 494 (2006) 296-301.

[9] Cai Q, Wang L, Wei B, Lin Q, Electrochemical performance of microarc oxidation films formed on AZ91D magnesium alloy in silicate and phosphate electrolytes. Surface & Coatings Technology, 200 (2006) 3727-3733.

[10] Weiyi M, Yong H, Study on Micro-Arc Oxidized Coatings on Magnesium in Three Different Electrolytes. Rare Material and Engineering, 39 (2010) 1129-1134

[11]    Ghasemi A, Raja VS, Blawert C, Dietzel W, Kainer KU, The role of anions in the formation and corrosion resistance of the plasma electrolytic oxidation coatings. Surface & Coatings Technology, 204 (2010) 1469-1478.

[12]    Hwang IJ, Shin KR, Lee JS, Ko YG,  Shin DH, Formation of black ceramic layer on aluminum alloy by plasma electrolytic oxidation in electrolyte containing Na2WO4. Materials Transactions, 53 (3) (2012) 559 -564

[13]    Lukiyanchuk IV, Rudnev VS, Kuryavyi VG, Boguta DL, Bulanova SB, Gordienko PS, Surface morphology, composition and thermal behavior of tungsten-containing anodic spark coatings on aluminum alloy. Thin Solid Films, 446 (2004) 54-60.

[14]    Rudnev VS, Lukiyanchuk LV, Baguta DL, Kon'shin VV, Rudnev AS, Gordienko PS, Sparkanodic oxide coatings formed on Al and Ti alloys in tungstate-containing phosphate-vanadate bath. Protection of Metals, 38[2] (2002) 191-195.

[15]    Lukiyanchuk LV, Rudnev VS, Kuryavyi VG, Gordienko PS, Anodic –spark layers on aluminum and titanium alloys in electrolyte. Russian Journal of Applied Chemistry, 77[9] (2004) 1460-1468.

[16]    Tseng C-C, Lee J-L, Kuo T-H, Kuo S-N, Tseng K-H, The influence of sodium tungstate concentration and anodizing conditions on microarc oxidation (MAO) coatings for aluminum alloy. Surface & Coatings Technology, 206 (2012) 3437-3443

[17]    Zhang C, Zhu l, Zhang Y, Ma J, Effect of several inorganic additives on microstructure and properties of microarc oxidation on aluminum alloy. Corrosion Science and Protection Technology, 25[6] (2013) 483-488.

[18]    He J, Luo Q, Cai Q, Li XW, Zhang DQ, Microstructure and photocatalytic properties of WO3/TiO2 composite films by plasma electrolytic oxidation. Materials Chemistry and Physics, 129 (2011) 242– 248

[19]    Wu X-Q, Xie F-Q, Hu Z-C, Wang L, Effects of additives on corrosion and wear resistance of microarc oxidation coatings on TiAl alloy. Transactions of Non-Ferrous Metal Society of China (English Edition), 20[6] (2010) 1032-1036.

[20]    He J, Cai QZ, Ji YG, Luo HH, Li DJ, Yu B, Influence of fluorine on the structure and photocatalytic activity of TiO2 film prepared in tungstate-electrolyte via micro-arc oxidation. Journal of Alloys and Compounds, 482 [1–2] (2009) 476-481.

[21]    Cui Z, Shao Z, Liu Z, Zhao L, Tian Y, Effect of additives on properties of ceramic coatings formed by micro-arc oxidation on AZ91D Mg alloy. Chinese Journal of Materials Research, 23[2] (2009) 193-198.

[22]    Zhao F, Liao AD, Zhang RF, Zhang SF, Wang HX, Shi XM, Effects of sodium tungstate on properties of micro-arc coatings on magnesium alloys. Trans Nonferrous Met Society China, 20 (2010) S683−687.

[23]    Li Z, Yuan Y, Sun P, Jing X. Ceramic coatings of LA141 alloy formed by plasma electrolytic oxidation for corrosion protection. ACS Applied Materials & Interfaces, 3 (2011) 3682–3690.

[24]    Ding J, Liang J, Hu L, Hao J-C, Xue Q-J, Effect of sodium tungstate on characteristics of microarc oxidation coatings formed on magnesium alloy in silicate-KOH electrolyte. Transactions of Non-Ferrous Metal Society of China, 17 (2007) 244-249.

[25] Sreekanth D, Rameshababun, Choudary KR, Rao KP, The role of electrolyte additives on the corrosion behaviour of ceramic coatings formed on ZM21 magnesium alloy by plasma electrolytic oxidation. Materials Science Forum, 710 920120 683-688.

[26] Hussein RO, Northwood DO and Nie X, The influence of pulse timing and current mode on the microstructure and corrosion behaviour of a plasma electrolytic oxidation (PEO) coated AM60B magnesium alloy. J. of Alloys and Compounds, 541 (2012) 41-48.

[27] Hussein RO, Nie X, Northwood DO, An investigation of ceramic coating growth mechanisms plasma electrolytic oxidation (PEO) processing. Electrochimica Acta, 112 (2013) 111– 119

[28] Ikonopisov S, Theory of electrical breakdown during formation of barrier anodic films. Electrochimica Acta, 22 (1977) 1077-1082.

[29] Zheng HY, Wang YK, Li BS, Han GR, The effects of Na2WO4 concentration on the properties of microarc oxidation coatings on aluminum alloy. Materials Letters, 59 (2005) 139-142.

[30] Hwang I J, Shin K R, Lee J S, Ko G Y, D. Shin H, Formation of Black Ceramic Layer on Aluminum Alloy by Plasma Electrolytic Oxidation in Electrolyte Containing Na2WO4. Materials Transactions, 53[3] (2012) 559 – 564.

[31] Liang J, Guo B, Tian J, Liua H, Zhou J, Liu W, Xu T, Effects of NaAlO2 on structure and corrosion resistance of microarc oxidation coatings forme on AM60B magnesium alloy in phosphate–KOH electrolyte. Surface & Coatings Technology, 199 (2005) 121 – 126

[32] Khaselev O, Weiss D, Yahalom J, Structure and composition of anodic films under continuous sparking. Corrosion Science, 43 (2001) 1295–1397.

[33] Curran J A, Clyne T W, Porosity in plasma electrolytic oxide coatings. Acta Materialia, 54 (2006) 1985–1993.

# CHAPTER 11

# CONCLUSIONS AND FUTURE WORK

## 11.1 General conclusions.

Current coating schemes are complex, multilayer systems that incorporate many different technologies and must be conducted very carefully in order to adequately protect magnesium and magnesium alloys from wear and corrosion in harsh service conditions. In order to achieve higher levels of protection, one of the most promising coating methods is the PEO technique.

This work has afforded us a greater understanding of the process mechanisms, particularly the plasma discharge behaviour. Quantitative studies have been performed relating processing to performance. It has been confirmed that a PEO processing of Mg alloys is strongly influenced by such parameters as electrolyte composition and concentration, current mode (unipolar, bipolar and hybrid (combination of both)) and substrate alloy (AM60B, AJ62 and AZ92D Mg-alloys). Generally, these parameters have a direct influence on the discharge behavior: type, size, duration, population density and temperature. The discharges play an essential role in the formation, and resulting composition of the 3-layer oxide structure, by influencing phase transformations, crystallization and sintering. This, then, affects the physical, mechanical and chemical properties of the coating. For PEO-coated materials, the primary enhancement of the corrosion and wear resistance comes from the 3-layer oxide structure (outer porous layer, dense intermediate layer, and dense interface layer), particularly the inner, dense barrier layer, but also the relatively dense intermediate layer.

## 11.2 Key findings

The key findings from this research can be divided into three main topic areas, namely:

A. Plasma Discharge Effects on Microstructure of Coating.

B. Coating Growth Mechanisms

C. Relationships between Processing Parameters and Performance (Corrosion and Wear).

## A. Plasma Discharge Effects on Microstructure of Coating:

In this topic area, the effects of (1) current mode, (2) current density, (3) magnesium alloy composition and (4) electrolyte concentration and composition were studied. The main conclusions were:

- Controlling or reducing the strong discharges (by bipolar current mode, appropriately controlling the ratio of the positive to negative pulse currents as well as their timing) had a significant positive effect on the plasma temperature profiles and leads to denser inner layer microstructures with less porosity.

- The fluctuations in the measured line intensities (different spike) support the discharge model and the resulting coating microstructures.

- Plasma electron temperatures were found to be in the range of 5000 - 7000 K for the unipolar case, 5200 - 6600 K for the bipolar case, 5500 – 7500K for the hybrid1 (unipolar followed by bipolar) case and 4200 – 7500 K for hybrid2 (bipolar followed by unipolar) case.

- The order of the combined current modes is essential, hybrid1 case improves the coating quality compared to other cases as the bipolar mode acts to repair the damage caused by the unipolar mode.

- A bipolar current mode improves the coating quality compared to the unipolar mode in terms of having a dense inner layer with fewer defects.

- The results showed that the anions in the electrolyte solution directly contributed to the coating formation process. Apart from MgO which is a common phase in the coatings, a specific phase, $MgAl_2O_4$, resulted from the aluminate electrolyte.


## B. Coating Growth Mechanisms

Processes including melting, melt-flow, re-solidification; diffusion, sintering and densification of the growing oxide are parts of the PEO coating growth process. The main conclusions are:

- In PEO process, the ceramic coating grows inwards to the alloy substrate

(inner layer) and outwards to the coating surface (outer layer) simultaneously. During the early stages, the coating grows mainly outwards. After the coating reaches a certain thickness the inner layer grows faster than the outer layer. However, at this time, the coating thickness continues to increase in both directions.

- The rates of growth of the outer and inner oxide layers are process parameter dependent. They result from a combination of three processes namely, (i) discharge processes, (ii) partial destruction of the outer layer due to strong discharges and (iii) diffusion process.

- Oxygen diffusion into the Mg-alloy substrate plays a leading role in coating growth. The growth rate of the coating is influenced by the plasma temperature, which enhances the rate of oxygen transport into the magnesium substrate.

**C. Relationships between Processing Parameters and Performance (Corrosion and Wear).**

A schematic describing these general relationships is given in Fig 11.1. The main conclusions are:

- The PEO process of Mg alloys is strongly influenced by such parameters as electrolyte composition and concentration, current or voltage applied and substrate alloy.

- Generally, these parameters have a direct influence on the discharging behavior: type, size, duration, population density and temperature.

- The discharges play an essential role in the formation and resulting composition of the 3-layer oxide structure, by influencing phase transformations, crystallization and sintering.

- This, then, affects the physical, mechanical and chemical properties of the coating.
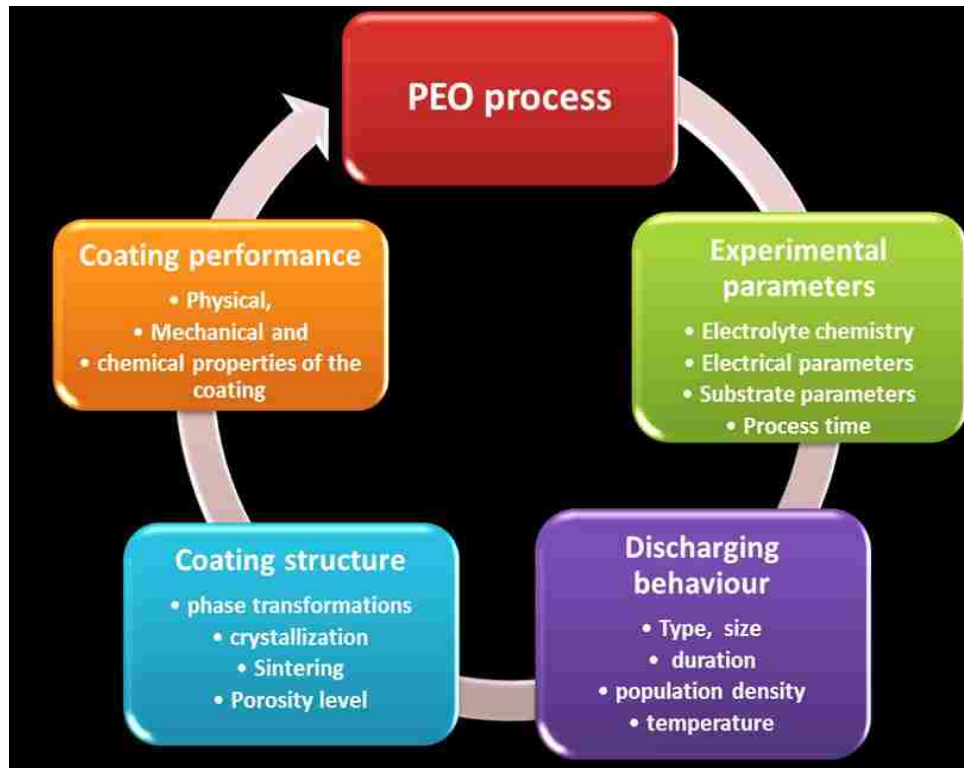
Fig 11.1 PEO process properties, mechanisms and performance [reproduced from Figure 10.1 in Chapter 10]

## 11.4    Major Advances:

The major advances from this work are in two areas:

### 11.4.1  Related discharge behaviour to coating formation mechanisms

- Plasma discharge characteristics including temperature, density and composition during discharge (relates to incorporation of elements from substrate and electrolyte) were identified using OES.
- Demonstrated that the PEO coatings grow in both the outward direction towards the surface and into the substrate. Developed a model for this coating growth that includes oxygen transport into the Mg alloys which is dependent on the plasma temperature.
- Controlling the strong B-type discharges had a significant positive effect on the plasma temperature profile and lead to denser inner layer microstructures with less porosity.

**11.3.2 Developed Processing-Structure-Performance relationships.**

- For PEO-coated materials, the primary enhancement of the wear and corrosion resistance comes from the 3-layer oxide structure: outer porous layer, intermediate layer and inner dense (barrier) layer.
- Relative thickness, microstructure and composition of the layers depends on both the material and the PEO processing parameters.
- The corrosion performance is more closely related to the protective nature of the dense oxide layer at the coating–substrate interface.
- The wear performance is effected mainly by intermediate layer. Since the coating is integral with the substrate, there is good adhesion.

**11.4 Suggestions For Future Work**

There exists significant potential for further work. Most importantly an examination of the voltage and current profiles during each discharge cycle needs to be done for understanding and developing a correlation between discharging behaviour (concentrating on the reduction of the strong discharge (type-B)) with coating microstructural and phase composition over a range of experimental conditions. Based on the results of the present study, the following suggestions are made for future work:

- An understanding and improvement of the process optimization, repeatability and efficiency.
- New experiments sets are required to give a physical interpretation of the EIS results and the equivalent circuits used.
- Investigate the possibility of achieving specific coating characteristics, e.g. reproducible and uniform coating thickness on complex-shape substrates by incorporating the OES technique into the PEO process control module.
- A promising new research direction lies in the selection of methods which could lower the discharging voltage, and eventually lower the energy consumption.
- Understanding the initiation step of the discharge events and the nonlinear growth rate of the oxide ceramic layer during early stage of the PEO coating is a key aspect of discharge behaviour which is not yet fully understood.

- Further improvement of the corrosion resistance mainly after longer immersion time, particularly by producing composite coatings, by co-deposition of materials including polymers and organic materials, within the PEO layers.

**VITA AUCTORIS**

NAME:                  Riyad Hussein

PLACE OF BIRTH:   Baghdad, Iraq

YEAR OF BIRTH:   1963

Education:             Baghdad University, Iraq

                        1981-1985 B.Sc. in Physics

                        Strathclyde University, U.K.

                        1986-1990, PhD in Plasma physics

                        University of Windsor, Canada

                        2008-2010, M. A. Sc. In Engineering Materials

                        University of Windsor, Canada

                        2011-2015, PhD in Engineering Materials.

# PUBLICATIONS DURING Ph.D. STUDY.

| BOOK AND BOOK CHAPTERS |
|---|

- Production of anti-corrosion coatings on light alloys (Al, Mg, Ti) by Plasma Electrolytic Oxidation (PEO), **Riyad O. Hussein,** Derek O Northwood, 'In: Developments in Corrosion Protection, (M. Aliofkhazraei, Ed.) InTech Open Publishers, ISBN 980-953-307-1100-2. **2013**

## JOURNAL PAPERS:

1. **Hussein R. O.**, Nie X. and Northwood D. O. (**2015**), Plasma electrolytic oxidation (PEO) coatings on Mg-alloys for improved wear and corrosion resistance, WIT Transactions on Engineering Sciences, 91, 163-176. (invited paper)
2. **Hussein R. O.,** Northwood D. O., (**2014**) Improving the performance of magnesium alloys for automotive applications, WIT Transactions on the Built Environment, 137, 531-544.
3. **Hussein R. O.,** Northwood D. O. and Nie X. (**2014**) Processing-Microstructure Relationships in the Plasma Electrolytic Oxidation (PEO) Coating of a Magnesium Alloy, Materials Sciences and Applications (MSA), 5 (3), pp. 124-139.
4. **Hussein,R.O.,** Nie, X., and Northwood, D.O., (**2014**) Processing-Structure-Properties-Performance Relationships for Mg-Alloys Coated Using Plasma Electrolytic Oxidation (PEO) Method, Materials Forum, 37, In press.
5. **Hussein R. O.,** Northwood D. O. and Nie X. (**2013**) The effect of processing parameters and substrate composition on the corrosion resistance of plasma electrolytic oxidation (PEO) coated magnesium alloys**,** Surface & Coatings Technology, 237, pp. 357-368.
6. **Hussein R. O.,** Nie X. and Northwood D. O. (**2013**) An investigation of ceramic coating growth mechanisms in Plasma Electrolytic Oxidation (PEO) processing, Electrochimica Acta 112, pp. 111-119.
7. **Hussein R. O.,** Nie X. and Northwood  D. O. (**2013**), The Application of Plasma Electrolytic Oxidation (PEO) to the Production of Corrosion Resistant Coatings on Magnesium Alloys: a Review, Corrosion and Materials 38 (1), pp. 53-63. **David Whitby Best Review Paper Award 2013, Australian Corrosion Association**
8. **Hussein R. O.,** Northwood D. O., Su, J.F. and Nie X. (**2013**) A study of the interactive effects of hybrid current modes on the tribological properties of a PEO (plasma electrolytic oxidation) coated AM60B Mg-alloy, Surface & Coating technology, 215 (2013) 421–430**.**
9. **Hussein R. O.,** Northwood D. O. and Nie X. (**2012**) The influence of pulse timing and current mode on the microstructure and corrosion behaviour of a plasma electrolytic oxidation (PEO) coated AM60B magnesium alloy, Journal of Alloys and Compounds, 541 , pp. 41-48.
10. **Hussein R. O.**, Nie X. and Northwood D. O. (**2012**) A spectroscopic and microstructural study of oxide coatings produced on a Ti-6Al-4V alloy by Plasma Electrolytic Oxidation, J. of Materials Chemistry and Physics, 134 (1) , pp. 484-492.
11. Wang Z., Nie X., Hu H., **Hussein R. O.,** (2012) In situ fabrication of blue ceramic coatings on wrought Al Alloy 2024 by plasma electrolytic oxidation,  Journal of

Vacuum Science and Technology A: Vacuum, Surfaces and Films, 30[2], Article number 021302.

12. **Hussein R.O.**, Zhang P., Northwood D.O. and Nie X. **(2011)** Improving the corrosion resistance of magnesium alloy AJ62 by a plasma electrolytic oxidation (PEO) coating process Corrosion and Materials 36 (3), pp. 38-49.

13. **Hussein R.O.**, Zhang P., Xia Y., Nie X. and Northwood D.O **(2011)** The effect of current mode and discharge type on the corrosion resistance of plasma electrolytic oxidation (PEO) coated magnesium alloy AJ62, Surface & Coatings Technology, 206 (7) , pp. 1990-1997.

## PEER REVIEWED CONFERENCE PAPERS

14. **Hussein R. O.,** Nie X. and Northwood D. O. (2014) The roles of the electrolyte composition and concentration on the corrosion resistance of the oxide coatings formed on AZ91D magnesium alloy by plasma electrolytic oxidation, Corrosion and Prevention 2014; Australia 2014; Code 109535

15. **Hussein R. O.,** Nie X. and Northwood D. O. (2014) Plasma Electrolytic Oxidation (PEO) Coatings on Magnesium Alloy AZ91D for Improved Corrosion and Wear Resistance, Combined Australian Materials Societies, CAMS2014 Conference, Sydney, Australia 26-28 November 2014, paper V1.3.

16. **Hussein R. O.,** Nie X. and Northwood D. O. **(2013)** Effect of cathodic current density on the corrosion protection of the oxide coatings formed on AZ91D magnesium alloy by plasma electrolytic oxidation. Corrosion and Prevention 2013", Australia 2013, paper no. 112.

17. Northwood D. O., **Hussein R. O.** and Nie X. (2011) Environmentally Friendly Surface Treatment of Light Alloy Materials for Automotive Applications. The 18th International Corrosion Congress in Perth, Australia 2011 2, pp. 825-836.

18. **Hussein R.O.**, Northwood D.O. and Nie X. **(2011)** An Investigation of the Influence of Hybrid Current Modes on the Plasma Behavior during Plasma Electrolytic Oxidation (PEO) Coating Process on Mg and Mg- Alloys, AVS 58th Annual International Symposium and Exhibition, paper number (353) and program number (SE+PS-WeA1) in Nashville, Tennessee, USA.